

NASA-CR-194163

## SUPERCONDUCTIVITY DEVICES: COMMERCIAL USE OF SPACE

### Annual Report

to

National Aeronautics and Space Administration  
Langley Research Center  
Hampton, VA 23665-5225

Period: July 3, 1992 - July 2, 1993

Principal Investigator:

Gene Haertling

Co-Investigator:

Eugene Furman

Supporting Investigators:

Chi-Shiung Hsi  
Guang Li

Contract No. NAG-1-1301

September 6, 1993

N94-14324

Unclas

G3/33 0185948

(NASA-CR-194163) SUPERCONDUCTIVITY  
DEVICES: COMMERCIAL USE OF SPACE  
Annual Report, 3 Jul. 1992 - 2 Jul.  
1993 (Clemson Univ.) 197 p



The Gilbert C. Robinson  
Department of Ceramic Engineering

College of Engineering

## **Table of Contents**

**Introduction**

**Part I. .... Processing and Characterization of Superconducting Thick Films**

**Part II. .... Development of PBZT, PLZT, PSZT and PMN Ceramics for Actuators**

**Part III. .... Characterization and Modeling of Rainbow Materials**

**Part IV. .... General Studies of Rainbow Processing, Properties and Devices**

**Part V. .... Presentations and Publications**

## I. Introduction

The high  $T_c$  ( $>95K$ ) superconducting ceramic materials, initially developed in 1987, are now being extensively investigated for a variety of engineering applications. These applications include such devices as conducting links, rotating and linear bearings, sensors, filters, switches, high  $Q$  cavities, magnets and motors. Some of these devices take advantage of the material's ability to lose all electrical resistance at a critical temperature ( $T_c$ ) while others make use of the repulsion forces generated between the magnetic field of a permanent magnet and a superconductor which is cooled below its  $T_c$ ; i.e., the Meissner effect.

A device involving the first of these effects; i.e., the loss of resistance at the onset of superconductivity, has been under various phases of development at Clemson University under the sponsorship of NASA Langley for the last four years. This device is a low thermal conductivity superconducting grounding link for the SAFIRE program.

A companion device to the grounding link in the SAFIRE application is the data link between the detectors and the preamps. In contrast to the former device which is a single conductor, the data link consists of a large number of electrically isolated leads of very small cross section which are designed to carry an electrical signal yet keep the thermal losses to a bare minimum. This application is obviously more demanding from a technical standpoint than the grounding link because the technologies involved in processing and fabricating small, multiple-leaded devices is considerably more complicated. A portion of the work included in this annual report involves various aspects of producing and characterizing a simple data link device; i.e., (1) screen printing of both 2223 BSCCO and 123 YBCO materials on substrates, (2) evaluation of the resulting superconducting properties and (3) the use of these materials as possible electrode materials for ferroelectrics at 77K.

In addition to this device, work is also being carried out on the development of solid-state electromechanical actuators which can be used in a number of applications in space such as cryopump motors, anti-vibration active structures and telescope mirror correctors. Considering any of these applications, the key to the successful development of a device is the successful development of a ceramic material which can produce maximum displacement per volt input. This is especially true of the cryocooler pump application where size, efficiency and reliability are of prime consideration. This report describes the work accomplished toward this goal in the past year, including (1) the fabrication and processing of high strain PBZT and PLZT electrostrictive materials, (2) the development of PSZT and PMN-based ceramics and (3) the testing and evaluation of these electrostrictive materials.

A new development effort has also been initiated in the actuator area. It consists of a new processing technology for preparing piezoelectric and electrostrictive ceramic materials. It involves a high temperature chemical reduction process which leads to an internal pre-stressing of the oxide wafer, thus the name **RAINBOW**, standing for **Reduced And Internally Biased Oxide Wafer**. Ceramics fabricated by this method produce bending-mode actuator devices which possess a factor of ten more displacement and load bearing capacity than present-day benders (unimorphs, bimorphs). This report summarizes the results obtained in the past year from studies of the RAINBOWS.

The report is divided into five parts with Part I dealing with the processing and screen printing of the superconducting BSCCO and 123 YBCO materials on substrates and PLZT ferroelectrics, Part II reporting on the electromechanical actuator compositional work, Part III dealing with the characterization of the RAINBOW devices, Part IV treating general subject areas of RAINBOWS and Part V covering presentations and publications in the last year.

**Part I.**

**Processing and Characterization of Superconducting Thick Films**

**SUPERCONDUCTIVITY DEVICES: COMMERCIAL USE OF SPACE**

**Annual Report**

**Screen Printed Y and Bi-Based Superconductors  
and  
YBCO and BSCCO Electrodes for Ferroelectric Materials**

to

**National Aeronautics and Space Administration  
Langley Research Center  
Hampton, VA 23665-5225**

**Principal Investigator:** Gene Haertling

**Supporting Investigator:** Chi-Shiung Hsi

**Contract No. NAG-1-1301**

**September 6, 1993**

## **Abstract**

A YBCO thick film containing 20% Ag<sub>2</sub>O with a  $T_c$  of 86.8K and a  $J_c$  of 108A/cm<sup>2</sup> was obtained. The film was fabricated by a two-step firing process, i. e. firing the film at 1000°C for 10 minutes and annealing at 970°C for 30 minutes. The two-step firing process, however, was not suitable for the multiple-lead YBCO sample due to the formation of the 211 green phase at 1000°C in the multiple-lead YBCO sample. A BSCCO thick film printed on a MgO coated MSZ substrate and fired at 845°C for 2 hours exhibited a superconducting behavior at 89K. Because of its porous microstructure, the critical current density of the BSCCO thick film was limited.

This report also includes the results of the YBCO and BSCCO materials used as oxide electrodes for ferroelectric materials. Extensive interaction was obtained between the PLZT 9.6/65/35 and the YBCO, and very low interaction was observed between the BSCCO and the PLZT. BSCCO superconductor on the PLZT substrate maintained its superconducting properties at liquid nitrogen temperature. The YBCO electroded PLZT showed higher remanent polarization and coercive field than the sample electroded with silver paste. A higher Curie temperature for the PLZT was obtained from the YBCO electroded sample. The BSCCO electroded sample, however, exhibited the same Curie temperature as that of a silver and Ni electroded samples. The apparent dielectric constant of the PLZT was influenced by the electroding materials. Dissipation factors of the ferroelectric samples increased when the oxide electrode was applied. Domain switching was found to be influenced by the electrode materials at low temperature. The BSCCO electroded sample showed the highest switching rate among the samples electroded by different materials.

## **I. Introduction.**

The results of two research subjects are included in this report; these are:

1. Screen Printed Y and Bi-Based Superconductors, and
2. A Novel Electroding Process for Ferroelectric Materials- YBCO and BSCCO Oxide Electrodes.

Those results are reported and discussed according to their subject.

## **II. Screen Printed Y and Bi-Based Superconductors.**

### **II.1 Introduction.**

In the previous report<sup>(1)</sup>,  $\text{YBa}_2\text{Cu}_3\text{O}_{7-x}$  superconductor thick films had been made on the YSZ substrates with  $T_c$  at 86.4K and  $J_c$  of  $50\text{A}/\text{cm}^2$ . Improvement in the electrical properties of the YBCO thick films are reported here. The YBCO thick films were printed on MSZ (Magnesium Stabilized Zirconia) substrates in order to eliminate cracks in the films. The fabrication conditions of the multiple-lead YBCO thick films were investigated in accordance with to the results of the single film process.

$(\text{Bi}_{1.6}\text{Pb}_{0.4})\text{Sr}_{1.9}\text{Ca}_{2.05}\text{Cu}_{3.05}\text{O}_x$  superconductor thick films were printed on different kinds of substrates, i.e. YSZ, BSCCO coated YSZ, MSZ, and MgO coated MSZ. The BSCCO thick films were sintered in air and a low oxygen atmosphere (6%  $\text{O}_2$ ) since a low oxygen atmosphere was found to be the best condition to maintain the BSCCO 2223 high temperature phase during sintering<sup>(2)</sup>.

### **II.2 Experimental Procedure.**

The YBCO superconductor powder was prepared by the conventional mixed oxides process<sup>(3)</sup>. The BSCCO superconductor powder was prepared by a chemical coprecipitation process. Lead, strontium, and calcium acetates were dissolved in acetic acid and water solution before they were mixed with bismuth and copper acetates. In order to dissolve the acetates, acetic acid and ammonium hydroxide were used to adjust the pH value of the mixed solution. The mixed solution became a clear blue solution after the acetates were completely dissolved. The coprecipitated powder was prepared by



pouring the acetate solution into an agitating oxalic acid solution. After coprecipitation, the slurry was dried in a vacuum dryer for 8 hours. A brown oxide powder was obtained after the dried oxalate powder was decomposed at 600°C for 4 hours. The oxide powder was calcined at 830°C for 24 hours and then calcined at 845°C for 30 hours for two additional times. After final calcination, the BSCCO superconductor powder processing was complete.

Superconductor pastes were prepared by mixing the YBCO and BSCCO superconductor powder with  $\alpha$ -terpineol in a 6:1 ratio. In order to increase adhesion of the green film, 10 wt% of binder (Metoramic Science Inc., B73305) was added to the YBCO paste and 5 wt% of binder was added to the BSCCO paste.

In the previous report<sup>(1)</sup>, YBCO thick films with 20 wt% Ag<sub>2</sub>O printed on the 8% YSZ (Yttrium Stabilized Zirconia) substrates showed higher  $T_c$  and  $J_c$  values than the films printed on the 211 (Y<sub>2</sub>BaCuO<sub>5</sub>) and SNT (Sr<sub>0.875</sub>(Ti<sub>0.75</sub>Nb<sub>0.25</sub>)O<sub>3</sub>) substrates. However, the cracks in the film limited the  $T_c$  and  $J_c$  value of the films. In the present work, MSZ (Magnesium Stabilized Zirconia) and 16% YSZ substrates, which had higher thermal expansion coefficients than the 8% YSZ substrate, were used as substrate materials. In addition, a YBCO thick film with 30% Ag<sub>2</sub>O was also prepared in order to increase the bounding between the YBCO grains.

Zirconia-based material, which has a lower thermal conductivity, are preferred in the SAFIRE application. The zirconia-based substrates with different amounts of Y<sub>2</sub>O<sub>3</sub> or MgO additives were used as substrate materials in the process. The substrates were made by a tape casting method and fired at 1600°C for 5 hours. Since BSCCO thick films printed on MgO substrates show better electrical properties than when they are printed on the other kinds of substrates<sup>(8,9)</sup>, some of the ZrO<sub>2</sub>-based substrates used for the BSCCO thick films were coated with MgO. The dip coating process was used to coat the MgO on the ZrO<sub>2</sub> substrate. Magnesium acetate dissolved in methanol was used as the coating solution. After the MgO was deposited on the substrates, they were fired at

1550°C for 30 minutes. A BSCCO coated ZrO<sub>2</sub> substrate was also used as a substrate material. This kind of substrate was prepared by melting a thin layer of BSCCO film on the top of the ZrO<sub>2</sub> substrate at 890°C for 20 minutes.

The superconductor thick films were deposited on the substrates by printing the pastes through a 200 mesh stainless steel screen. Two kinds of patterns, single and multiple-lead, were printed on the substrates. The single sample size was 1 cm wide and 4 cm long. The multiple-lead sample had 15 lines. The size of each line was 20 mils width and 1500 mils long. The space between each lines was 20 mils.

The YBCO thick films were sintered at 960 to 990°C for 5 minutes to 1 hour, in an oxygen atmosphere. After sintering, the samples were cooled to room temperature at a 2° C/min rate. A two step firing process was also used to fire the YBCO thick film. The firing conditions of the two step firing process were 1000°C for 10 minutes and 970°C for 30 minutes. The BSCCO films were fired at temperature from 830° to 855°C for 10 minutes to 4 hours in air or 8% oxygen atmosphere. After the YBCO films were fired, electrodes (as determined in a previous contract No. NAG-1-820), were applied to the YBCO thick films. Silver electrodes were fired onto the BSCCO thick films at 845°C for 12 minutes.

Critical temperatures of the samples showing zero resistance,  $T_c$ , were measured by the four-point method. The  $J_c$ s of the films were measured at 1  $\mu$ V/cm level at 77K.

## **II.3 Results and Discussion.**

### **II.3.1 YBCO thick films printed on zirconia-based substrates.**

A YBCO thick film with 30 wt% Ag<sub>2</sub>O was printed on 8% YSZ substrate and fired at 990°C for 10 minutes. The film had lower resistivity than the films with 10 or 20 wt% Ag<sub>2</sub>O, at room temperature. During the critical temperature measurement, the resistance of the film decreased with decreasing measuring temperature. The film showed

an onset behavior at 96K, as indicated by the curve a in Figure 1. However, the film was not in the superconducting state at liquid nitrogen temperature.

The YBCO thick film with 20 wt% Ag<sub>2</sub>O printed on the MSZ substrate and fired at 980°C for 10 minutes had a lower resistivity than the film printed on the YSZ substrate. From the sample's x-ray diffraction result, partial preferred orientation in the (001) direction was observed, as shown in Figure 2. Metallic behavior was observed during the critical temperature measurement, as presented by curve b in Figure 1. The YBCO film on the MSZ substrate, however, was not in the superconducting state at liquid nitrogen temperature. There was no onset temperature observed from the  $T_C$  measurement of this sample.

When the YBCO thick film was printed on the 16% YSZ substrate, a Y<sub>2</sub>BaCuO<sub>5</sub> green phase was observed after the film was fired at 980°C for 30 minutes. A YBCO thick film printed on a 8% YSZ substrate and fired at the same conditions as the previous sample had a  $T_C$  at 84.4K. Serious interaction between the YBCO thick film and the 16% YSZ substrate occurred at 980°C. Increasing the Y<sub>2</sub>O<sub>3</sub> content in the YSZ substrate resulted in an increased reaction rate between YBCO and YSZ substrate. Therefore, the MSZ and 16% YSZ substrate would not be appropriate substrate materials for the YBCO superconductor thick films.

### **II.3.2 Two steps firing process.**

Figure 3 presents the  $T_C$  curve of a sample heat-treated by a two step firing process. The YBCO film was melted at 1000°C in the first step and, then, was annealed at 970°C for 30 minutes in the second step. The film crystallized and possessed partial preferred orientation during second step annealing, as shown in Figure 4. This film had a  $T_C$  of 86.8K at a 1mA measuring current. The  $J_C$  of the film was 108 A/cm<sup>2</sup>, which was about two times the  $J_C$  value obtained by the single step firing. The increase in  $T_C$  and  $J_C$  might be caused by the elimination of cracks, since the resistivity of the film, at room temperature, was lower than the film made by the single step process.

### **II.3.3 YBCO multi-lead sample.**

Multiple-lead YBCO thick films with 10 or 20wt% Ag<sub>2</sub>O were printed on the 8% YSZ substrates. The multiple-lead films were sintered by a one- or two-step process. When the films were sintered by the two-step process, i. e. firing at 1000°C for 10 minutes and annealing at 970°C for 30 minutes, a 211 (Y<sub>2</sub>BaCuO<sub>5</sub>) green phase appeared on the film surface. The 211 green phase was still observed in the film when the firing conditions were changed to 1000°C for 5 minutes and annealing at 960°C for 30 minutes. At firing temperatures higher than 990°C, the YBCO 211 green phase formed in the multiple-lead YBCO sample. The two-step firing process, which had a firing temperature at 1000°C in the first firing step, was not an appropriate fabrication process for the multiple-lead YBCO sample.

The YBCO 211 green phase was not observed in the multiple-lead thick films when the firing temperature was lower than 990°C. Figure 5 shows the T<sub>c</sub> curve of a multiple-lead YBCO thick film printed on 8% YSZ substrate and fired at 985°C for 12 minutes. The film had a T<sub>c</sub> of 86.3K at 20μA measuring current. When the measuring current increased to 50μA, the critical temperature of the sample decreased to 82.3K. Table 1 lists the critical temperatures of the YBCO multiple-lead thick films fired at different conditions. Relatively high critical temperature samples were obtained when the samples were fired at 980°C for 12 minutes. The highest J<sub>c</sub> of the multiple-lead thick films were obtained from the films with 10wt% Ag<sub>2</sub>O and fired at 980°C for 12 minutes; i.e., 0.9 A/cm<sup>2</sup>.

### **II.3.4 BSCCO thick film printed on YSZ substrate.**

Although there was no second phase found from the x-ray diffraction pattern of the films, the BSCCO thick films printed on the YSZ substrates were not in the superconducting state at liquid nitrogen temperature after they were sintered at 830 to 850°C for 1 to four hours. When the film was fired at temperature higher than 860°C, the BSCCO 2212 phase was observed. The films also exhibited semiconducting behavior in

the critical temperature measurement. Serious interaction was observed between the BSCCO thick film and YSZ substrate. In order to eliminate the interaction between the BSCCO thick films and YSZ substrates, MgO coatings were applied to the YSZ substrates. The YSZ substrates became brittle after being coated with 10 layers of MgO. Deformation of the coated substrate was also observed after it was fired at 1550°C for 30 minutes. They were easily broken during the printing process.

A thin layer of BSCCO was coated on the YSZ substrate by a dip coating process and fired at 880°C for 10 minutes. The thin BSCCO film showed a preferred orientation in the (001) direction of the BSCCO 2212 phase, as shown in Figure 6. A BSCCO thick film deposited on the BSCCO coated YSZ substrate and fired at 845°C for 60 minutes possessed a critical temperature of 88.4K, as revealed by Figure 7. The BSCCO thin film coated on the YSZ substrate was found to be a high conductivity material, and thus, YSZ was not considered as an appropriate substrate material for the SAFIRE application.

### **II.3.5 BSCCO thick film on MSZ substrate.**

The electrical properties of the BSCCO thick films were improved, when the films were fired in an 8% oxygen atmosphere. A BSCCO thick film printed on MSZ substrate and fired at 845°C for 2 hours had a  $T_c$  of 82K at 20 $\mu$ A measuring current. The BSCCO thick film printed on MSZ substrate did not show superconducting behavior at liquid nitrogen temperature when it was heat-treated at 845°C for 2 hours in air. The improvement in the electrical properties of the BSCCO thick films was also enhanced by applying a MgO buffer layer between the BSCCO superconductor and the MSZ substrate. Figure 8 shows the  $T_c$  curve of a BSCCO thick film printed on a MSZ substrate with 5 layers MgO coating. The film was fired at the same conditions as the former sample, which had no MgO buffer layer. The critical temperature of this film increased to 89K at 20 $\mu$ A measuring current, which was 7K higher than the sample without the MgO buffer layer. The film consisted of a BSCCO 2223 phase as shown by the x-ray diffraction pattern in Figure 9. The BSCCO superconductor thick films usually had relatively low

critical currents and critical temperatures when they were sintered at 845°C. It might be because of a porous microstructure in the film as seen in Figure 10. A more dense microstructure was obtained from the film fired at 860°C or higher, as shown in Figure 11. The crystal structure of the film sintered at 860°C, however, was a BSCCO 2212 phase, which has a lower critical temperature than the BSCCO 2223 phase. Therefore, the best firing conditions of the BSCCO thick films printed on YSZ substrates were at 845°C for 1 to 2 hours in low oxygen atmosphere. Applying the MgO buffer layer was also recommended.

## II.4 Summary.

The following is the summary of the fabrication conditions for the YBCO and BSCCO thick films printed on the Zirconia-based substrates:

### 1. YBCO thick film.

Substrate material : 8% YSZ.

Film composition :  $\text{YBa}_2\text{Cu}_3\text{O}_{7-x}$ .

Firing condition

Heating rate : 3°C/min.

Firing temperature : 990°C, 10 minutes.

Cooling rate : 2°C/min.

### 2. BSCCO thick film.

Substrate material : MSZ with MgO coating.

Film composition :  $(\text{Bi}_{1.6}\text{Pb}_{0.4})\text{Sr}_{1.9}\text{Ca}_{2.05}\text{Cu}_{3.05}\text{O}_x$ .

Firing condition

Heating rate : 3°C/min.

Firing temperature : 990°C, 10 minutes.

Cooling rate : 2°C/min.

### **III. The use of YBCO and BSCCO Oxide Electrodes for Ferroelectric Devices.**

#### **III.1 Introduction.**

Having a same structure as ferroelectric perovskites,  $\text{YBa}_2\text{Cu}_3\text{O}_{7-x}$  (YBCO) and  $(\text{Bi}_{1.6}\text{Pb}_{0.4})\text{Sr}_{1.9}\text{Ca}_{2.05}\text{Cu}_{3.05}\text{O}_x$  (BSCCO), which have significant higher electrical conductivity than ferroelectric materials, offer a possibility that they could be used as electrode materials for ferroelectrical materials. Also because they have similar crystal parameters and chemistry, the YBCO and BSCCO show a strong structural compatibility with ferroelectric materials. The dielectric and ferroelectric properties of a PZT thin film were reported to be improved by applying the YBCO as the bottom electrode of a thin film<sup>(4,5)</sup>. Identical results were obtained from YBCO and gold electroded PZT substrates<sup>(6)</sup>.

In this report, the electrical properties, i. e. dielectric and ferroelectric properties, of the YBCO and BSCCO electroded ferroelectric materials are included. The superconducting properties of the YBCO and BSCCO films on the substrates were investigated. The interaction between the PLZT and oxide electrodes and the superconducting properties of the YBCO and BSCCO films were also studied.

#### **III.2. Experimental Procedure.**

Ferroelectric ceramics of compositions PLZT(9.5/65/35) and PBNZT (8/2/55/45) were used as substrate materials in this study. Electrode materials used were  $\text{YBa}_2\text{Cu}_3\text{O}_{7-x}$ ,  $(\text{Bi}_{1.6}\text{Pb}_{0.4})\text{Sr}_{1.9}\text{Ca}_{2.05}\text{Cu}_{3.05}\text{O}_x$ , and silver paste(Du Pont 7095). The YBCO and BSCCO powders were prepared by conventional mixing oxide processes<sup>(1,3)</sup>. The YBCO powder was also mixed with  $\text{Ag}_2\text{O}$  in ratios of 30% $\text{Ag}_2\text{O}$  : 70%YBCO and 50% $\text{Ag}_2\text{O}$  : 50%YBCO. The electrodes were applied to the ferroelectric materials by a painting process. Oxide pastes were prepared by mixing the YBCO or BSCCO with  $\alpha$ -terpineol in a 3:1 ratio. Ni electrodes were prepared by an electroless

plating technique. According to the electrode materials applied and the type of the substrate used, the firing conditions of the electrodes were determined. The silver electrodes were fired at 550°C for 30 minutes. The YBCO electrodes were fired at a temperature from 920 to 940°C for 30 minutes to 2 hours. The BSCCO electrodes were heat-treated at temperature from 840 to 870°C for 1 to 2 hours. Dielectric constant vs. temperature and dissipation factor vs. temperature of the samples were measured. The P-E loops of the samples were measured in the temperature range from room temperature (22°C) to liquid nitrogen temperature (-195.5°C). The interaction between the YBCO and BSCCO oxide electrodes and PLZT ceramics was studied by observing the x-ray diffraction pattern of a mixture of the respective oxide powder with the PLZT powder. The mixed powders were pressed into pellets and firing at the same conditions as those used for the electrode preparation processes. The superconducting properties of the oxide electrodes were measured by a four-point probe method.

### **III.3 Results and Discussion.**

#### **III.3.1 Silver electrodes on PLZT (9.5/65/35).**

In order to investigate the influence of the oxide electrodes on the ferroelectric material, the properties of the ferroelectric materials with silver electrodes were used as references for the properties of the oxide electroded samples. Figure 12 shows the P-E loops of a silver electroded sample at different temperatures. At room temperature, this sample was similar to a slim loop ferroelectric since it had only a small memory. When the measuring temperature was lowered to -80°C, the sample exhibited more ferroelectric behavior which was caused by a phase transformation in the material. The remanent polarization ( $P_R$ ) and coercive field ( $E_C$ ) of the sample at this temperature were 24.7  $\mu\text{C}/\text{cm}^2$  and 11.2 KV/cm, respectively. The domain switching kinetics, however, were retarded by lowering the measuring temperature. It took about 2 minutes to saturate the loop of the sample at -80°C compared to 10 seconds at room temperature and at 0°C.



The dielectric constants of the sample at different temperatures were indicated in Figure 13. The silver electroded sample had a Curie temperature at 50°C. Figure 13 also shows the dissipation factor of the sample as a function of temperature.

### **III.3.2 YBCO electrodes on PLZT (9.5/65/35).**

Good interfacial adhesion between the YBCO electrodes and the PLZT substrate was observed when the sample was fired at 940°C for more than 1 hour, however, when the electrodes were fired at temperatures lower than 930°C, the YBCO film showed poor adhesion. The resistivity of the YBCO film on the PLZT at room temperature was more than three order magnitude higher than the resistivity of the YBCO bulk material, and the film showed semiconducting behavior. The resistance of the YBCO film increased with decreasing temperature. A green phase of composition  $\text{Y}_2\text{BaCuO}_5$  was obtained from the sample fired at 950°C or higher.

The top x-ray diffraction pattern in Figure 14 shows the fired YBCO-PLZT mixed powder. The sample was prepared by mixing the YBCO and the PLZT powder in the weight ratio of 1:1 and was fired at 940°C for 1 hour. An insulting  $\text{Y}_2\text{BaCuO}_5$  was found as the major phase of the heat-treated powder with YBCO and PLZT as minor phases. A trace of PbO was also observed from the diffraction pattern. There are some peaks in the diffraction pattern which have not yet been identified. Extensive reaction between the YBCO and PLZT materials was observed when the materials were mixed and heated at these conditions. The high resistivity of the YBCO film formed on the PLZT substrate, therefore, is believed to be due to the formation of  $\text{Y}_2\text{BaCuO}_5$  phase at YBCO-PLZT interface.

At room temperature, a slim loop was obtained from the YBCO electroded PLZT sample which was fired at 940°C for 1 hour. The polarization of the sample at 10 KV/cm ( $P_{10}$ ) and 20 KV/cm ( $P_{20}$ ) of this sample were 12.8 and 24.1  $\mu\text{C}/\text{cm}^2$ , respectively. When the sample was cooled to -58°C, the sample possessed a ferroelectric behavior as

indicated by the loop C in Figure 15. The retardation of the domain switching at low temperature, as seen in the silver electroded PLZT, was not observed from this sample at temperatures of  $-58^{\circ}\text{C}$  and  $-88^{\circ}\text{C}$ . These loops were plotted in about 10 seconds. When the YBCO electroded sample was cooled to  $-195.5^{\circ}\text{C}$  (LN temperature), the  $E_C$  of the sample increased to  $21.5\text{ KV/cm}$ , as listed in Table 2. It became more difficult to switch the domains of the PLZT material when the sample temperature decreased. The  $P_R$  of the sample also increased with decreasing the temperature.

Silver electrodes were painted on both sides of the YBCO electroded PLZT sample, after its electrical properties were measured. Since low contact resistance and ohmic contact interface were found in the high density silver paste (Cermalloy, C8710) and YBCO superconductor interface<sup>(7)</sup>, this paste was applied onto the YBCO electroded sample and fired at  $900^{\circ}\text{C}$  for 12 minutes. The sample became a silver-YBCO-PLZT (SYP) one dimensional composite, after the silver electrodes were fired on the sample. Figure 16 shows the P-E loops of the SYP sample at different temperatures. As a slim P-E loop was observed with the YBCO electroded sample, a slim loop was also observed with the SYP sample at room temperature. The  $P_{10}$  of the loop was  $12.0\text{ }\mu\text{C/cm}^2$ , and the  $P_{20}$  was  $21.1\text{ }\mu\text{C/cm}^2$ . When the temperature was decreased to  $-50^{\circ}\text{C}$  or lower, the P-E loop of the SYP sample had about the same remanent polarization ( $P_R$ ) value as the YBCO electroded sample. The coercive field ( $E_C$ ) of the SYP electroded sample was higher than the YBCO electroded sample. More square loops were obtained from the SYP sample than those measured from YBCO electroded sample. The  $P_R$  values of the YBCO and SYP electroded samples became constant at temperatures between  $-80$  and  $-100^{\circ}\text{C}$ . In this temperature range, the  $E_C$  values of the YBCO and SYP electroded samples still increased with decreasing temperature. For this PLZT material, the difficulty of domain switching increased with decreasing temperature. The different temperature P-E loops of a 30%  $\text{Ag}_2\text{O}$  - YBCO (SY) electroded sample, which was fired at  $930^{\circ}\text{C}$  for 1 hour, are shown in Figure 17. At the same temperature as silver and YBCO electroded

sample, the SY electroded sample had  $P_R$  and  $E_C$  values between the  $P_R$  and  $E_C$  values of those sample. Increasing the silver content in the electrodes decreased the  $P_R$  and  $E_C$  values of the PLZT material.

As can be seen from Table 2, the  $P_R$  and  $E_C$  of the PLZT samples electroded with the Ni were close to zero from room temperature to  $0^{\circ}\text{C}$ . However, the  $P_R$  and  $E_C$  of the samples electroded with the silver and YBCO-based materials increased when those sample were cool down to  $0^{\circ}\text{C}$ . At approximately  $-80^{\circ}\text{C}$ , the  $E_C$  value of the Ni electroded sample was about half of the  $E_C$  values measured from the samples electroded with the silver and YBCO-based materials. The  $E_C$  of the samples increased continuously with decreasing temperature. At liquid nitrogen temperature, the  $E_C$  values of the samples electroded with the YBCO-based materials were about  $60\text{kV/cm}$ . The  $P_R$ s of the silver and YBCO-based electroded samples increased to approximately  $25\text{ }\mu\text{C/cm}^2$  as the temperature was cooled to  $-80^{\circ}\text{C}$ . As the temperature was cooled further,  $P_R$  increased only slightly. At liquid nitrogen temperature, the sample electroded with pure YBCO had highest  $P_R$  values among the samples electroded with different materials. However, the sample electroded with silver paste had the lowest  $P_R$  value of  $28.6\text{ }\mu\text{C/cm}^2$ .

From room temperature to  $0^{\circ}\text{C}$ , all the loops measured from the samples were saturated in about 10 seconds. The domain switching kinetics were retarded by lowering the measuring temperature. The sample electroded by the silver exhibited the lowest domain switching rate at liquid nitrogen temperature. The time to saturate the loop of this sample was about 80 minutes. While domain switching was slow for silver electroded samples, relative faster domain switching was observed in the Ni and oxide electroded samples. It took about 30 minutes to saturate the loop of the Ni electroded sample. The time to saturate the hysteresis loop of the YBCO-based electroded samples decreased from 20 minutes to 2 minutes by adding  $\text{Ag}_2\text{O}$  to the electrode. The hysteresis loops of the silver, Ni and YBCO-based electroded samples at liquid nitrogen temperature are given

from Figure 18 through Figure 20. Appendix I display the hysteresis loops of the silver, Ni and YBCO-based electroded samples at different measuring temperature.

Figure 21 shows the dielectric constants of samples with Ni, silver and YBCO-based electrodes as a function of temperature. The dielectric constant of the YBCO-based electroded samples were lower than those of the silver and Ni electroded samples. The Curie temperature of the YBCO-based electrode samples increased to 80°C or higher. The dissipation factors of the samples were higher than those of the silver and Ni electroded samples at the same measuring temperature. After the electrical properties of the YBCO electroded sample were measured, the YBCO electrodes were removed from the both sides of the PLZT sample by lapping. The lapped PLZT was then coated with Ni electrodes. This sample had the same dielectric constant as the PLZT sample electroded by Ni only. The bulk of the PLZT material with the YBCO electrode maintained its structural and physical properties after removing the YBCO and electroding with Ni. Therefore, the lower dielectric constant and shift of the Curie temperature measured from the YBCO electroded sample was attributed to the formation of a interfacial layer between the PLZT and the electrodes. This interface lowered the apparent capacitance of the sample by having the effect of forming a capacitor in series with the unreacted PLZT. With this lower apparent capacitance, the calculated dielectric constant was lower. In addition, because of the formation of the second phase, the dissipation factors of the YBCO electroded samples were higher than for the samples with the Ni and silver electrodes, as shown in Figure 22.

### **III.3.3 BSCCO electrodes on PLZT (9.5/65/35).**

A BSCCO electroded PLZT sample, which was fired at 845°C for 2 hours, exhibited metallic behavior and was in a superconducting state at 85.5K as revealed by Figure 23. This sample possessed a slim P-E loop at room temperature as shown in Figure 24. The  $P_{10}$  and  $P_{20}$  values of the sample were 13.3 and 24.6  $\mu\text{C}/\text{cm}^2$ , respectively.

Figure 25 shows the dielectric constant and dissipation factor of the sample at different temperatures. The BSCCO electroded sample had a Curie temperature of 50°C which was the same as the Curie temperature of the silver and Ni electroded samples. After the PLZT-BSCCO mixed powder was fired at 860°C for 18 minutes, there was no second phase found from the x-ray diffraction pattern of the mixed powder, as indicated by the bottom x-ray diffraction pattern in Figure 14. Very low reaction between the PLZT and the BSCCO was observed from the mixture. This low reaction allowed the BSCCO to maintain its superconductivity on the PLZT substrate. The interface between the BSCCO electrode and the PLZT, therefore, had less influence on the PLZT properties than the YBCO-PLZT interface. The dissipation factor of the BSCCO electroded PLZT was higher than the silver electroded sample.

At liquid nitrogen temperature, the BSCCO electroded sample had the lowest  $E_C$  value of 44.6 kV among all the sample prepared in this research. The  $P_R$  value of the BSCCO electroded sample at liquid nitrogen temperature was 34.5  $\mu\text{C}/\text{cm}^2$ . The fastest domain switching was found from the sample electroded with the BSCCO material. The time to saturate the loop of the sample was only 20 seconds. The hysteresis loop obtained from this sample is shown in Figure 26.

### **III.3.4 YBCO electrode on PBZNT**

Figure 27 shows the room temperature P-E loops of the PBZNT substrates electroded with silver paste and YBCO. The same results were obtained from the silver electrode and YBCO electroded samples. The YBCO electrode was fired at 920°C for 1 hour. When the YBCO electrode on the PBNZT was fired at 930°C or higher, the electrode became green, which was due to formation of 211 ( $\text{Y}_2\text{BaCuO}_5$ ) phase.

The  $E_C$  values of the YBCO electroded PBNZT increased from 12 kV/cm to about 30 kV/cm when the measuring temperature decreased from room temperature to -80°C. The  $P_R$ s of the samples remained constant at different temperature, while the

hysteresis loops of the samples became square with decreasing the measuring temperature. The P-E loops of YBCO electroded PBZNT substrates at different temperatures are displayed in Appendix II.

#### **III.4 Summary.**

The followings is a summary of the results obtained:

1. BSCCO showed strong possibilities to be used as an electrode materials for ferroelectric devices, especially at liquid nitrogen temperature.
2. Reaction between the PLZT and YBCO electrode influenced the ferroelectric properties and dielectric constant of the PLZT (9.5/65/35).
3. Higher dissipation factor was obtained from the oxide electroded sample.
4. BSCCO electroded PLZT showed the fastest domain switching.
5. Because very little reaction was found between the BSCCO and PLZT, the PLZT materials could also be considered as substrates for BSCCO superconductors.

**Reference:**

1. C. S. Hsi and G. H. Haertling, NASA annual report, Contract No. NAG-1-1301, 1992.
2. W. Zhu and P. S. Nicholson, Appl. Phys. Lett. 61 [6], 717-719 (1992).
3. C. S. Hsi and G. H. Haertling, NASA annual report, Contract No. NAG-1-1127, 1992.
4. R. Ramesh, A. Inam, W. K. Chan, F. Tillerot, B. Wilkens, C. C. Chang, T. Sands, J. M. Tarascon, and V. G. Keramidas, Appl. Phys. Lett., 59 [27], 3542-3544 (1991).
5. R. Ramesh, W. K. Chan, B. Wilkens, A. Inam, F. Tillerot, T. Sands, J. M. Tarascon, and V. G. Keramidas, J. Electron. Mat., 21 [5], 513-518 (1992).
6. A. Srivastava, A. Bhalla, and L. E. Cross, Ferroelectrics, 122, 234-251 (1991).
7. C. S. Hsi, G. H. Haertling, and M. D. Sherrill, Rev. Sci. Instrum., 62 [5], 1317-1320 (1991).
8. T. Hashimoto, T. Kosaka, Y. Yoshida, K. Fueki, and H. Koinuma, Jpn. J. Appl. Phys., 27, L384-L386 (1988).
9. K. Hosjino, H. Takahara, and M. Fukutomi, Jpn. J. Appl. Phys., 27, L1297-L1299 (1988).

Table 1: Critical temperature of multiple-lead YBCO thick films prepared at different temperatures.

Firing temperature( $^{\circ}\text{C}$ )	Firing time(min)	Critical temperature(K)
970	10	80
970	60	80.7
980	12	83.3
985	12	86.3



Table 2: The remanent polarization ( $P_R$ ) and coercive field ( $E_C$ ) of the PLZT (9.5/65/35) with different electrodes. The samples were measured at different temperatures.

Electrode material	<u>Firing conditions</u>		Test Temperature( $^{\circ}\text{C}$ )	$P_R(\mu\text{C}/\text{cm}^2)$	$E_C(\text{kV}/\text{cm})$
	Temp( $^{\circ}\text{C}$ )	Time(min.)			
Silver paste	550	30	22	5.0	4.5
			0	7.8	6.5
			-80	24.7	11.2
			-195.5	28.6	53.7
YBCO	940	60	22	1.2	1.0
			0	3.6	2.5
			-58	22.0	17.0
			-88	26.5	21.5
			-195.5	40.0	60.5
30% $\text{Ag}_2\text{O}$ -YBCO	930	60	22	3.0	2.0
			-50	13.0	6.5
			-80	22.0	15.0
			-100	25.3	20.5
			-195.5	30.5	60.5
Ni metal	Electroless Coating		22	-	-
			0	-	-
			-50	7.8	3.5
			-80	22.8	7.6
			-100	26.9	13.8
			-195.5	30.0	46.0
BSCCO	860	18	22	-	-
			0	-	-
			-50	8.0	2.8
			-80	21.5	6.7
			-199.5	34.5	44.6

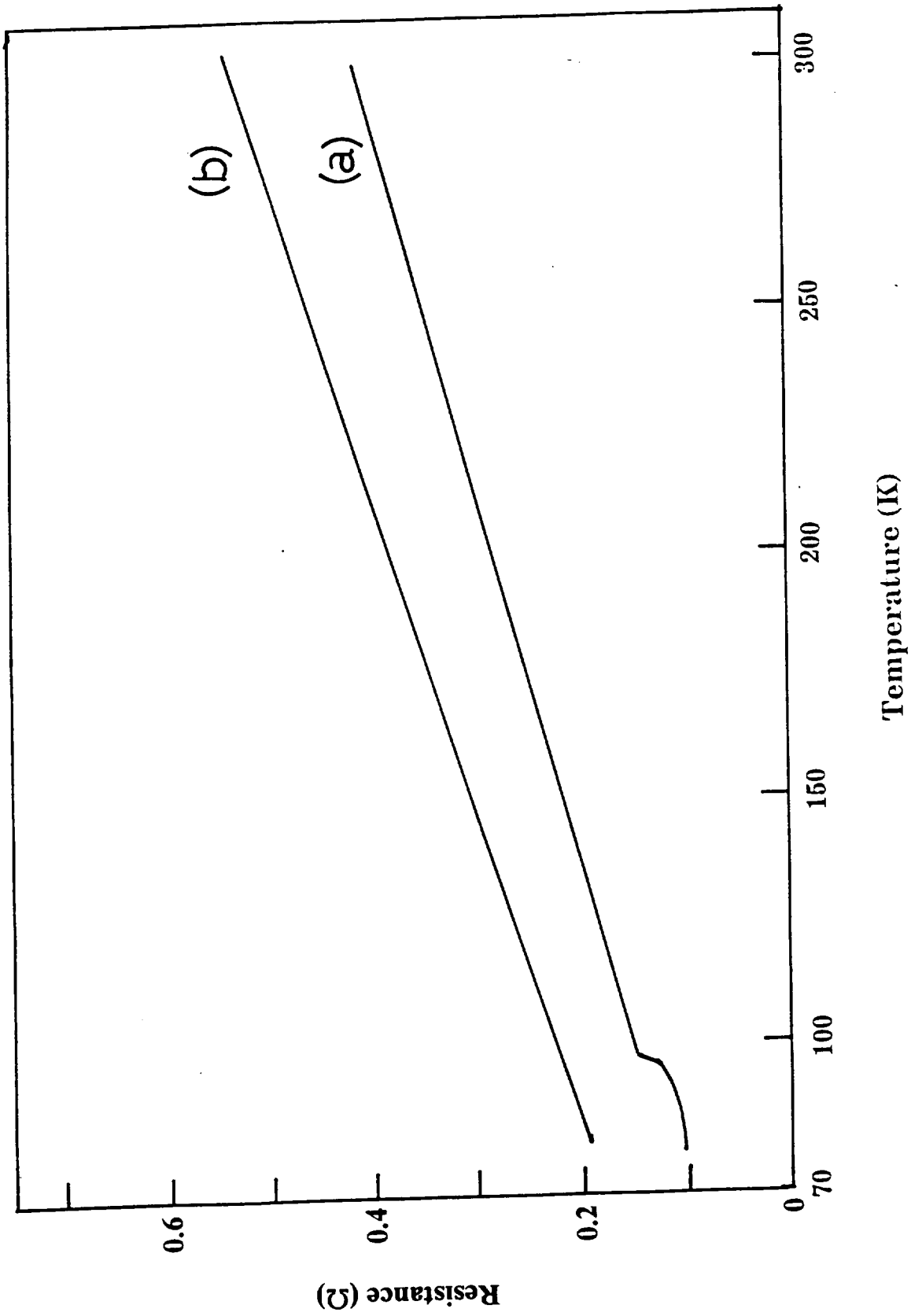


Figure 1: Resistance vs. temperature of (a) 30% $\text{Ag}_2\text{O}$ -YBCO thick film printed on YSZ and (b) 20% $\text{Ag}_2\text{O}$ -YBCO thick film printed on MSZ substrate.

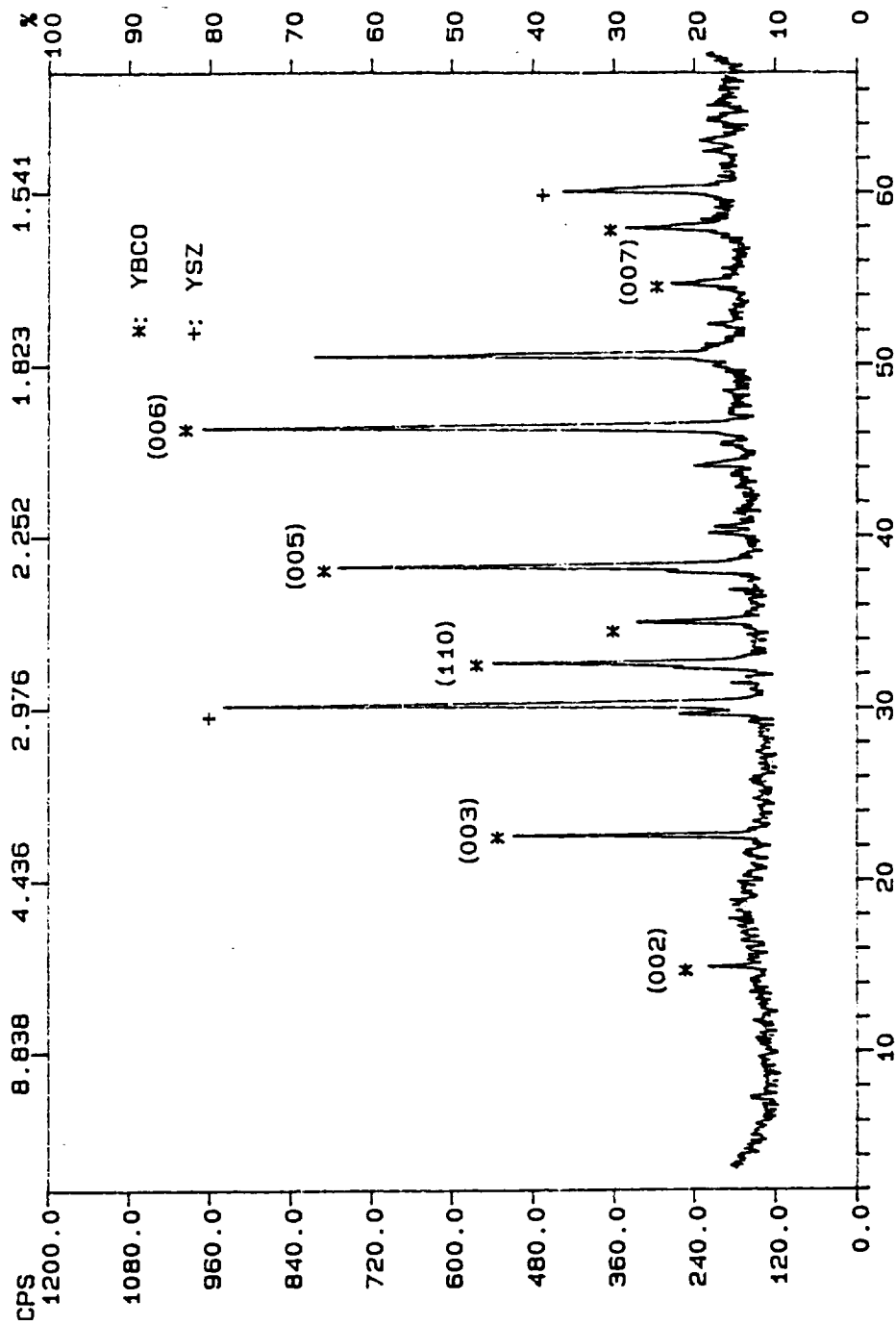


Figure 2: X-ray diffraction pattern of a 20%Ag<sub>2</sub>O-YBCO thick film printed on MSZ substrate.

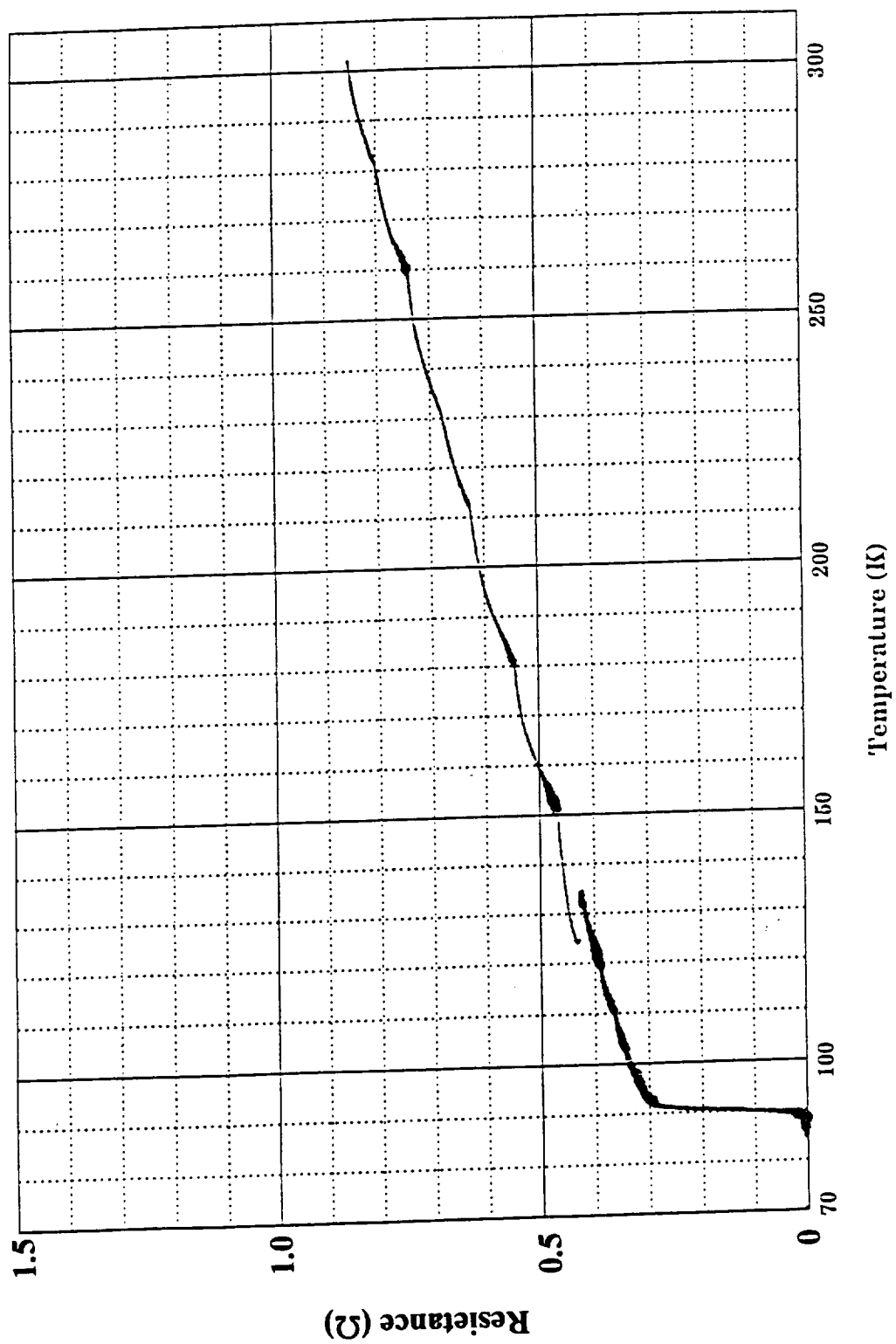


Figure 3:  $T_c$  curve of a YBCO thick film prepared by the two step firing process.

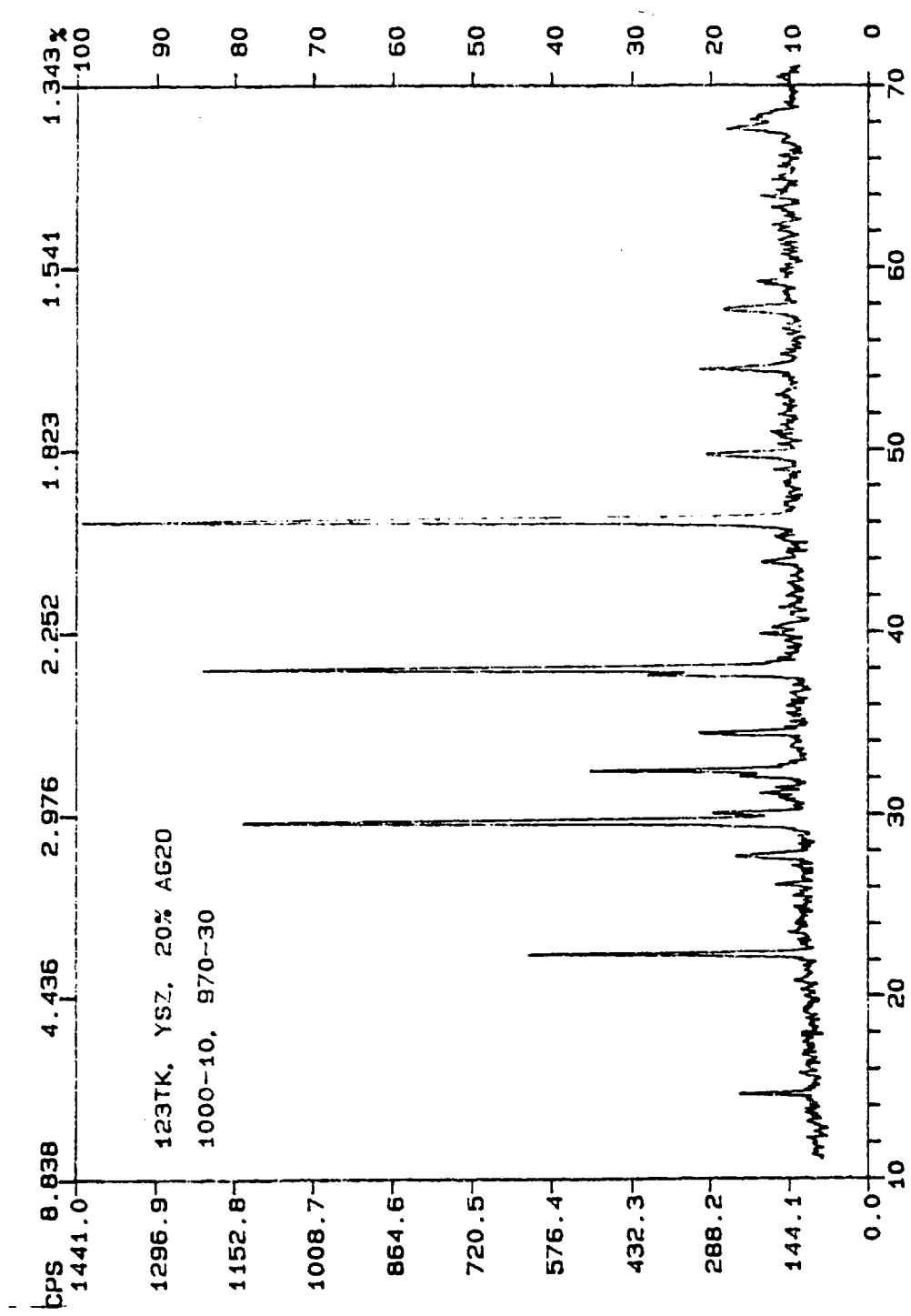


Figure 4: X-ray diffraction pattern of a YBCO thick film prepared by the two step firing process.

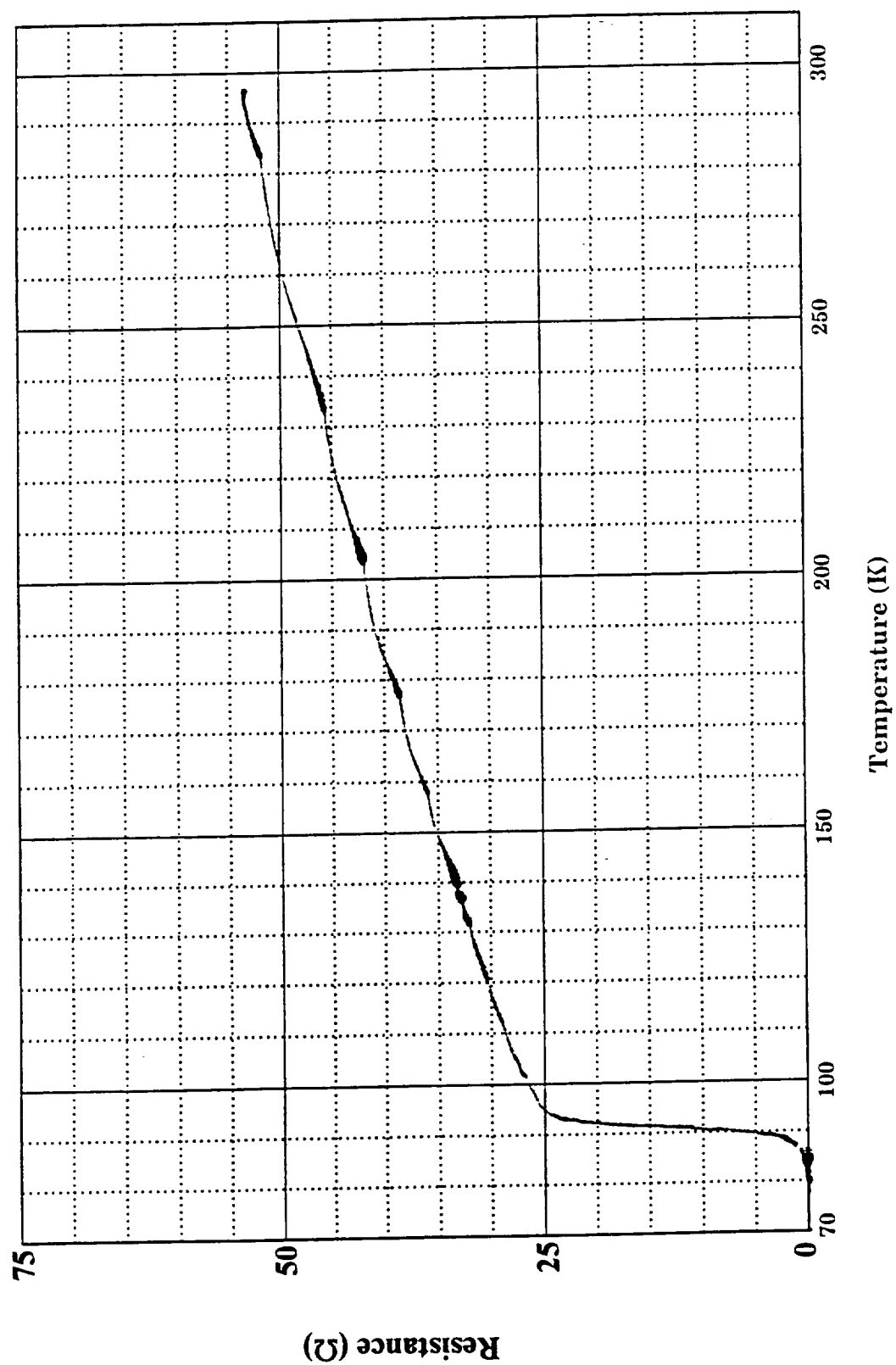


Figure 5:  $T_c$  curve of a multiple-lead YBCO thick film printed on YSZ and fired at 985°C for 12 minutes.

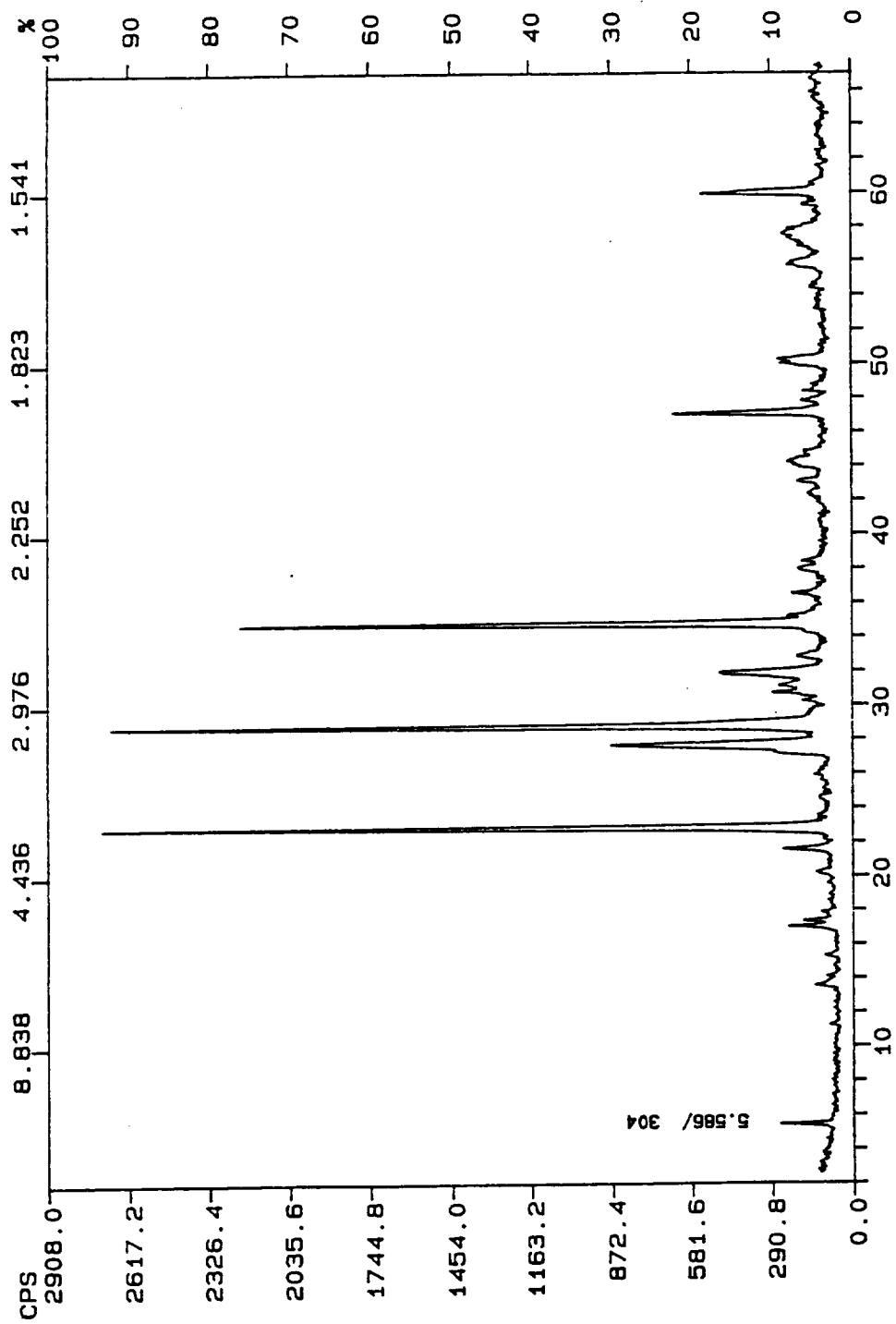


Figure 6: X-ray diffraction pattern of a BSCCO coated YSZ substrate.

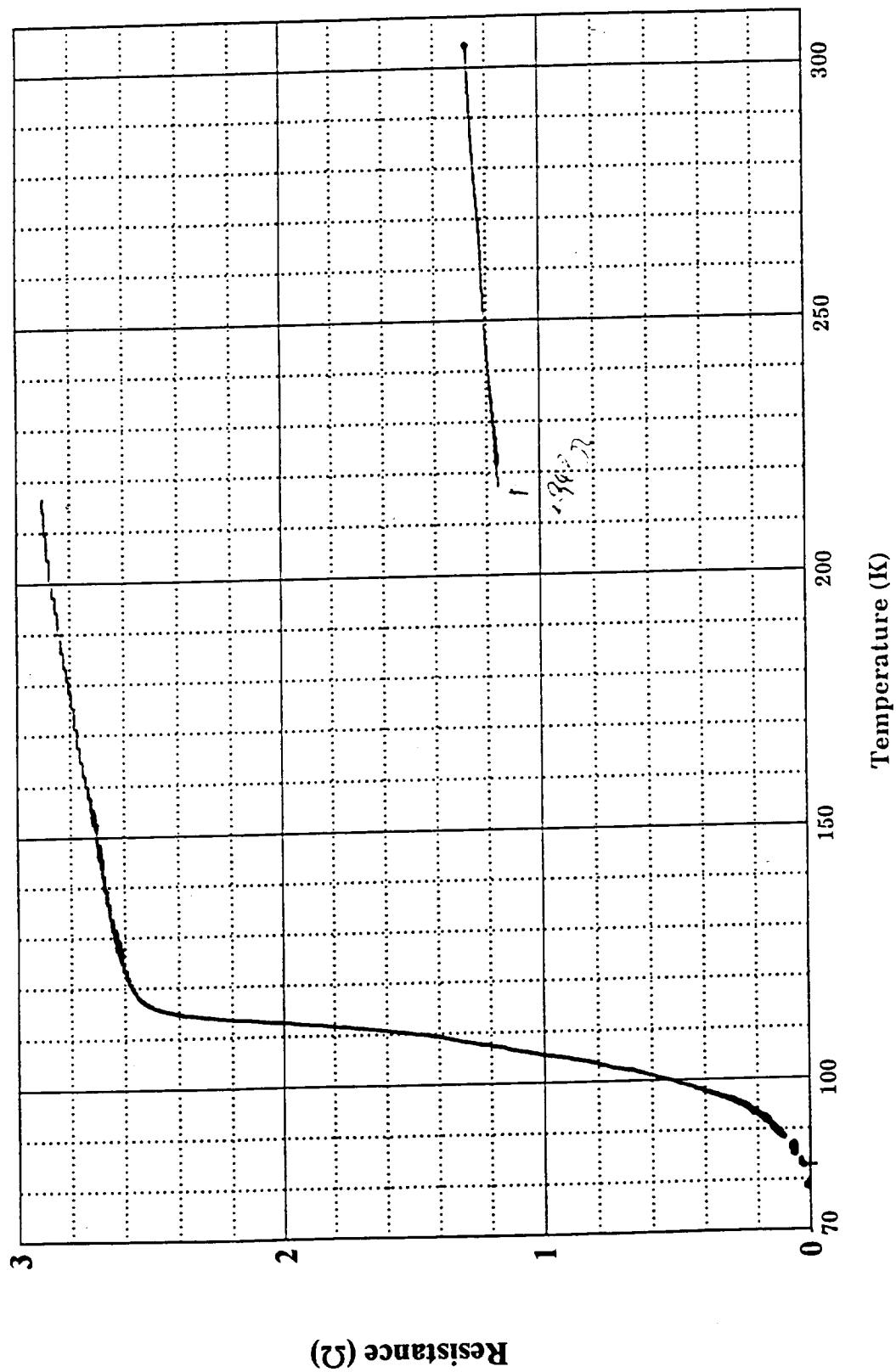


Figure 7:  $T_c$  curve of a BSCCO thick film deposited on the BSCCO coated YSZ substrate. The film was fired at 845°C for 2 hours.



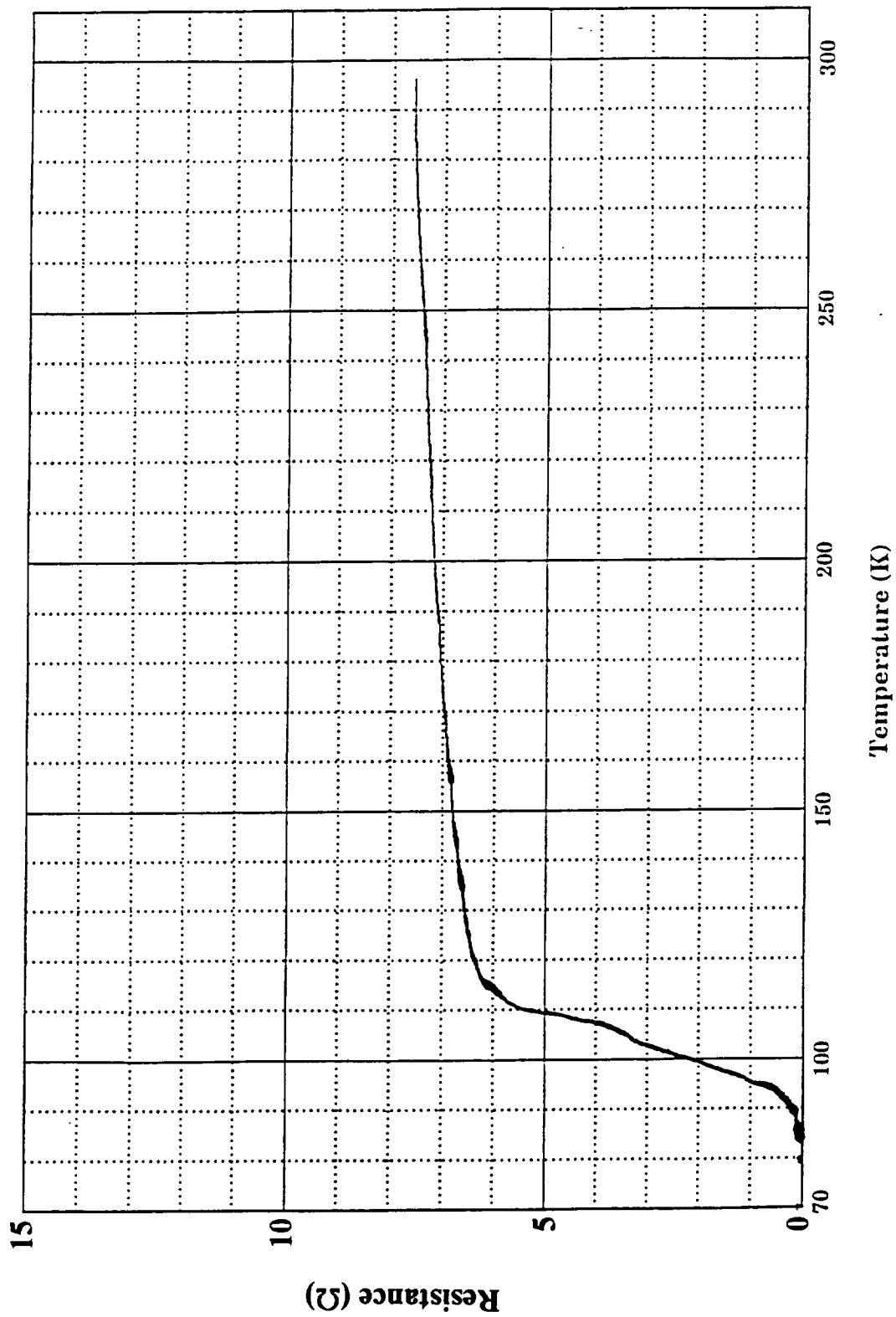


Figure 8:  $T_c$  curve of a BSCCO thick film printed on a MSZ substrate with 5 layers MgO coating. The film was fired at 845°C for 2 hours.

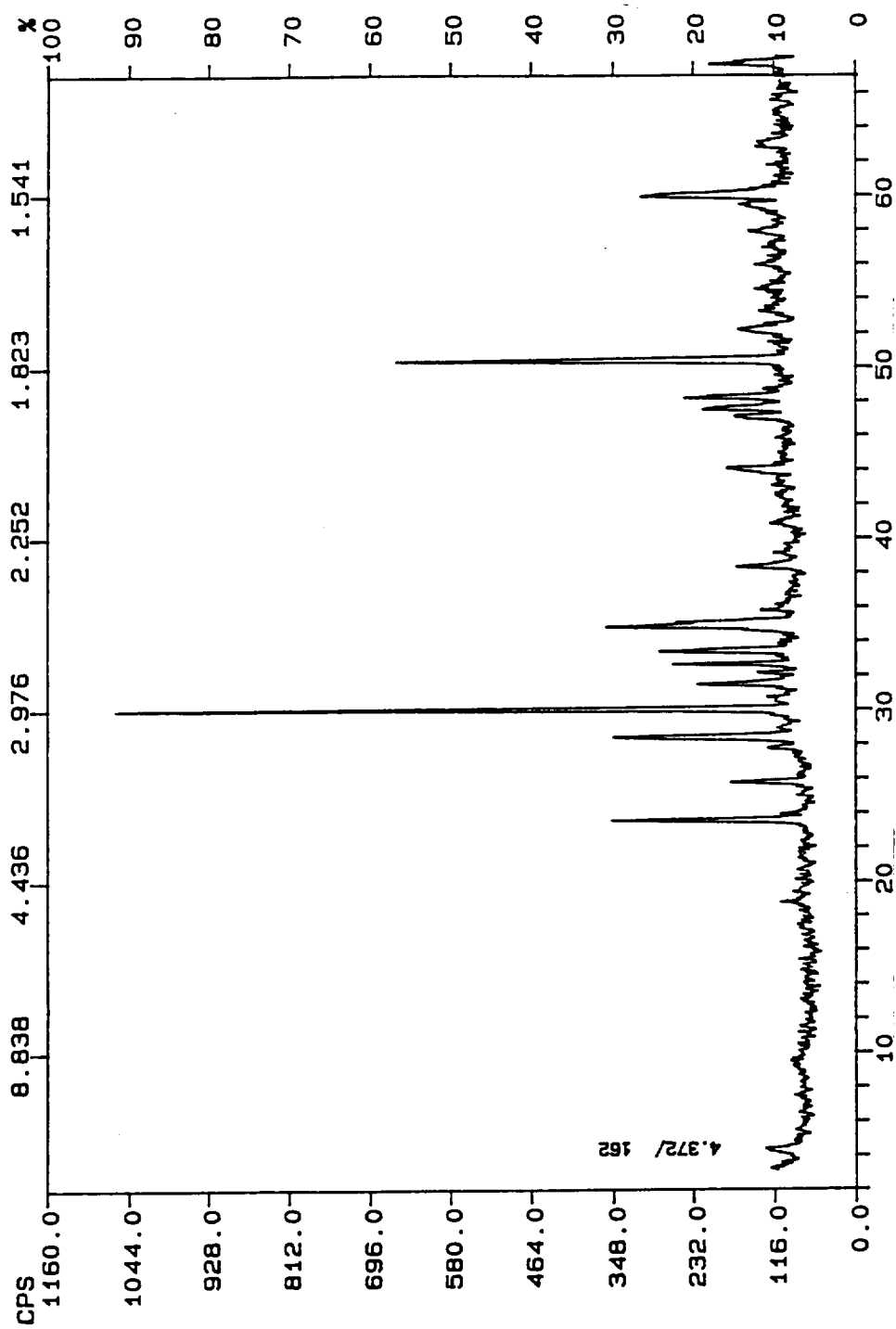


Figure 9: X-ray diffraction pattern of a BSCCO thick film printed on a MSZ substrate with 5 layers MgO coating. The film was fired at 845°C for 2 hours.

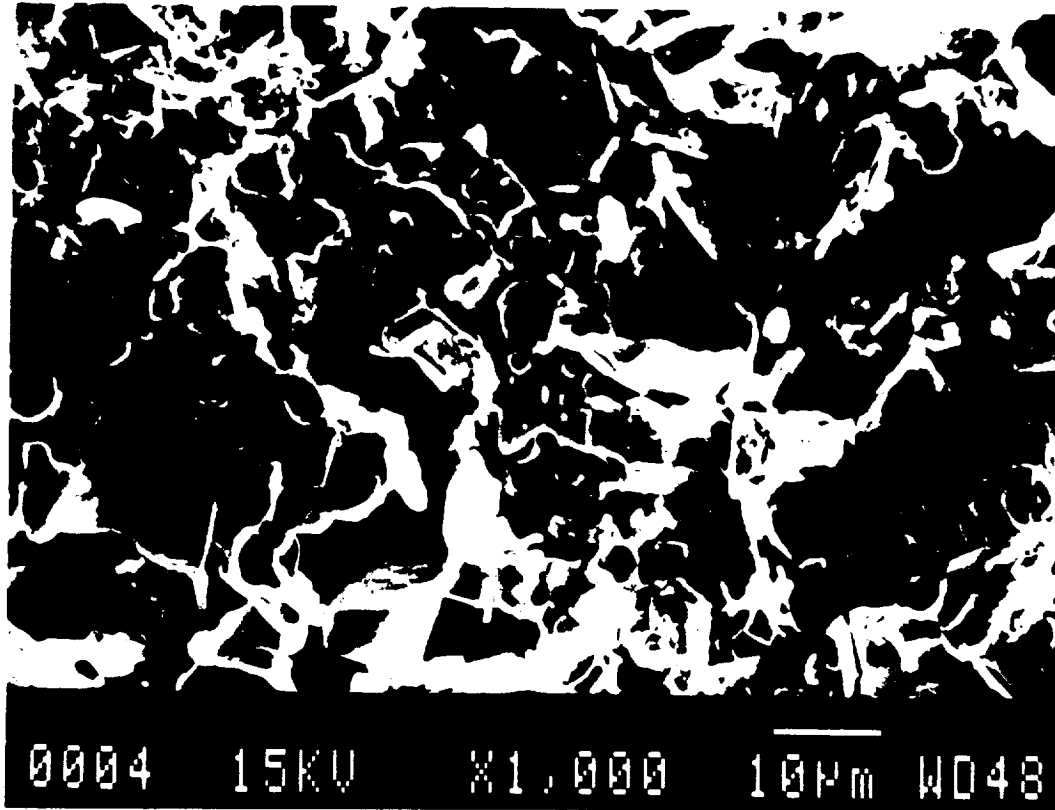


Figure 10: Microstructure of a BSCCO thick film printed on a MSZ substrate with 5 layers MgO coating. The film was fired at 845°C for 2 hours.

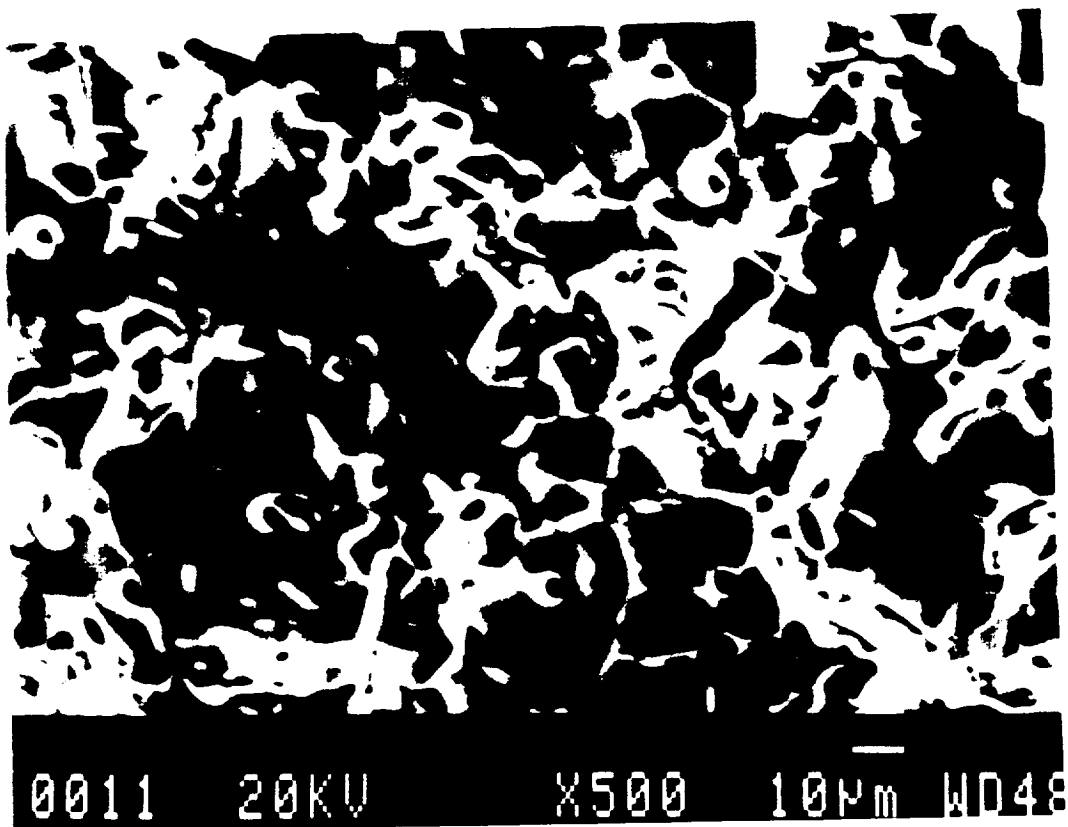


Figure 11: Microstructure of a BSCCO thick film printed on a MSZ substrate. The film was fired at 870°C for 30 minutes.

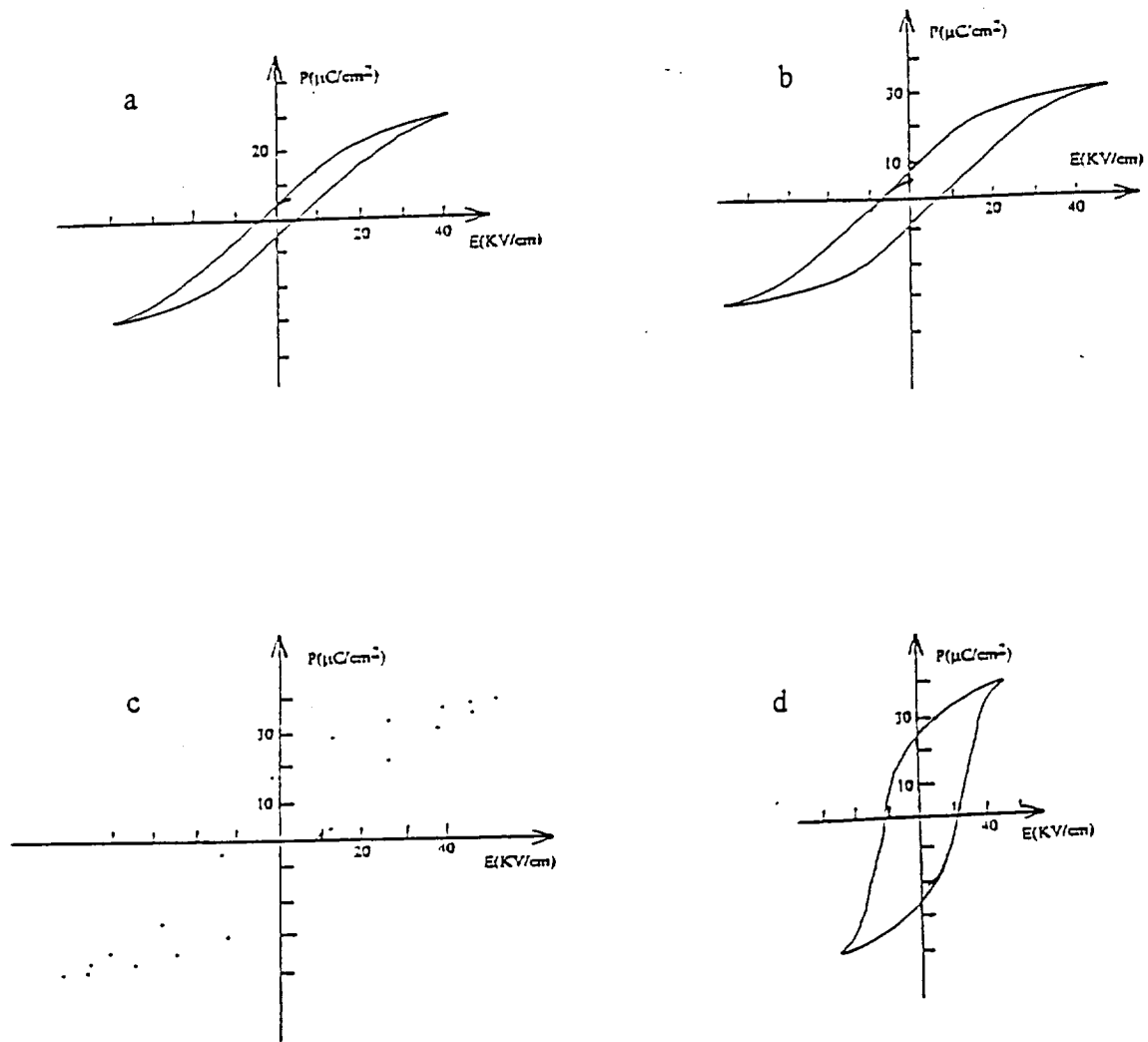


Figure 12: P-E loop of a silver electroded PLZT (9.5/65/35) at different measuring temperature. The sample was fired at 500°C for minutes. a: 22°C, b: 0°C, c: -50°C, d: -80°C.

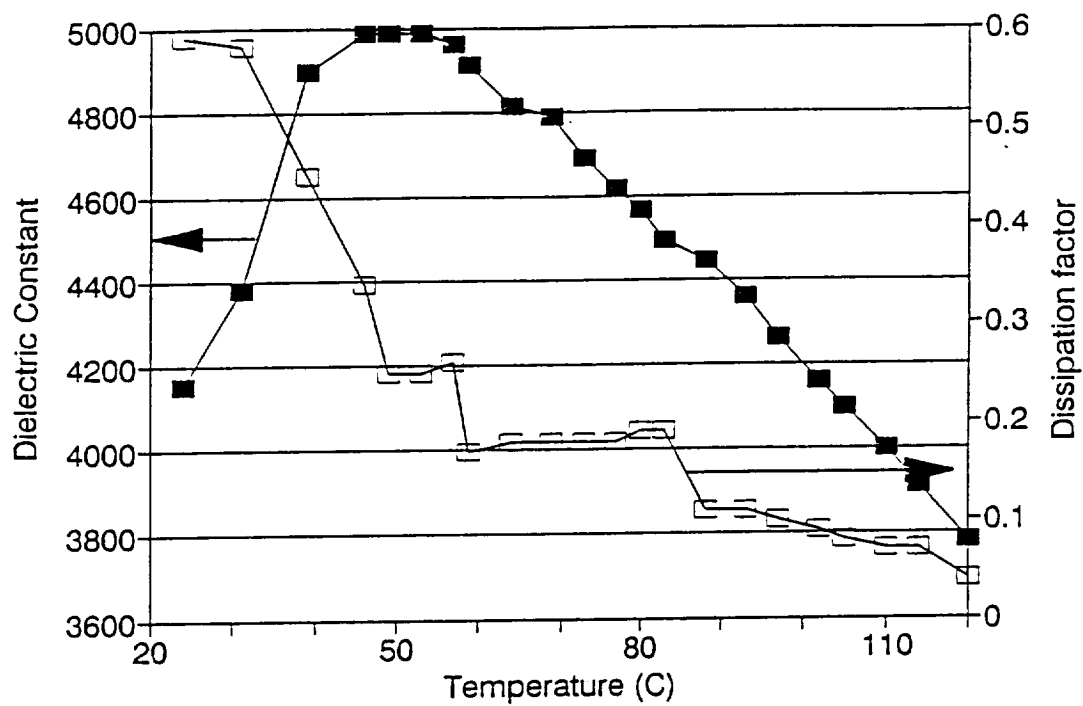


Figure 13: Dielectric constant and dissipation factor of a silver electroded sample. The sample was fired at 550°C for 30 minutes.

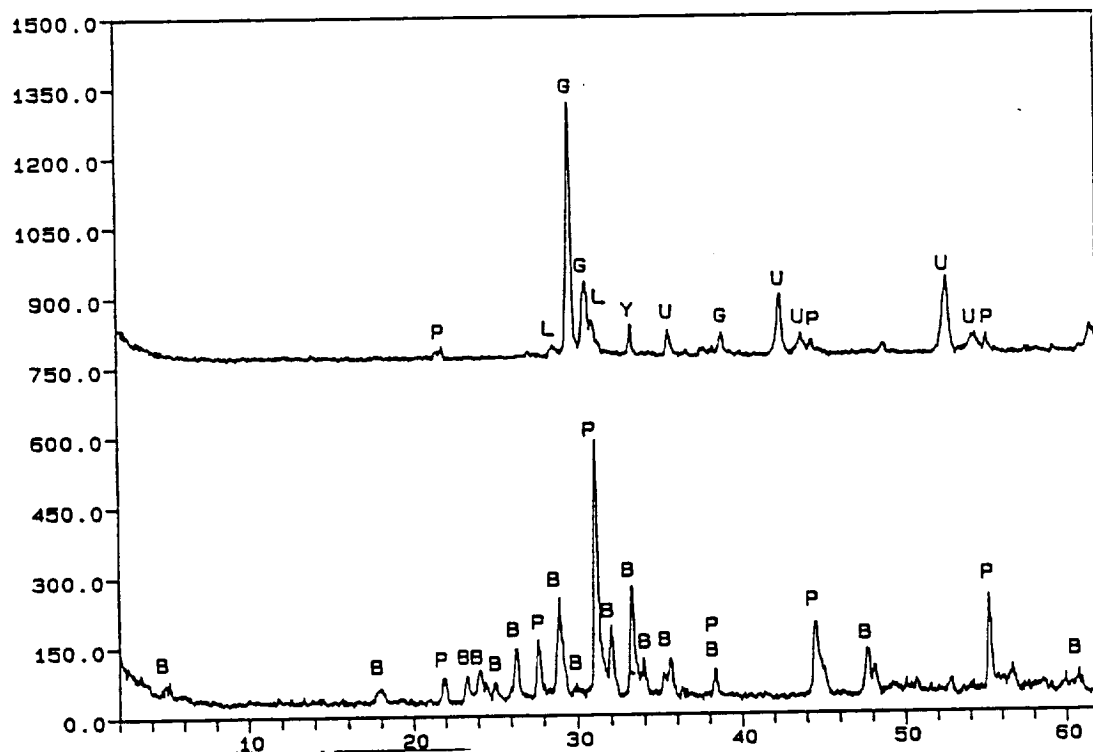


Figure 14. X-ray diffraction pattern of the fired YBCO-PLZT (top) and the fired BSCCO-PLZT (bottom) powder. G:  $\text{Y}_2\text{BaCuO}_5$ , Y:  $\text{YBa}_2\text{Cu}_3\text{O}_{7-x}$ , L:  $\text{PbO}$ , B: BSCCO and U: unknown.

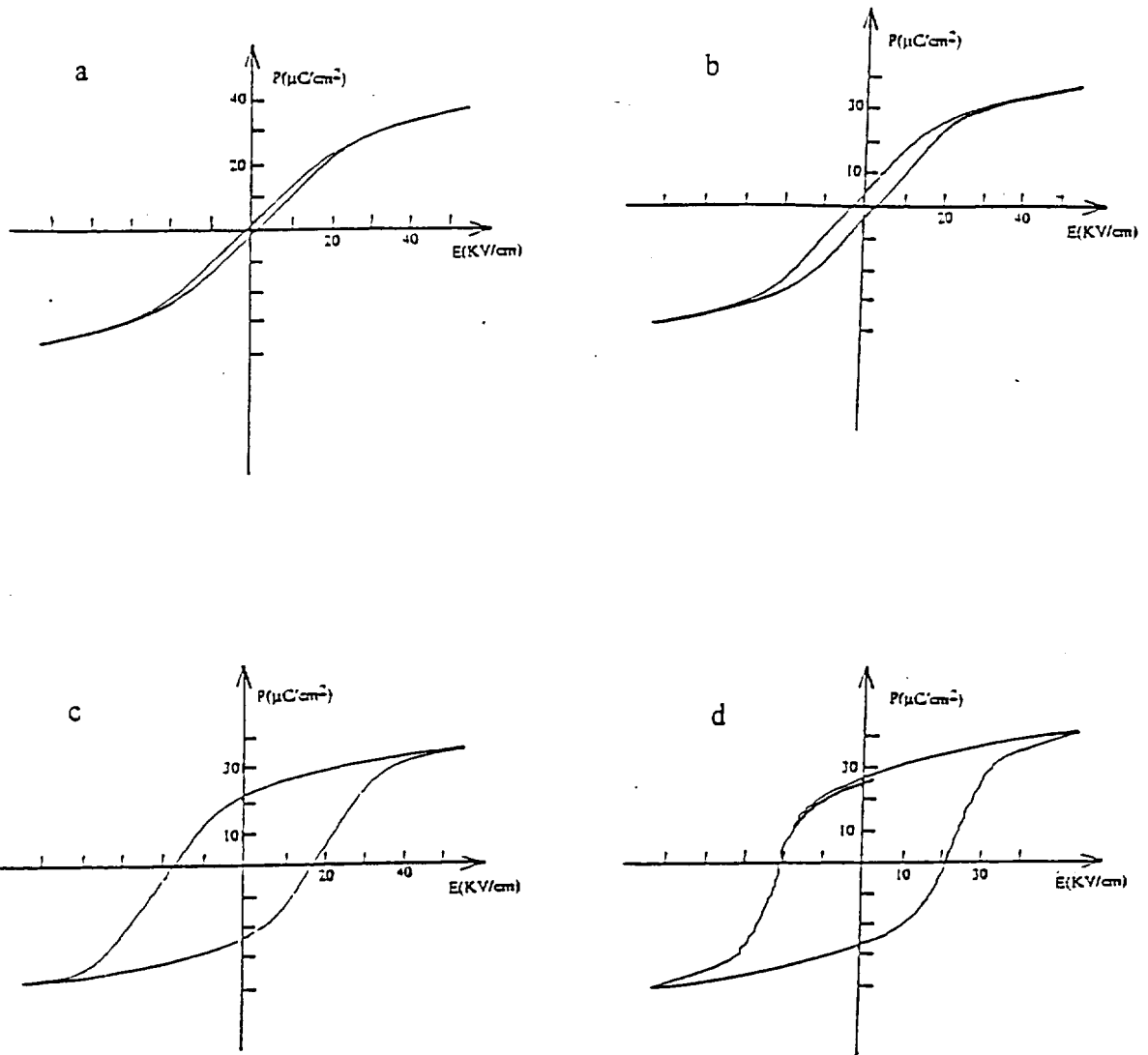


Figure 15: P-E loops of a YBCO electroded PLZT (9.5/65/35) at different temperature. The sample was fired at 940°C for 1 hour. a: 22°C, b: 0°C, c: -58°C, d: -88°C.



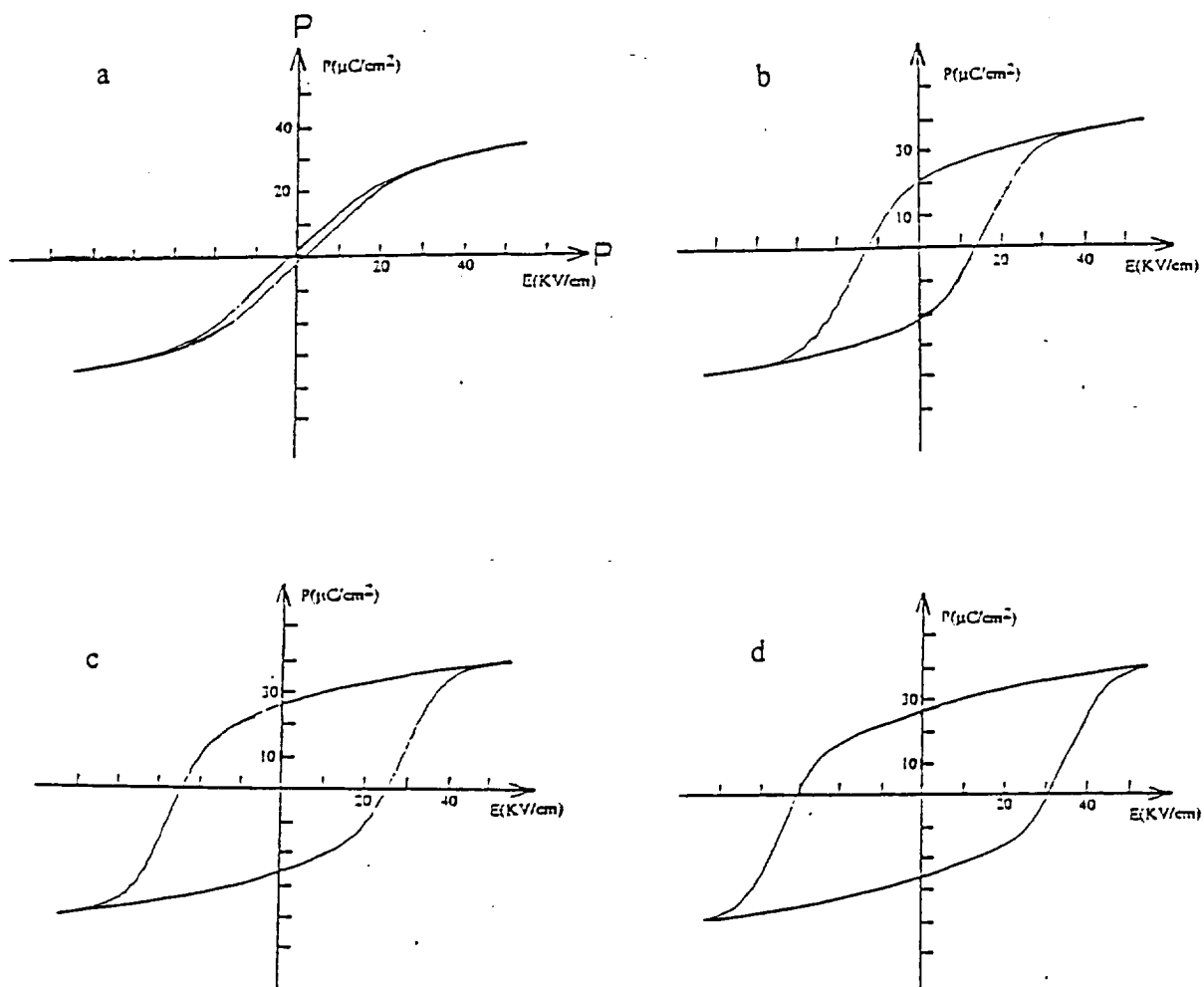


Figure 16: P-E loops of a SYP electroded PLZT (9.5/65/35) at different temperature.

The silver electrodes were fired at 900°C for 12 minutes. a: 22°C, b: -50°C, c: -80°C, d: -100°C.

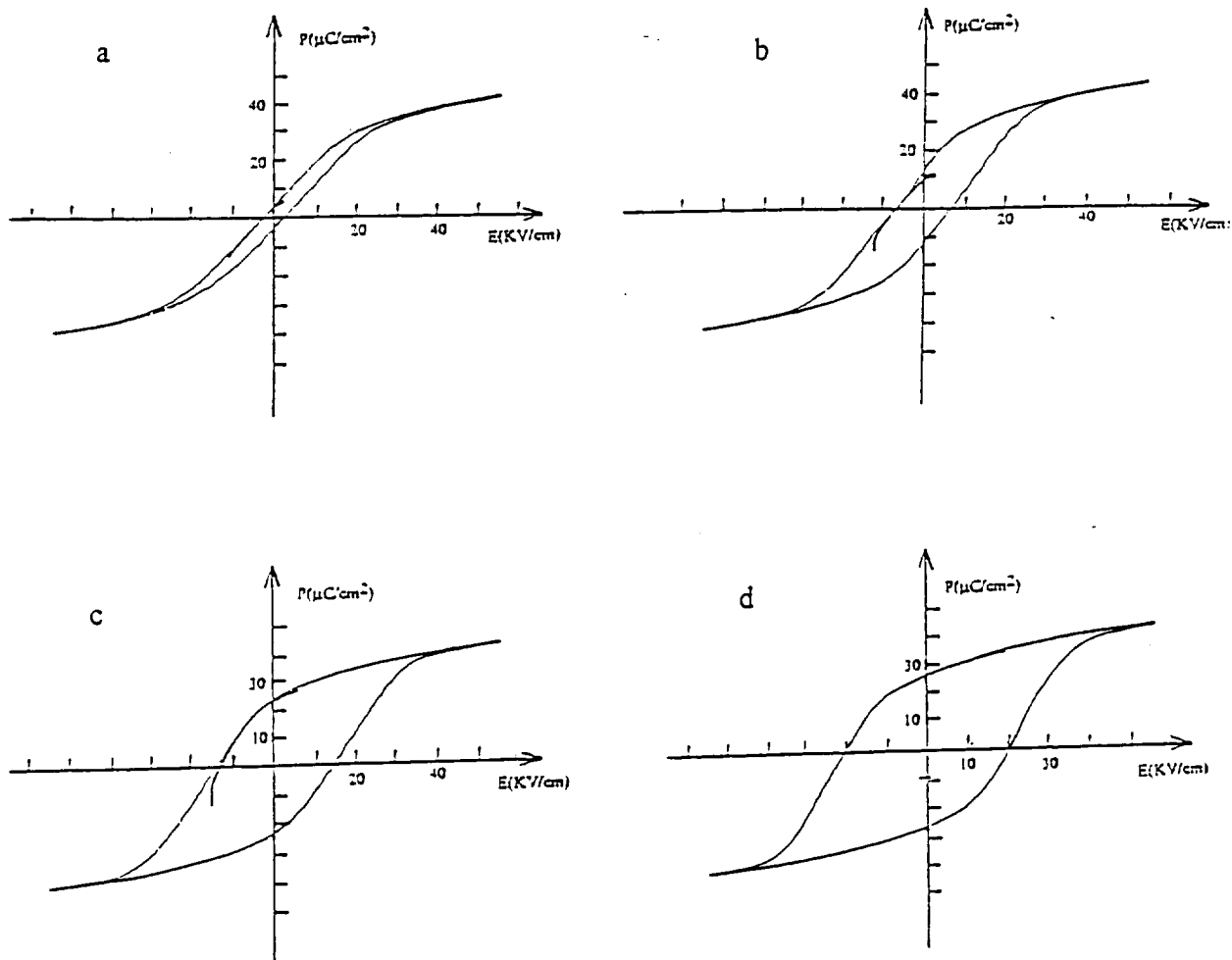


Figure 17: P-E loops of a SY electroded PLZT (9.5/65/35) at different measuring temperature. The sample was fired at 930°C for 1 hour. a: 22°C, b: -50°C, c: -80°C, d: -100°C.

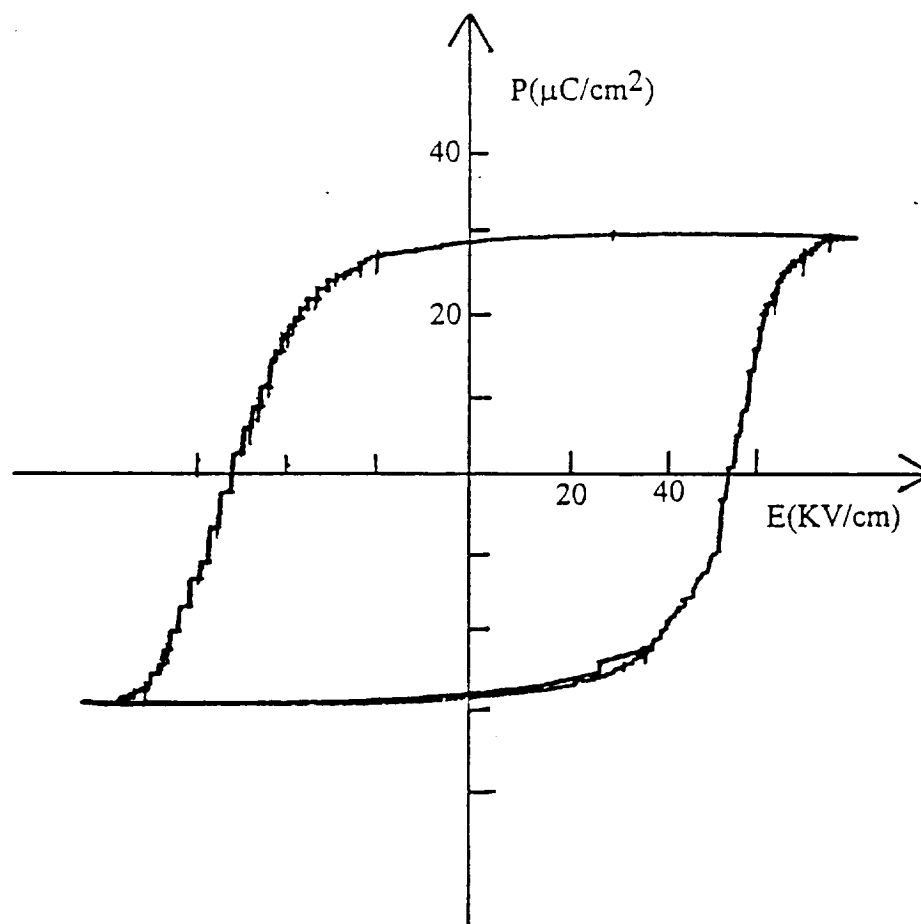


Figure 18. P-E loop of a silver electroded PLZT 9.5/65/35 at liquid nitrogen temperature.

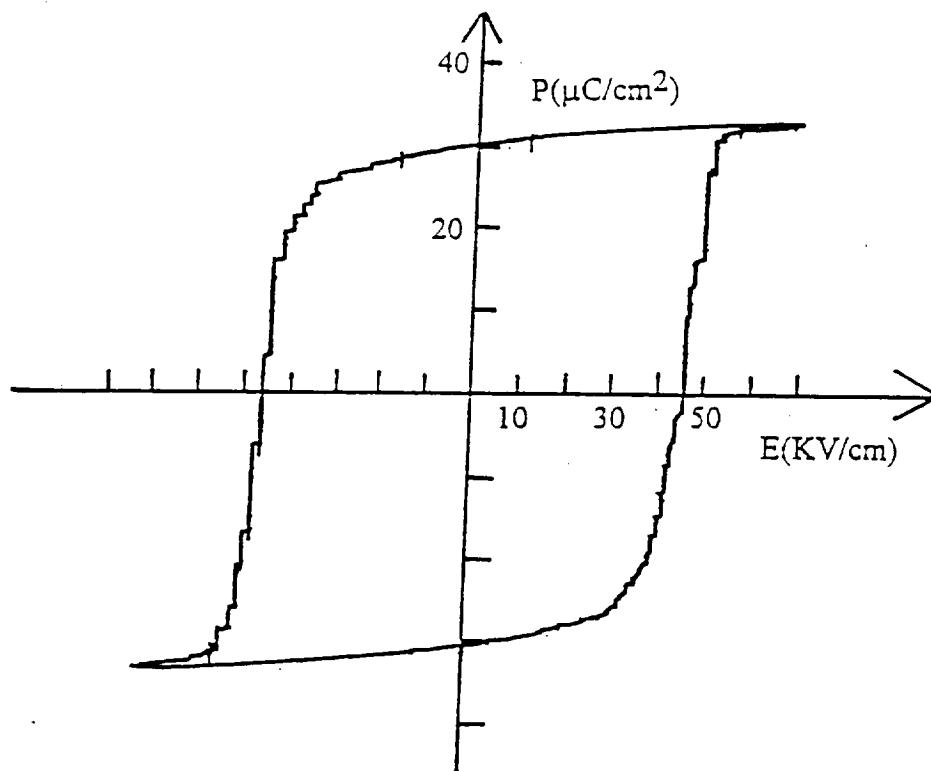


Figure 19 P-E loop of a Ni electroded PLZT 9.5/65/35 at liquid nitrogen temperature.

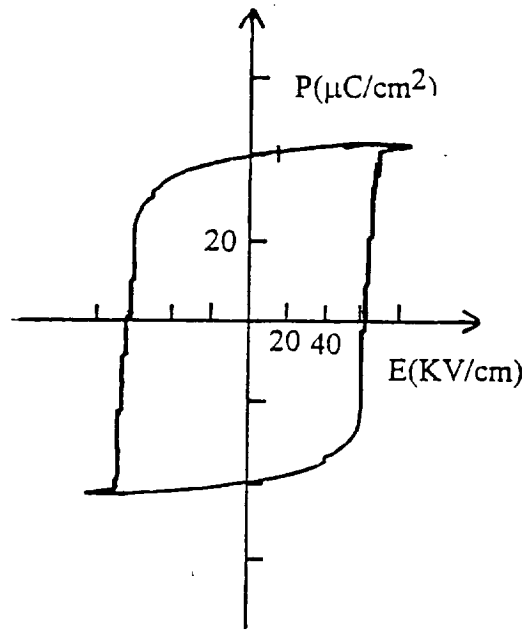


Figure 20. P-E loop of a YBCO electroded PLZT 9.5/65/35 at liquid nitrogen temperature.

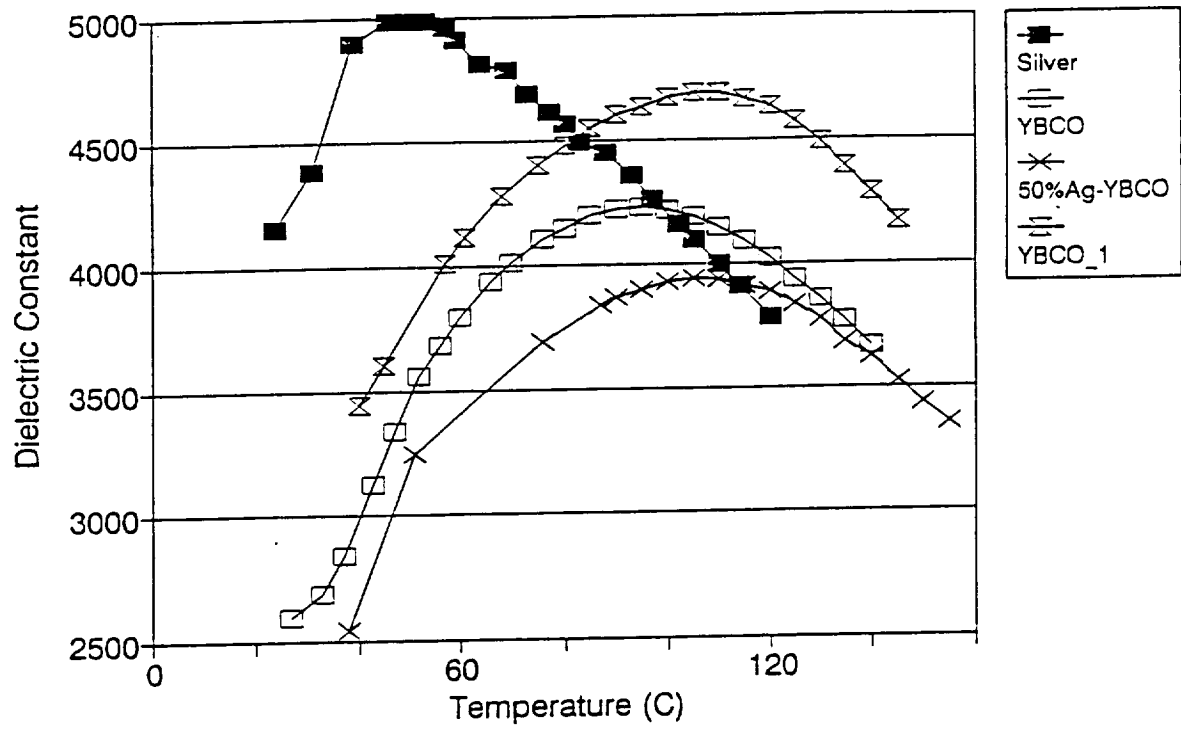


Figure 21: Dielectric constant of different electroded samples at different temperature. YBCO: sample thickness was equal to 15 mil, YBCO\_1: sample thickness was equal to 27 mil.

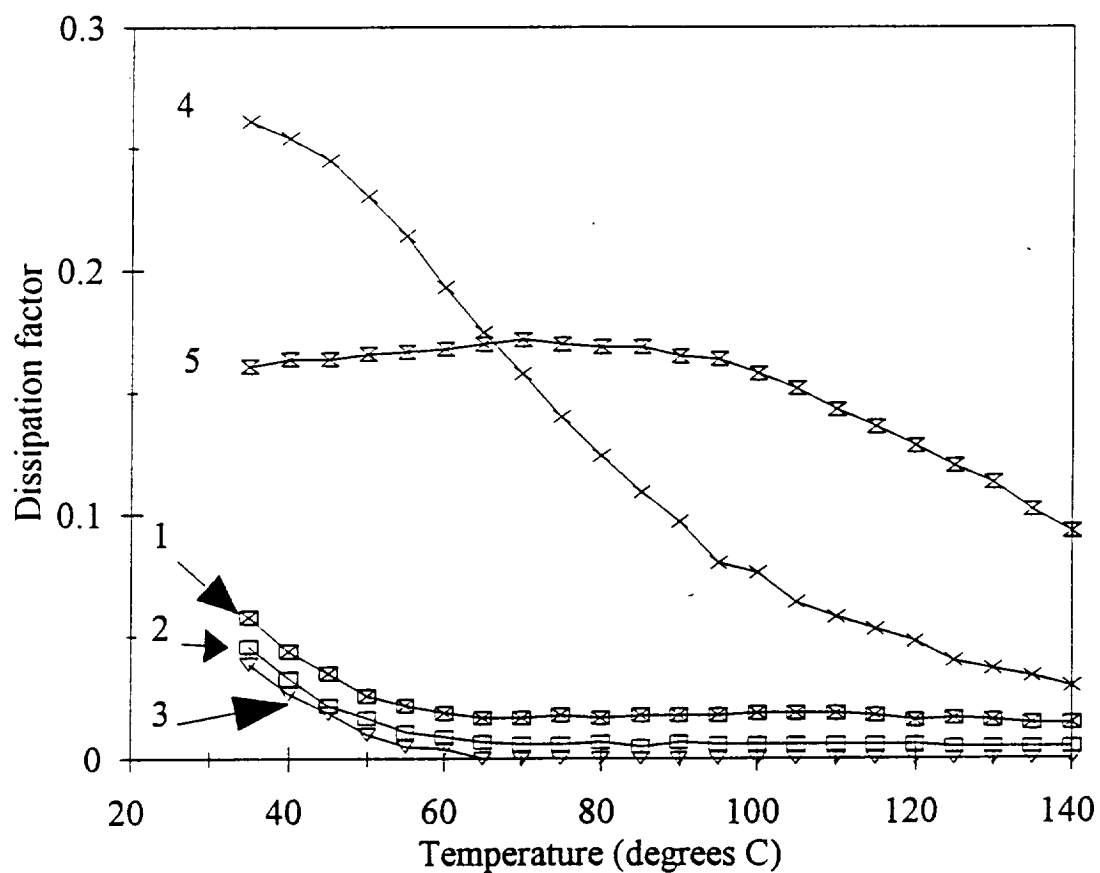


Figure 22: Dissipation factors of PLZT samples measured with different electrode.

1: BSCCO, 2: Ni, 3: silver, 4: 70 wt.% YBCO-30 wt.% Ag<sub>2</sub>O, 5: YBCO.

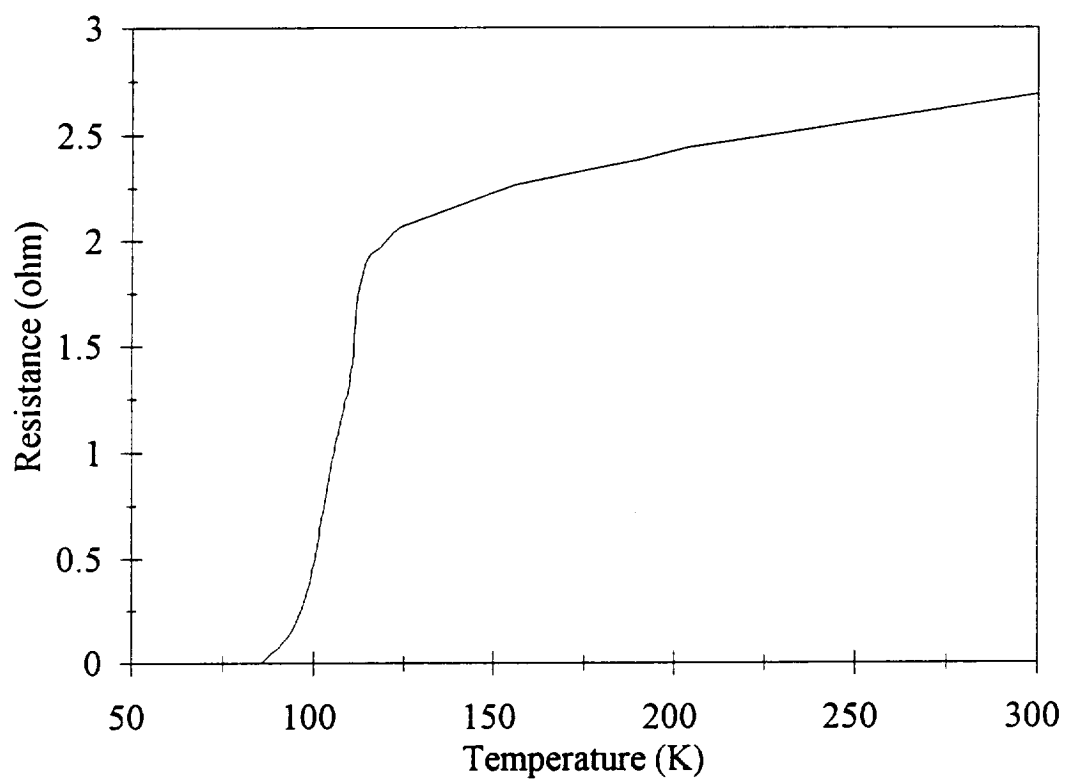


Figure 23.  $T_c$  curve of a BSCCO thick film painted on the PLZT substrate.



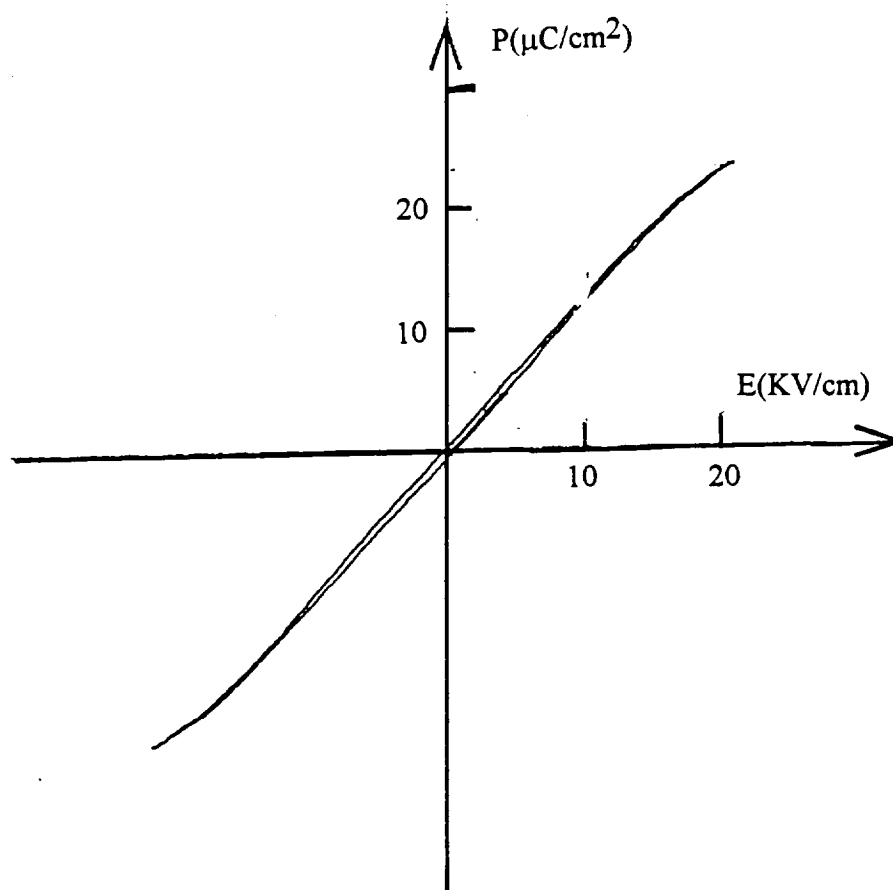


Figure 24: P-E loop of a BSCCO electroded PLZT (9.5/65/35) at room temperature. The sample was fired at 845°C for 2 hours.

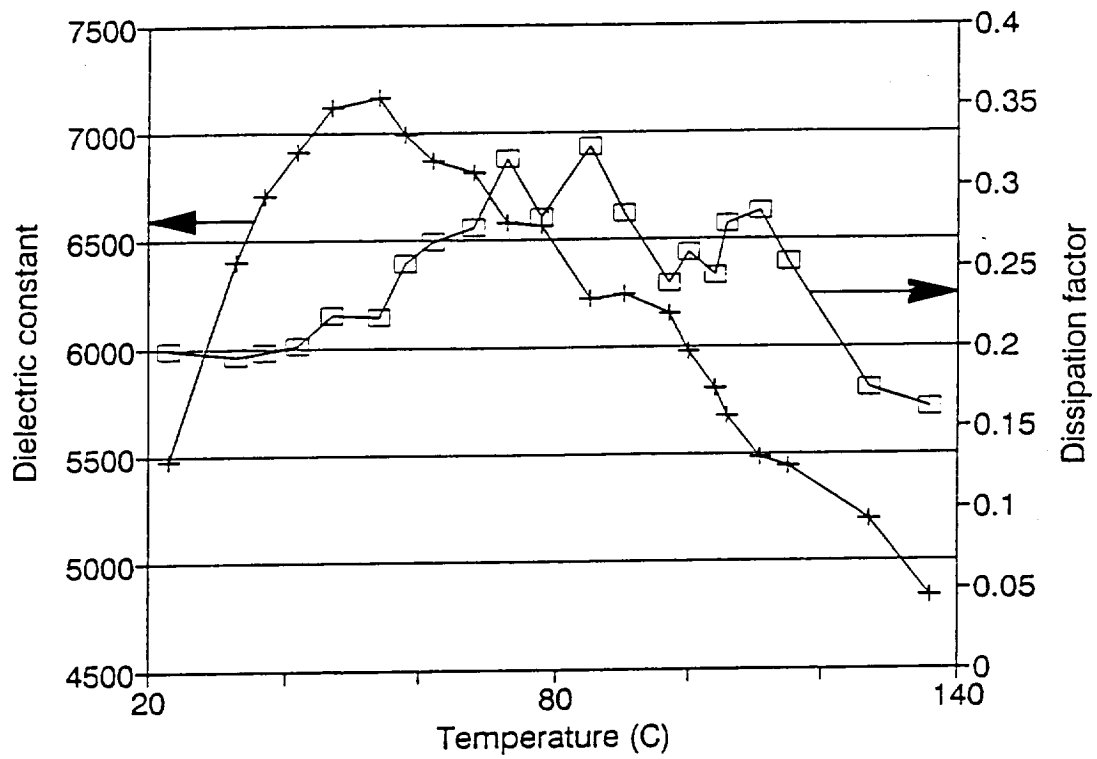


Figure 25: Dielectric constant and dissipation factor of a BSCCO electroded PLZT (9.5/65/35) at different temperature. The sample was fired at 845° for 2 hours.

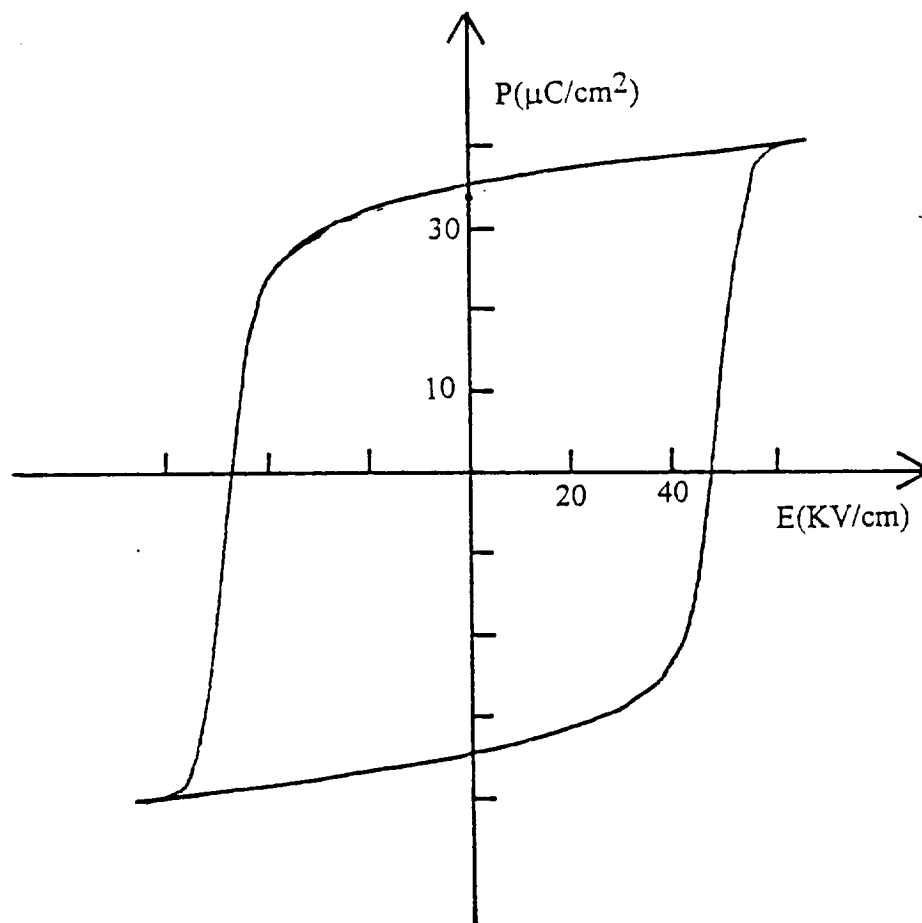


Figure 26. P-E loop of a BSCCO electroded PLZT at liquid nitrogen temperature.

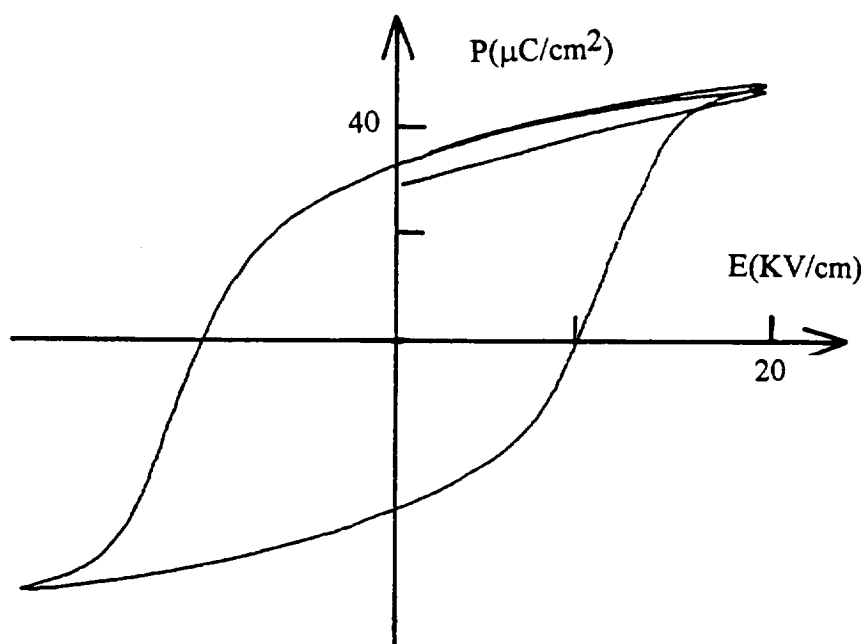
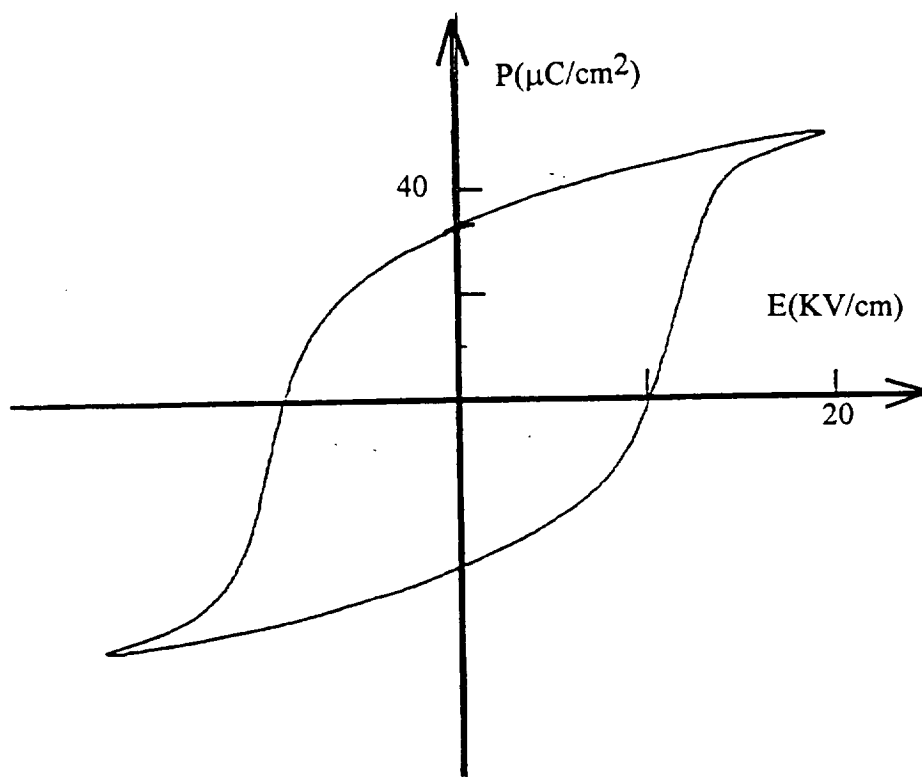
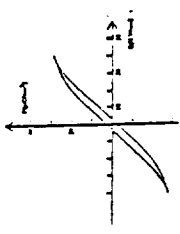
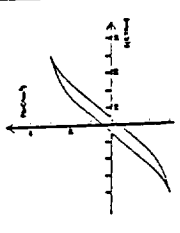
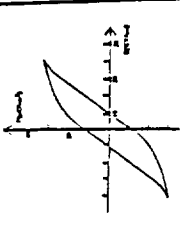
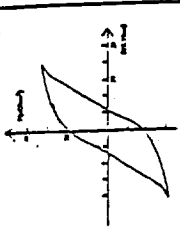
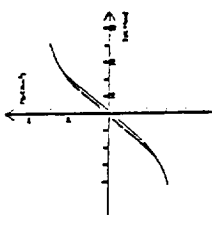
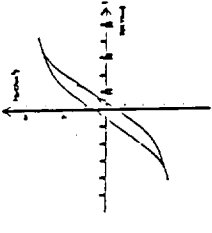
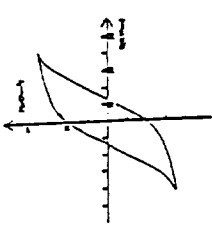
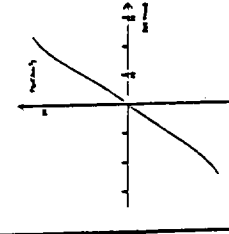
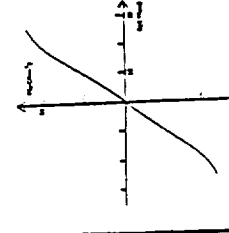
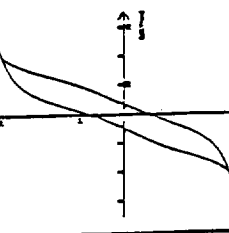
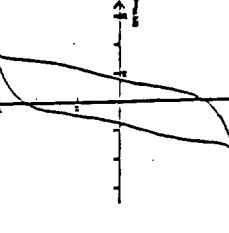
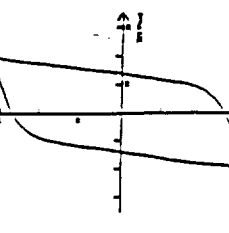
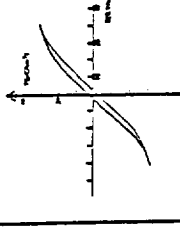
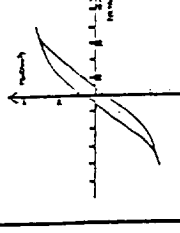
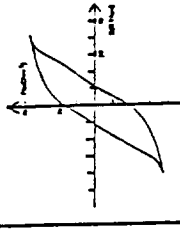
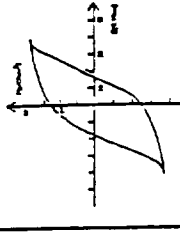
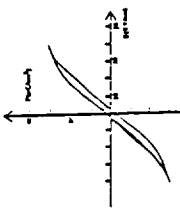
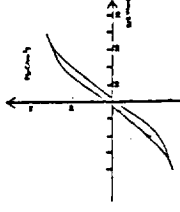
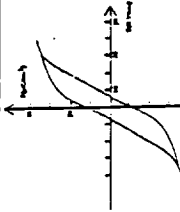
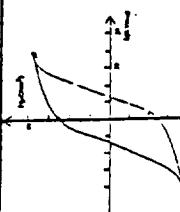
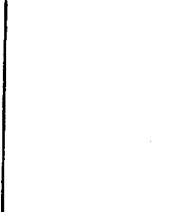
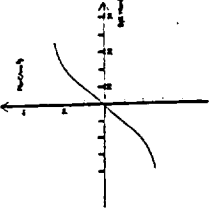
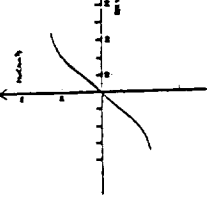
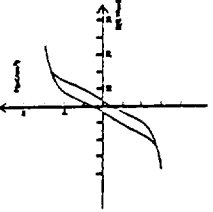
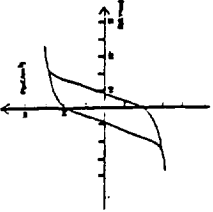
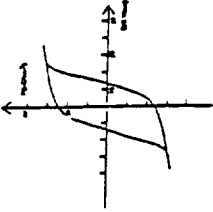


Figure 27: P-E loops of the PBNZT substrates electroded with silver and YBCO electrodes. The YBCO electrode was fired at 920°C for 1 hour.

Appendix I: P-E loops of different electroded samples at different temperature.

	Room Temperature	0°C	-50°C	-80°C	-100°C
Silver on PLZT(9.5/65/35) 500°C 30 minutes. $\Lambda = 1.68\text{cm}^2$ , $t = 0.0381\text{cm}$					
123 on PLZT(9.5/65/35) 940°C 30 minutes. $\Lambda = 1.70\text{cm}^2$ , $t = 0.0381\text{cm}$					
123 on PLZT(9.5/65/35) → polished → Ni on PLZT $\Lambda = 1.70\text{cm}^2$ , $t = 0.61\text{ cm}$					
50%Ag-123 on PLZT(9.5/65/35) 930°C 60 minutes. $\Lambda = 1.55\text{cm}^2$ , $t = 0.0381\text{cm}$					

	Room Temperature	0°C	-50°C	-80°C	-100°C
Silver on PLZT(9.5/65/35) 500°C 30 minutes. $\Lambda = 0.6154\text{cm}^2$ , $t = 0.0381\text{cm}$					
123 on PLZT(9.5/65/35) 940°C 60 minutes. $\Lambda = 0.595\text{cm}^2$ , $t = 0.0381\text{cm}$					
Ag- 123 on PLZT(9.5/65/35) 900°C 10 minutes. $\Lambda = 0.595\text{cm}^2$ , $t = 0.0381\text{cm}$					
30%Ag-123 on PLZT(9.5/65/35) 930°C 60 minutes. $\Lambda = 0.6154\text{cm}^2$ , $t = 0.0381\text{cm}$					

<p>Silver on PLZT(9.5/65/35) 870°C 30 minutes. <math>\Lambda = 1.70\text{cm}^2</math>, <math>t = 0.0381\text{cm}</math></p>	<p>Room Temperature</p> 	<p>0°C</p> 	<p>-50°C</p> 	<p>-80°C</p> 	<p>-100°C</p> 
<p>Ni on PLZT(9.5/65/35) <math>\Lambda = 1.70\text{cm}^2</math>, <math>t = 0.0381\text{cm}</math></p>					

Appendix II: P-E loops of silver and YBCO electroded PBZNT at different temperature.

Sample Conditions	Room Temperature	0°C	-50°C	-80°C
123 on PBNZT 920°C 60 minutes. $A = 0.726\text{cm}^2$ , $t = 0.038\text{cm}$				
Ag-123 on PBNZT 900°C 10 minutes. $A = 0.726\text{cm}^2$ , $t = 0.038\text{cm}$				



## **Part II.**

### **Development of PBZT, PLZT, PSZT and PMN-Based Ceramics for Actuators**

# **SUPERCONDUCTIVITY DEVICES: COMMERCIAL USE OF SPACE**

## **Annual Report**

### **Development of PBZT and PLZT Ceramics for Electrostrictive Actuators**

to

National Aeronautics and Space Administration  
Langley Research Center  
Hampton, VA 23665-5225

Principal Investigator:

Gene Haertling

Supporting Investigator:

Guang Li

Contract No. NAG-1-1301

September 6, 1993

## 1. Introduction

Our previous investigations [1] on the  $(\text{Pb}_{1-x}\text{Ba}_x)(\text{Zr}_{1-y}\text{Ti}_y)\text{O}_3$  (PBZT) system indicate that the PBZT family belongs to a ceramic system with large electric field induced (electrostrictive) strains which possess many potential applications in electronic and optically controlled system as well as precision machinery. Current work is a continuation of the previous investigations with an objective that remains focused on the dielectric and electrostrictive properties of materials.

In this report, more compositions from the PBZT system were selected to be investigated so that the special regions of interest in the PBZT phase diagram were included. The dielectric properties and electrostrictive strains of the samples were measured. Several important parameters, such as  $E_c$ ,  $P_R$ ,  $P_{10}$ ,  $S$  and  $\Delta S$ , were evaluated. Additionally some  $(\text{Pb},\text{La})(\text{Zr},\text{Ti})\text{O}_3$  (PLZT) samples of different compositions were prepared by conventional mixed-oxide processing and hot-pressing. The corresponding properties of the PLZT samples were determined and compared with PBZT.

## 2. Sample Preparation

The compositions of PBZT ceramics investigated are indicated in the  $\text{BaZrO}_3$ – $\text{BaTiO}_3$ – $\text{PbZrO}_3$ – $\text{PbTiO}_3$  phase diagram shown in Figure 1. The compositions were so chosen that most of them are situated along several lines in the phase diagram, either with constant Pb/Ba ratio or constant Zr/Ti ratio, which cover the regions of special interest.

Conventional mixed-oxide processing techniques were employed to prepare all of the PBZT samples. A flowchart of the processing is given in Figure 2. Reagent grade  $\text{PbO}$ ,  $\text{ZrO}_2$ ,  $\text{TiO}_2$ ,  $\text{BaCO}_3$  and  $\text{Bi}_2\text{O}_3$  were used as starting raw materials. Here  $\text{Bi}_2\text{O}_3$  was introduced mainly as an additive to enhance sinterability. Unless specified, 2 atom%  $\text{Bi}_2\text{O}_3$  was used. Weighed components were first mixed for 30 minutes, and then calcined at 925 °C for two hours. The calcined powder was milled for 6 hours in distilled water using a polyethylene jar and  $\text{Al}_2\text{O}_3$  balls. Sample pellets were obtained by pressing the milled powder with distilled water into plates of about 1.2x1.2x0.125 inches at a pressure of 7000 psi. The pellets were sintered at 1250 °C for 4 hours

in a closed alumina crucible with a flowing oxygen atmosphere. Higher sintering temperatures ( about 1300 °C ) were adopted for the samples with  $Zr/Ti > 74/26$ . To avoid the loss of PbO from samples during sintering, a PbO-rich atmosphere was maintained by placing an equimolar mixture of PbO and  $ZrO_2$  in the crucible. Sintered samples were then lapped to dimensions of 426x364x30 mil. The largest surfaces of the lapped samples were electroded with electroless nickel plating.

The PLZT samples are classified as two groups. One of them, called sintered PLZT samples, followed the same preparation procedures as those described above for PBZT. Another group, called hot-pressed samples, were prepared by means of a hot-pressing technique. These samples were hot-pressed at 1200 °C with a pressure of 2000 psi for 4 hours.

### 3. Measurements of Sample Properties

The dielectric properties of samples were measured at 1 kHz with an LCR meter ( LEADER, LCR-7450-01). The temperature dependence of dielectric constant and loss factor were obtained by placing samples in an environmental chamber ( DELTA DESIGN, 1740) in which samples were first cooled down to -20 °C and then measured at a heating rate of 3 °C/min up to 180 °C. The measurement of the relationship between polarization  $P$  and electric field  $E$  was carried out using conventional P-E hysteresis loop equipment. The submersion method in distilled water was employed to evaluate sample density.

An experimental device for the detection of electric field induced strains is depicted in Figure 3. An LVDT ( linear variable differential transformer ) was used as the displacement sensor. Details of the device have been given previously in the reference [1]. An electric field was applied to the samples continuously between negative and positive maxima ( 20 kV/cm ). The measured results were recorded on a X-Y plotter.

Sample crystal structures were monitored with an X-ray diffractometer ( Scintag XDS 2000™ ) with a filtered Cu radiation.

### 3. Results and Discussion

The important data of all the PBZT samples with different compositions obtained in this investigation are given in Table 1. The first six blocks of Table 1 illustrate, respectively, the dielectric and related properties of the compositions along the lines marked in the PBZT phase diagram of Figure 1. The variations of dielectric constant with barium content at constant Zr/Ti ratio, mainly the vertical lines 1–4 in Figure 1, are plotted in Figure 4. As shown in Figure 4, all four curves with different Zr/Ti values exhibited a maximum as barium content was increased, which were caused by the structural change from the rhombohedral  $F_R$  or tetragonal  $F_T$  phase to the paraelectric  $P_C$  phase. Figure 5 shows the change of dielectric constant with Ti concentration at constant Pb/Ba ratios; i.e., the horizontal lines 5 and 6 in Figure 1. A peak was found at about 20 atom% of titanium with Pb/Ba=73/27, which is consistent with the phase boundary given by Ikeda [2] as seen in Figure 1. No abrupt change in dielectric constant was observed near the  $F_R$  and  $F_T$  phase boundary at Pb/Ba=73/27, suggesting a strong compositional diffusion in this region. The presence of this boundary is indicated by the change of X-ray diffraction patterns with composition as given in Figure 6, whereby the intensity peaks featured by the tetragonal phase vanished as the sample composition varied across the boundary into the  $F_R$  phase. Similarly, the location of the  $F_T$  and  $P_C$  boundary at Zr/Ti=40/60 was determined from the X-ray measurement results as shown in Figure 7. Figure 8 illustrates the temperature dependence of dielectric constant and loss factor for some selected compositions along the lines 2, 4 and 5 in Figure 1. As anticipated, the temperatures of maximum dielectric constant, that is, the Curie points, decreased with decreasing Pb/Ba ratio along the lines 2 and 4, and with decreasing Zr/Ti ratio along the line 5 near the  $F_R$  and  $F_T$  phase boundary. In all cases the dielectric constant maxima appeared broad and became more diffuse as barium concentration was increased, and the magnitude of the corresponding loss factors dropped gradually above the Curie temperatures. This is an indication of the occurrence of structural relaxation. As for the sample density, no significant change was observed over the compositions studied. A desirable sintered density for those compositions with high Zr/Ti ratio was achieved by using higher sintering temperatures.

The relationships between polarization  $P$  and electric field  $E$  for all the PBZT samples were

measured. The coercive electric field  $E_c$ , the remanent polarization  $P_R$  and the polarization at an electric field of 10 kV/cm  $P_{10}$  for most of the samples were determined and are listed in Table 1. Figures 9–11 show the P–E relationships for the compositions along the lines 2, 3 and 4+6 in the phase diagram of Figure 1, respectively. The P–E relationship of some representative compositions was also projected on the PBZT phase diagram, as is depicted in Figure 12. It is evident in Figures 9–12 that as the barium concentration increased the P–E curves varied from the characteristics of a ferroelectric to a relaxor and then to a paraelectric phase. These three phases are generally identified, respectively, by a relatively square P–E hysteresis loop, a slim loop P–E curve with little or no memory and a linear P–E relationship. Based on this and the dielectric properties discussed above, a wide region characteristic of relaxor phase was outlined, which is indicated by the shadowed area in Figure 12. It is noted that the relaxor phase occurs mostly in between the  $F_R$  and  $P_c$  phases and becomes more narrow as it extends into the  $F_T$  phase.

The electric field induced ( electrostrictive ) lateral strain  $S_2$  of all the PBZT samples and longitudinal strain  $S_l$  of some samples were investigated. The curves of lateral strain vs. electric field for selected samples are presented in Figures 13 and 14. The S–E relationship of some representative compositions are also displayed in the phase diagram, as shown in Figure 15. It can be seen that as sample composition was changed from the ferroelectric phases into the relaxor phase the hysteresis of strain–electric field curves was reduced, and the variation of the strains with electric field strength approached a quadratic relationship exhibiting the characteristics of electrostrictive materials. The values of the strains  $S_{l,10}$ ,  $S_{2,10}$ ,  $\Delta S_{l,10}$  and  $\Delta S_{2,10}$  whose meanings are given in Table 1, were evaluated and are listed in Table 1 for comparison. It is noted that in general the strains are proportional to polarization, with a varied extent depending on the compositions involved. Both the total strains  $S$  and the differential strains  $\Delta S$  were found to reach a maximum in the vicinity of the  $F_R$  and  $F_T$  phase boundary, whose values are among the highest discovered in the PBZT ceramic system.

Table 2 and Figure 16 show the influence of the  $\text{Bi}_2\text{O}_3$  additive on the PBZT system. In addition to it significantly enhancing sample density, as initially expected,  $\text{Bi}_2\text{O}_3$  behaved as if

an extra amount of equivalent BaO were added in the original pure PBZT composition, which is manifested as the P–E loop becoming slimmer with increasing bismuth content. This result is self-evident since Bi ions in the PBZT are substituted for Pb ions in A site of the perovskite structure as are Ba ions, which favors paraelectric over ferroelectric phases.

The dielectric and field induced strain properties of a number of hot-pressed PLZT ceramics are presented in Table 3. Analogous to the PBZT ceramics, the field induced strains were found to be strongly associated with the magnitude of polarization. The variations of polarization and lateral strain with electric field for the compositions with La=5.5 atom% are shown in Figures 17 and 18, respectively. Of the PLZT compositions studied, maximum total lateral strains  $S_{2,10}$  (as high as  $14.8 \times 10^{-4}$ ) occurred at the compositions close to the rhombohedral and tetragonal ferroelectric boundary where the polarization was maximized, as shown in Figure 19. The maximum of the differential lateral strain was, however, found to occur in the neighborhood of the intersection among the rhombohedral, tetragonal ferroelectric and relaxor phases. The relationship between polarization and electric field and the change of lateral strain with electric field for several compositions near the intersection with Zr/Ti=65/35 are given in Figures 20 and 21, respectively. Among the compositions displayed in Table 3, the composition 8.6/65/35 exhibits the largest  $\Delta S_{2,10}$  value. Approximately speaking, as indicated in Figures 18 and 21, the strain increases linearly with electric field for the samples with relatively square P–E loop, whereas it varies with the square of field strength for those with a slim P–E loop. The later is usually referred to as electrostrictive strain. Large differential strain near ferroelectric and relaxor phase boundaries could be interpreted according to the behavior of microdomains under external and local electric fields. As shown in Figure 22, the microstructures of samples with composition close to the boundaries are characterized by isolated polar microdomains embedded in a matrix of nonpolar phase [4] [5]. In this situation, an internal depolarization field is induced to electrically compensate the corresponding microdomain so that the total energy is minimized. Upon the application of an external electric field to a sample, microdomains rotate and trend to align to the external electric field, thus generating strains macroscopically. At the same time, a local

electric field  $E_f$  is built up due to the rotation of microdomains away from the associated depolarization fields. When the external electric field is reduced, these local fields force the microdomains back to their initial directions. As a result, the sample is able to recover its initial shape with little remanent strain. For samples with large remanent polarization, ferroelectric domains are only separated by a thin domain wall and hence able to compensate each other electrically. In this case, there exists no such local field as described above that restores sample shapes when the external electric field is removed.

Table 4 lists the properties of sintered PLZT samples. Compared with the hot-pressed samples, the sintered samples exhibit no significant difference in dielectric constant. However, the electric field induced strains are approximately 15% less for sintered samples than for the hot-pressed. A probable reason for this may be the lower density of the former. The strain values of the sintered PLZT samples were found to be slightly higher than those of the highest found in the PBZT.

#### 4. Conclusions

(1) A region in the PBZT room temperature phase diagram was revealed to exhibit the characteristics of a relaxor phase, which is situated between the rhombohedral ( or tetragonal ) and the paraelectric phases.

(2) A broad maximum in room temperature dielectric constant was identified within the relaxor phase area. No significant anomaly in dielectric constant along the rhombohedral and tetragonal boundary which was found in this study, suggesting a strong compositional diffusion in this compositional region. The location of the phase boundary was determined from the X-ray phase diffraction patterns.

(3) Remanent polarization and coercive field of PBZT samples decrease drastically at the ferroelectric and relaxor phase boundaries with decreasing Pb/Ba ratio.

(4) The electric field induced strains of the PBZT samples were found to be proportional to the polarization with a varied proportionality factor depending on the compositions involved.



Both total and differential strains reach a maximum in the vicinity of the rhombohedral and tetragonal boundary.

(5) The  $\text{Bi}_2\text{O}_3$  additive significantly increased the density of pure PBZT samples.

(6) Very large electric field induced ( electrostrictive ) strains were discovered in the PLZT ceramics. The total strains are maximized around the boundary between the rhombohedral and tetragonal phases while the differential strains exhibit a maximum at the ferroelectric-relaxor boundaries. The later could be explained by the combined effect of local and external electric fields on microdomains.

(7) Sintered PLZT samples possess electric field induced strains about 20% smaller than those of the hot-pressed samples, resulting probably from the lower density of the sintered samples. The strain values of the sintered PLZT are slightly higher than those found in the PBZT.

## 5. References

- [1] G. Haertling and G. Li, *Commercial Use of Space*, an annul report in the department of Ceramic Engineering, Clemson University, August 28, 1992.
- [2] T. Ikeda, *J. Phys. Soc. Japan*, vol. 14(2), p168 (1959)
- [3] G. H. Haertling and C. D. Land, *J. Am. Cer. Soc.*, vol. 54, p1 (1971).
- [4] Z. W. Yin, *J. J. Appl. Phys.*, vol. 24, suppl. 24-2, p442 (1985).
- [5] M. Yokosuka and M. Marutake, *J. J. Appl. Phys.*, vol. 25, No. 7, p981 (1986).

Table 1. Properties of PBZT ceramics.

	Dielectric Constant	tg $\delta$ (%)	$\rho$ (g/cm <sup>3</sup> )	$E_c$ (kV/cm)	$P_R$ ( $\mu\text{C}/\text{cm}^2$ )	$P_{10}$	$\Delta S_{2,10}$ $\times 10^4$	$S_{2,10}$ $\times 10^4$	$\Delta S_{1,10}$ $\times 10^4$	$S_{1,10}$ $\times 10^4$
19/84/16	460	4.4	6.88	5.0	20	26	-0.30	-1.20		
23/84/16	5250	11.5	6.97	1.5	4	26	-2.50	-2.53		
27/84/16	6270	11.1	6.94	2.0	3	20	-2.20	-2.20		
32/84/16	6370	5.7	6.98	2.5	4	18	-0.55	-0.55		
35/84/16	4110	1.9	6.97		1	8				
15/70/30	630	3.2	7.32	6.0	34	39	-1.30	-4.40	--	--
20/70/30	1960	4.2	7.32	4.0	32	34	-1.80	-5.00	--	
25/70/30	5830	9.5	7.28		4	26	-4.27	-4.47	10.3	11.2
26/70/30	6110	9.7	7.22		3	21	-3.46	-3.46	--	
27/70/30	6400	10.0	7.19		3	18	-2.74	-3.10	8.50	8.50
29/70/30	7680	12.8	7.07		1	12	-1.20	-1.20	5.20	5.20
32/70/30	7790	6.6	7.05			8	-0.65	-0.65	--	
35/70/30	6730	2.3	6.99			6	-0.33	-0.33	--	--
43/70/30	5940	2.0	6.94			5	-0.33	-0.33	--	--
19/57/43	1450	2.6	7.38	5.0	34	40	-2.83	-10.00	--	--
23/57/43	3350	5.6	7.38	4.0	30	32	-3.00	-8.40	--	--
25/57/43	4110	8.1	7.35	3.0	17	27	-4.13	-7.20	--	--
27/57/43	5140	8.4	7.36	2.0	7	24	-5.53	-5.67	--	--
29/57/43	5410	8.7	7.34	2.0	4	19	-3.13	-3.67	--	--
32/57/43	6230	10.7	7.38		2	15	-1.10	-1.10	--	--
35/57/43	6270	7.8	7.38		1	11	-0.45	-0.45	--	--
40/57/43	4820	3.1	7.35			7	-0.25	-0.25	--	--
27/80/20	9180	11.0	7.07		1	19	-1.80	-1.80		
27/76/24	8050	11.1	7.16		2	19	-2.00	-2.00		
27/72/28	6480	10.1	7.18		2	17	-2.57	-2.57		
27/70/30	6400	10.0	7.19		3	18	-2.74	-3.10	8.50	8.50
27/68/32	6670	11.1	7.19		3	17	-2.47	-2.47	--	2.75
27/64/36	6090	10.8	7.26		4	18	-2.67	-2.73	--	--
27/60/40	5230	8.4	7.38	2.0	5	22	-3.67	-3.75	--	--
27/55/45	4760	7.8	7.34	2.5	10	24	-5.33	-5.67	--	--
27/52/48	4410	7.4	7.40	4.0	20	32	-4.34	-7.39	--	--
27/50/50	3840	4.2	7.40	7.5	21	29	-3.29	-6.18	--	--
27/47/53	2250	4.0	7.36	10.0	20	23	-2.00	-5.33	--	--

Table 1. Properties of PBZT ceramics ( continued ).

	Dielectric Constant	tg $\delta$ (%)	$\rho$ (g/cm <sup>3</sup> )	$E_c$ (kV/cm)	$P_R$ ( $\mu$ C/cm <sup>2</sup> )	$P_{10}$	$\Delta S_{2,10}$ $\times 10^4$	$S_{2,10}$ $\times 10^4$	$\Delta S_{1,10}$ $\times 10^4$	$S_{1,10}$ $\times 10^4$
35/40/60	1730	2.0	7.18	12.0	19	25	-1.10	-3.33		
40/40/60	4950	8.3	7.24	2.5	2	10	-1.10	-1.20		
45/40/60	5860	7.7	7.22			8	-0.40	-0.40		
40/35/65	1280	2.2	7.18	14.0	17	21	-1.10	-2.33		
40/40/60	4950	8.3	7.24		2	10	-1.10	-1.20		
40/45/55	5380	5.4	7.22		1	6	-0.20	-0.20		
40/50/50	6130	5.0	7.33		1	10	-0.20	-0.20		
40/57/43	4820	3.1	7.34			6			--	--
23/76/24	6030	9.9	7.06		4	22	-2.70	-2.80		
25/60/40	4490	7.4	7.34	3.0	20	36	-5.60	-7.00	--	--
25/55/45	4640	7.8	7.36	3.5	20	28	-3.20	-6.40	--	--
29/55/45	4800	8.8	7.29	2.0	2	18	-3.53	-3.80	--	--

Note: tg  $\delta$  is the loss factor,  $\rho$  the density,  $E_c$  the coercive field,  $P_R$  the remanent polarization,  $P_{10}$  the polarization at an electric field of 10 kV/cm,  $\Delta S_{2,10}$  ( lateral ) and  $\Delta S_{1,10}$  ( longitudinal ), the differential strains, are defined as the difference between the strains at an electric field of 10 kV/cm and 0 kV/cm,  $S_{2,10}$  and  $S_{1,10}$  are, respectively, the total lateral and longitudinal strains at an electric field of 10 kV/cm.

Table 2. Influence of additive Bi<sub>2</sub>O<sub>3</sub> on the properties of pure PBZT ceramics.

	Dielectric Constant	tg $\delta$ (%)	$\rho$ (g/cm <sup>3</sup> )	$E_c$ (kV/cm)	$P_R$ ( $\mu$ C/cm <sup>2</sup> )	$P_{10}$	$\Delta S_{2,10}$ $\times 10^4$	$S_{2,10}$ $\times 10^4$	$\Delta S_{1,10}$ $\times 10^4$	$S_{1,10}$ $\times 10^4$
27/70/30 <sub>0</sub> *	4020	4.5	6.92	3.5	7	24	-3.70	-4.00		
27/70/30 <sub>1</sub>	5230	8.2	7.07	2.0	3	22				
27/70/30 <sub>2</sub>	6310	10.0	7.19	2.0	3	21	-3.33	-3.33		
27/70/30 <sub>3</sub>	6660	11.0	7.27	1.5	3	20	-1.80	-1.80		

\* the mole percentage of bismuth oxide.

Table 3. Properties of hot-pressed PLZT ceramics

	Dielectric Constant	tg $\delta$ (%)	$\rho$ (g/cm <sup>3</sup> )	$E_c$ (kV/cm)	$P_R$ ( $\mu$ C/cm <sup>2</sup> )	$P_{10}$	$\Delta S_{2,10}$ $\times 10^4$	$S_{2,10}$ $\times 10^4$	$\Delta S_{1,10}$ $\times 10^4$	$S_{1,10}$ $\times 10^4$
55560	1820	3.2		7.0	30	37	-5.3	-15.2		
55565	2320	3.0		9.0	27	31	-4.5	-13.7		
55570	1920	3.8		8.5	30	36	-4.2	-13.5		
55575	1600	3.7		8.0	32	36	-4.0	-13.5	10.0	36.5
55580	1690	3.8		8.0	32	36	-4.0	-14.0		
55585	1750	3.8		7.5	32	34	-3.8	-14.2	10.0	39.6
79700/6	5070	5.9		3.5	22	27	-2.7	-8.3		
79700/10	4800	5.8		2.0	5	24	-6.0	-7.7	20.0	23.7
120400	1130	2.2		12.0	20	22	-5.4	-3.0		
20540	1270	2.6		12.0	32	36	-3.8	-12.4		
23660/Sn	1120	2.3		7.0	32	36	-0.7	-2.0		
60650	1180	2.8		5.5	31	35	-2.7	-11.0	9.0	34.2
70650	2600	2.1		5.0	28	34	-2.4	-13.5		
80650	4970	4.1		3.0	23	33	-4.0	-12.0		
86650	5540	5.3		1.0	4	31	-8.2	-8.8		
88650	5700	5.9			1	30	-5.4	-5.7		
90650	6090	6.6				23	-3.6	-3.6	5.7	5.8
95650	6760	6.8				22	-2.4	-2.4		
96650	5750	6.0				17	-0.9	-0.9		
140650	1880	0.6				3				
50550	1760	2.5		12.0	27	33	-4.0	-11.2		
50560	1720	3.2		10.0	29	34	-4.7	-13.1		
50570	1560	3.5		9.5	30	34	-4.5	-13.0	10.0	28.0

Note: tg  $\delta$  is the loss factor,  $\rho$  the density,  $E_c$  the coercive field,  $P_R$  the remanent polarization,  $P_{10}$  the polarization at an electric field of 10 kV/cm,  $\Delta S_{2,10}$  ( lateral ) and  $\Delta S_{1,10}$  ( longitudinal ), the differential strains, are defined as the difference between the strains at an electric field of 10 kV/cm and 0 kV/cm,  $S_{2,10}$  and  $S_{1,10}$  are, respectively, the total lateral and longitudinal strains at an electric field of 10 kV/cm. 60650 denotes 6.0/65.0/35 (La/Zr/Ti).

Table 4. Properties of sintered PLZT ceramics.

	Dielectric Constant	tg $\delta$ (%)	$\rho$ (g/cm <sup>3</sup> )	$E_c$ (kV/cm)	$P_R$ ( $\mu$ C/cm <sup>2</sup> )	$P_{10}$ ( $\mu$ C/cm <sup>2</sup> )	$\Delta S_{2,10}$ $\times 10^4$	$S_{2,10}$ $\times 10^4$	$\Delta S_{1,10}$ $\times 10^4$	$S_{1,10}$ $\times 10^4$
55550	2250	2.6	7.55	12.0	30	37	-3.6	-9.4		
55560	2300	2.7	7.42	11.0	30	36	-4.0	-10.9		
55570	1820	3.2	7.33	7.7	34	40	-3.8	-12.6		
55580	1580	3.3	7.55	6.5	30	34	-2.8	-12.2		
55590	1590	2.7	7.56	7.0	32	34	-2.8	-12.6		
55600	1660	3.2	7.56	6.5	34	37	-3.7	-13.7		
55560/1	2830	2.6	7.67	11.0	34	39	-4.5	-11.3	--	--
86650/1	4890	6.7	7.58	3.0	20	27	-5.4	-8.3	--	--
86650/2	5370	6.9	7.61	3.0	20	33			--	--
86650 <sub>1</sub>	5120	6.7	7.61	4.0	34	37			--	--
86650 <sub>2</sub>	4530	6.9	7.61	4.0	34	37			--	--

86650<sub>1</sub>: K906 Milled ZrO<sub>2</sub>; 86650<sub>2</sub>: CS Milled ZrO<sub>2</sub>.

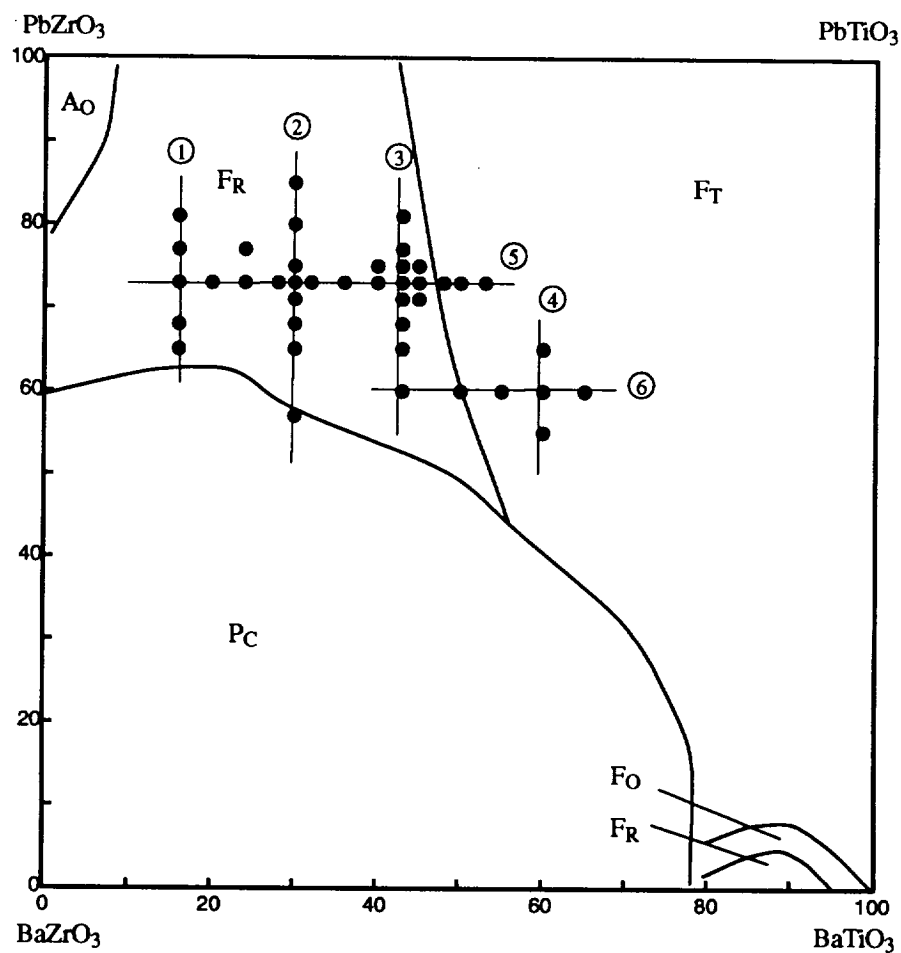


Figure 1. Room temperature phase diagram for the system  $\text{PbZrO}_3\text{--PbTiO}_3\text{--BaZrO}_3\text{--BaTiO}_3$  (PBZT). where  $F_R$  denotes rhombohedral phase,  $F_T$  tetragonal phase and  $P_C$  paraelectric phase [2].

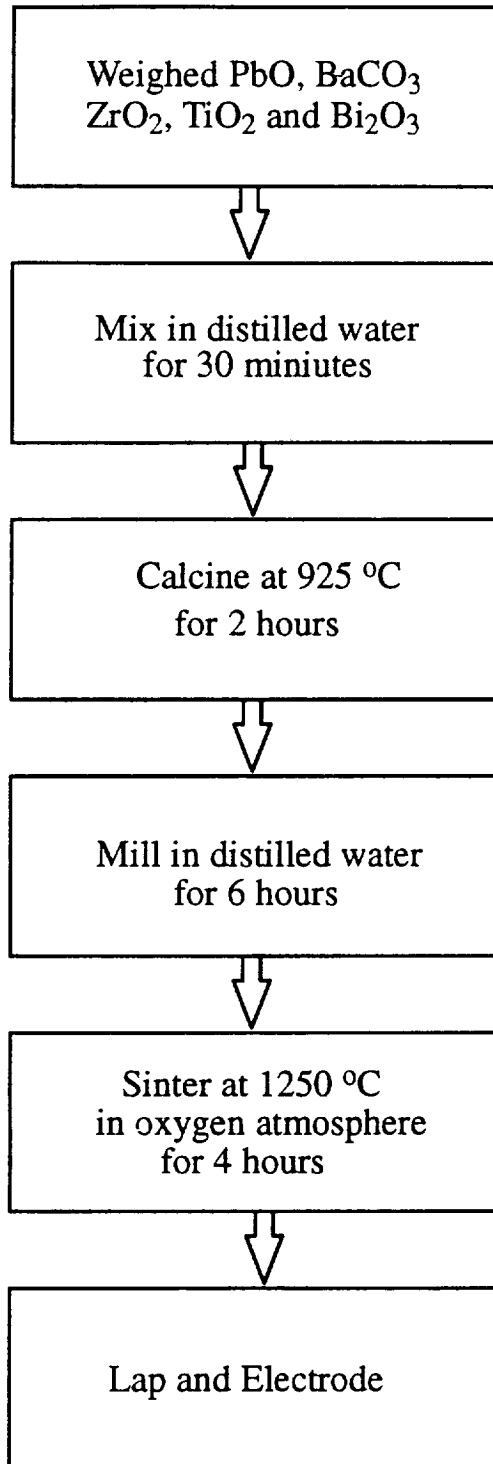


Figure 2. Flowchart of PBZT processing.

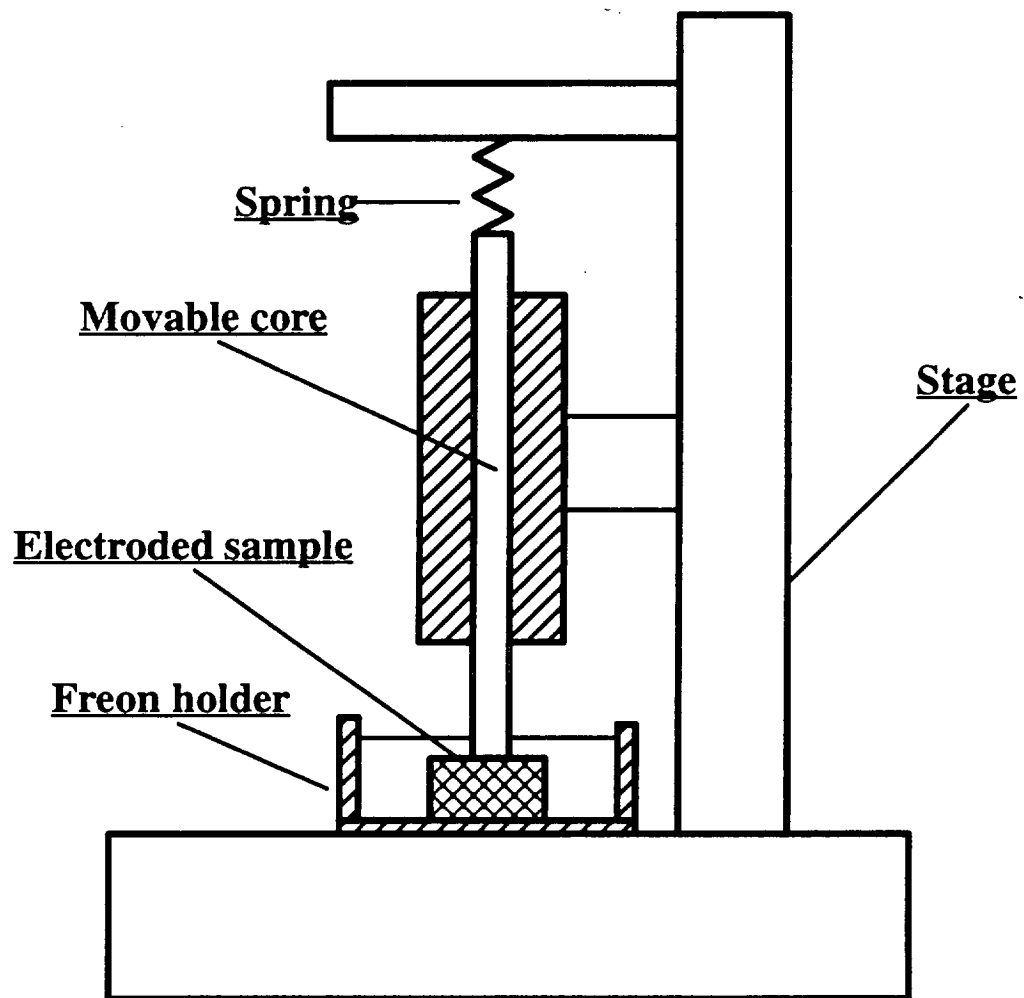


Figure 3. Device for measurement of electric field induced strains.



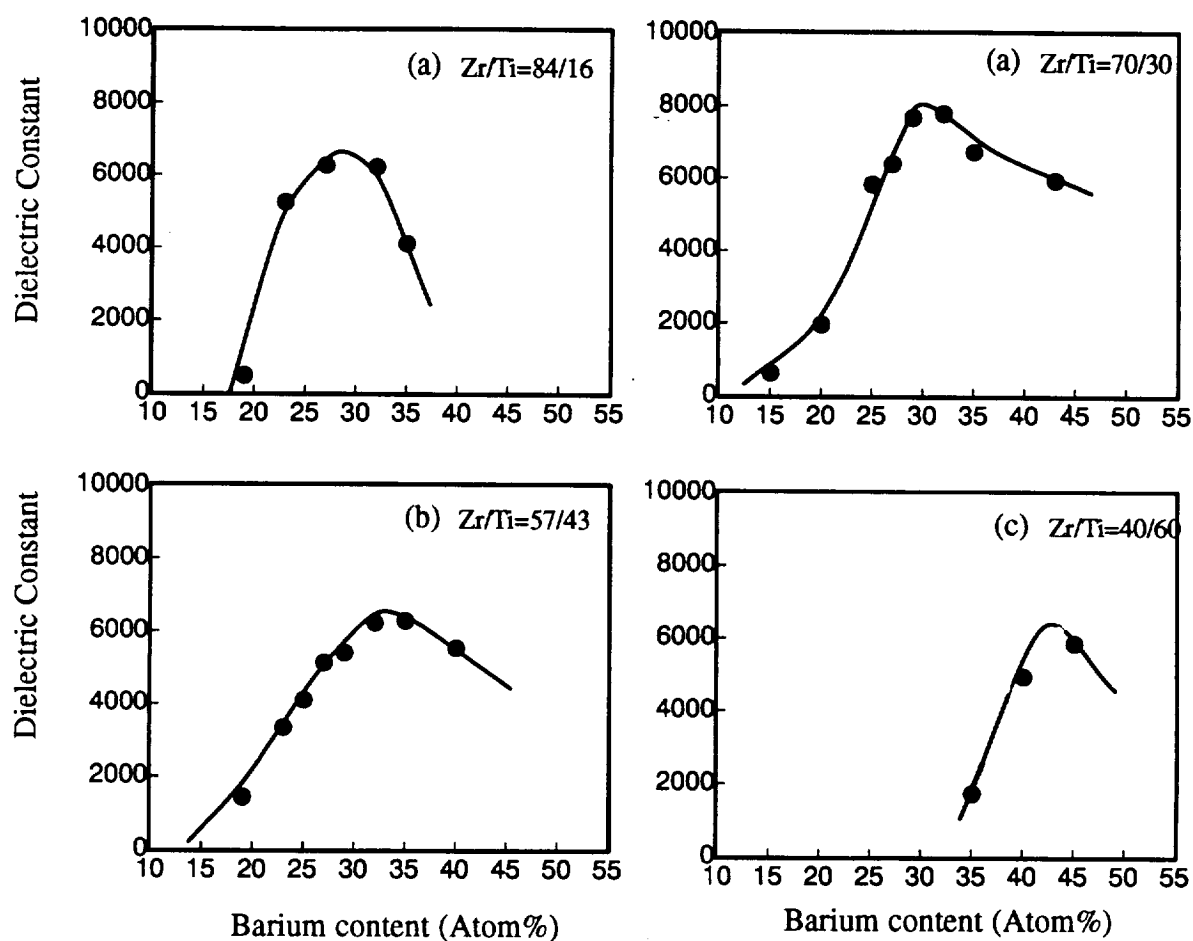


Figure 4. Variation of dielectric constant with barium content at constant Zr/Ti ratios.

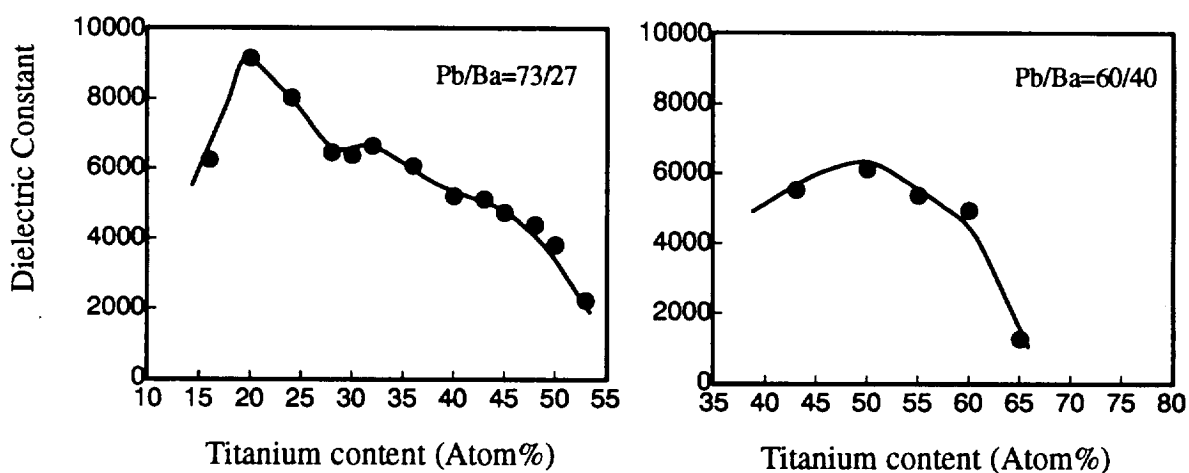


Figure 5. Variation of dielectric constant with titanium content at constant Pb/Ba ratios.

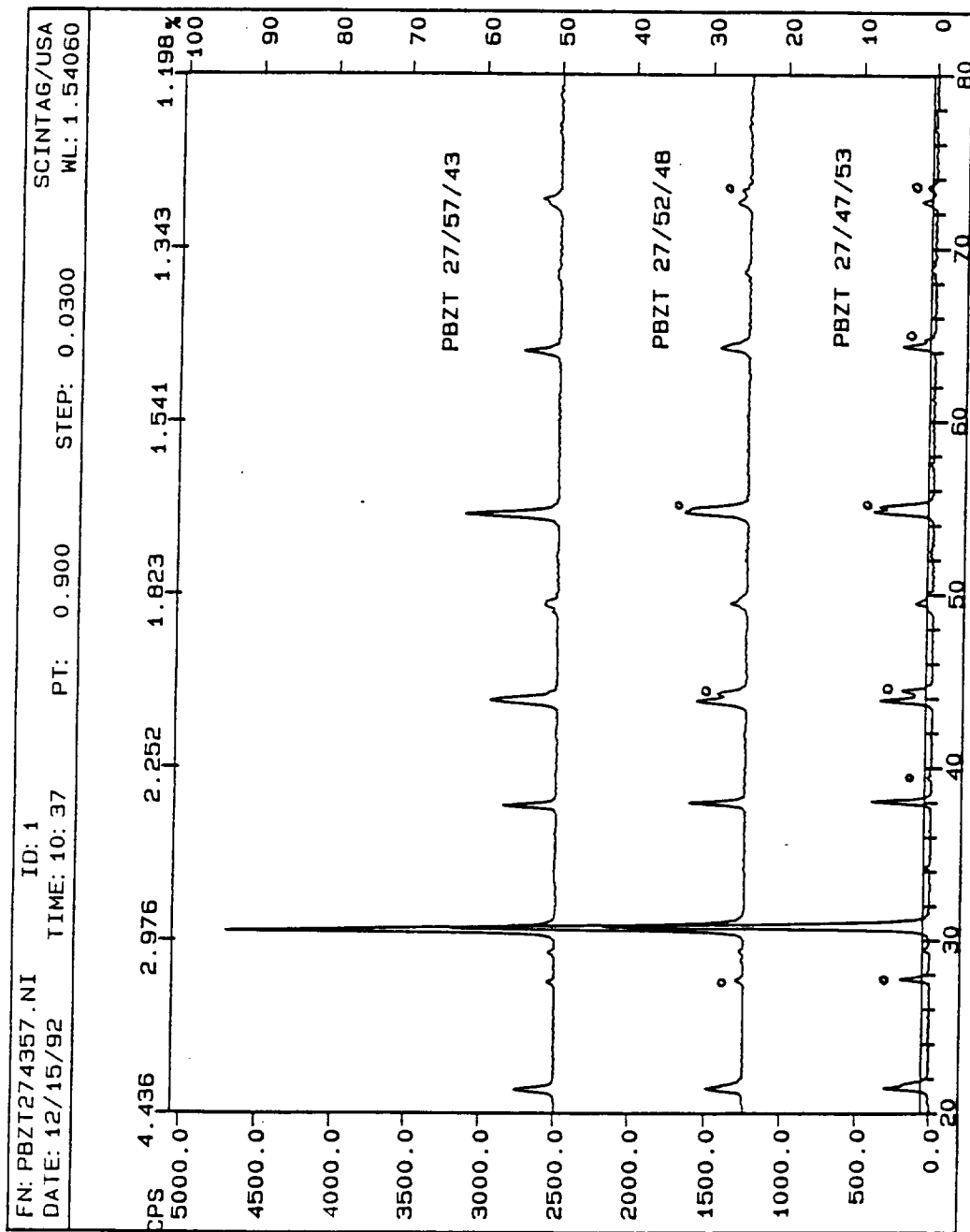


Figure 6. X-ray diffraction pattern of PBZT ceramics with Pb/Ba=73/27. o indicates the characteristic peaks of the tetragonal phase.

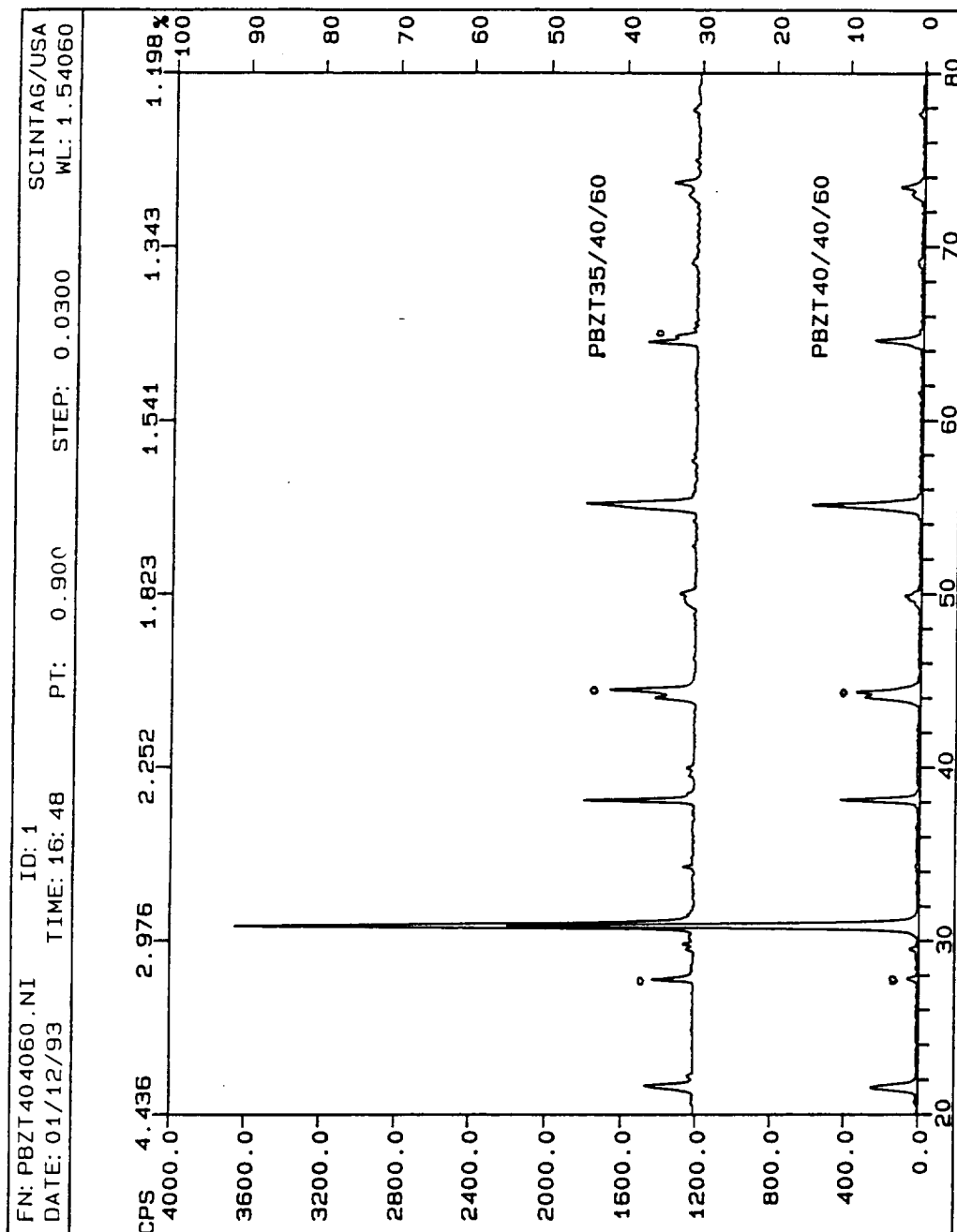


Figure 7. X-ray diffraction pattern of PBZT ceramics with Zr/Ti=40/60. o indicates the characteristic peaks of rhombohedral phase.

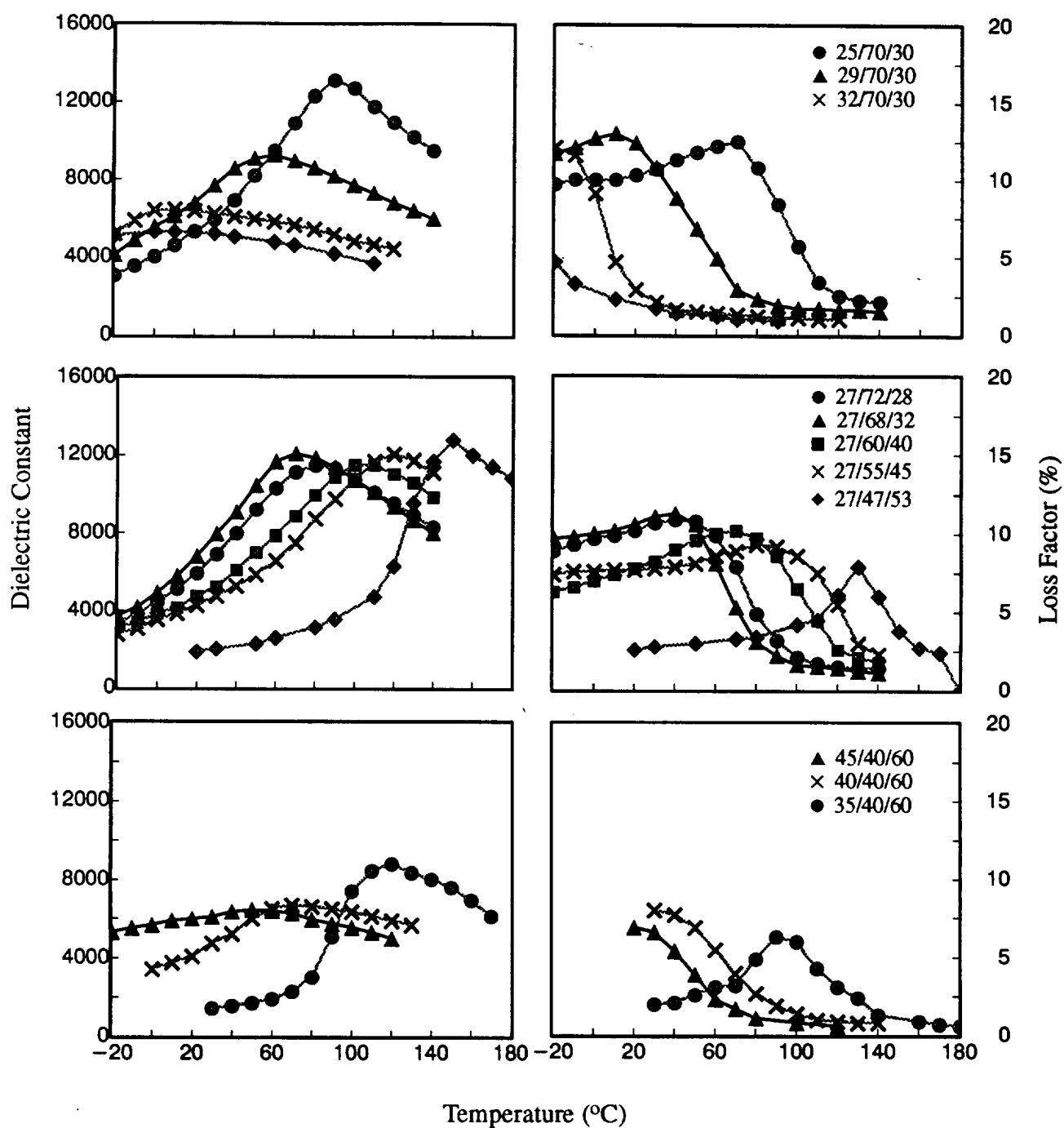


Figure 8. Temperature dependence of dielectric constant and loss factor for the PBZT compositions with constant Zr/Ti ratios ( top and bottom) and with constant Pb/Ba ratio (middle).

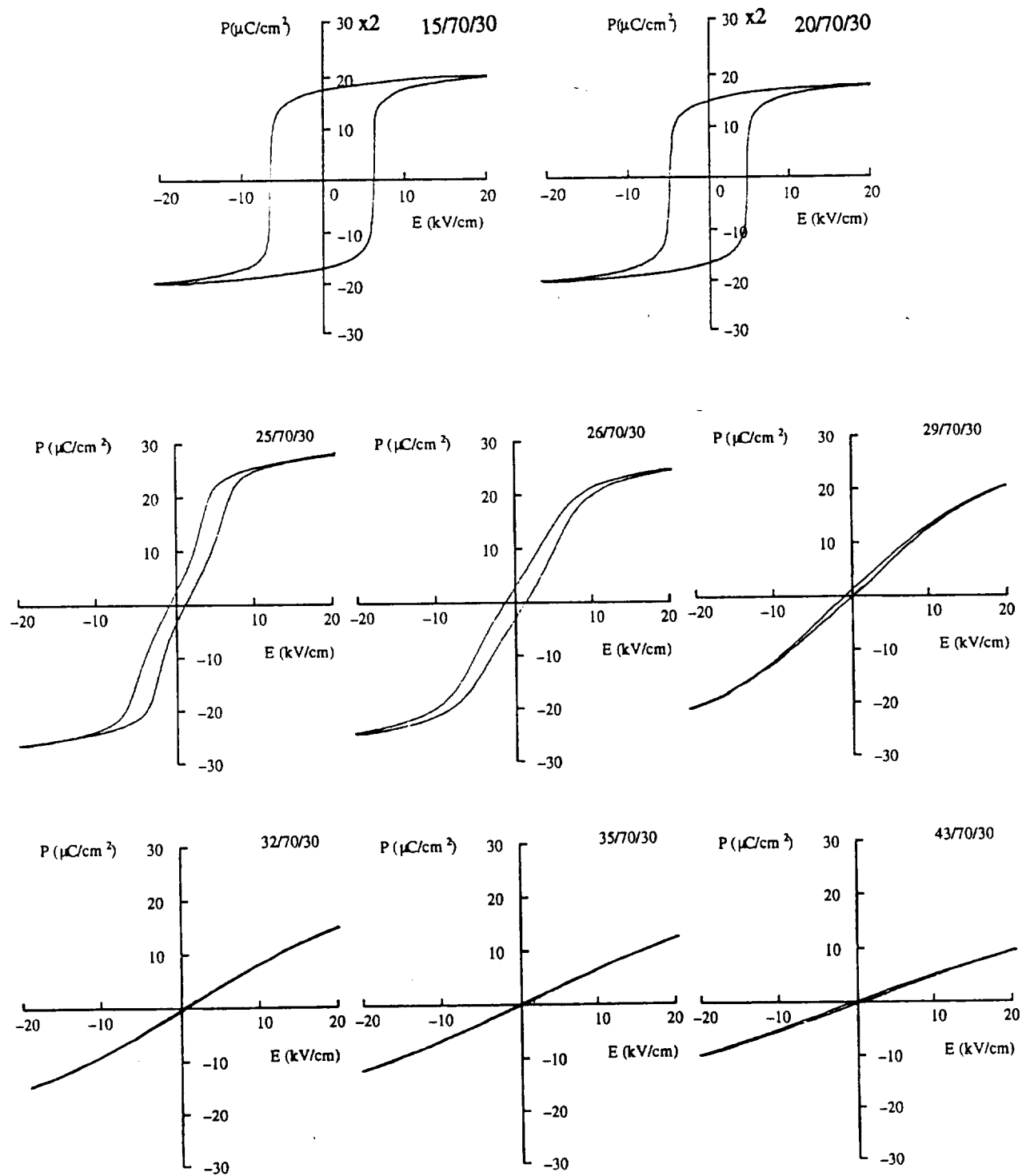


Figure 9. Relationship between polarization and electric field for the PBZT ceramics with Zr/Ti=70/30.

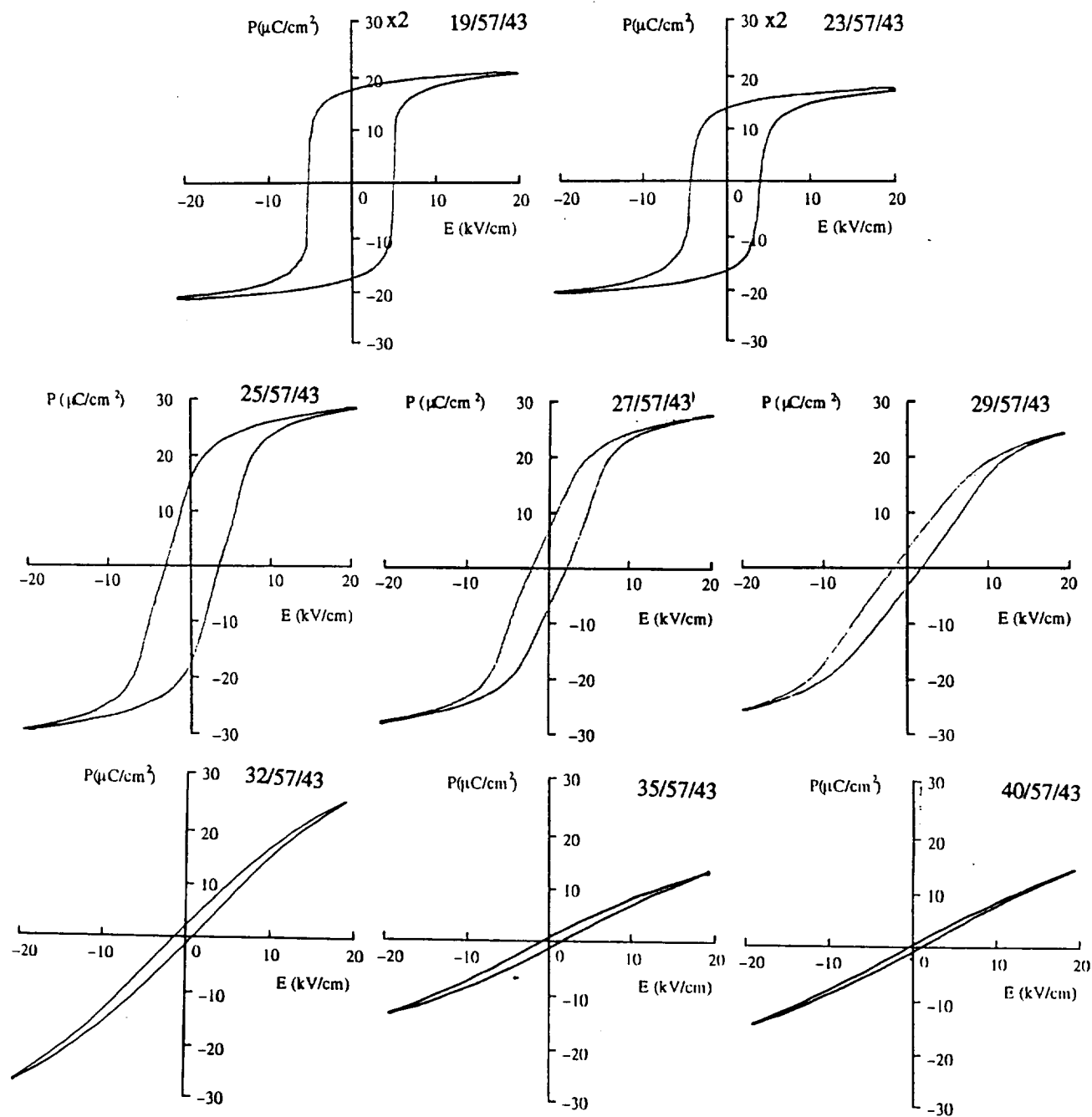


Figure 10. Relationship between polarization and electric field for the PBZT ceramics with Zr/Ti=57/43.

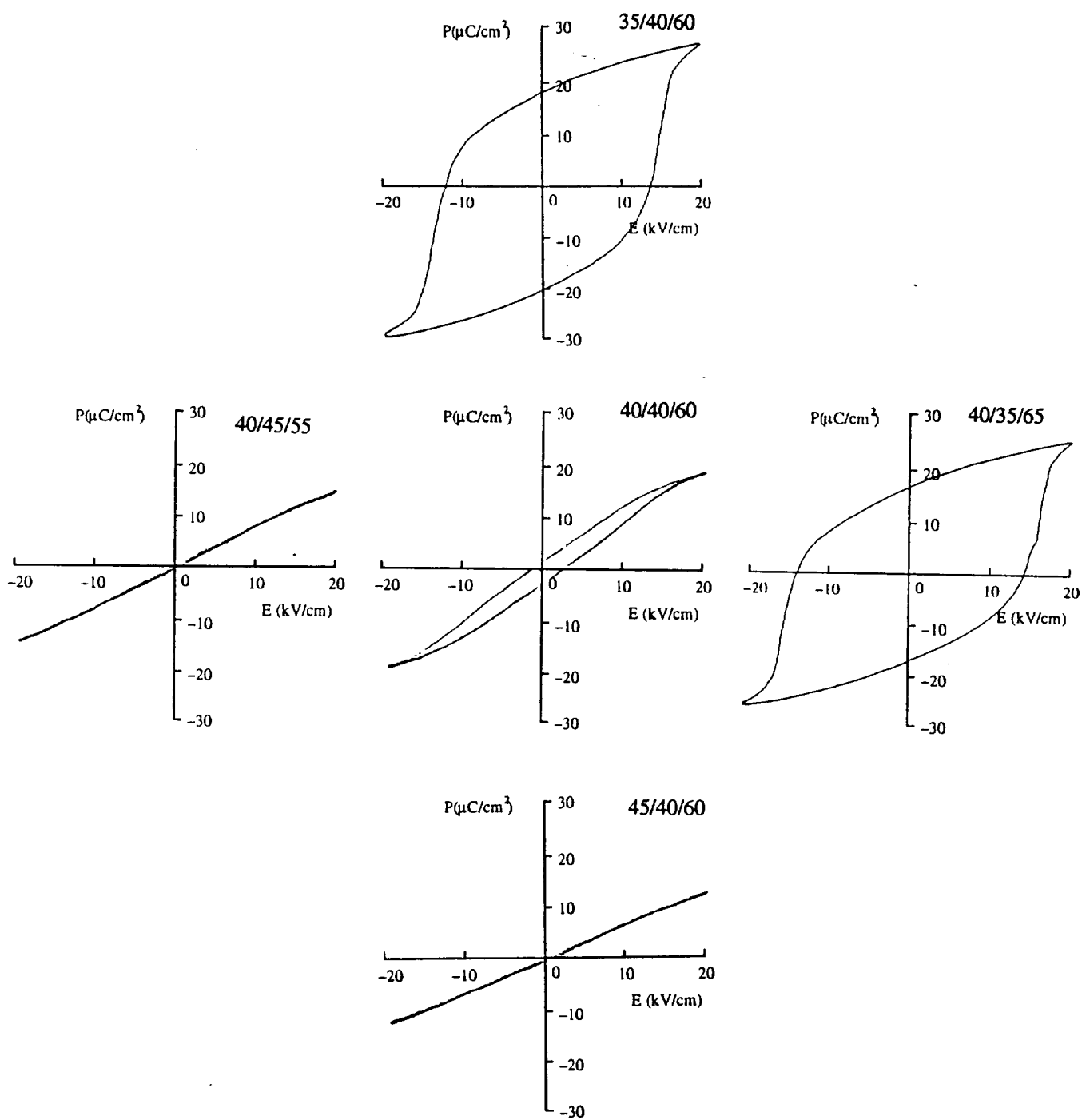


Figure 11. Relationship between polarization and electric field for the PBZT ceramics with Zr/Ti=40/60 and Pb/Ba=60/40.

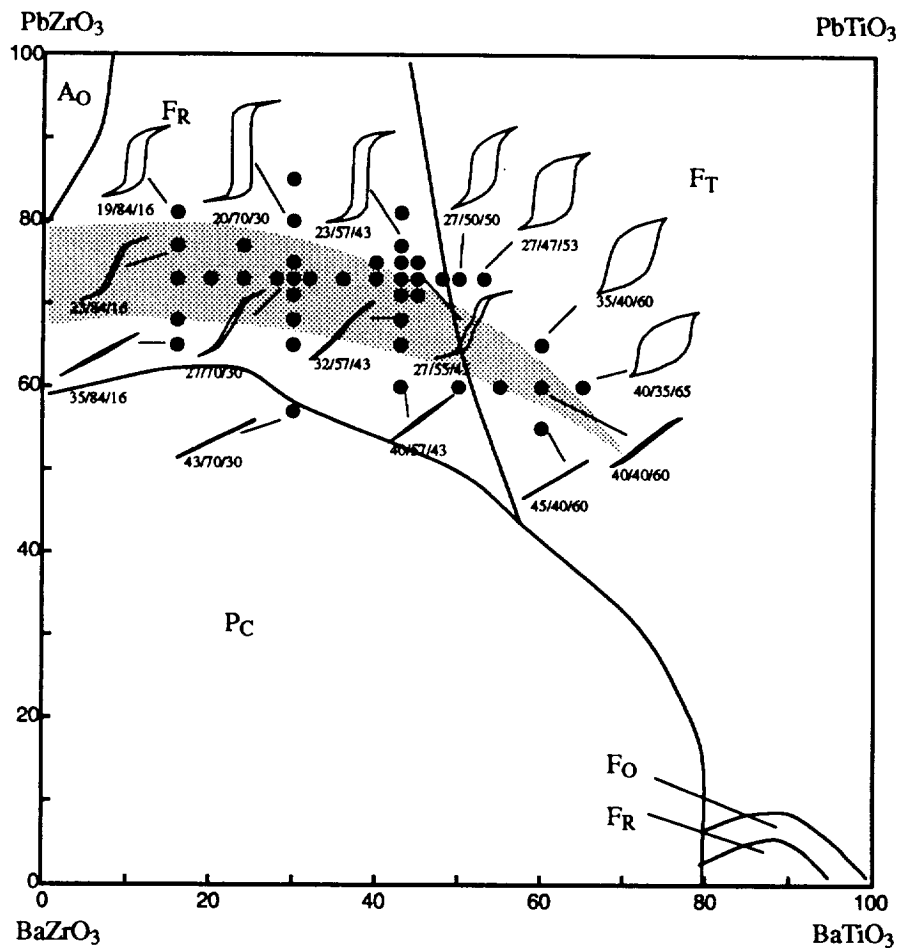


Figure 12. P-E relationship with corresponding composition in the room temperature phase diagram of the PBZT system. Shadowed area represents relaxor phase region.



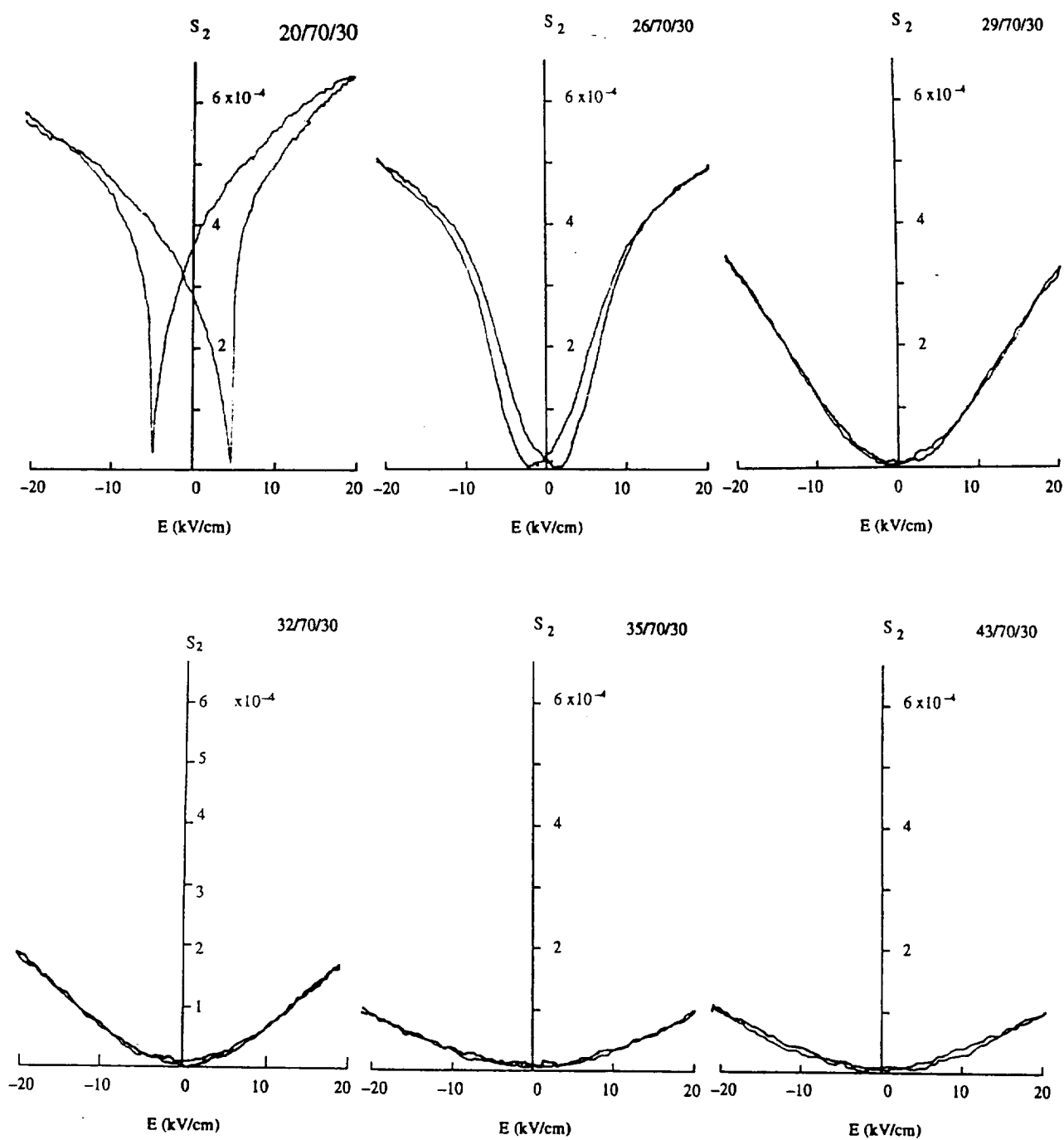


Figure 13. Variation of lateral strain with electric field for the PBZT ceramics with Zr/Ti=70/30.

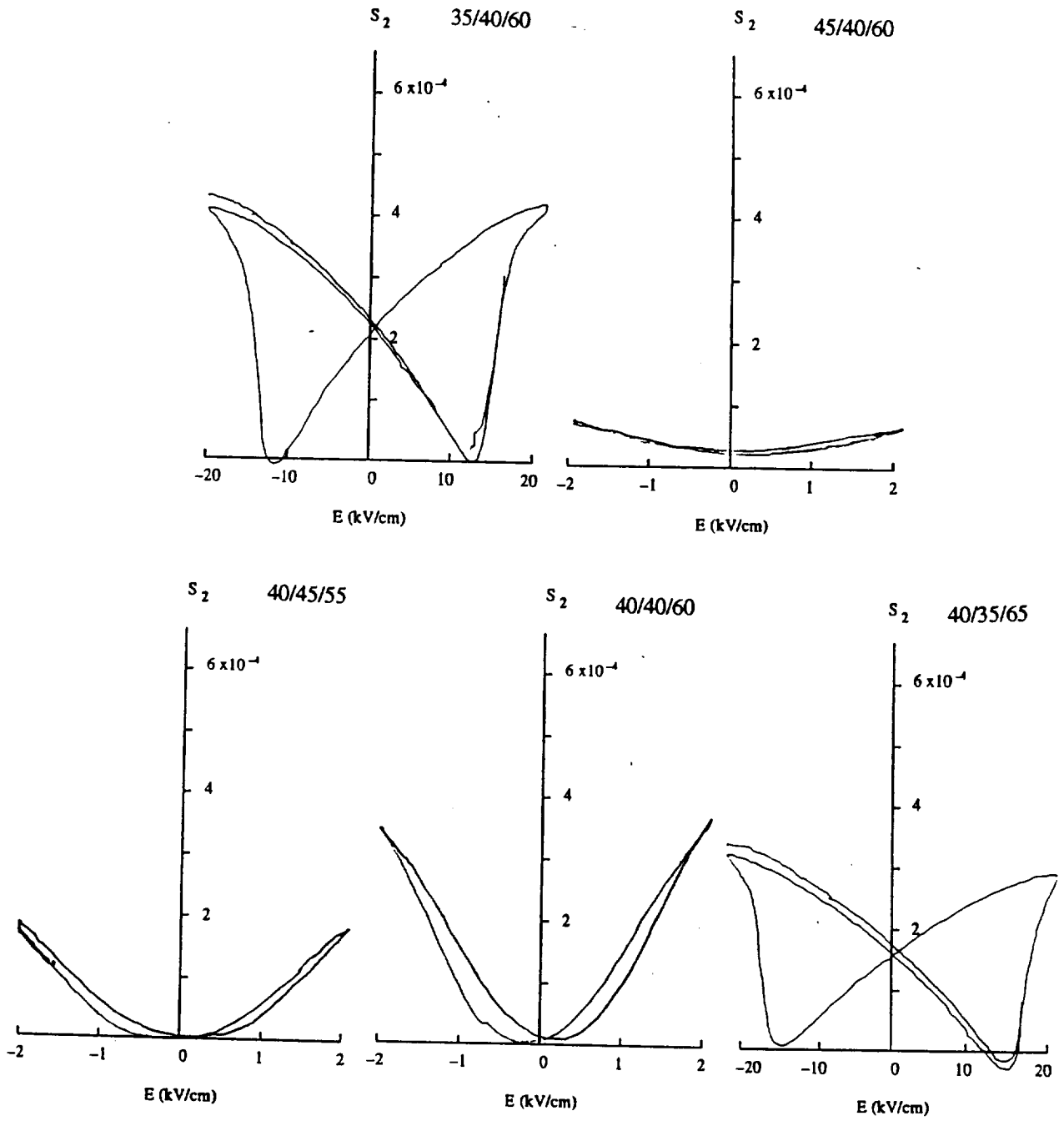


Figure 14. Variation of lateral strain with electric field for the PBZT ceramics with Zr/Ti=40/60 and Pb/Ba=60/40.

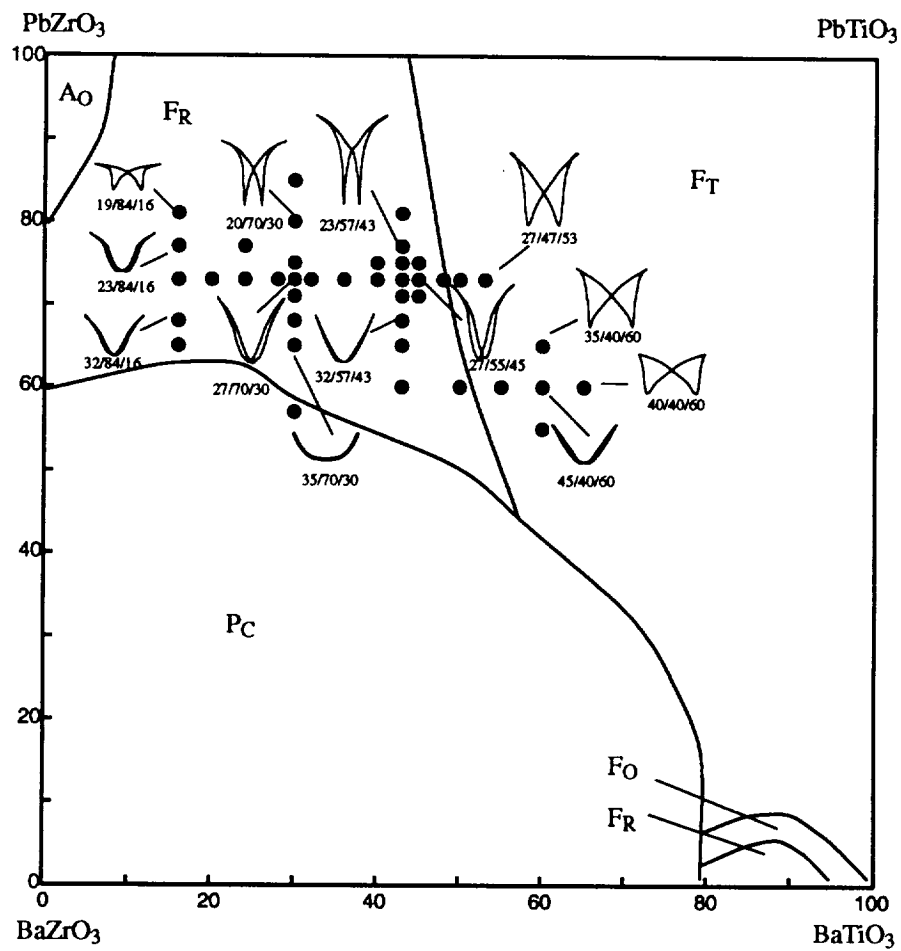


Figure 15. S-E relationship with corresponding composition in the room temperature phase diagram of the PBZT system.

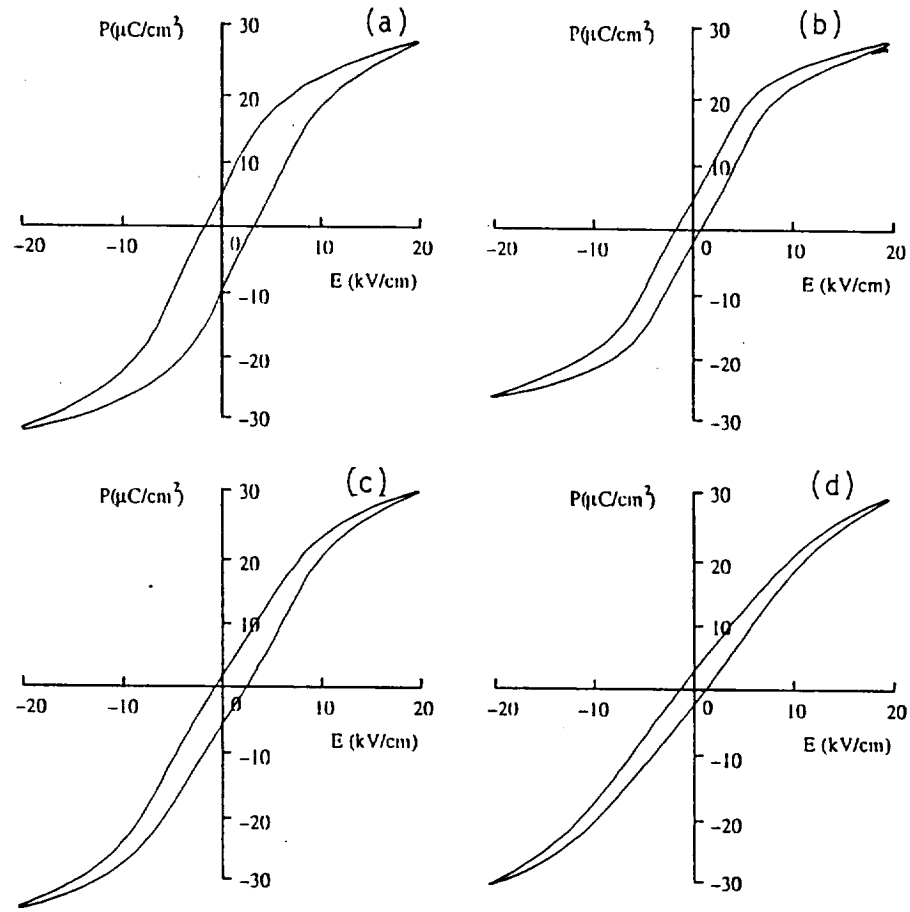


Figure 16. Influence of additive Bi<sub>2</sub>O<sub>3</sub> on the P-E relationship of PBZT 27/70/30; (a) 0 Atom% Bi<sub>2</sub>O<sub>3</sub>, (b) 1 Atom%, (c) 2 Atom% and (d) 3 Atom% Bi<sub>2</sub>O<sub>3</sub>.

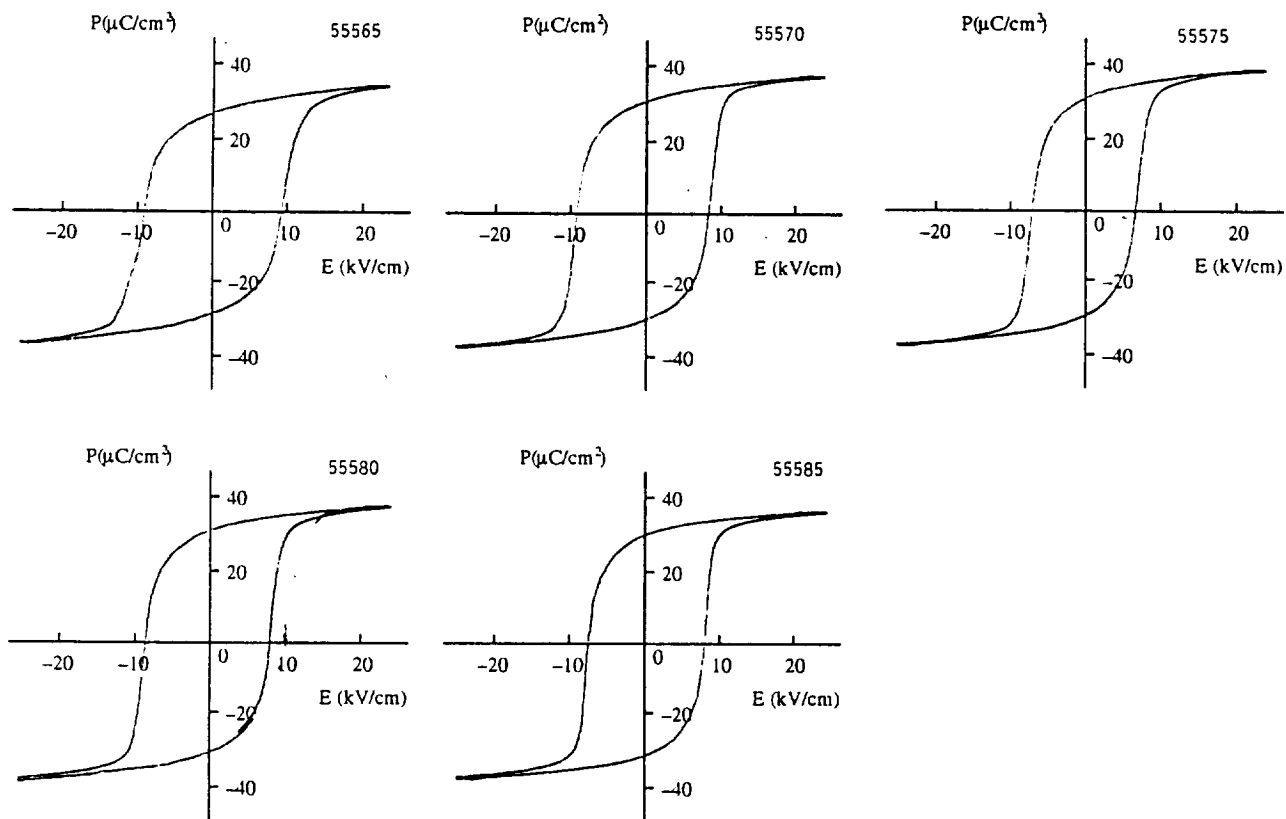


Figure 17. Relationship between polarization and electric field for the PLZT ceramics with La=5.5 Atom%.

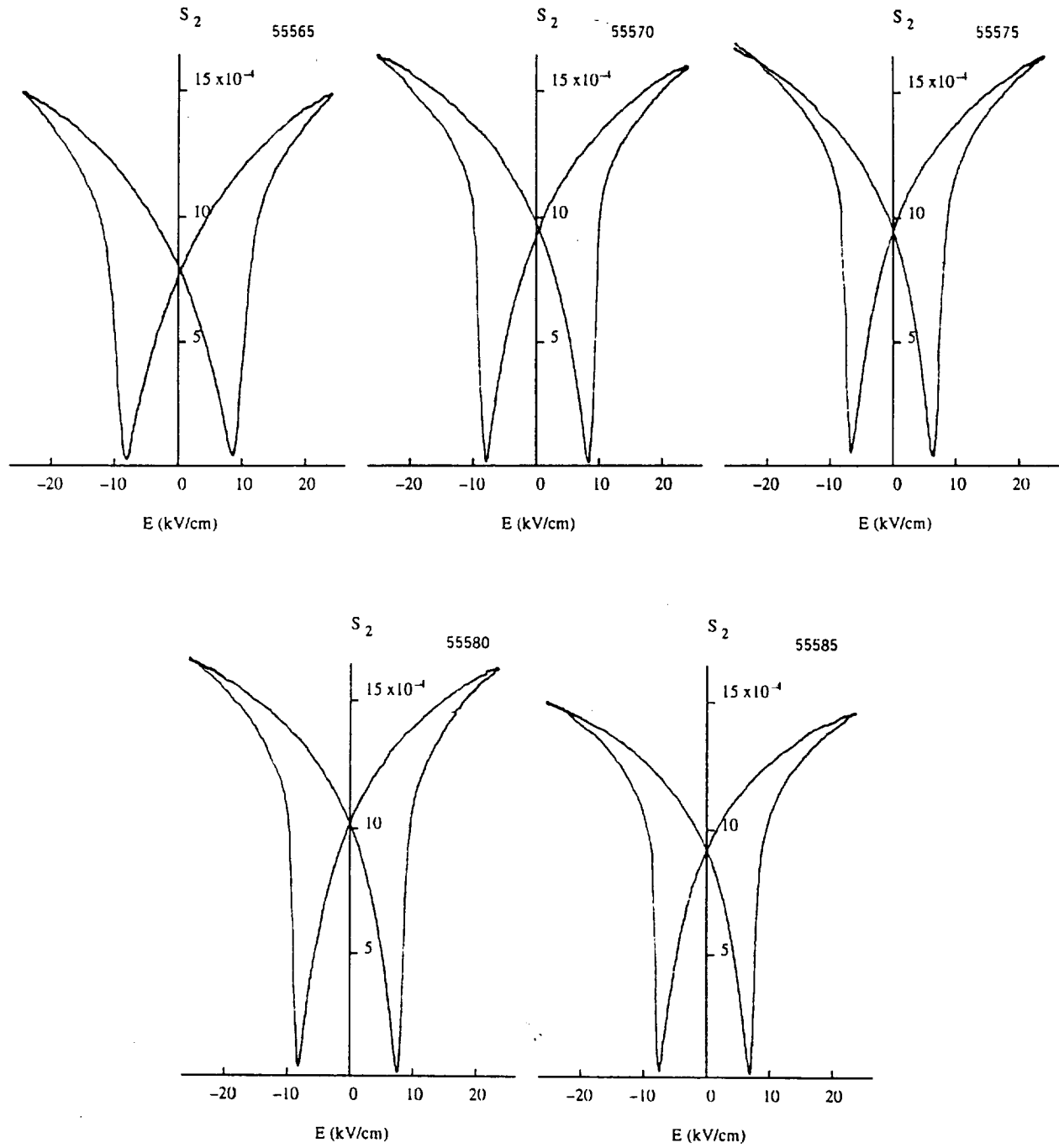


Figure 18. Variation of lateral strain with electric field for the PLZT ceramics with La=5.5 Atom%.

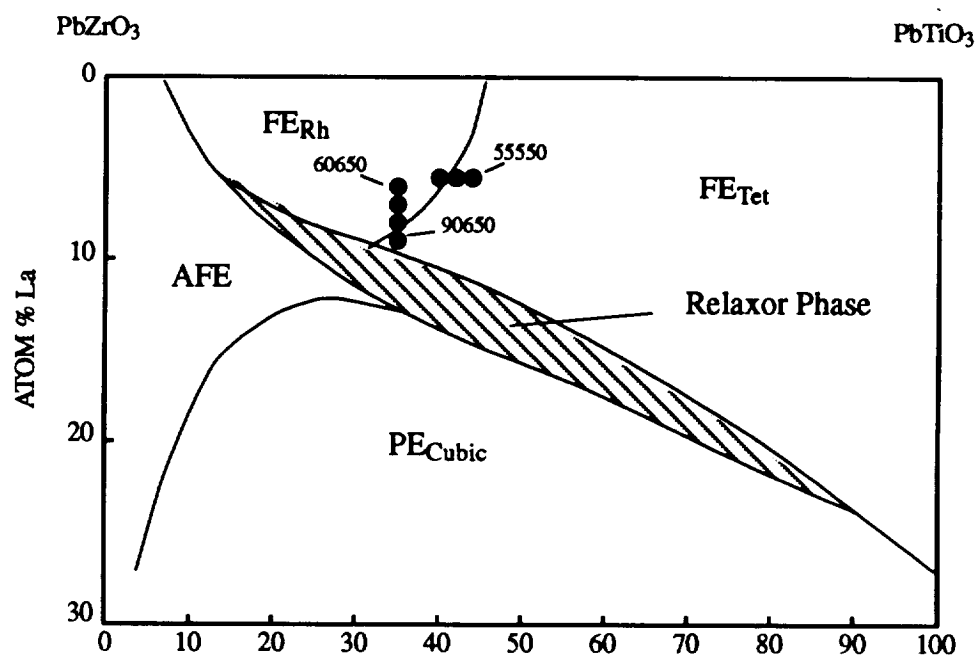


Figure 19. Room-temperature phase diagram of PLZT system [3].

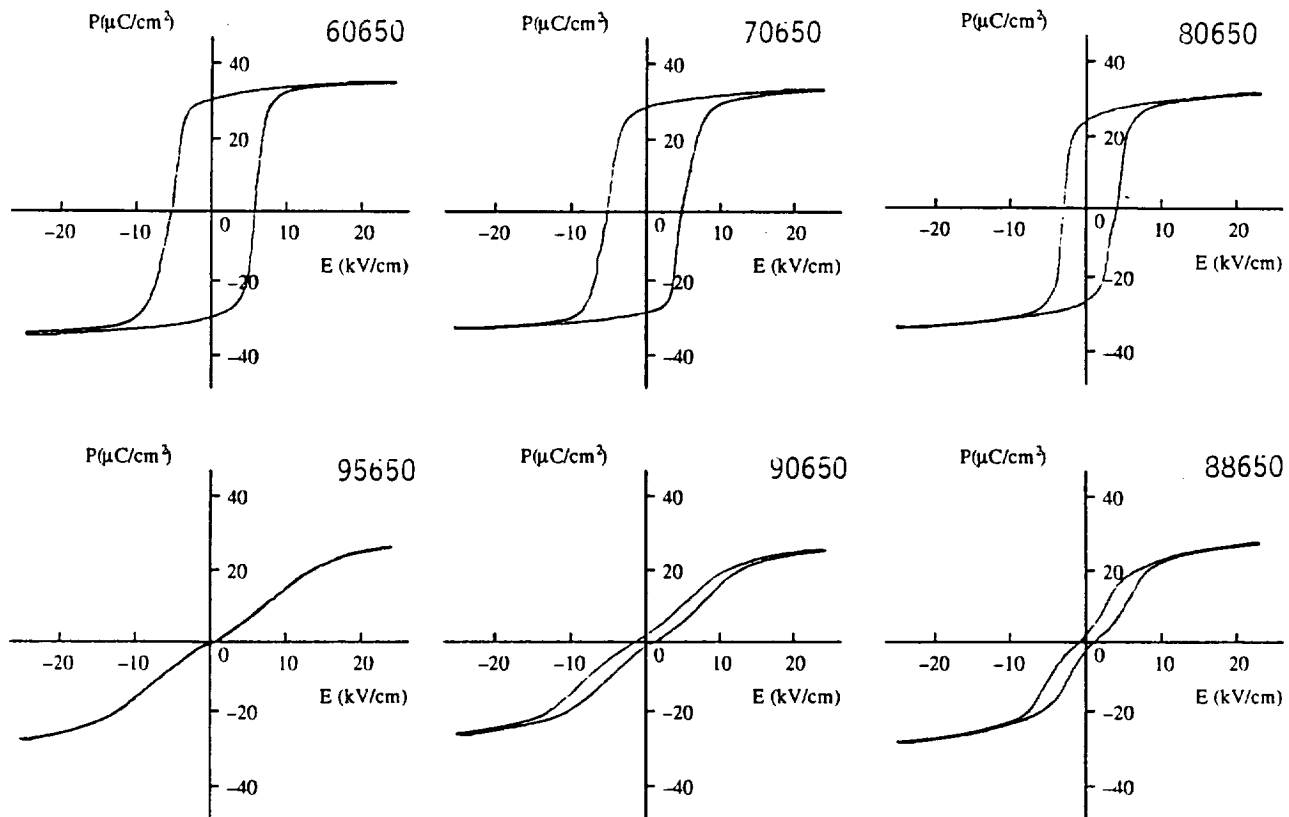


Figure 20. Relationship between polarization and electric field for the PLZT ceramics with  $\text{Zr}/\text{Ti}=65/35$ .



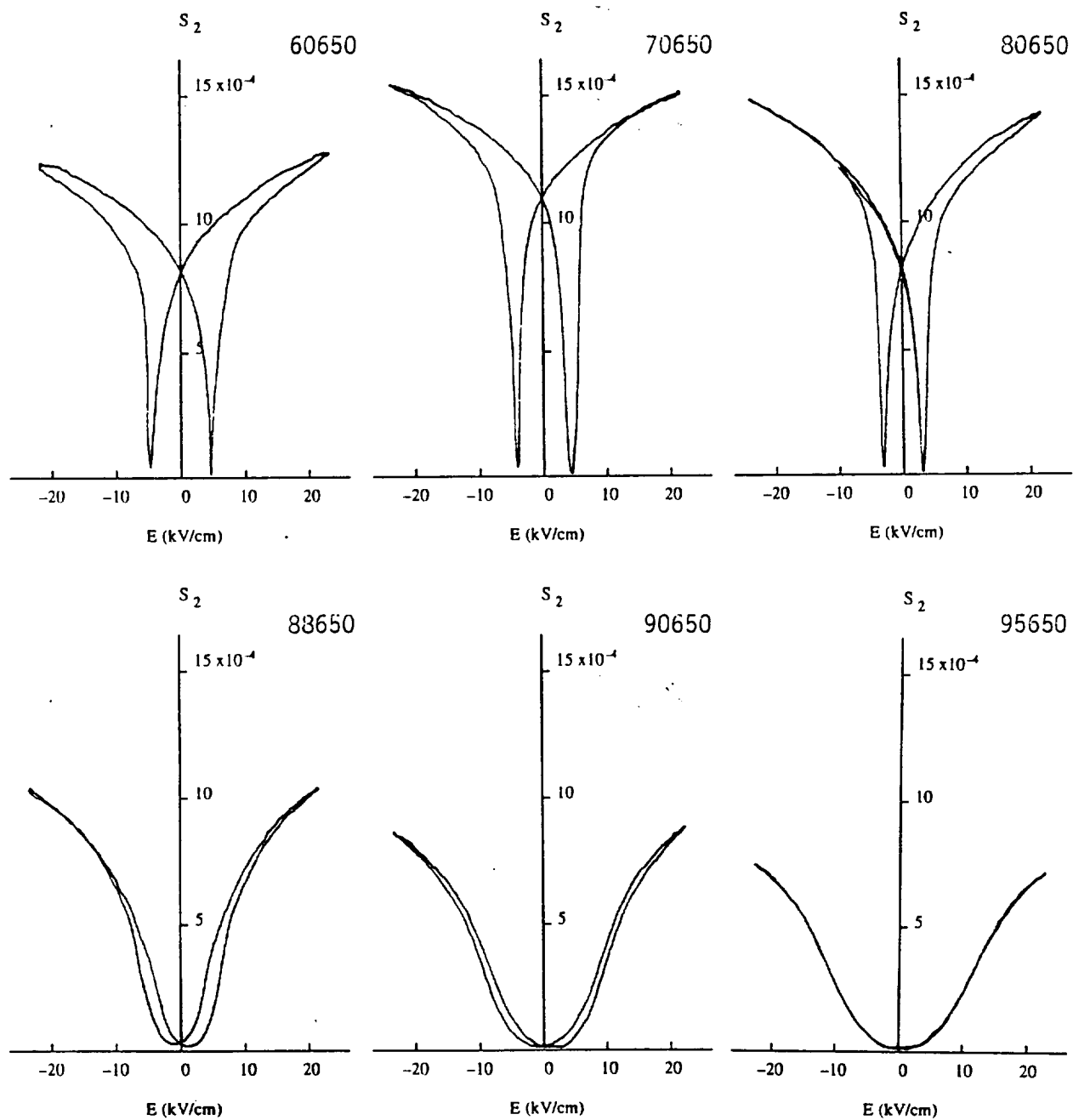


Figure 21. Variation of lateral strain with electric field for the PLZT ceramics with  $Zr/Ti=65/35$ .

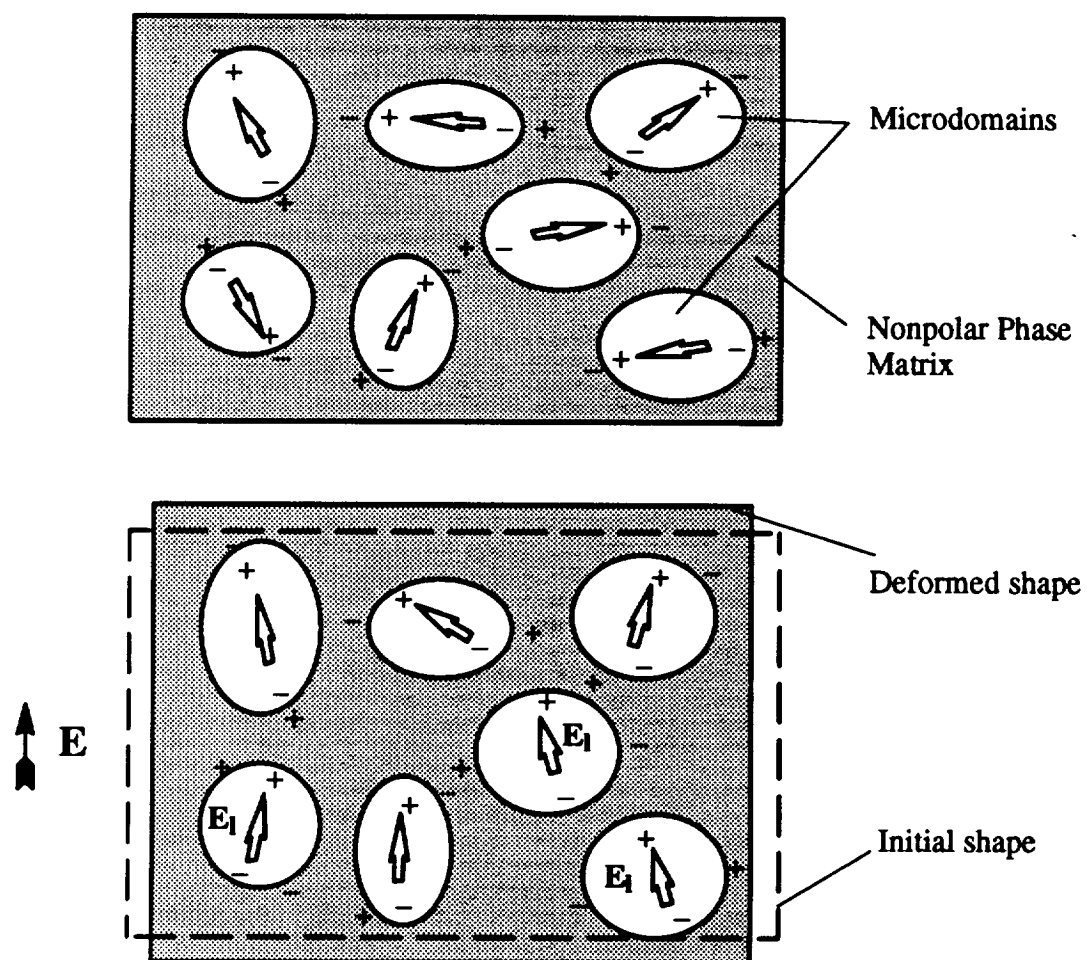


Figure 22. Microdomain rotation under external and local electric fields.

**SUPERCONDUCTIVITY DEVICES: COMMERCIAL USE OF SPACE**

**Annual Report**

**Development of PSZT and PMN-Based Ceramics for Electrostrictive Actuators**

to

National Aeronautics and Space Administration  
Langley Research Center  
Hampton, VA 23665-5225

Principal Investigator: Gene Haertling

Supporting Investigator: Guang Li

Contract No. NAG-1-1301

September 6, 1993

## 1. Introduction

The objective of our current investigation is the development of ferroelectric ceramic actuators, with emphasis placed on discovering and characterizing those materials with large electric field-induced strains or electrostrictive effects. Thus far, we have carefully investigated the relevant properties of a large number of compositions in the PLZT and the PBZT ceramic systems. Excellent field-induced strain and electrostrictive properties have been observed in these systems, especially PLZT [1]. In both systems there exist a relaxor phase region as well as a rhombohedral-tetragonal morphotropic phase boundary where the field-induced strain and related properties are optimized. As a result, a variety of compositions are available which can be utilized for actuators of various purposes.

Along with the PLZT and the PBZT ceramic systems, two other ceramic systems, namely the La-doped  $\text{Pb}(\text{Sn}, \text{Zr}, \text{Ti})\text{O}_3$  (hereafter PSZT) and the  $\text{Pb}(\text{Mg}_{1/3}\text{Nb}_{2/3})\text{O}_3$  ( hereafter PMN )-related ceramics, also display promise as actuator materials, and hence deserve a detailed investigation.

In the phase diagram of PSZT ceramics there is a boundary between the ferroelectric rhombohedral and antiferroelectric tetragonal phases [2]. Near this boundary, the antiferroelectric (AF) and ferroelectric (FE) phases possess similar free energies. Consequently, the antiferroelectric phase can be switched to the ferroelectric phase under high electric fields. Because of the significant difference in the volume of the unit cells of these two phases, large strains are expected from switching or phase transition.

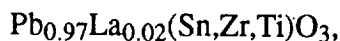
PMN-based ceramics are relaxor ferroelectrics and exhibit very high dielectric constants at room temperature. Large electrostrictive effects were reported in the solid solution of PMN (0.9) and  $\text{PbTiO}_3$  (0.1) relaxor ceramics [3]. In addition, it is very probable that large field-induced strains are produced in the compositions located on the morphotropic boundaries in the PMN- $\text{PbTiO}_3$ - $\text{PbZrO}_3$  ceramic system.

In this report, the preparation and processing of La-doped PSZT and PMN-related ( including PMN-PT and PMN- $\text{PbTiO}_3$ - $\text{PbZrO}_3$  ) ceramic samples are described. The

measurements of the electric field-induced ( electrostrictive ) strains and relevant properties for the samples are presented. The experimental results are discussed in comparison with other ferroelectric ceramics previously investigated.

## 2. Sample Preparation

The formula of the lanthanum-doped PSZT ceramics can be expressed by



in which 2 atom% La was used to substitute for Pb ions in the A-sites of  $\text{ABO}_3$  perovskite structure while the ratios of Sn/Zr/Ti were varied. The PSZT compositions chosen for study were situated in the vicinity of the  $A_T$ - $F_R$  ( antiferroelectric tetragonal-ferroelectric rhombohedral ) phase boundary, with most located within the  $A_T$  region, as illustrated by the solid dots on the phase diagram in Figure 1(a).

Conventional mixed-oxide processing techniques were employed to prepare the PSZT specimens. The starting raw materials were reagent grade  $\text{PbO}$ ,  $\text{SnO}_2$ ,  $\text{ZrO}_2$ ,  $\text{TiO}_2$  and  $\text{La}_2\text{O}_3$ . After weighing, all the components were ball mixed in distilled water for 30 minutes, then calcined at  $900^\circ\text{C}$  for four hours. The calcined powder was milled for 8 hours with polyethylene using a polyethylene jar and zirconia media. Green pellets were obtained by pressing the milled powder with distilled water into disks of 0.1 in. in thickness and 1 in. in diameter at a pressure of 7000 psi. The pellets were then sintered at  $1280$ – $1320^\circ\text{C}$  for 4 hours in a closed alumina crucible with a flowing oxygen atmosphere. To avoid the loss of  $\text{PbO}$  from samples during sintering, a  $\text{PbO}$ -rich atmosphere was maintained by placing an equimolar mixture of  $\text{PbO}$  and  $\text{ZrO}_2$  in the crucible. Sintered samples were then lapped to dimensions of  $426 \times 364 \times 30$  mil. The major surfaces of the lapped samples were electroded with electroless nickel plating for measurement of sample properties.

Six compositions of PMN-related ceramics were selected for study. As is indicated in the phase diagram of the PMN-PZ-PT solid solution shown in Figure 1(b), two of the six compositions lie along the edge connecting the end members PMN and PT, which are called PMN-PT1

and PMN–PT2 respectively. The essential formulas of the PMN–PT ceramics are identical to those given in an earlier report [4]. Two atom% excess of PbO and MgO were added to the original formulas in the current study. The other four compositions, called PMNZT, are located inside the phase diagram and represented by the ratio of the ions in the B–sites of the perovskite structure; for instance, PMNZT 65/10/25 means 65 atom% of ( $\text{Mg}_{1/3}\text{Nb}_{2/3}$ ), 10 atom% Zr and 25 atom% Ti in the B–sites. For all of the PMN–related samples, about 1–2 atom% Ba ions were used to replace Pb ions in the A–sites to stabilize the desired perovskite phase. In the preparation of the PMN–related samples, MgO and  $\text{Nb}_2\text{O}_5$  powders were first combined to synthesize the compound  $\text{MgNb}_2\text{O}_6$ . This step is believed to be of importance in minimizing the unwanted pyrochlore phase in the final product. Other preparation procedures were basically the same as those used for the above–mentioned PSZT samples except that the powders of PMN–related samples were calcined at 800 °C for 3 hours, and the calcined powders were milled in distilled water for 6 hours and sintered at 1180–1250 °C.

Some of the ceramics mentioned above were also fabricated by means of a hot–pressing technique for comparison. The conditions used for hot–pressing were 1200 °C at a pressure of 2000 psi for 4 hours.

### 3. Measurements

The dielectric properties of samples were measured at 1 kHz with an LCR meter ( LEADER, LCR–7450–01). The measurement of the relationship between polarization  $P$  and electric field  $E$  was carried out using conventional P–E hysteresis loop equipment. The submersion method in distilled water was employed to evaluate sample density.

An experimental device for the detection of electric field induced strains was made, in which an LVDT ( linear variable differential transformer, 050 DC–E Lucas Schaeritz Co. ) was used as the displacement sensor. Details of the device can be found in the reference [1]. An electric field varying continuously between negative and positive maxima was applied to the samples. The magnitudes of the maximum electric fields depended on the type of samples to be

measured. The measured results were recorded on a X–Y plotter.

The PMN–related ceramics were checked for the perovskite phases prior to sintering by an X–ray diffractometer ( Scintag XDS 2000<sup>™</sup> ) with a filtered Cu radiation.

#### 4. Experimental Results

##### (1) La–doped PSZT ceramics

The dielectric, ferroelectric and field–induced strain properties of the PSZT samples obtained in this study are illustrated in Table 1. The polarization hysteresis loops for the compositions having a constant Ti content of 10 atom% are shown in Figure 2. Typical double hysteresis loops of antiferroelectrics were found for all of these samples. The values of anti–ferroelectric–ferroelectric (AF–FE ) phase transition field  $E_{AF}$  and the reverse transition field  $E_{FA}$  for these samples were evaluated and are shown in Table 1. A minimum of  $E_{AF}$  or  $E_{FA}$  was observed near the composition 64/26/10 ( Zr/Sn/Ti ), suggesting that the  $A_T$ – $F_R$  phase boundary shown in Figure 1(a) should be convex toward the  $A_T$  phase at that composition. Initial curves, i.e. those corresponding to initial field increase applied on a virgin sample as shown in Figure 2, display a higher value of  $E_{AF}$  than those resulting from the subsequent cycles of electric field variation. This difference implies that the antiferroelectric phase is more easily switched during the subsequent variation of electric fields or the randomly–oriented initial state has lower energy. As the composition moves away from the  $A_T$ – $F_R$  phase boundary within the  $A_T$  phase, the transition field strength increases whereas the maximum induced polarization decreases, as evidenced by comparing the hysteresis loops shown in Figures 2 and 3. On the other hand, the samples on or in the immediate vicinity of the boundary exhibit completely different features in polarization hysteresis loops. As demonstrated in Figure 4 for two of these compositions, during the initial electric field increase, the samples were switched from an antiferroelectric phase to ferroelectric phase but remained in the FE phase for the subsequent change of electric fields, that is to say, the samples underwent an irreversible field–forced phase transition ( note that the original state can be recovered by thermal depoling ).

The hysteresis loop of the sample 62/28/10 fabricated by hot-pressing techniques is also shown in Figure 3. The general features of the loop are very similar to those of the same composition prepared by mixed-oxide processing. However, the hot-pressed sample exhibits much steeper and more complete phase switching during the variation of electric fields between negative and positive maxima. In addition, the hot-pressed sample possesses higher saturation polarization than the mixed-oxide processed sample, probably because the former has higher density and homogeneity.

Figure 5 shows the variation of transverse strains with electric field for the samples with constant Ti content. The curves of first switching cycle and those after several cycles are displayed in the figure. Digital-like loops of strain vs. electric field were observed. These loops were found to be closely associated with the electric field-polarization relations as shown in Figure 2, i.e. large strain changes occurred at the fields of switching between AF and FE phases. It was discovered that the strains from the initial switching of AF to FE phase are considerably smaller than the subsequent switching cycles for all of these samples, though the induced polarizations between them are very close. This phenomenon is ascribed to the random distribution of initial antiferroelectric phase. For other samples that are located within the antiferroelectric tetragonal phase  $A_T$ , a similar strain variation with electric field was obtained, which is depicted in Figure 6. For samples on the  $A_T$ - $F_R$  phase boundary as shown in Figure 4, an abrupt increase in strain occurred at the initial phase switching, followed by a loop typical of ferroelectric phase, i.e. a butterfly-like curve. It is noted that, in contrast to those resulting from the domain switching of ferroelectric phases, the transverse strains generated by the phase transitions in the PSZT samples are positive since the antiferroelectric phase has smaller unit cell lengths for all dimensions. Figure 6 also shows the strain loop of hot-pressed sample. Similar to the corresponding polarization loop, it was found that change of strain from the phase switching is more abrupt in the hot-pressed sample; but the saturation strain appears to be smaller than that of the sintered sample. Such smaller strain in hot-pressed samples is probably due to a different microstructure.



The longitudinal strains were also investigated and their variation with fields are essentially the same in shape as the transverse except that the amplitude of the longitudinal strains is much greater. Two such curves are shown in Figure 7. Table 1 lists the values of both transverse and longitudinal saturation strains for every composition studied. It can be seen that the saturation longitudinal strains are about 3–4 times as large as the transverse.

Table 1 also illustrates the properties of two PSZT samples sintered at 1280 °C. It can be seen that these samples have very close overall properties to those sintered at 1320 °C, implying that the sintering temperature is broad for the PSZT ceramics.

#### (b) PMN-related ceramics

The PMN–PT ceramics studied were briefly mentioned in one of our previous reports [4]. The difference of the current study from the previous one lie in that the basic compositions were modified in the current study by excess PbO and MgO to improve synthesis of the perovskite phase. The data of the PMN–PT1 and PMN–PT2 ceramics obtained in this study, as is shown in Table 2, indeed display a significant improvement in the properties compared to the previous results. Both of the PMN–PT ceramics studied exhibited characteristics of relaxor ferroelectrics, thus having a slim polarization hysteresis loop. Accordingly, little hysteresis is seen on the change of strain with electric field for these samples, as is illustrated in Figure 8. This is the most significant advantage of PMN–PT ceramics over other ferroelectrics. It is interestingly noticed that the PMN–PT2 sample has a much higher dielectric constant but a smaller strain than does the PMN–PT1 sample. This result indicates that the large strains produced in PMN–PT ceramics are caused by both high dielectric constant and electrostrictive coefficients as other papers have suggested [5].

The experimental results of the PMNZT ceramics are presented in Table 2 and Figures 9–10. The first two of the PMNZT compositions, i.e. 30/30/40 and 25/25/40, listed in Table 2 are located on the rhombohedral–tetragonal morphotropic phase boundary. The X-ray diffraction pattern of the sample 30/30/40, as is seen in Figure 11(a), shows that this sample is more on the side of tetragonal phase. It was found that the values of the dielectric constant, remanent

polarization and field-induced strains of these two samples approach those of PLZT 5.5/59/41 ceramics ( also shown in Table 2 for comparison ). A transverse strain of 0.125% was observed for both of these ceramics. The other two PMNZT samples, namely the 65/10/25 and 50/10/40, lie near the tetragonal–psudocubic phase boundary and close to PMN–PT ceramics as shown in Figure 3. Figure 11(b), the X-ray diffraction pattern, indicates that the sample 65/10/25 contains a fraction of pyrochlore phase. Because of very small strains and large hysteresis, these compositions are unfavorable as actuator materials, which is clearly evidenced by the strain data shown in Table 2 and Figure 10.

#### 4. Discussion

Pan et al. investigated the field-induced strains from the phase transition of PSZT ceramics on the  $A_T$  and  $F_R$  boundary a few years ago [6]. Their results show that a number of the PSZT compositions possess a longitudinal strain of over 0.5% resulting from the AF–FE phase transition. The value of the strain as high as 0.87% was claimed on sample #6 ( corresponding to the sample 66/23/11 with our notation ) in their study, which is the highest field-induced strains ever reported on ferroelectric and related materials. In our investigation we also included the sample 66/23/11. We obtained, however, completely different results on this sample from those reported by Pan et al.. As is shown in Table 2 and Figure 6, the sample 66/23/11 in our case exhibits a stable ferroelectric phase after application of an initial switching field. The longitudinal strain of this sample, even including the portion caused by the initial phase switching, is only about 0.45%. The greatest strain found in our study is on the sample 62/28/10, which is about 0.46%.

A typical longitudinal field-induced strain of about 0.40% was found on the PLZT 5.5/59/41 in our previous investigations, but at a much lower applied field ( 10 kV/cm ) than that for the PSZT ceramics ( fields of 30–50 kV/cm are normally required for a forced AF–FE phase transition ). Under a high applied field, say 35 kV/cm, PLZT ceramics display strains of the same order or greater than PSZT ceramics. Nevertheless, the PSZT ceramics still belong to one of ceramic materials exhibiting the highest field-induced strains; furthermore, the digital-like

strain patterns make them attractive for special-use actuators.

For most ferroelectric materials the field-induced strains are polarization-controlled in nature, that is, the strains are strongly related to induced polarization. This relationship has been justified by the fact that the ceramics of high field-induced strains are commonly found in the neighborhood of phase boundaries, a typical example of which is PLZT ceramics. Since the PMNZT ceramics involve the solid solution of a multi-component system, the mechanisms contributing to the polarization are in principle multifold, and thus high strains as well as good piezoelectric properties are anticipated. Optimal piezoelectric properties have been found for the compositions in the vicinity of the morphotropic phase boundary of the PMNZT system [7]. In our study of these ceramics, however, although large field-induced strains were found for the compositions on the morphotropic boundary, the magnitudes are apparently lower than the best found in PLZT ceramics. This is beyond our primary expectation. One of the reasons could be that we have not yet identified the compositions with maximum strain. Another reason is the difficulty of preparing sufficiently homogeneous samples out of multi-component systems. More investigations are needed before drawing definite conclusions on these ceramics.

## 5. Summary and Conclusion

The field-induced strains and related properties of a number of La-doped PSZT ceramics located in the vicinity of the  $A_T$  and  $F_R$  phase boundary were investigated. Large strains (0.28–0.46%), resulting from the field-forced transition between antiferroelectric and ferroelectric phases, were observed for most of the compositions studied. A longitudinal strain as large as 0.46% was obtained and found to be on the same order as that found in PLZT 5.5/59/41. This value, however, appears to be much lower than those reported on the same system by Pan et al.. The reason is not yet understood. Some compositions that are very close to the phase boundary experienced an irreversible switching from  $A_T$  to  $F_R$  phase upon application of electric fields. The strains from such switching are moderate.

Several PMN-related ferroelectric ceramics were studied for their potential use for

actuators. Use of excess PbO and MgO in fabricating PMN-PT solid solution ceramics was found to significantly improve the electrical properties of these ceramics. However, the magnitude of field-induced strains is still low compared to those of the PLZT, PBZT and PSZT ceramics. The advantage of PMN-PT ceramics lies in the fact that the field-induced strains of these ceramics are electrostrictive in nature and thus possess very good reproducibility relative to other conventional ferroelectrics. As for the PMNZT ceramics studied, the compositions located near the morphotropic boundary possess overall properties resembling PLZT 5.5/59/41. The other compositions were found to be undesirable as far as their use for actuators is concerned. The best composition of PMNZT system has not yet been identified.

## 6. References

- [1] G. Haertling and G. Li, *Commercial Use of Space*, Part 2, a semiannual report in the department of Ceramic Engineering, Clemson University, March 31 (1993).
- [2] D. Berlincourt, *IEEE Trans. Sonics Ultrason.* SU-13, p 116 (1966).
- [3] L. E. Cross, S. J. Jang and R. E. Newnham, *Ferroelectrics*, Vol.23, p 187 (1980).
- [4] G. Haertling and G. Li, *Commercial Use of Space*, Part 2, an annual report in the department of Ceramic Engineering, Clemson University, August 28 (1992).
- [5] V. Sundar and R. E. Newnham, *Ferroelectrics*, Vol.135, p 431 (1992).
- [6] W. Pan, Q. Zhang, A. Bhalla and L. C. Cross, *J. Am. Ceram. Soc.*, vol. 72 [4], p 571 (1989).
- [7] H. Ouchi, K. Nagano and S. Hayakawa, *J. Am. Ceram. Soc.*, vol. 48 [12], p 630 (1965).

Table 1. Properties of PSZT ferroelectric ceramics.

	Dielectric Constant	$\text{tg } \delta$ (%)	$\rho$ (g/cm <sup>3</sup> )	$E_{AF}$ (kV/cm)	$E_{FA}$	$P_s$ ( $\mu\text{C}/\text{cm}^2$ )	$S_{2,S}$ $\times 10^4$	$S_{1,S}$ $\times 10^4$
--	------------------------	----------------------------	--------------------------------	---------------------	----------	--	----------------------------	----------------------------

Sintering temperature 1320 °C

60/30/10 Zr/Sn/Ti	830 994*	1.6 2.7*		43	21	30	6.1	32.1
62/28/10 Zr/Sn/Ti	940 882*	1.9 3.5*		30	9.5	32	8.5	45.7
64/26/10 Zr/Sn/Ti	997 913*	1.9 4.3*	7.86	28	1.0	31	7.9	28.0
66/24/10 Zr/Sn/Ti	1043 990*	1.2 6.0*	7.71	30	9.0	31	8.2	45.3
68/22/10 Zr/Sn/Ti	957 940*	1.2 7.1*		35	2.0	34	7.7	38.2

61.5/28/10.5 Zr/Sn/Ti	973 815*	1.2 1.6*		30	4.3	30	7.5	31.1
62.5/28/9.5 Zr/Sn/Ti	738 652*	1.8 1.5*		49	27	30	2.5	
67/24/09 Zr/Sn/Ti	742 677*	1.4 4.9*	7.69	41	22	28	7.1	
64.5/26/9.5 Zr/Sn/Ti	772 633*	1.8 1.5*		44	22	29	4.7	19.1

66/23/11 <sub>HP</sub> Zr/Sn/Ti	1120	2.3		Ferro <sup>^</sup>		38	5.5	45.2*
62/28/10 <sub>HP</sub> Zr/Sn/Ti	807 1056*	1.0 1.8*		36	16	35	6.6	36.5
64/25/11 Zr/Sn/Ti	510 950*	3.3 2.3*		Ferro <sup>^</sup>		34	5.0	
63.5/26/10.5 Zr/Sn/Ti	687 570*	1.3 3.2*		Ferro <sup>^</sup>		32		12.1

Sintering temperature 1280 °C

64/26/10 Zr/Sn/Ti	1014 885*	2.4 3.2*	7.76	31	2.0	31	8.3	
66/24/10 Zr/Sn/Ti		1.2 12.2*		31	9.0	31	8.7	

Note:  $\text{tg } \delta$  is the loss factor,  $\rho$  the density,  $E_{AF}$  the switching field from antiferroelectric to ferroelectric phase and  $E_{FA}$  the reverse switching field,  $P_s$  the saturation polarization,  $S_{2,S}$  and  $S_{1,S}$  are, respectively, the transverse and longitudinal saturation strains. \* indicates the dielectric constant measured before poling. HP=hot pressing. ^ have a stable ferroelectric phase. \* includes strain from initial switching.

Table 2. Properties of sintered PMN-PT, PMNZT and PLZT ferroelectric ceramics.

	Dielectric Constant	tg $\delta$ (%)	$\rho$ (g/cm <sup>3</sup> )	$E_c$ (kV/cm)	$P_R$ ( $\mu$ C/cm <sup>2</sup> )	$P_{10}$	$\Delta S_{2,10}$ $\times 10^4$	$S_{2,10}$ $\times 10^4$	$\Delta S_{1,10}$ $\times 10^4$	$S_{1,10}$ $\times 10^4$
--	------------------------	--------------------	--------------------------------	------------------	--------------------------------------	----------	------------------------------------	-----------------------------	------------------------------------	-----------------------------

PMN-PT

PMN:PT1	17530	5.1	7.86	0	0	20	-2.3	-2.3		
PMN:PT2	20020	5.4	8.01	0	0	18	-2.0	-2.0		

PMNZT

30/30/40 (MN)/Z/T	2020 2550*	3.6 2.3*	7.66	7.5	32	35	-4.5	-12.5		28.7
25/35/40 (MN)/Z/T	1450 1440*	2.8 2.8*		6.5	35	37	-3.6	-12.5		27.8
65/10/25 (MN)/Z/T	2850 2380*	5.2 4.3*		3.5	20	24	-2.3	-3.8		
50/10/40 (MN)/Z/T	2080 2070*	6.2 2.1*		10.5	21	27	-2.8	-4.5		

PLZT

55590	1590	2.7	7.56	7.0	33	36	-3.7	-13.7		40.3
-------	------	-----	------	-----	----	----	------	-------	--	------

Note: tg  $\delta$  is the loss factor,  $\rho$  the density,  $E_c$  the coercive field,  $P_R$  the remanent polarization,  $P_{10}$  the polarization at an electric field of 10 kV/cm,  $\Delta S_{2,10}$  ( lateral ) and  $\Delta S_{1,10}$  ( longitudinal ), the differential strains, are defined as the difference between the strains at an electric field of 10 kV/cm and 0 kV/cm,  $S_{2,10}$  and  $S_{1,10}$  are, respectively, the total lateral and longitudinal strains at an electric field of 10 kV/cm. \* indicates the dielectric constant measured before poling.

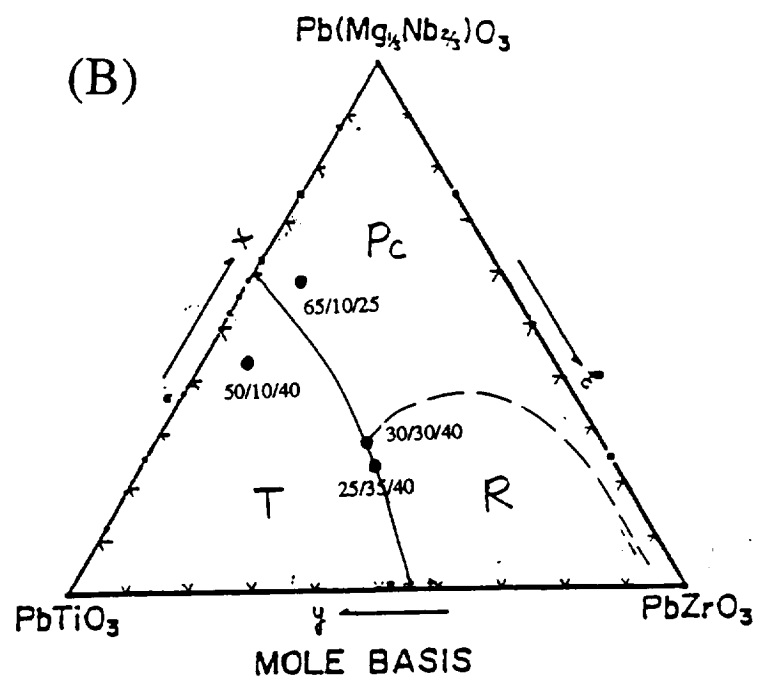
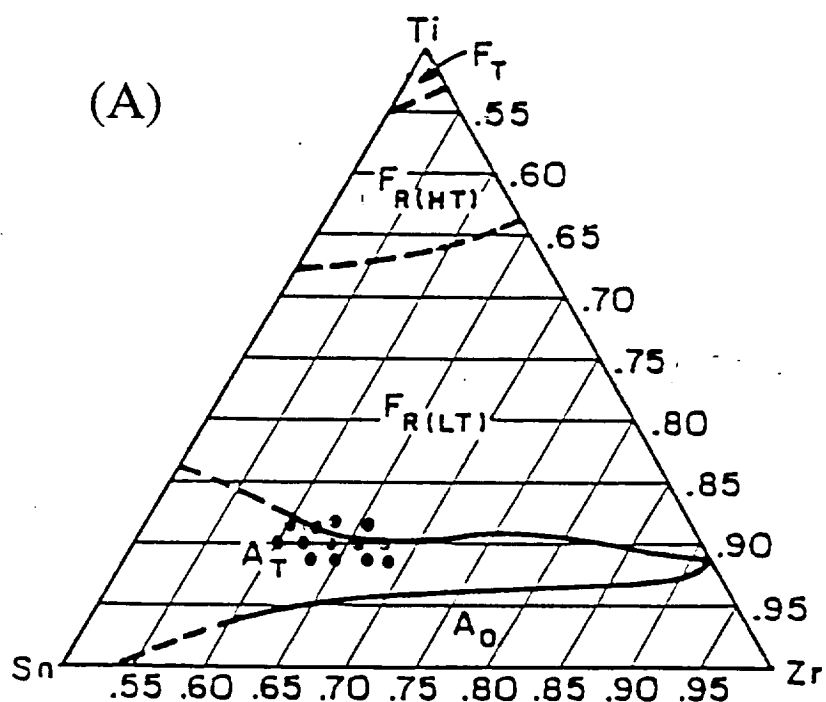


Figure 1. (a) Ternary phase diagram for the system  $\text{Pb}_{0.97}\text{La}_{0.02}(\text{Zr},\text{Sn},\text{Ti})\text{O}_3$  at room temperature, where  $A_T$  denotes antiferroelectric tetragonal phase and  $F_R$  ferroelectric rhombohedral phase [6]. (b) Room temperature phase diagram of  $\text{Pb}(\text{Mg}_{1/3}\text{Nb}_{2/3})\text{O}_3$ - $\text{PbZrO}_3$ - $\text{PbTiO}_3$ , where T=ferroelectric tetragonal, R=ferroelectric rhombohedral and Pc=ferroelectric pseudocubic [7]

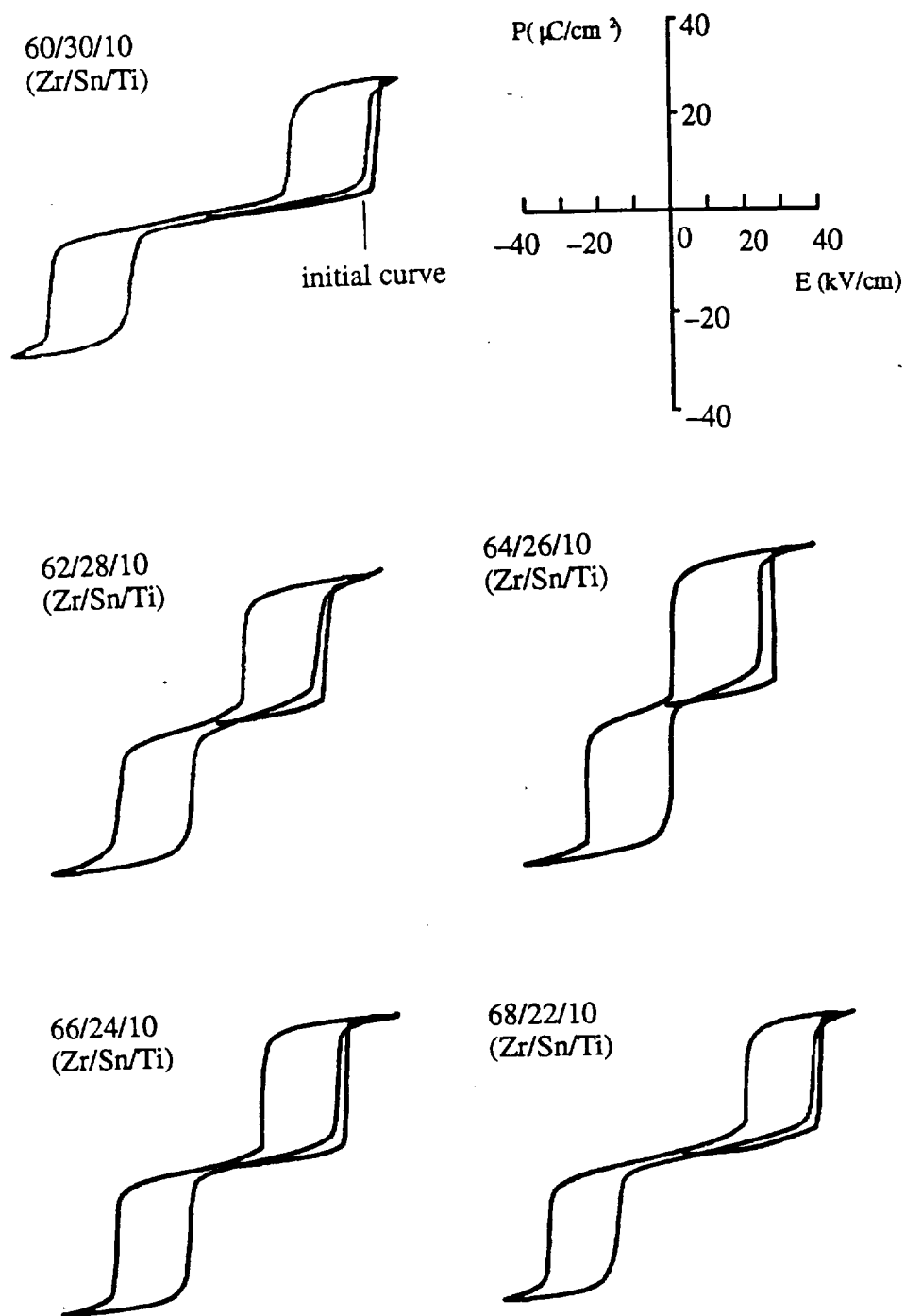


Figure 2. Polarization-electric field relations of the PSZT ceramics having constant Ti=10 atom%.



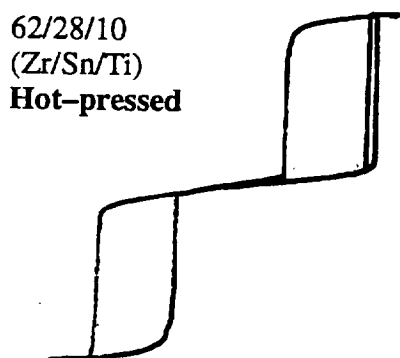
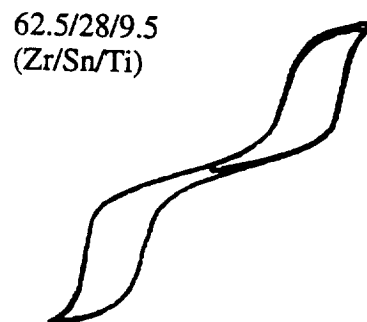
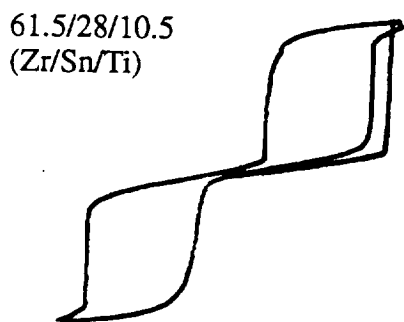
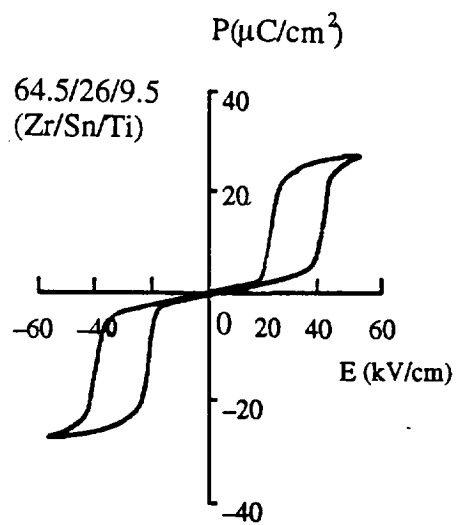
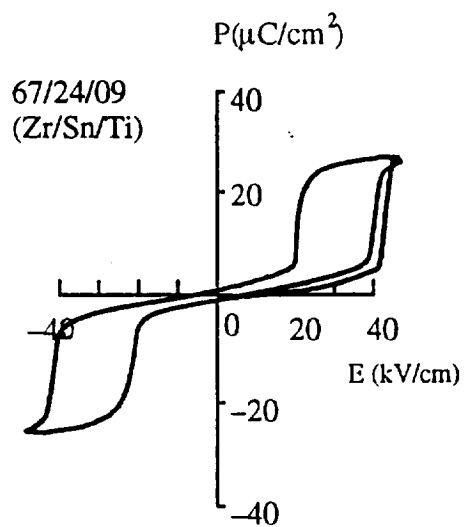


Figure 3. Relationship between polarization and electric field for PSZT ceramics. ( the graphics on column have an identical scale )

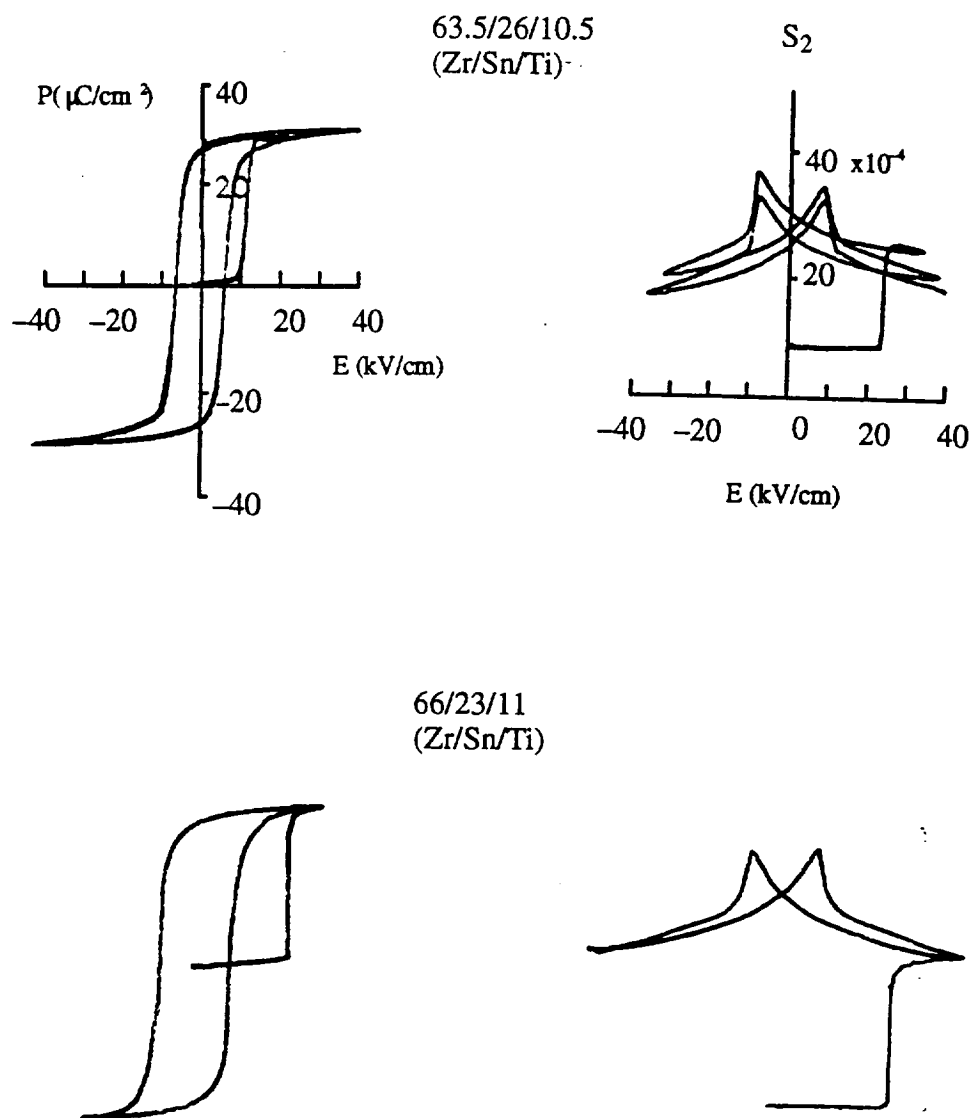


Figure 4. Changes of polarization and transverse strain with electric field for the PSZT ceramics displaying an irreversible  $A_T$  to  $F_R$  phase transition. ( the graphics on column have an identical scale )

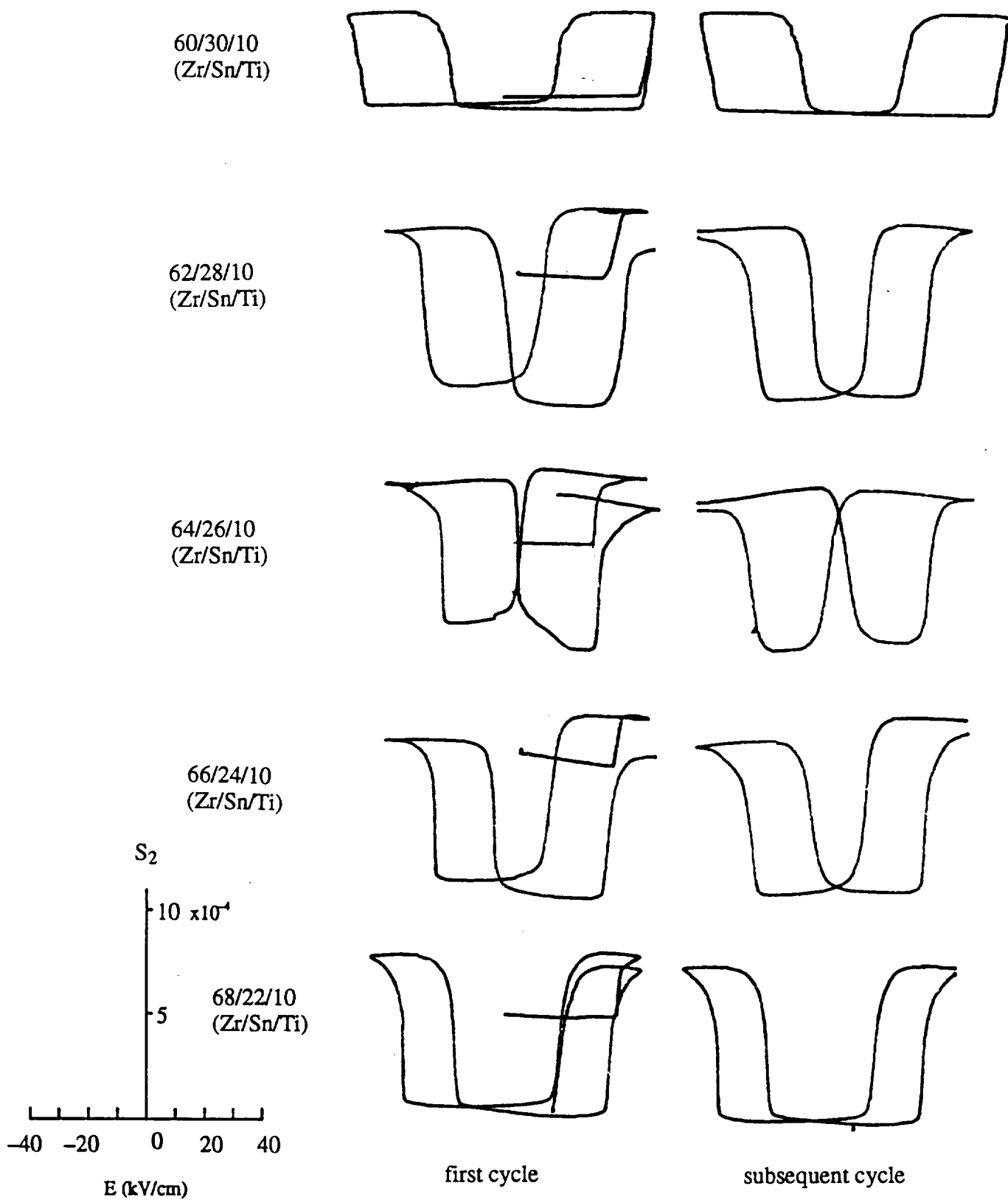


Figure 5. Variation of transverse strain with electric field for the PSZT sample with constant Ti content.

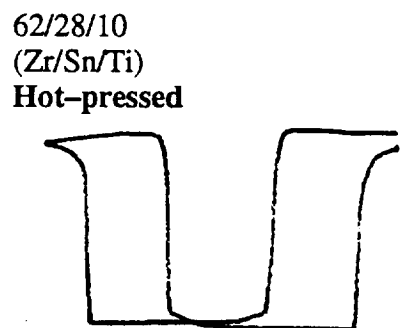
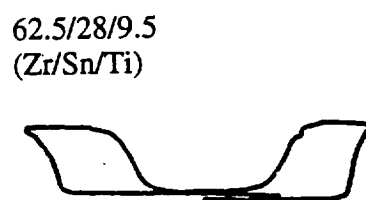
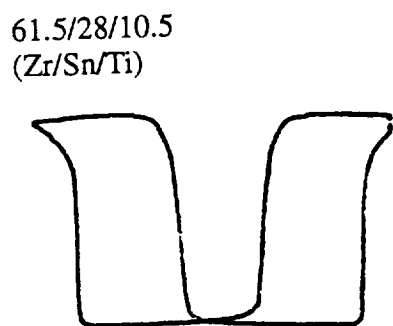
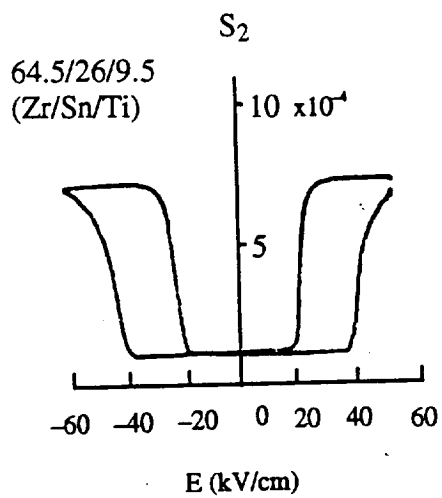
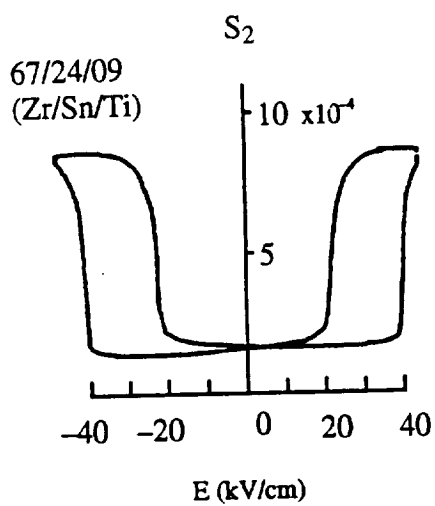


Figure 6. Relations of transverse strain vs. electric field for for PSZT ceramics.

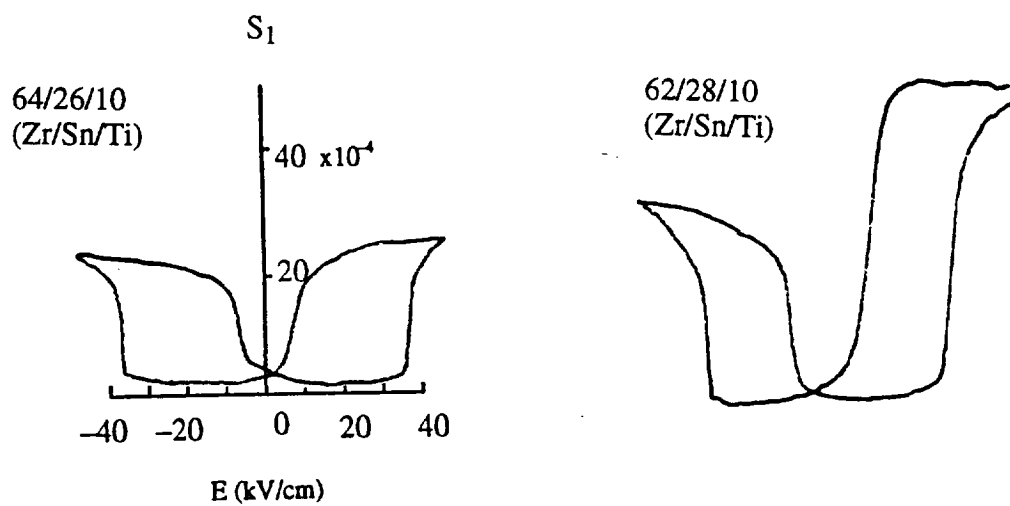


Figure 7. Examples of longitudinal strain vs. electric field of PSZT ceramics.

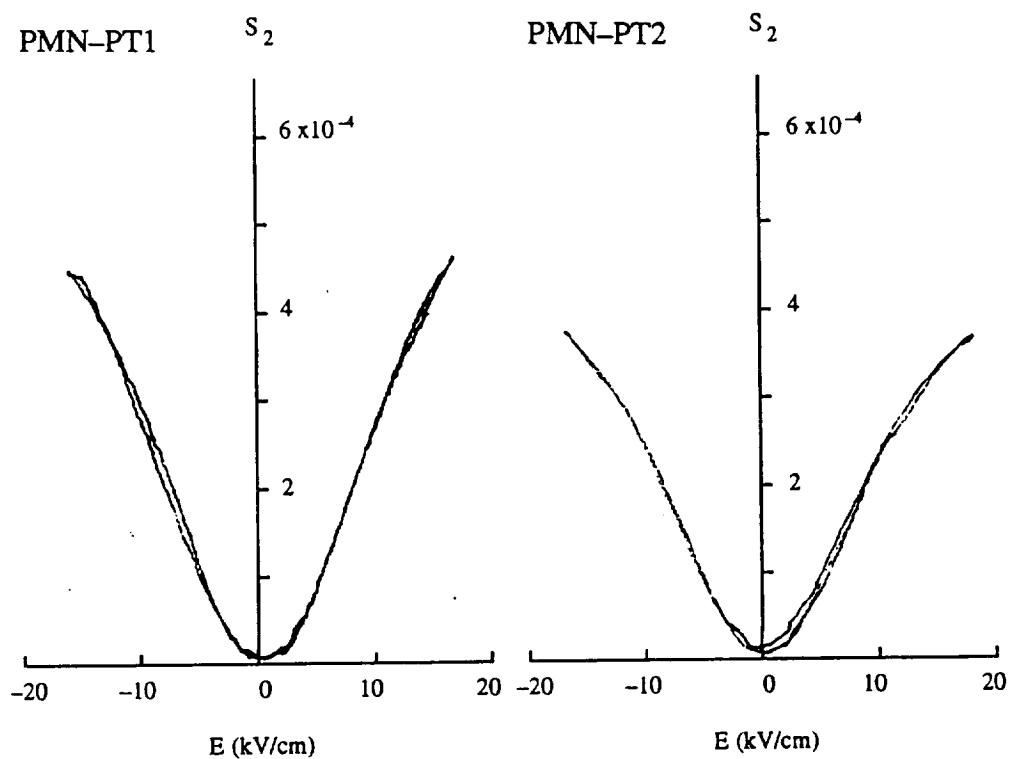


Figure 8. Variation of transverse strain with field strength for PMN-PT ceramics.

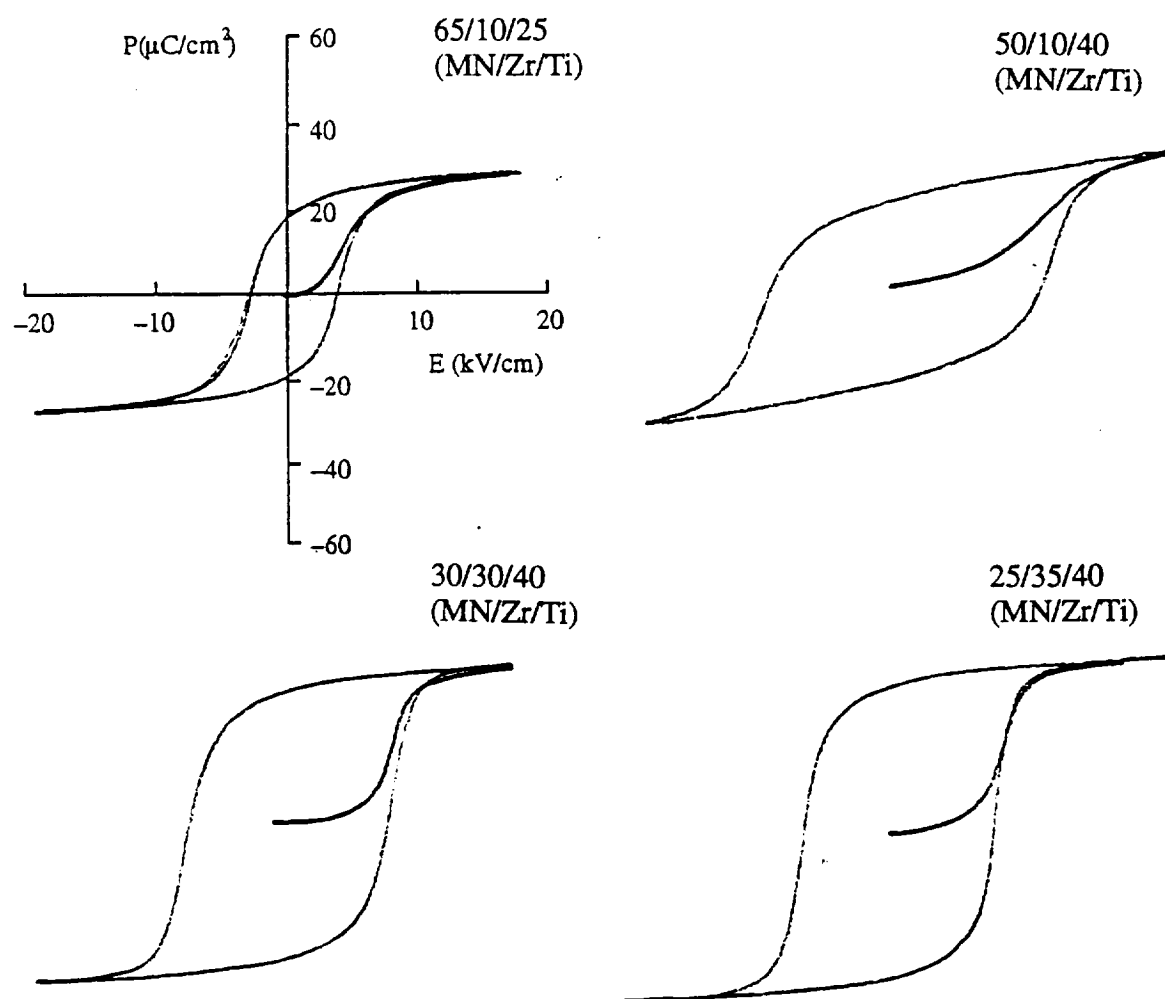


Figure 9. Relationship between polarization and electric field of PMNZT ceramics.

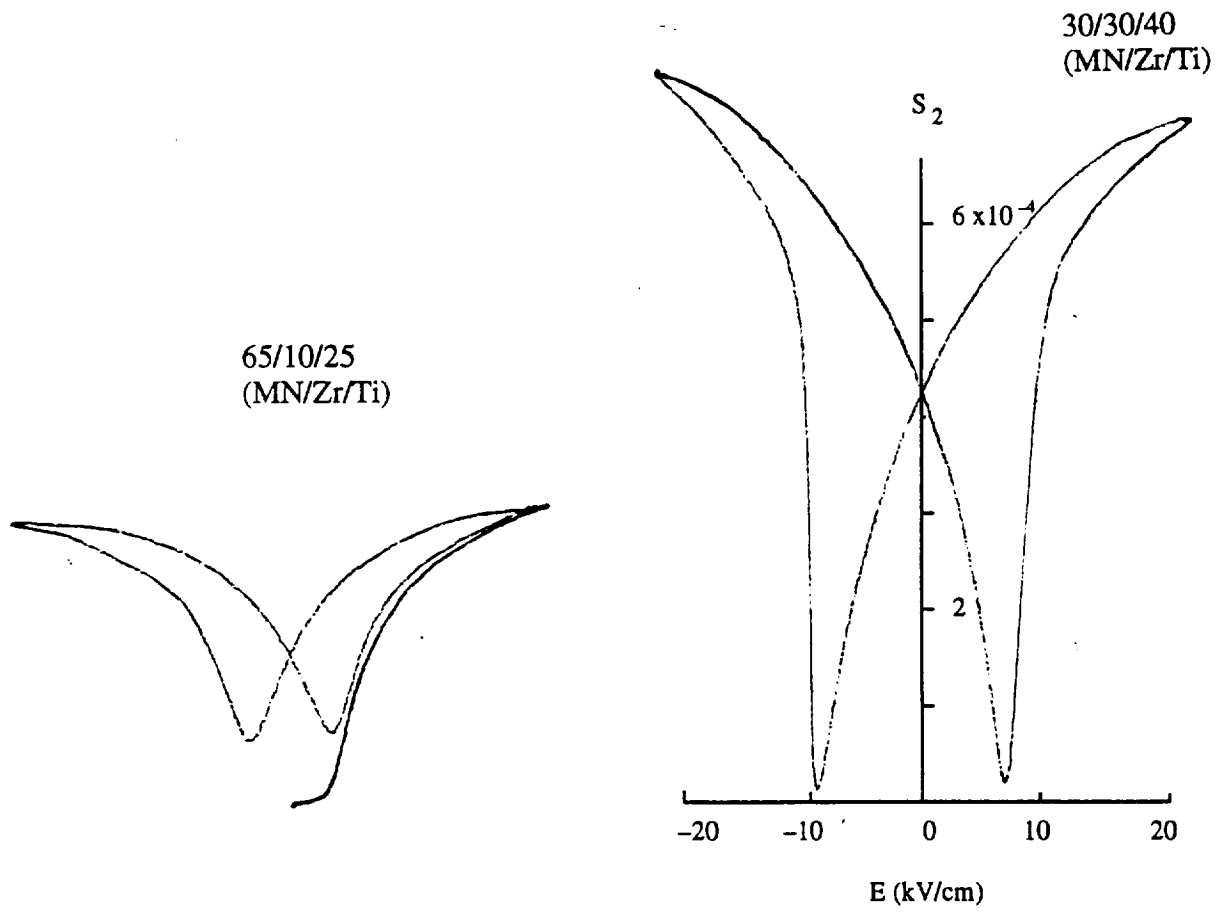
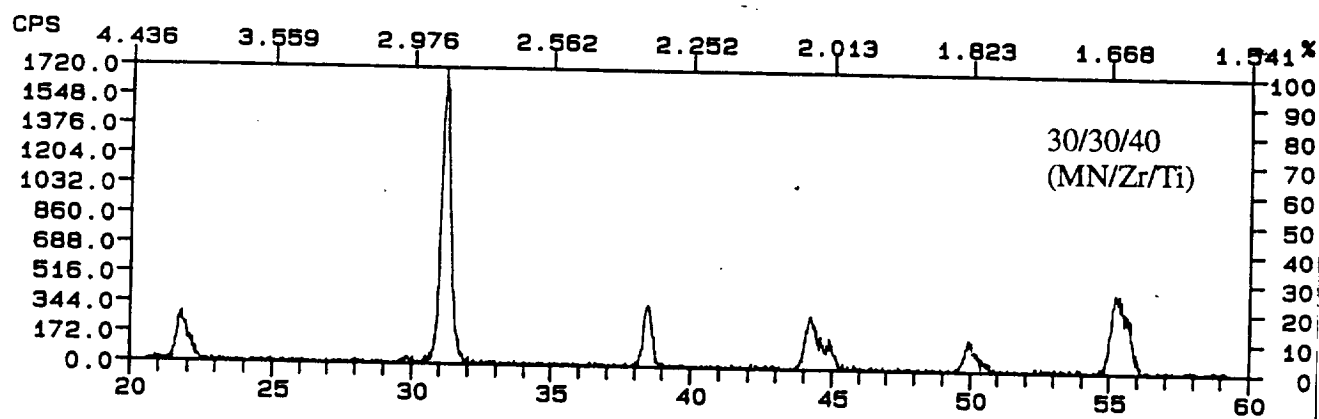


Figure 10. Variation of transverse strain with electric field for PMNZT ceramics.

(A)



(B)

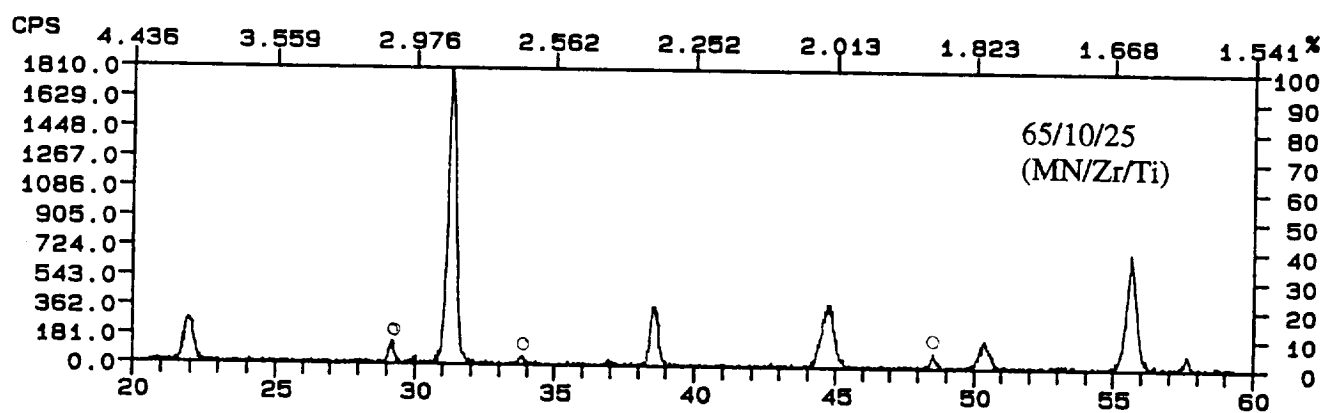


Figure 11. X-ray diffraction patterns of PMNZT ceramics.

( ○ corresponds to pyrochlore phase )



**Part III.**

**Characterization and Modeling of Rainbow Materials**

**SUPERCONDUCTIVITY DEVICES: COMMERCIAL USE OF SPACE**

**Annual Report**

**Characterization and Modeling of Rainbow Materials**

to

National Aeronautics and Space Administration  
Langley Research Center  
Hampton, VA 23665-5225

Principal Investigator:  
Gene Haertling

Co-Investigator: Eugene Furman

Contract No. NAG-1-1301

September 6, 1993

## **Characterization of the RAINBOW Devices**

### **I. Introduction**

This report summarizes the progress in characterization of RAINBOW (Reduced And Internally Biased Oxide Wafer) devices for the past year. Relevant information from the Semiannual Report is reproduced here<sup>1</sup>, but the emphasis of the report is on the work performed in the last six months.

There is considerable interest at the present time in the development of materials and devices capable of producing displacements above those achieved with monolithic ferroelectric transducers. Some of the applications where such materials can be used are micro pumps, portable speakers, ultrasonic cleaners, laser deflectors, intruder alarms, hydrophones, and micropositioners. Should a device have significant non linearity in a response, additional applications may include adaptive structures with tunable properties.

RAINBOW technology represents a novel approach for producing devices capable of large displacement. There is a trade-off between the load carrying capability of the RAINBOW and the displacement range of the devices. A RAINBOW device is obtained as a result of partial reduction of sintered ceramic which was initially fired in an oxidizing atmosphere, resulting in a composite consisting of oxidized/reduced layers with a 2-2 connectivity<sup>2</sup>. Because of the decrease in volume during the reduction and the higher coefficient of thermal expansion, the reduced layer would be in tension and the original oxide layer in compression at room temperature if a sample is not permitted to develop the curvature. To reduce interfacial stress, samples develop curvature, which also alters stress distribution elsewhere.

In its mode of operation, a RAINBOW device is similar to the piezoelectric monomorph, which consists of a metal layer bonded to the piezoelectric ceramic<sup>3</sup>. In comparison to the monomorph, in which the layers are bonded near room temperature, RAINBOW devices are characterized by a significantly higher level of internal stress.

In principle, any piezoelectric, ferroelectric, or antiferroelectric material with high electrical conductivity in a reduced state and low conductivity in the oxidized state can be considered for a RAINBOW device. In practice, materials with large electromechanical coupling coefficients are the best candidates for the transducer applications.

Traditionally, piezoelectric materials have been used as electromechanical sensors and actuators. More recently, electrostrictive materials based on PMN, PLZT, and other compositions have been found to have superior properties for a number of applications. Electrostrictive materials are preferred in applications where low hysteresis and high electric field are needed; piezoelectric materials are superior in applications requiring linearity of the response. RAINBOW devices can be based on either electrostrictive or piezoelectric response, and can address a number of applications mentioned earlier.

## **II. RAINBOW Characterization**

Lead lanthanum zirconate titanate (PLZT) materials were found to be reducible in a carbon-rich atmosphere<sup>4,5</sup>. As a result of a partial reduction of the PLZT samples, the structures shown in Figure 1 were obtained. The reduced PLZT layer is highly conducting and was used as the electrode. Air-dried silver paint was applied to the reduced and oxidized layers. Measurements of the dielectric loss ( $\tan \delta$ ) indicate that the oxide layer of the RAINBOW device retained its insulating properties, since the observed losses are comparable to those seen in the bulk PLZT ceramics.

Scanning electron microscopy was used to characterize interfaces between the reduced layer and oxide layer. The results are shown in Figure 2. The reduced layer extends approximately 100 microns into these samples. The interfaces have good mechanical integrity — no cracks were observed in the vicinity of the interfaces. The width of the reduced layer can be controlled by the duration and the temperature of the reduction cycle.

The experimental setup for studying strain as a function of the applied electrical field was constructed and tested. Figure 3 shows the schematic diagram of the equipment. The waveform generator capable of producing sinusoidal, square, and triangular waveforms is connected to the amplifier. The amplifier is rated at  $\pm 500$  V, 2000 Hz, and 80 mA. In addition, it permits application of DC voltage to be added to the amplified signal. A probe positioned on the top electrode serves a dual purpose: it connects the top electrode to the

amplifier and functions as a magnetic core for the linear variable differential transformer (LVDT). The LVDT produces a voltage which is proportional to the displacement of the sample. A signal conditioner attached to the LVDT converts the AC signal to DC, and this signal is then stored in the storage oscilloscope. Voltage applied to the sample is also stored in the oscilloscope, and the data is presented in both time domain and X-Y domain. This setup is used to study the large-signal, low-frequency displacement characteristics of the RAINBOW devices.

Samples characterized by electrostrictive or piezoelectric responses were investigated. Piezoelectricity is observed in PLZT samples with the maximum in the dielectric constant at high temperatures. For the materials with the maximum in the dielectric constant near room temperature, electrostrictive response is observed. Since the addition of lanthanum to PZT reduces the transition temperature, compositions with higher lanthanum content are more likely to exhibit electrostrictive response at room temperature.

An example of the RAINBOW device with the electrostrictive response at low frequency (1.22 Hz) is shown in Figure 4 for PLZT 9.5/65/35. This figure contains two parts. In the upper portion of the plot, time dependence of the applied voltage and the induced displacement are shown. In the lower portion of the plot, the displacement is shown on the vertical axis as a function of the applied voltage. Inspection of the top portion of the figure indicates that the frequency of the displacement is double that of the applied voltage. This is consistent with the electrostrictive response, in which the strain is proportional to the square of the electric field. The maximum span of the displacement is 21.9 microns, corresponding to the maximum voltage span of 254 V. The figure shows that the displacement of the sample is primarily downward. This is in agreement with the previously determined negative value of  $Q_{12}$  for PLZT ceramics. A negative  $Q_{12}$  implies a contraction of the oxide layer which is parallel to the interface with the reduced layer when voltage is applied. This contraction reduces the compressive stress in PLZT at the interface, permitting a new equilibrium state for the RAINBOW device with a lower curvature. A reduction in the curvature of the RAINBOW device is accompanied by the downward motion of the sample.

The asymmetry of the strain for the two polarities should be noted. Asymmetry may be rooted in the nature of the reduced layer. This layer acts as an electrode. Little is known at this time about the conductivity of the reduced layer near its interface with the oxide layer. Conduction through the ceramic particles in the reduced layer near the interface is

likely to be important. In particular, the depolarization fields in PLZT may depend on the type of conduction (p-type or n-type) of the ceramic particles in the reduced layer<sup>6</sup>.

Another contribution to the asymmetric response may be caused by the bending moment existing across the PLZT layer which may contribute to the domain alignment. Another important factor is that the top portion of the oxide layer is in tension (confirmed by XRD and finite element modeling), and its bottom portion is in compression. Thus different domain structure should be stable in different portions of the oxide region to minimize the internal stress. Complicated domain structure closely coupled to the internal stress may have a significant effect on the field-induced strain of a RAINBOW device.

A typical low-frequency response for a RAINBOW device, based on the piezoelectric PLZT 6.0/59.5/40.5 composition, is shown in Figure 5. Low frequency implies operation significantly below the lowest antiresonant frequency of the device. A well-defined hysteresis loop, characteristic of the piezoelectric response, can be seen at the bottom of the figure. Asymmetry of the displacement response for the two polarities of the applied voltage are seen. The origin of the asymmetry is similar to the one described for the electrostrictive case above.

The strain in the top portion of Figure 5 is shown with respect to the equilibrium position. The equilibrium position is defined as the position of the top surface of the sample with no external voltage applied. Prior to the application of the voltage, the LVDT housing is moved with respect to the needle to read zero volts. From the top portion of the figure it is clear that the resistance of the RAINBOW device with respect to the downward displacement of the sample is smaller than for the upward displacement. A probable explanation is that downward displacement is associated with the reduction of the mechanical energy stored in the sample; the opposite occurs for the upward displacement. The shape of the displacement/electric field curve is consistent with the strain of the RAINBOW device being controlled by the  $d_{31}$  coefficient.

For the piezoelectric RAINBOW devices it is useful to determine the level of linearity of the strain response as a function of the applied voltage. In Figure 6 peak-to-peak strain in PLZT 6.0/59.5/40.5 is plotted as a function of the applied peak-to-peak voltage (twice the amplitude of the sinusoidal voltage). It can be observed that a roughly linear response exists for a wide range of voltages studied.

The impedance of several RAINBOW devices was studied as a function of frequency following the IEEE standard. This is a convenient technique for studying the location of antiresonant and antiresonant frequencies. Representative results are summarized in Table 1. Low lying resonant modes are bending modes, and the fundamental planar mode occurs at a much higher frequency (approx. 70 KHz).

For the modeling work described below several other parameters were determined experimentally for the oxide and reduced layers of a RAINBOW. Thermal expansion for the oxide layer was done from room temperature to 975 °C in air; nitrogen atmosphere was used for the reduced layer over the same temperature range. The Pulse / Echo method was used to determine Young's modulus and Poisson's ratio for the oxide and reduced samples. Densities were determined using the water immersion method. All of these tests were performed on PLZT 5.5/57/43 nominal composition. Table 2 summarizes the results.

Resonant mode frequencies depend on the thickness of a RAINBOW. It can be seen in Figure 7 the first mode's resonant frequency increases with the thickness of the RAINBOW. Other factors apparently are important for the planar mode.

### **III. Modeling**

The accumulated weight of the experimental data indicates that RAINBOW devices can be used in a number of applications, including pumps and miniature speakers. There is a need to understand which factors contribute to a RAINBOW's performance.

We have initiated finite element modeling (FEM) using the ABAQUS commercial software package. Because of its versatility, FEM of piezoelectric materials is gaining in popularity<sup>7</sup>. ABAQUS's environment permits modeling of electromagnetic, elastic and piezoelectric properties of materials and devices. It is well suited for modeling of the piezoelectric RAINBOW devices. Current limitation of this package, and to our knowledge of other packages, is the inability to model nonlinearities associated with piezoelectricity and electrostrictive properties.

**Table 1.** Experimental Resonance / Antiresonance Spectra of RAINBOW Devices  
1.25 inch diameter, 20 mil thickness, 3:1 oxide / reduced thickness ratio.

Composition	Resonant Frequency (Hz)	Antiresonant Frequency (Hz)
5.5 / 57 / 43	1505	1534
	1611	1642
	6517	6547
	6956	7100
	7351	7368
	7538	7608
	16059	16816
	17250	18116
	31890	32290
	67900	76740
	109700	112300
	170000	176400
6.0 / 59.5 / 40.5	1893	1969
	7457	7814
	~ 9135	very weak
	18600	19200
	~ 33000	very weak
	71500	77700
	90600	91800
	177600	182200

**Table 2.** Experimental data obtained for the PLZT 5.5/57/43 oxide and reduced layers.

Property	Oxide layer	Reduced layer
Density (gm/cm <sup>3</sup> )	7.93	8.00
Young's modulus (N/m <sup>2</sup> )	7.79*10 <sup>10</sup>	6.86*10 <sup>10</sup>
Poisson's ratio	0.377	0.381
Thermal Expansion (°K <sup>-1</sup> )	~5*10 <sup>-6</sup>	~10*10 <sup>-6</sup>



RAINBOW modeling includes three major parts: definition of material properties and sample geometry, modeling of the cool down from the reducing temperature to room temperature, and determination of a response to the specified set of boundary conditions.

For the complete definition of the piezoelectric, elastic, dielectric, and thermoelastic properties of a piezoelectric ceramic, a large number of tensor properties are needed. There are very few electroceramics for which all of these properties are characterized sufficiently for the modeling to be a predictive tool. Fortunately, PZT 5A is well characterized and should have properties similar to PLZT ceramics with low lanthanum content. Piezoelectric, dielectric, and elastic constants of PZT 5A were used for modeling together with the experimentally determined Young's modulus, Poisson's ratio, densities, and thermal expansion values for the reduced and oxide monolithic PLZT samples. Reduced sample data was obtained on the samples following their complete reduction.

The parameters and sample geometry were then fed into two different models. The simpler model is a two dimensional axisymmetrical model. A full three dimensional model was also developed primarily for better characterization of the resonant modes. The two dimensional model was used for the bulk of the work because of its lower computational demands. A good agreement was obtained between the two models in prediction of the field-induced displacements. For example, for the sample with the diameter of 3.175 cm (1.25 inches), thickness of 0.3 mm, and oxide/reduced layer ratio of 2:1, the three dimensional model predicted a displacement of 858 microns on cooling and 43.6 microns with 500 volts (single polarity applied). For the same dimensions the axisymmetric model predicted 866 microns displacement on cooling and 42.6 microns for the 500 volts case.

During the cool down it was preferable to use nonlinear analyses because of the considerable stiffening of the structure in this step. Use of the nonlinear cool down step resulted in a 22% lower displacement of the RAINBOW's center point from the undeformed state as compared to the linear cool down step. Stiffening of the RAINBOW structure during the cool down is further confirmed by comparison of the resonant modes in the RAINBOW which is cooled down from 975 °C to one which experienced no cool down (a hypothetical RAINBOW made at room temperature simply by bonding the reduced layer and PLZT). The first six modes for the two structures are shown in Table 3

**Table 3.** Effect of cool down on the resonant properties of a RAINBOW .

1.25 in. dia., 20 mil thick, 3:1 oxide / reduced thickness ratio, short circuit; 60 elements .

Condition	Mode #1	Mode #2	Mode #3	Mode #4	Mode #5	Mode #6
Cool down	2240	9407	22569	41251	63459	65191
No cool down	1564	9032	22228	40833	63120	64420

Higher antiresonant frequencies are obtained for the structure which experienced a cool down step, which is consistent with the stiffening of the structure. Anti resonant modes correspond to the open circuit condition, and were obtained by specifying the potential on a single surface of the RAINBOW. Short circuit conditions correspond to the resonant mode, and were obtained by specifying the same potential on the top and bottom surfaces of a RAINBOW.

The number of elements used in the modeling has much greater effect on the prediction of the resonant frequencies than the static field-induced displacement. For the calculation of the resonant and antiresonant modes using axisymmetric model, a structure based on 60 elements gave satisfactory results (about 2 % stiffer than the model with 120 elements); for the static field-induced displacement the model with only 15 elements was sufficient (same displacement as 60 element model).

For each vibration mode, a separation between the resonant and antiresonant modes indicates the strength of the piezoelectric coupling - large separation of the modes represents stronger coupling between the driving electric field and the mechanical vibration. An example of the resonant and antiresonant calculated response of the RAINBOW is shown in Table 4. The fifth mode is particularly strong, and it represents the fundamental planar mode as seen in Figure 8. In this figure first six resonant and antiresonant modes are shown. The planar mode has noticeable coupling to the bending modes. It is interesting to note that the sixth mode resonant and antiresonant frequencies occur between resonant and antiresonant frequencies of the much stronger fifth mode. It can be seen that for the first mode a higher oxide/reduced thickness ratio results in a lower antiresonant frequency; in the case of the other modes, the reverse is true.

**Table 4.** Calculated resonant and antiresonant response of a RAINBOW device.  
1.25 in. dia., 20 mil thick, 60 elements.

Oxide/Reduced Thickness Ratio	Antiresonant Frequency (Hz)	Antiresonant Frequency (Hz)
4 : 1	2171	2269
	9476	9739
	22803	23251
	41731	42431
	63265	75253
	65821	66744
	94245	95630
3 : 1	2240	2353
	9407	9739
	22569	23141
	41251	42135
	63459	74788
	65191	66197
	93383	94800
2 : 1	2317	2453
	9281	9777
	22213	23143
	40632	42130
	63551	74004
	64609	66276
	92150	95075

**Table 5.** Effect of the Boundary Conditions on Antiresonant Frequencies of a RAINBOW.

1.25 inch diameter, 20 mil thickness, oxide / reduced thickness ratio 2:1.

Boundary Condition	Antiresonant Frequency (Hz)
Sideways Constraint	2453
	9777
	23137
	42117
	66277
	74008
No Sideways Constraint	1653
	7320
	18507
	35263
	57072
	74043

**Table 6.** Experimental Effect of the Boundary Conditions on Antiresonant Frequencies of a RAINBOW.

1.25 inch diameter, 20 mil thickness, 2:1 oxide / reduced thickness ratio.

Boundary Condition	Antiresonant Frequency (Hz)
No Sideways Constraint	1534
	1630
	6547
	7100
	7368
	7608
	16816
	18116
	32290
	76740
Sideways Constraint	112300
	176400
	3844
	4189
	5900
	very weak ~10900
	12533
	very weak ~14370
	27000
	76969
	108400
	176400

The effect of the mechanical constraints on the resonances of RAINBOW devices is significant. As is shown in Table 5, restricting the periphery of the RAINBOW to move only in a horizontal plane results in larger antiresonant frequencies as compared to the RAINBOW with this restriction removed. A similar behavior is observed experimentally, as shown in Table 6.

The experimental shift to higher frequencies is stronger than that predicted by the model. This is principally due to friction introduced on the lateral displacements by the sample holder. There is no friction for the lateral movement introduced by the model.

The field-induced displacement of a RAINBOW as a function of its diameter is shown in Figures 9A and 9B. The displacement is proportional to the square of the diameter for diameters less than 2 cm (for a 0.501 mm thick sample). For larger diameters the model predicts a slowdown in the growth of the displacement. In these samples there is a flattening out of the central portion of the RAINBOW, as can be seen in Figure 10.

For a constant voltage, the model predicts a rapid increase in the displacement as the thickness of the reduced layer increases, as is shown in Figure 11. This increase in the displacement is related to the lower Young's modulus of the reduced layer as compared to that of the oxide layer. In comparison, the cool down displacement has a maximum when the oxide/reduced thickness ratio is close to 1:1.

Our models predict reasonably well the resonant characteristics of the RAINBOW devices but significantly underestimate the field - induced displacement. It is likely that we greatly underestimate the effective  $d_{31}$  of the oxide layer in the model input. All possible nonlinear contributions to the effective  $d_{31}$  were ignored. More work is clearly needed in this area.

#### **IV. Conclusions**

The feasibility of obtaining large displacements with the RAINBOW devices has been shown. Large strains were obtained with electrostrictive and piezoelectric devices. The displacement of the RAINBOW device was shown to be controlled by the  $d_{31}$  coefficient for the piezoelectric compositions and by the  $Q_{12}$  coefficient for the electrostrictive compositions. Low frequency bending modes were observed from the study of electrical

impedance. FEM of RAINBOW is in reasonable agreement with experimental observation of piezoelectric resonance, but underestimates field-induced strain.

## V. References

1. E. Furman and G.H. Haertling, NASA semi-annual report, Contract No. NAG-1-301, 1992.
2. R.E. Newnham, D.P. Scinner and L.E. Cross, Mat. Res. Bull. 13, 525 (1978).
3. J.G. Smits and W. Choi, IEEE Trans. Ultrasonics, Ferroel., and Frequency Control 38, 3, 256 (1991).
4. G.H. Haertling and C.E. Land, J. Am. Ceram. Soc. 54, 1 (1971).
5. G.H. Haertling, Proc. 4th Int. SAMPE Electronics Conf. 699 (1990).
6. P. Wurfel and I.P. Batra, Phys. Rev. B8, 5126 (1973).
7. R. Leach, IEEE Trans. Ultrasonics, Ferroel., and Frequency Control 37, 2, 233 (1990).



## Typical RAINBOW Sample

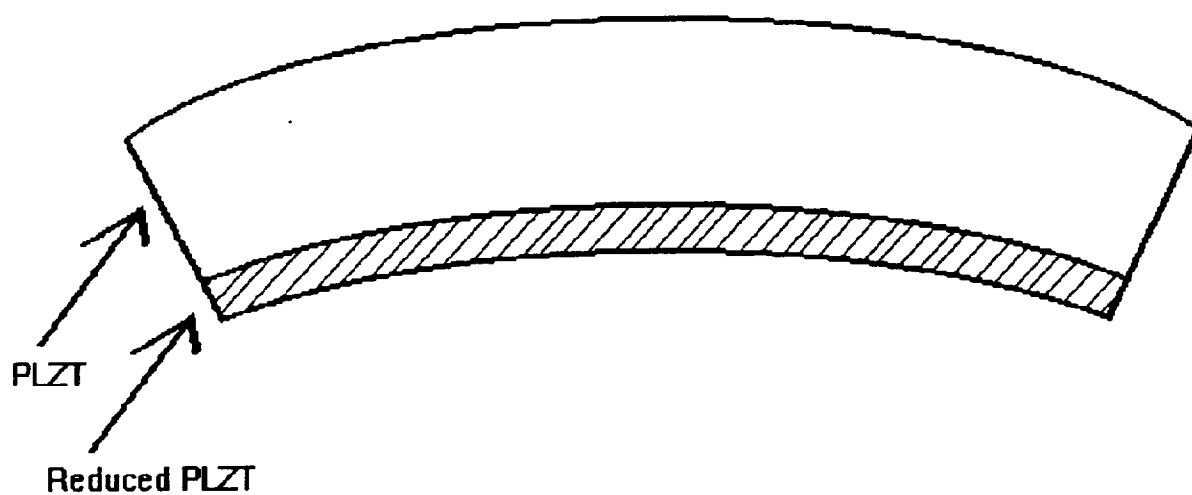
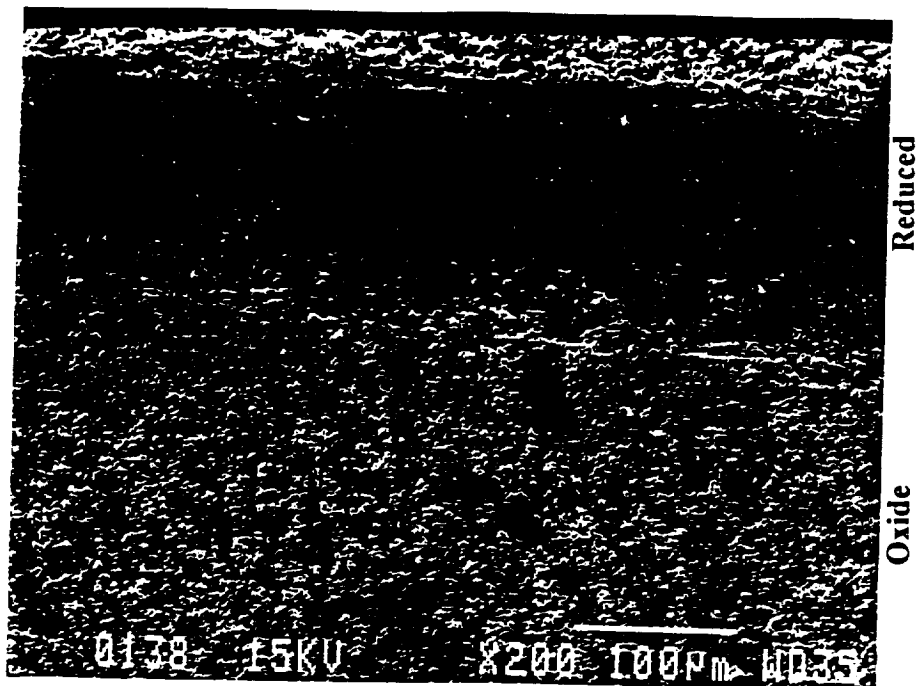
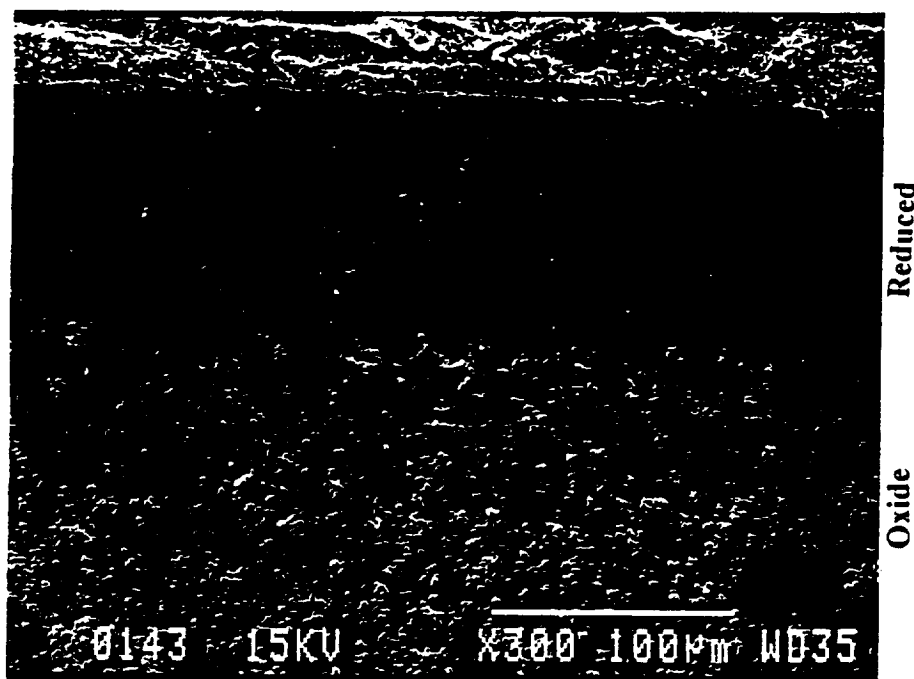


Figure 1. RAINBOW structure.



PLZT 7.9/70/30



PLZT 8.6/65/35

Figure 2. Cross sections of the RAINBOW devices

# Schematic Diagram for Strain Measurements

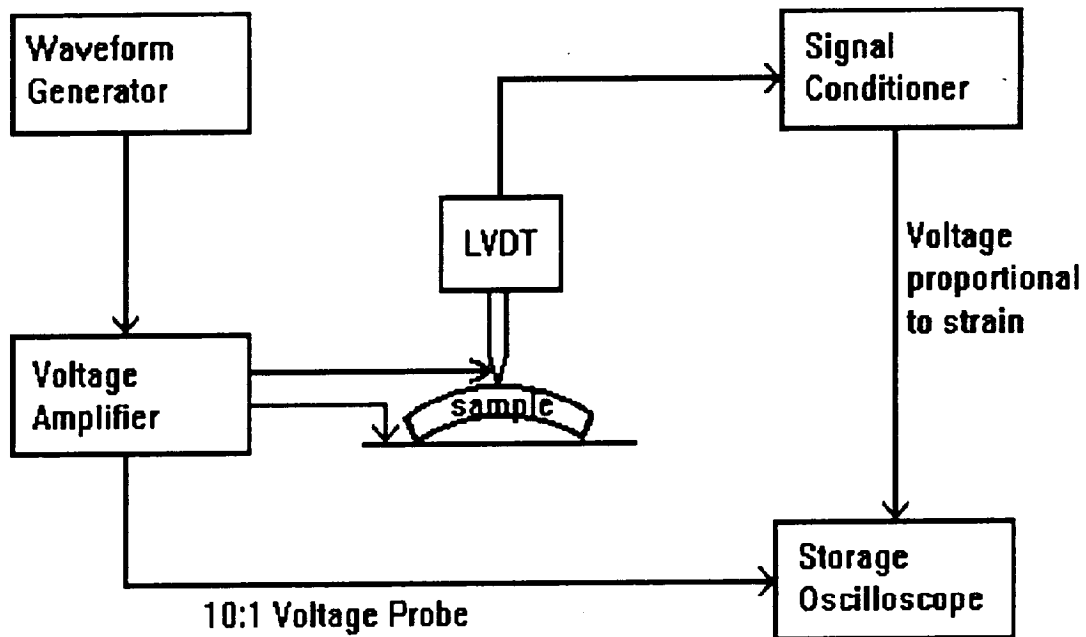
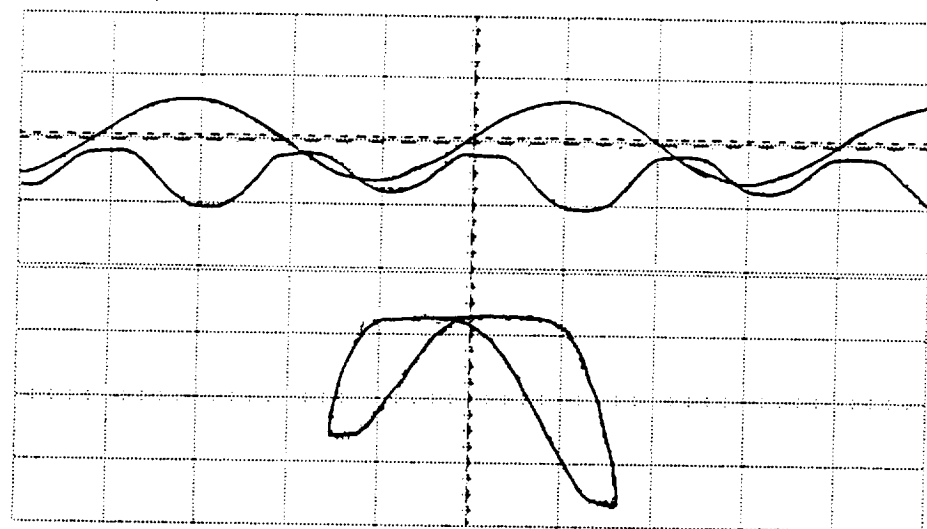


Figure 3. Schematic diagram of the displacement measuring equipment.



-1.00000 s      0.00000 s      1.00000 s  
 200 ms/div      repetitive

	current	minimum	maximum	average
Vp-p(1)	254.118 V	6.27451 V	254.118 V	236.415 V
Vp-p(2)	175.686mV	175.686mV	210.196mV	184.650mV
frequency(1)	1.22195 Hz	1.21602 Hz	1.22195 Hz	1.22104 Hz

	Sensitivity	Offset	Probe	Coupling
Channel 1	200 V/div	0.00000 V	50.00 :1	dc (1M ohm)
Channel 2	200 mV/div	0.00000 V	1.000 :1	dc (1M ohm)
Function 1	58.0 mV/div	-116.000 mV	Function -	2 vs 1

Figure 4. Electrostrictive response of the RAINBOW device based on composition 9.5/65/35.

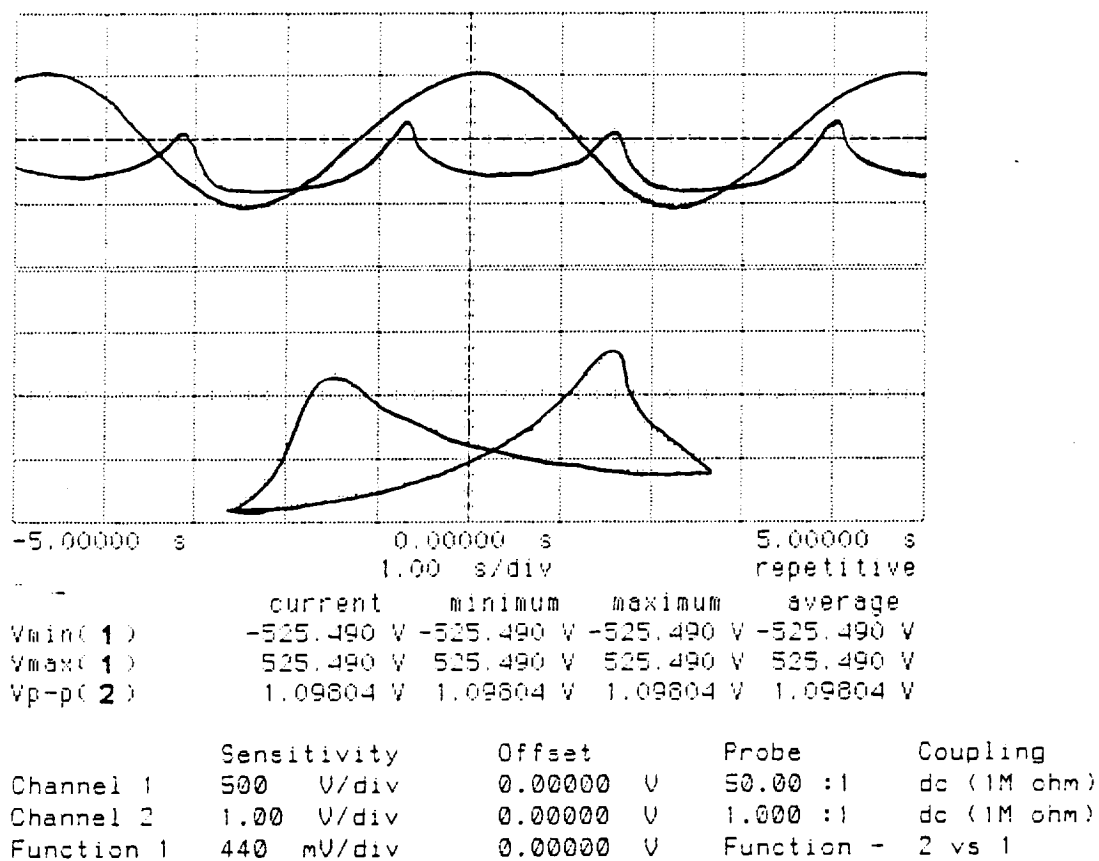


Figure 5. Piezoelectric response of the RAINBOW device based on composition 6.0/59.5/40.5 .

PLZT 6/59.5/40.5 reduced 975 C/90 min.

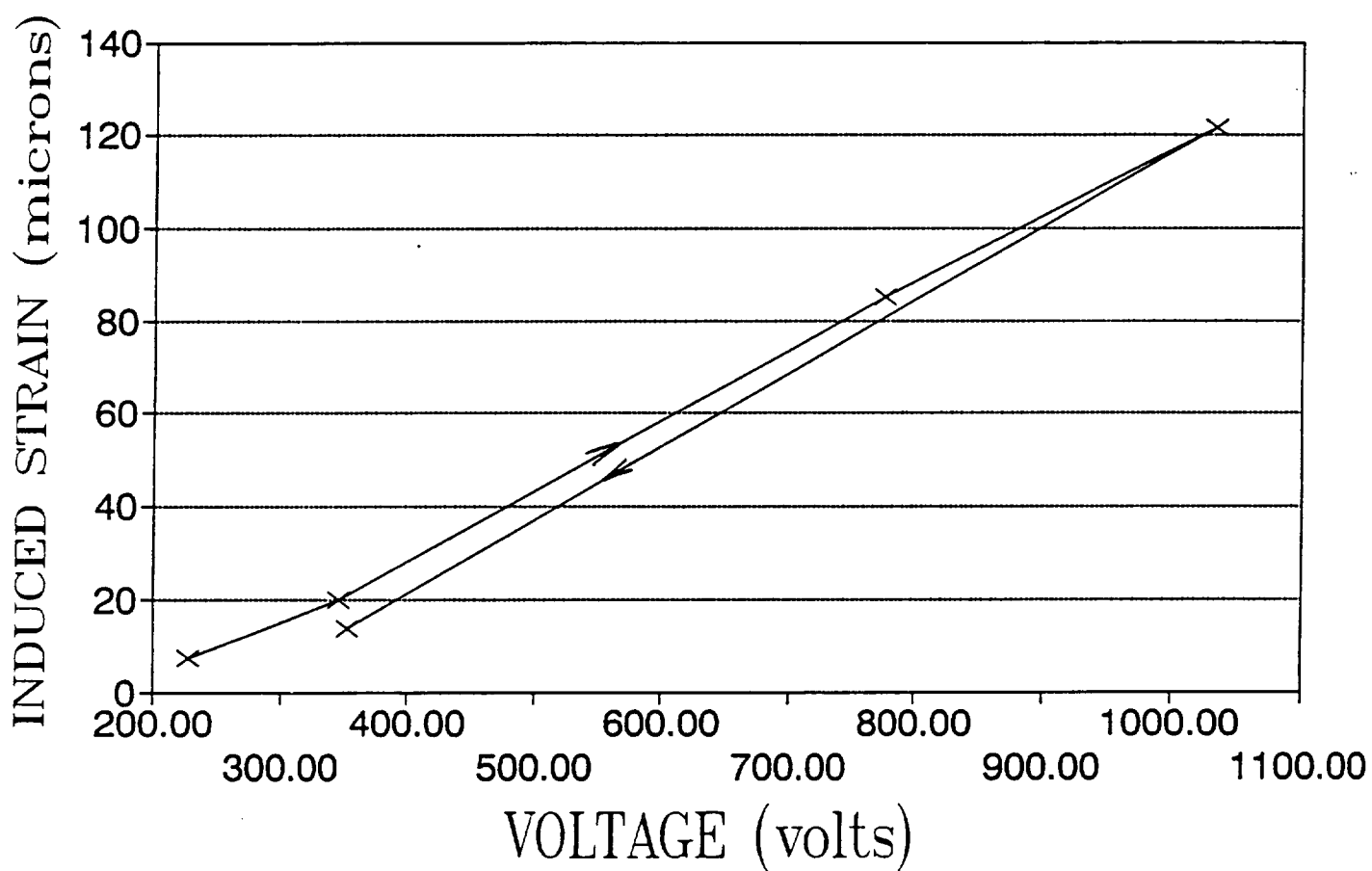


Figure 6. Peak-to-peak strain as a function of peak-to-peak voltage.

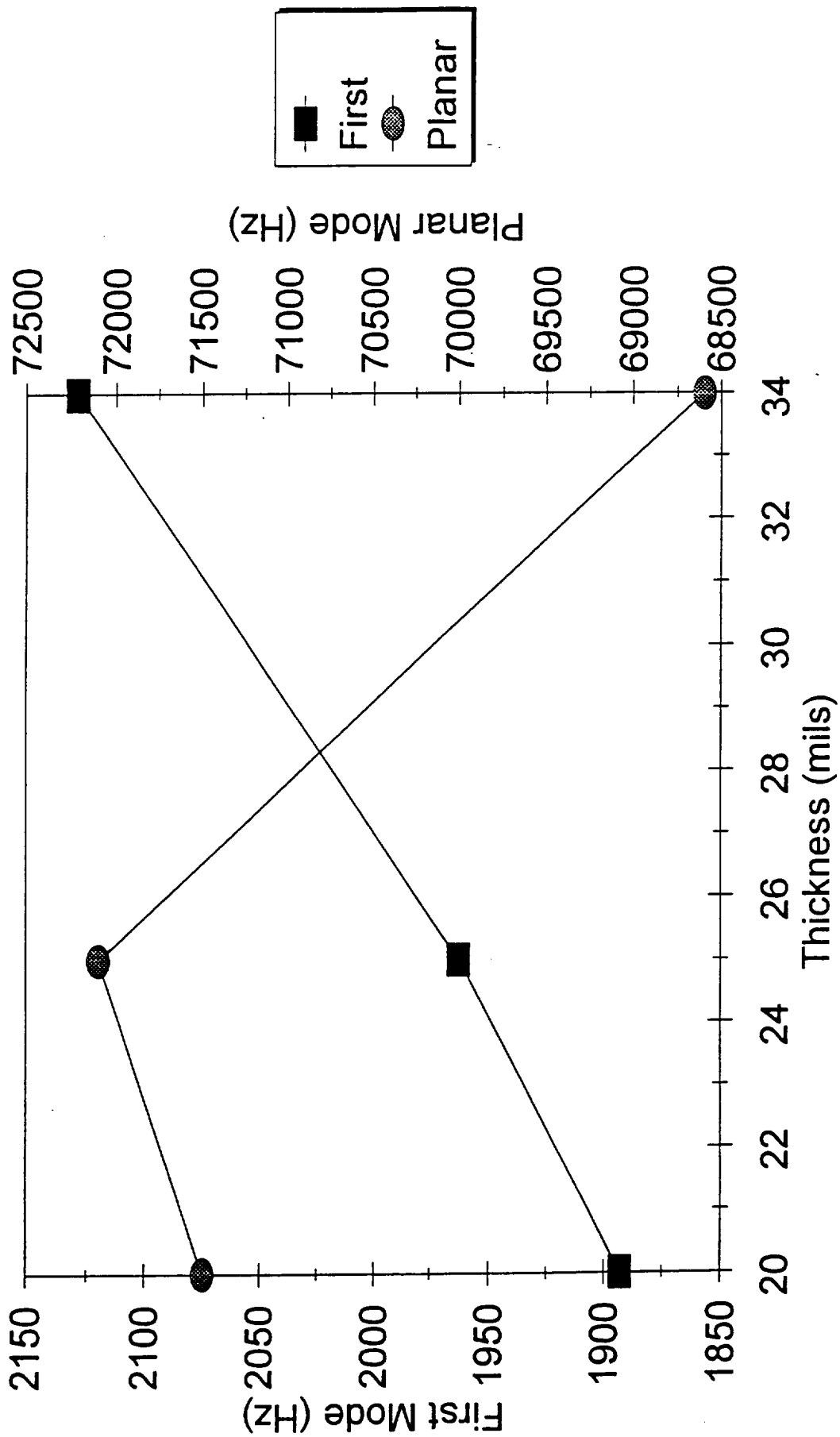


Figure 7. Influence of thickness on the first and planar resonant modes of 3.175 cm diameter RAINBOW wafers with 6.0/59.5/40.5 composition.

Axisymmetric model, 60 elements, 3:1 oxide / reduced thickness ratio.

Diameter: 3.175 cm (1.25 in.)

Thickness: 0.0508 cm (20 mil)

### RESONANCE



### ANTIRESONANCE

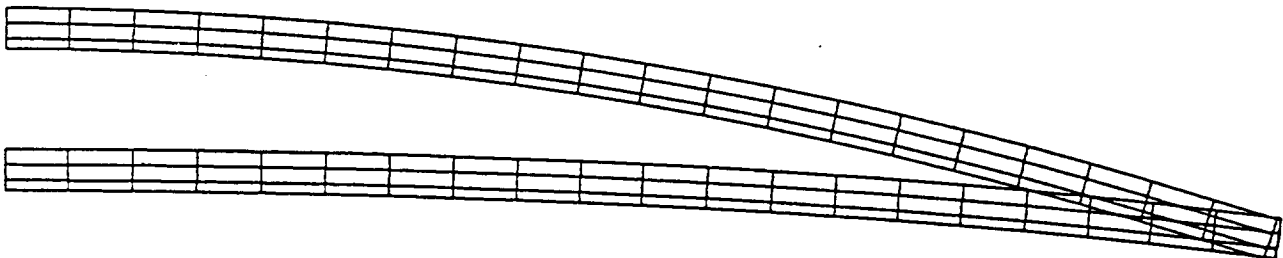


Figure 8A. First resonant and antiresonant modes.

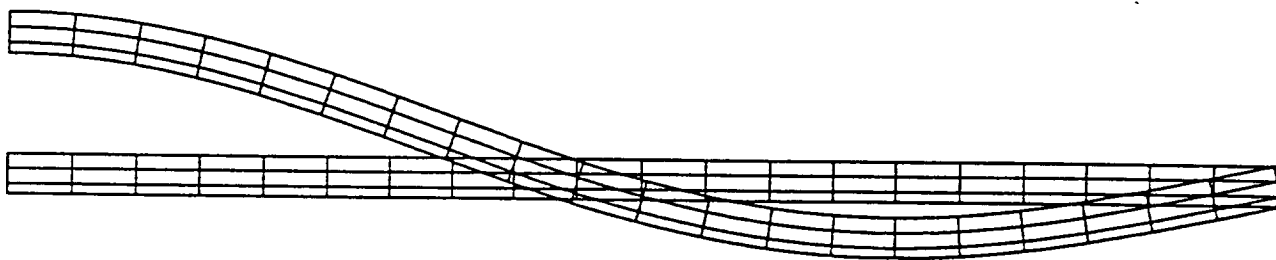


Axisymmetric model, 60 elements, 3:1 oxide / reduced thickness ratio.

Diameter: 3.175 cm (1.25 in.)

Thickness: 0.0508 cm (20 mil)

### RESONANCE



### ANTIRESONANCE

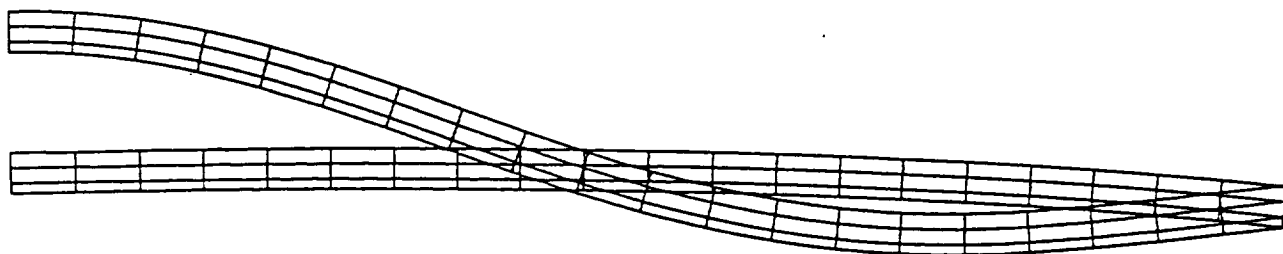


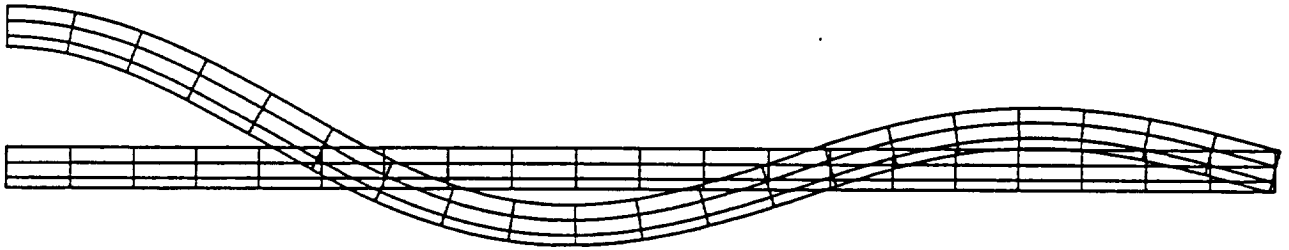
Figure 8B. Second resonant and antiresonant modes.

Axisymmetric model, 60 elements, 3:1 oxide / reduced thickness ratio.

Diameter: 3.175 cm (1.25 in.)

Thickness: 0.0508 cm (20 mil)

### RESONANCE



### ANTIRESONANCE

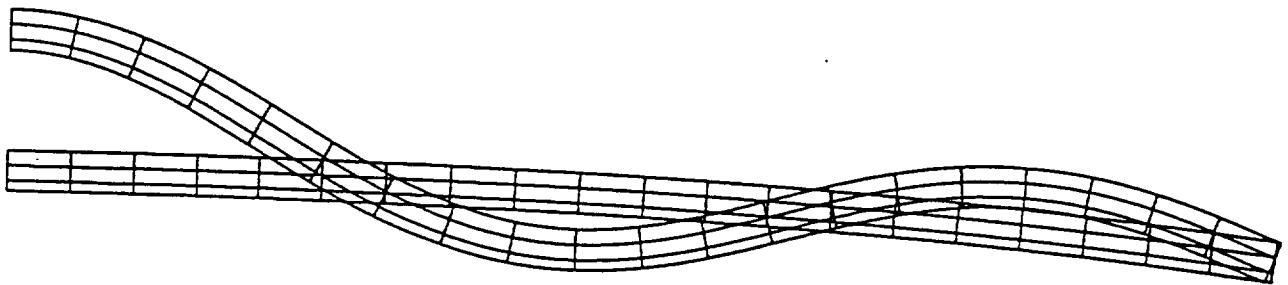


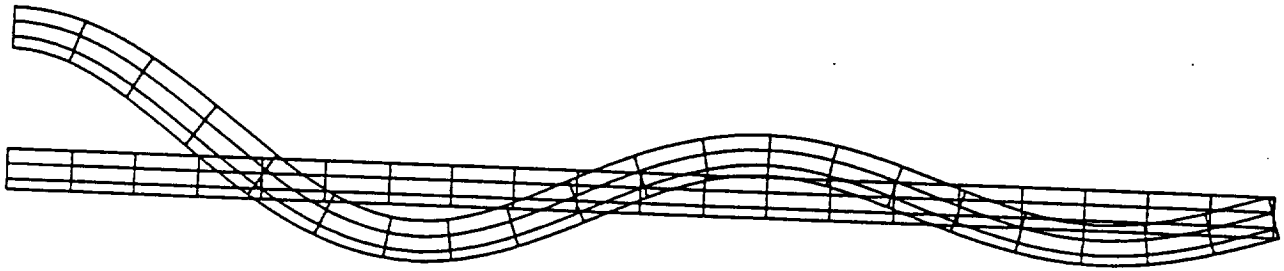
Figure 8C. Third resonant and antiresonant modes.

Axisymmetric model, 60 elements, 3:1 oxide / reduced thickness ratio.

Diameter: 3.175 cm (1.25 in.)

Thickness: 0.0508 cm (20 mil)

### RESONANCE



### ANTIRESONANCE

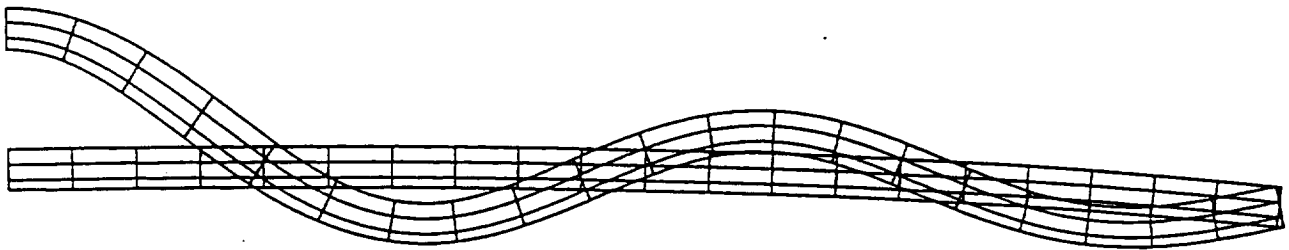


Figure 8D. Fourth resonant and antiresonant modes.

Axisymmetric model 60 elements, 3:1 oxide / reduced thickness ratio.

Diameter: 3.175 cm (1.25 in.)

Thickness: 0.0508 cm (20 mil)

## RESONANCE



## ANTIRESONANCE



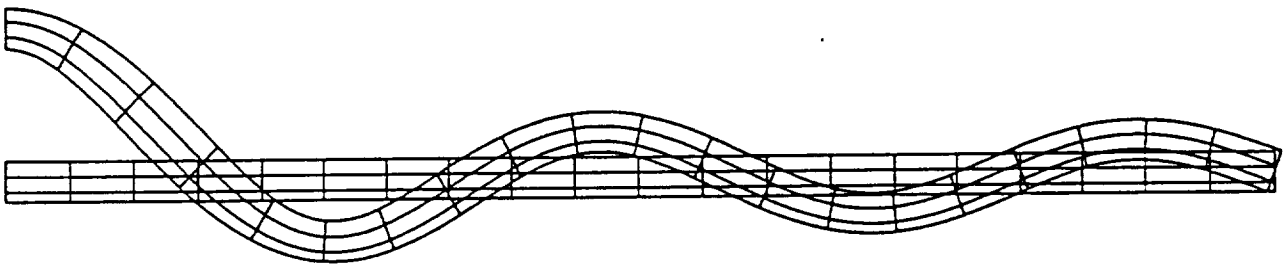
Figure 8E. Fifth resonant and antiresonant modes.

Axisymmetric model, 60 elements, 3:1 oxide / reduced thickness ratio.

Diameter: 3.175 cm (1.25 in.)

Thickness: 0.0508 cm (20 mil)

## RESONANCE



## ANTIRESONANCE

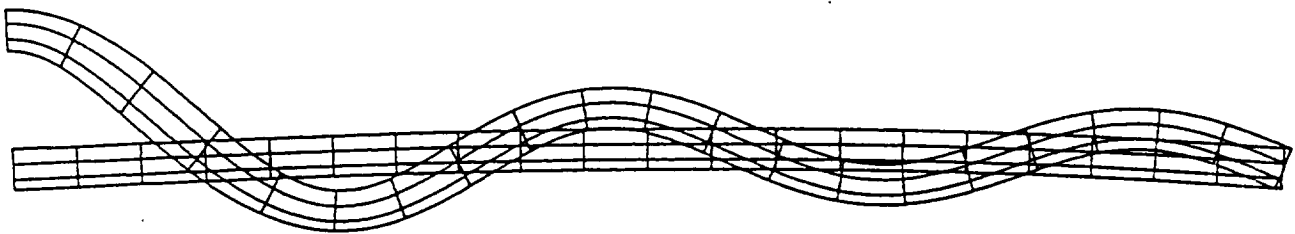


Figure 8F. Sixth resonant and antiresonant modes.

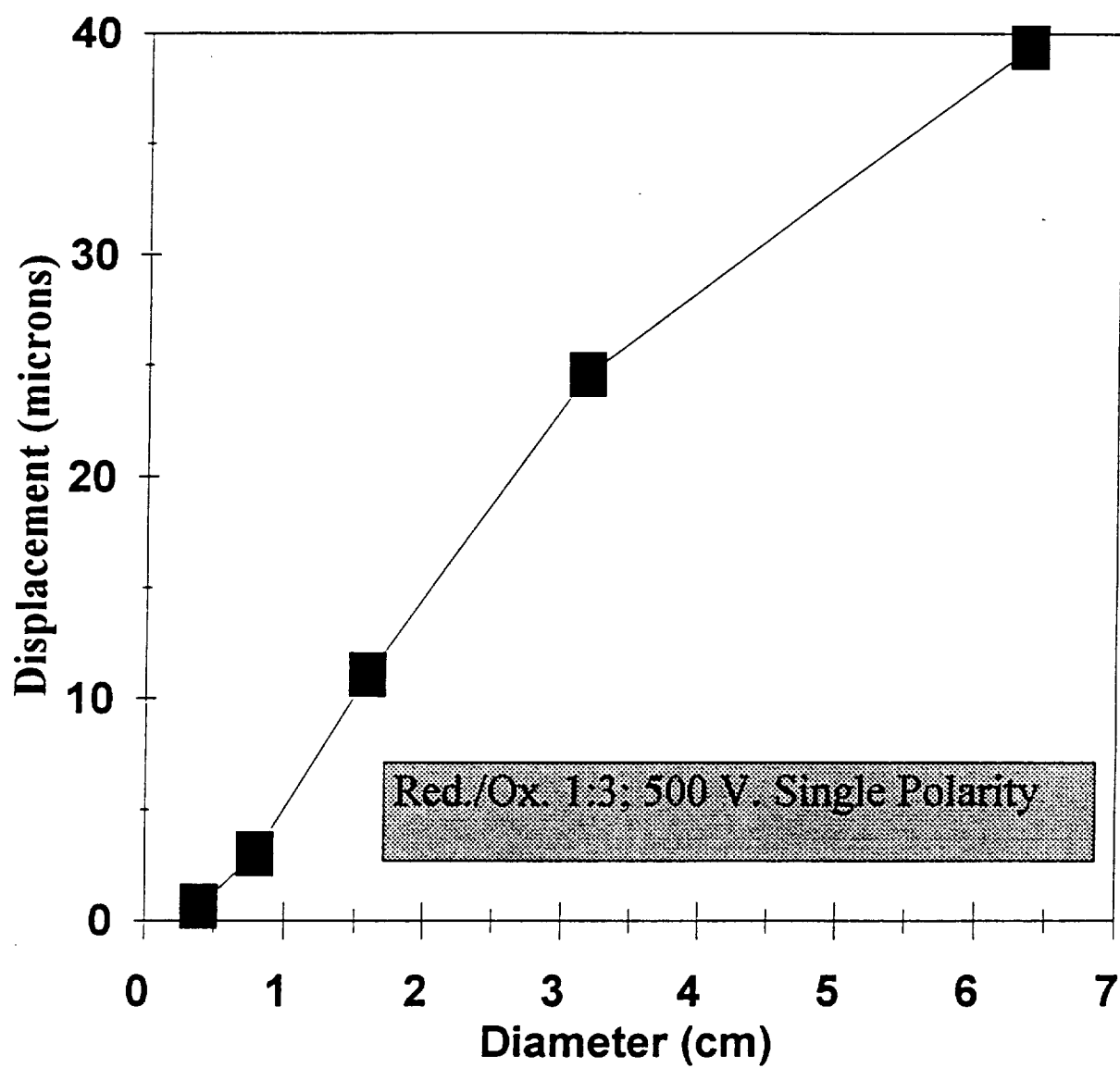


Figure 9A. The field - induced displacement as a function of RAINBOW diameter.

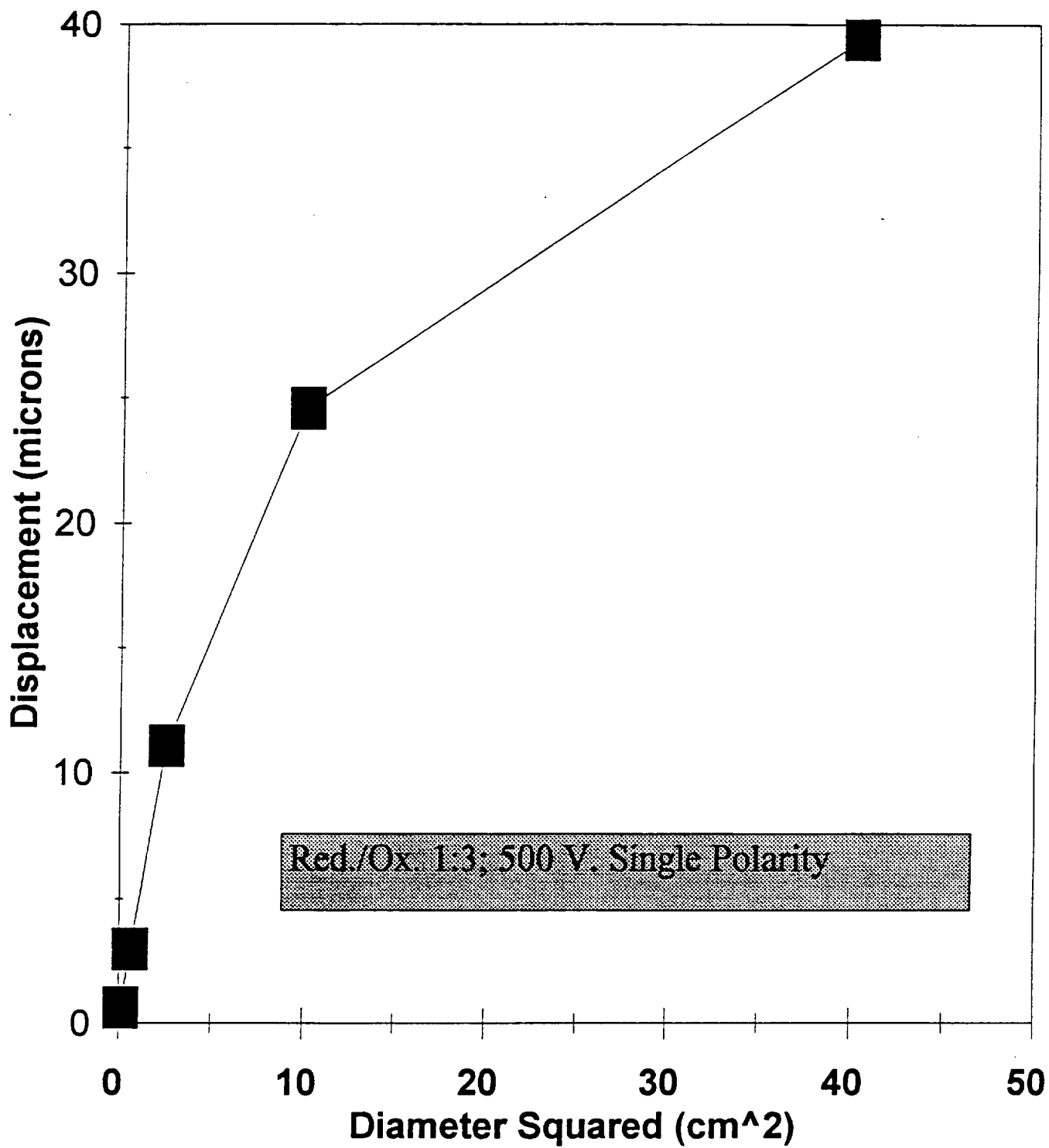
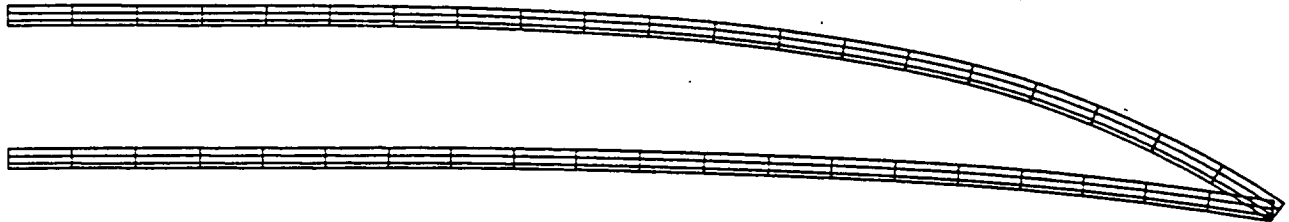


Figure 9B. The field - induced displacement as a function of RAINBOW diameter squared.

**2.5 in. diameter**



**0.625 in. diameter**

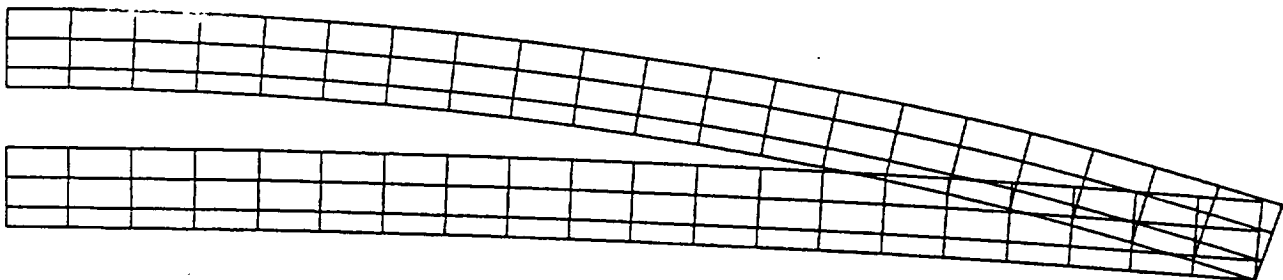


Figure 10. Field - induced displacements of RAINBOWs with different diameters. 3:1 oxide / reduced thickness ratio, 20 mil thick, 500 V applied. Initial structure has smaller curvature.



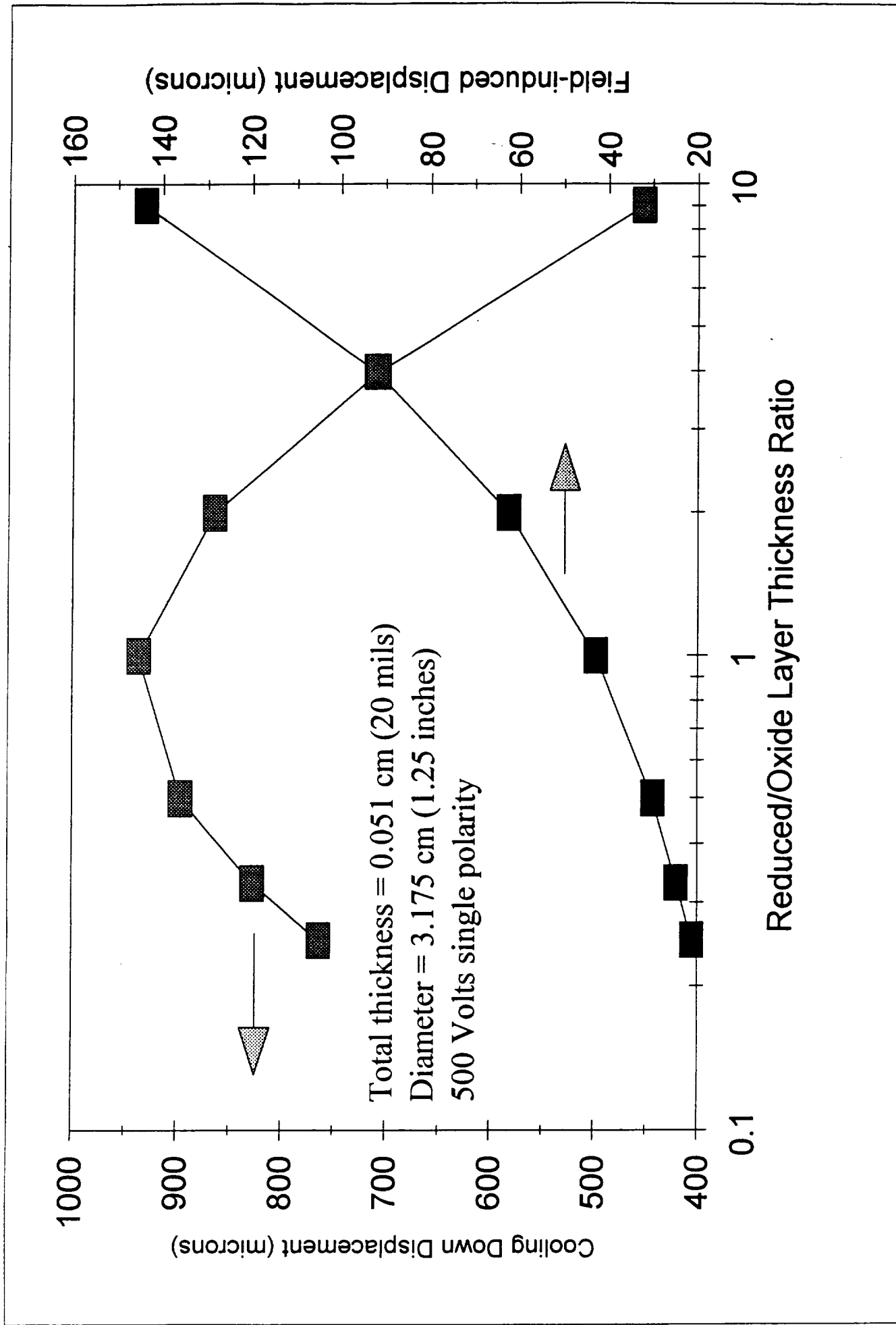


Figure 11. Effect of the reduced/oxide layer thickness ratio on the displacement of the RAINBOW.

**Part IV.**

**General Studies of Rainbow Processing, Properties and Devices**

# **Rainbow Ceramics - A New Type of Ultra-High Displacement Actuator**

Gene H. Haertling  
Clemson University, Clemson, SC, 29634-0907

## **Abstract**

A new processing method for producing ultra-high displacement, monolithic transducer ceramics has recently been developed. The technique consists of selectively reducing one surface of a high lead-containing piezoelectric or electrostrictive wafer with solid carbon (graphite) in an oxidizing atmosphere at an elevated temperature. The resulting stress-biased wafer is referred to as a Rainbow ceramic because of its unique, domed structure which leads to high electromechanical displacement and enhanced load bearing capability. In this study, the characteristics of several PLZT compositions were evaluated as Rainbow benders. Axial displacements as high as 1 mm and sustained pressures to 0.6 MPa were obtained from single Rainbow elements. Cascading eight of the elements in series yielded a total displacement of 5.1 mm. Temperature compensation was demonstrated in a Rainbow clamshell arrangement of two elements by selecting compositions with off-setting properties.

## **I. Introduction**

In the last several years, the technology of using piezoelectric and electrostrictive ceramic materials as solid state actuators for small ( $<10$  microns) and precise mechanical movement devices has undergone considerable investigation and development.<sup>1-6</sup> More recently, it has become quite evident that these same types of solid state devices are desirable in newer applications requiring very large displacements (in excess of 1000 microns) such as linear motors, cavity pumps, switches, loud speakers, noise-canceling devices, variable-focus mirrors and laser deflectors. Since the direct extensional strain in most piezoelectric or electrostrictive ceramic materials is a few tenths of one percent, at best, a means of amplifying this strain is essential to their successful use in these applications.

Some well known techniques for producing large displacements in these materials include flextensional composite structures, unimorph benders and bimorph benders; however, each of these technologies has their limitations in regard to size, weight, maximum displacement or load bearing capability. A more recent device, the Moonie, was reported by Sugawara, et.al. in 1992.<sup>7</sup> This metal-ceramic composite actuator is a type of flextensional transducer which is able to convert and amplify (by approximately ten times) the radial displacement of a piezoelectric disk into a linear axial motion. Displacements as high as 20 microns have been achieved at a sustaining stress of 0.5MPa.

When considering the stress/strain capabilities of all of these technologies, it is evident that there is still a real need for additional techniques which will produce even higher strains or displacements while, at the same time, being able to sustain reasonable stresses or loads. This paper will describe such a technology. It is a new type of monolithic ceramic bender which is capable of achieving very high axial displacements of greater than 1000 microns (40 mils) and sustaining moderate pressures of approximately 0.6 MPa (85 psi). Known as a Rainbow (Reduced And INternally Biased Oxide Wafer) ceramic, this unique structure possesses a wider range of stress/strain characteristics than other bender types, and thus, promises to find application in a multitude of future devices. Key features of these Rainbow are their simplicity, quick processing, ease of fabrication, surface mountable configuration and low cost. The particular ranges and regions for each of the technologies previously mentioned are shown on a stress/strain diagram in Figure 1.

## II. Description of the Rainbow Technology

In its most basic sense, the Rainbow technology consists of a new processing method for treating conventional, high lead-containing piezoelectric or electrostrictive ceramic wafers such as PZT, PLZT, PBZT, PSZT and PMN. It involves the high temperature chemical reduction of one surface of a wafer, thereby producing an stress-biased, dome-like structure as shown schematically in Figure 2. The stress achieved in the ceramic by means of the single-sided reduction process is a critical feature of the structure. Since it produces a state of tension toward the bottom or reduced (concave) side of the wafer and compression toward the top or unreduced side, the wafer assumes either a dome or saddle shape, depending on the magnitude of the stress and the diameter-to-thickness ratio of the wafer. When both the stress and the diameter-to-thickness ratio are high, the Rainbow wafer takes on the higher-profile, saddle shape. The change in shape of the wafer after reduction is believed to be due to the reduction in volume of the reduced layer (largely metallic lead) compared to the unreduced material, as well as the differential thermal contraction between the reduced and unreduced layers on cooling to room temperature.

The reduced side of the piezoelectric serves as (1) a mechanical support for the device, (2) the source of the internal stress and (3) one of the device electrodes. Although, for operation it is only necessary to deposit one additional electrode on top of the unreduced piezoelectric, it is beneficial to also electrode the reduced layer in order to insure good contact for the electrical leads. Use of the reduced piezoelectric as a stress-biasing support member as well as one of the electrodes effectively eliminates the bonding problems usually encountered in transducer fabrication and operation.

After attaching leads to the two electrodes, the device is completed and ready for activation with an appropriate voltage. Like other piezoelectric devices, Rainbows can be operated with a dc, pulse dc, or ac voltage, however, the largest displacements are usually achieved when driven with ac at frequencies less than 40 Hz. In operation, the dome height of the Rainbow varies as a function of the magnitude and polarity of the

voltage. The axial motion, thus produced, is largely a consequence of the lateral contraction produced in the material via the lateral piezoelectric coefficient; and therefore, the materials with the highest  $d_{31}$  coefficients generate the highest displacements. This is also true for the electrostrictive materials; i.e., those with the largest lateral coefficients produce the highest motion.

Rainbows can also be stacked in order to amplify a given linear motion. Since each individual device approximates one-half of a clamshell structure, two of them can be placed together to form a completed clamshell. These two Rainbow elements can then be operated mechanically in series to produce twice the displacement of one element. Additional elements, in pairs of two, can be added to form a linear actuator of unusually high displacement in a relatively small volume. Electrically, the cascaded units can be operated in series or parallel; in the series case the connections are simpler but more voltage is required to maximize the displacement, whereas in the parallel case more displacement is achieved at a lower voltage but at the expense of more complicated lead arrangements.

The Rainbow structure has been produced in both atmosphere fired and hot pressed ceramics, particularly the PLZT piezoelectric and electrostrictive compositions such as 2/53/47, 5.5/56/44, 8.6/65/35 and 8/70/30. Since these materials are also pyroelectric and ferroelectric in nature, Rainbow devices produced from them can rightly be considered as multifunction, smart components. This multifunction characteristic is important since it substantially increases the number of potential applications. Typical devices include linear actuators, reciprocating and cavity pumps, switches, speakers, benders, vibrators, hydroprojectors and receivers, optical deflectors, variable focus mirrors/lenses, accelerometers, relays, acoustic-canceling devices, sensors and smart systems. Of these, the first ten have already been demonstrated in prototype devices.

### III. Experimental Procedures

Piezoelectric and electrostrictive PLZT compositions were prepared from the raw material oxides via a conventional mixed-oxide process. Calcining was carried out at 975°C for two hours in closed alumina crucibles. The milled and dried powders were first cold pressed as pre-form slugs and then hot pressed at 1200°C for 6 hours at 14 Mpa. This procedure yielded a fully dense material with a grain size of approximately five microns. Subsequent steps in the fabrication of the wafers included grinding of the slug diameter, slicing the slug into wafers and finish lapping of the wafers to the prescribed thickness.

A Rainbow was produced from a lapped part by placing the wafer on a flat carbon (graphite) block which was resting on a zirconia carrier plate. A second zirconia plate was placed on top of the wafer in order to shield that side of the wafer from chemical reduction. The assembly was inserted into a small box furnace maintained at a temperature of 975°C. After approximately one hour at temperature, the assembly was removed and allowed to cool to room temperature in the open air. When cool, the

dome-shaped wafer was removed from the carbon block, brushed lightly to remove any metallic lead particles and then electroded with DuPont silver epoxy paint (#5504N) at 200°C for 30 minutes. A more complete description of a similar process was previously reported.<sup>8</sup>

Standard electrical measurements of capacitance, dissipation, dc hysteresis loop, planar coupling and dc strain loop were carried out on each of the wafers. More extensive long term testing was performed on selected materials by mounting the leadless wafers in a dial indicator assembly as shown schematically in Figure 2. This setup permitted external weights to be applied to the sample during testing. For the pressure measurements, a special air cell was constructed which allowed high pressure to be applied to the top of the wafer and atmospheric pressure on the bottom side during electrical operation.

#### IV. Experimental Results

Two types of actuator materials were tested in this study; i.e., piezoelectric, atmosphere sintered PLZT 5.5/56/44 and electrostrictive, hot pressed PLZT 8.6/65/35. Their displacement characteristics as a function of voltage are given in Figure 3 with wafer thickness and voltage drive as additional parameters. As may be seen, displacements as high as 57% were obtained for the particular wafers tested. As expected, the thinner wafers yielded the highest displacements. Comparing the displacements of the piezoelectric and electrostrictive materials in the figure, the former was generally lower than the latter when operated dc (one polarity only) but was substantially higher when driven ac (open diamonds). The ac case for 8.6/65/35 was not shown since electrostrictors have the same displacement for voltages of either polarity. An additional note is that 5.5/56/44 was significantly better than 8.6/65/35 at low voltages, but this was also expected, as a result of the linear vs. quadratic behavior of the two types of materials.

Displacement and pressure data for PLZT 5.5/56/44 as a function of wafer thickness are presented in Figure 4. The left ordinate scale represents the maximum allowable pressure differential across the wafer thickness before the wafer "bottoms out" to the planar surface and stops flexing (usually <0.5mm thickness) or the wafer mechanically fractures (>0.5mm thickness). The right ordinate log scale is the percent displacement (based on wafer thickness) of the device when operated at 450 volts dc under just the loading of the dial gage spring (80 grams). Also indicated on the figure are the wafer thickness regions where the saddle and dome modes of operation are dominant for a wafer 31.75 mm (1.25 in.) in diameter. The data shown in the figure indicate that Rainbow displacements span an unusually large range from zero to at least 500% with actual displacements up to 1 mm (0.040 in.) for a 0.2 mm (0.008 in.) thick wafer. Of course, such large displacements are not possible when operating under significant pressure differentials, as shown in the figure, or under moderate point loading situations (not shown). The maximum point load capability measured to date is 10 kg.

on a 31.75 mm diameter, 1.5 mm thick disk.

The temperature characteristics of selected PLZT compositions 8.6/65/35 and 7/65/35 are given in Figure 5. Since 8.6/65/35 has a Curie point around room temperature, it exhibited a reduction in displacement on increasing temperature whereas 7/65/35, having a Curie point at about 140°C, experienced an increasing displacement with rising temperature. When these two elements are placed back-to-back as in a clamshell configuration, their net displacement as a function of temperature was very low, resulting in a nearly temperature independent Rainbow unit. Temperature compensation can be refined even further by mixing-and-matching more elements in units of two.

When several units are stacked together, not only can temperature compensation be effected but total displacement can also be maximized. The maximum displacement obtained to date with a group of four clamshell units (eight Rainbow wafers) is 5.1 mm (0.2 in.).

A considerable amount of additional information on processing, properties and devices possible from the new Rainbow technology is also included in this report as supplementary figures in Appendix A. These figures are self-explanatory to a large extent and are given here in order to include as much information as possible in this annual report.

## V. Conclusions

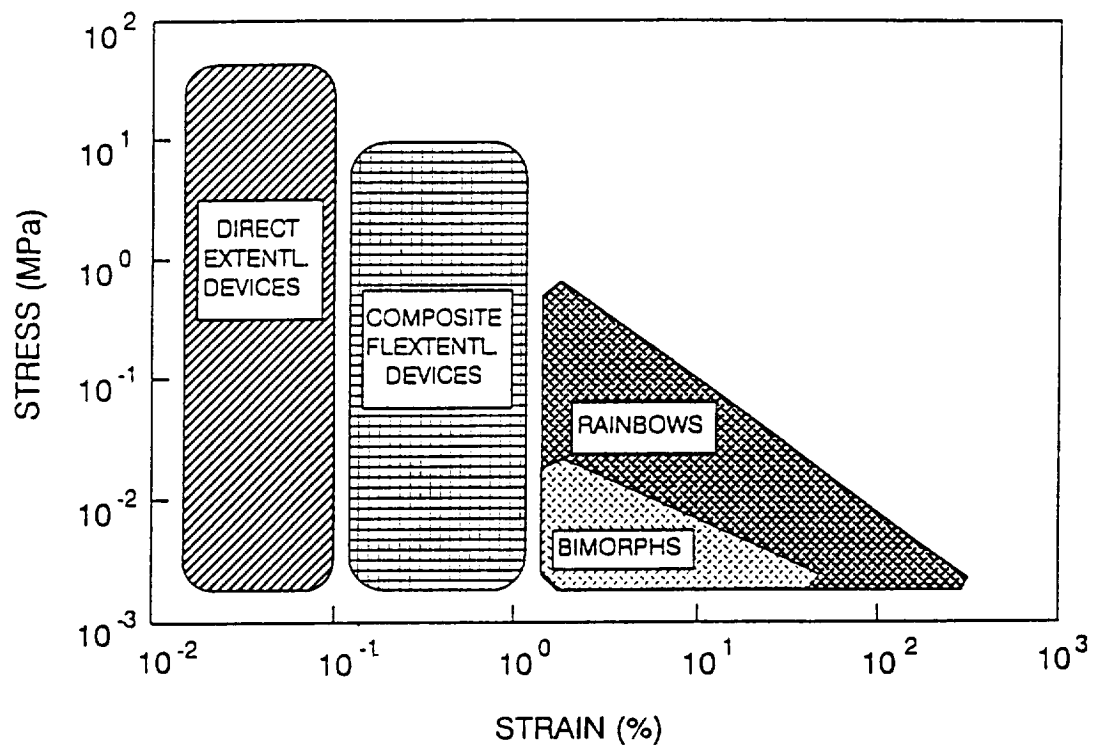
A new type of monolithic ceramic bender (designated as a Rainbow) which is capable of achieving ultra-high axial displacements (up to 500% or more, based on wafer thickness) and sustaining moderate loads of approximately 10 kg. has recently been developed. Actual displacements as high as 1 mm were obtained from single element devices 0.2 mm thick. The Rainbow structure was achieved in commercially available atmosphere sintered or hot pressed piezoelectric and electrostrictive ceramics by means of a high temperature chemical reduction process. Desirable features of the Rainbows were found to be their simplicity, moderate load bearing capability, temperature compensation characteristics, easy fabrication and low cost. It is anticipated that this technology will have numerous applications in commercial and industrial markets.

## References

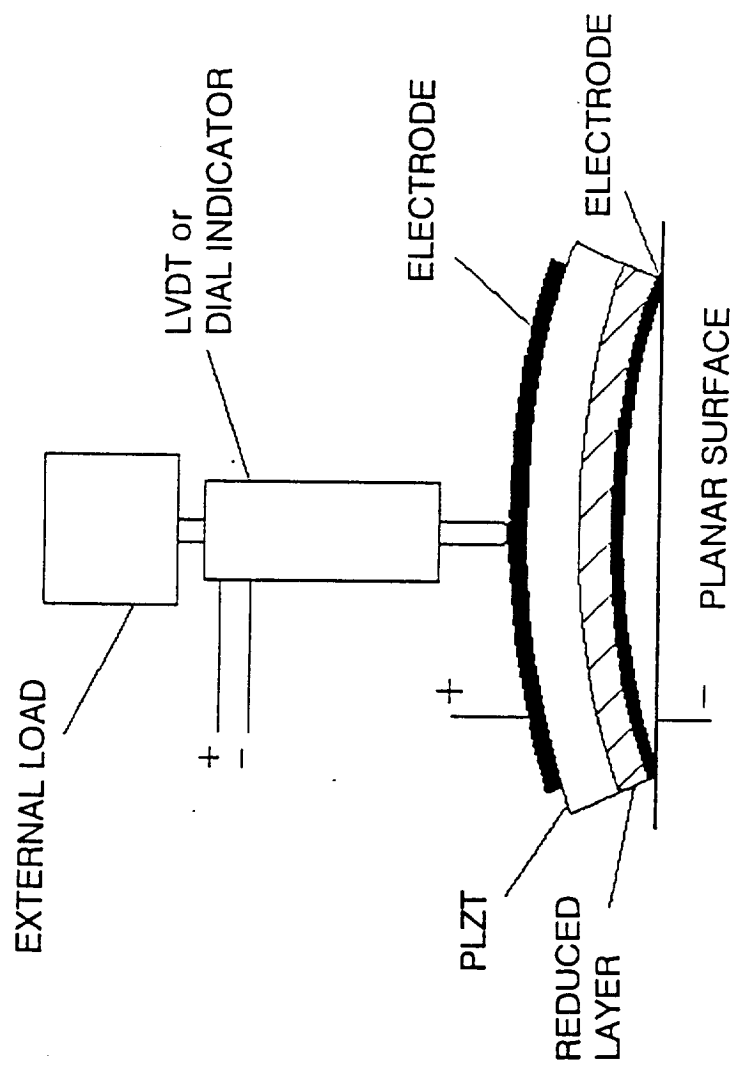
1. H. Honmou, R. Ishikawa and S. Takahashi, "Automatic Optical Fiber Polarization Control System Using Multilayer Piezoelectric Actuators," Japan. J. Appl. Phys., 24, Supplement 24-3, 187-89 (1985)
2. K. Uchino, "Electrostrictive Actuators: Materials and Applications," Bull. Am. Ceram. Soc., 65, (4) 647-52 (1986)

3. K. Uchino, M. Yoshizaki, K. Kasai, H. Yamamura, N. Sakai and H. Asakura, "Monomorph Actuators Using Semiconductive Ferroelectrics," Japan. J. Appl. Phys., 26, (7) 1046-49 (1987)
4. M.A. Ealey and P.A. Davis, "Standard SELECT Electrostrictive Lead Magnesium Niobate Actuators for Active and Adaptive Optical Components," Opt. Engr., 29, (11) 1373-82 (1990)
5. W.P. Robbins, D.L. Polla and D.E. Glumac, "High-Displacement Piezoelectric Actuator Utilizing a Meander-Line Geometry - Part I: Experimental Characterization," IEEE Trans. Ultrasonics, Ferroelectrics and Freq. Control, 38, (5) 454-67 (1991)
6. Q.C. Xu, S. Yoshikawa, J.R. Belsick and R.E. Newnham, "Piezoelectric Composites with High Sensitivity and High Capacitance for Use at High Pressures," IEEE Trans. Ultrasonics, Ferroelectrics and Freq. Control, 38, (6) 634-39 (1991)
7. Y. Sugawara, K. Onitsuka, S. Yoshikawa, Q. Xu, R.E. Newnham and K. Uchino, "Metal-Ceramic Composite Actuators," J. Am. Ceram. Soc., 75, (4) 996-98 (1992)
8. G.H. Haertling, "Reduction/Oxidation Effects in PLZT Ceramics," Proc. of the 4th Intl. SAMPE Elect. Conf., p. 699-711, Albuquerque, June 12-14 (1990)

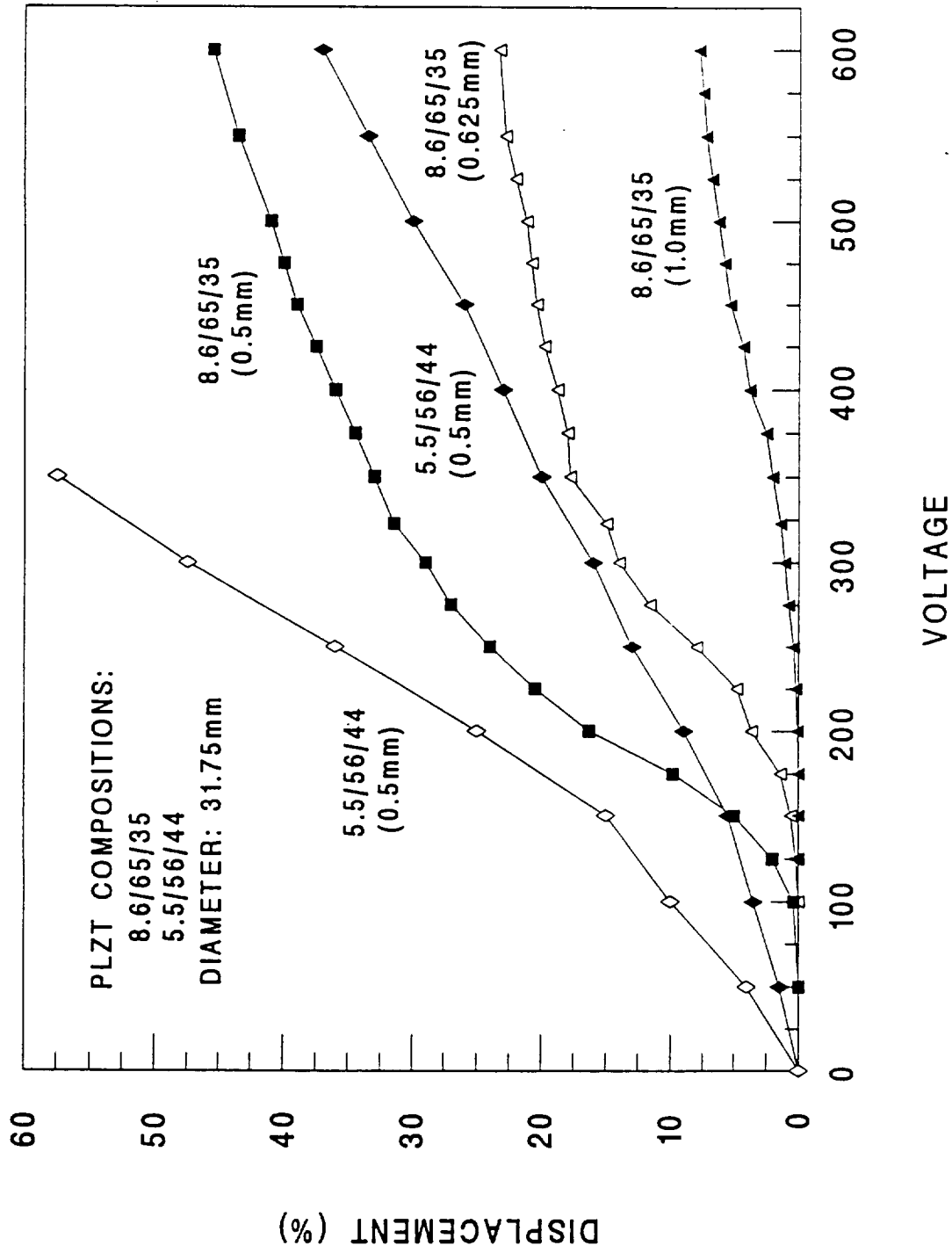




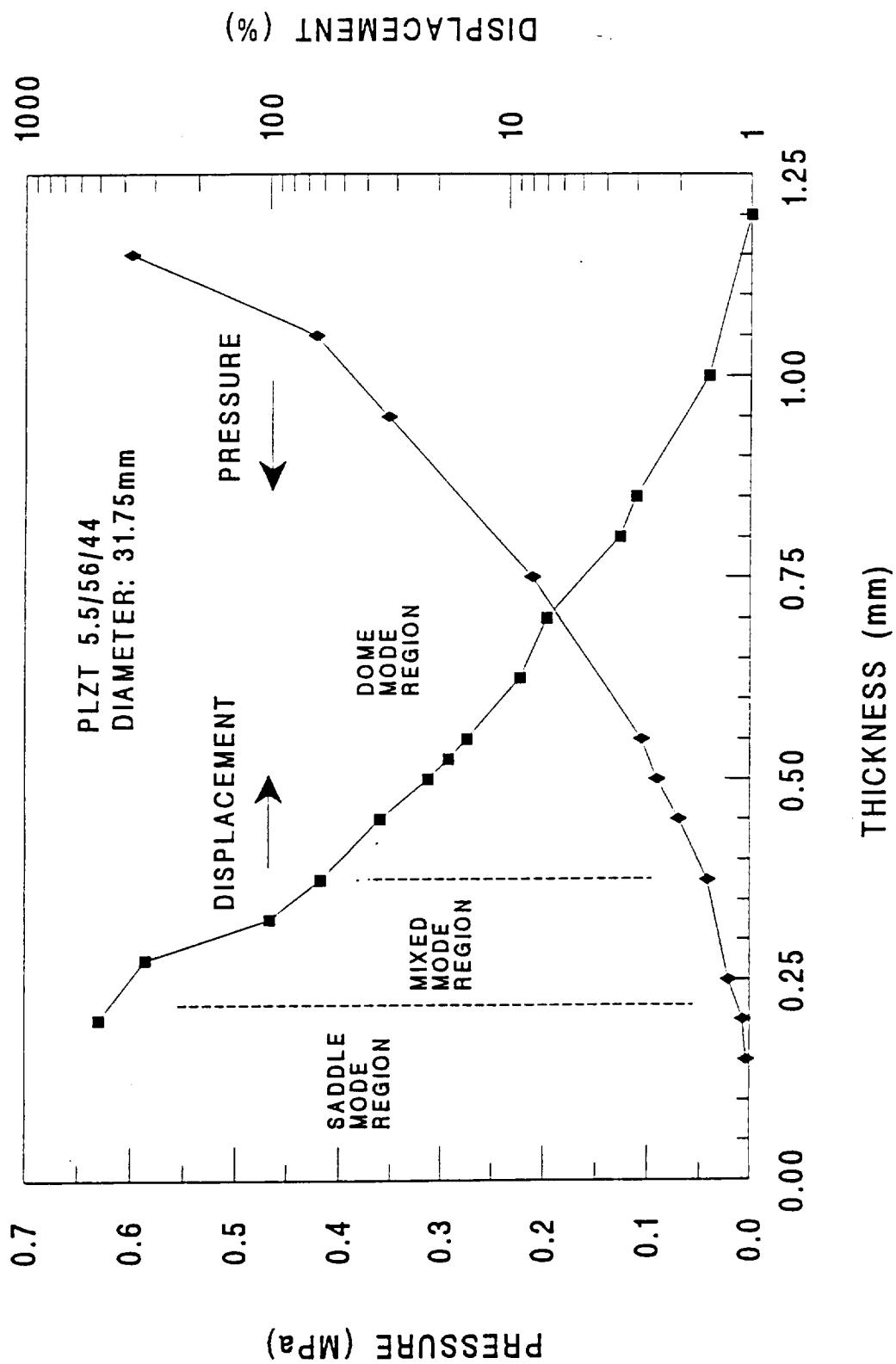
1. A Comparison of Ceramic Actuator Technologies.



2. Experimental Setup for Measuring Displacement of Rainbows (Rainbow wafer shown in cross-section).

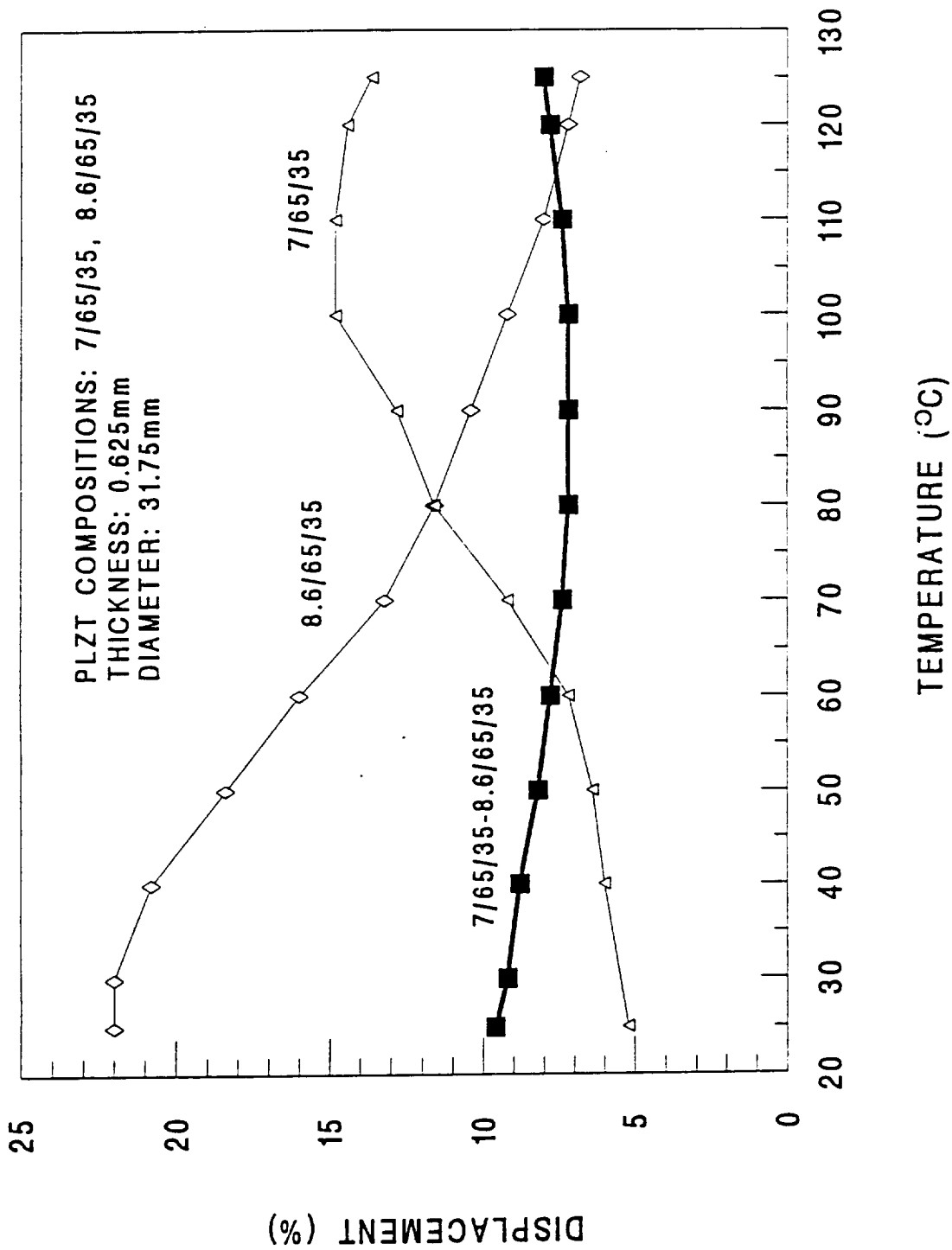


3. Rainbow Actuator Characteristics of Selected PLZT Compositions (open diamonds indicate ac voltage - all others dc, wafer thickness in parentheses).



4. Effect of Wafer Thickness on Pressure and Displacement Behavior of PLZT

Rainbows.



5. Temperature Dependent Displacement Characteristics of Indicated Compositions (open symbols) and for Temperature Compensated Rainbow Clamshell (heavy line).

## Appendix A.

The electromechanical properties of a selected number of PLZT piezoelectric and electrostrictive materials are shown in a number of figures in this section. They are given here without comment or description in the interest of disseminating them as expeditiously as possible. Some figures are replots of data to make them more useful and easy to obtain the desired information. The compositions for most of the work shown in the figures are of the piezoelectric type (typical: 5.5/56/44) and electrostrictive type (typical: 8.6/65/35).

The trade-offs of strain, point load, displacement, thickness and wafer diameter are given in Table 1. Although the values in the table are only approximate (being derived from rule-of-thumb observed relationships), they are considered to be real numbers in that the values presented can be obtained or exceeded in actual devices. As noted in the table notes, the displacements and strains are those achievable with a positive pulse at 450 volts. Less voltage will, of course, produce less displacement and strain; however, higher voltage will produce more. Also, bipolar pulses (or ac) will produce more displacement and strain than indicated in the table; more specifically, approximately twice as much.

A number of proof-of-principle demonstration devices have been constructed. These include piston-type motors, cavity pumps, speakers, laser deflection devices, sensors, hydrophones, relay switches, fans and multifunction devices. All of these are in various stages of testing. In addition, life testing was carried out on one 1.25 inch diameter, 20 mil thick Rainbow piezoelectric wafer at 500 Hz. After 8 weeks of continuous operation consisting of  $2.4 \times 10^9$  cycles at 350 volts (bipolar), there was no noticeable change in the amount of displacement (strain) at the given voltage. More work will be done in the future on device development, testing and evaluation. Present work is focusing on a cavity pump for space applications (cryogen pump) which necessitates the characterization of the Rainbow devices at 77K and an evaluation of their suitability for long term operation at these low temperatures.

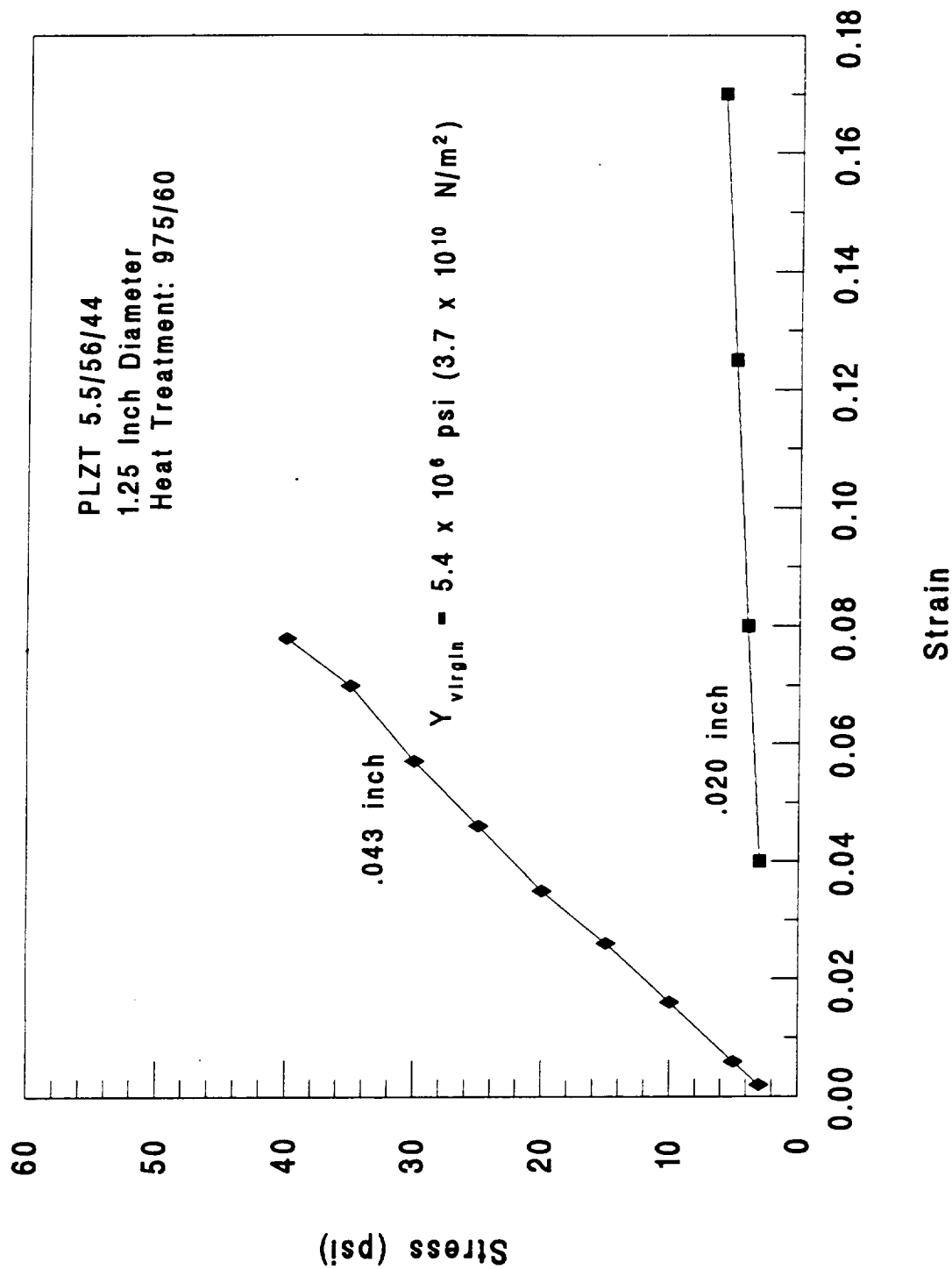


Figure 4. Elastic Modulus Characteristics of PLZT 5.5/56/44 Rainbow Wafers at Indicated Thicknesses

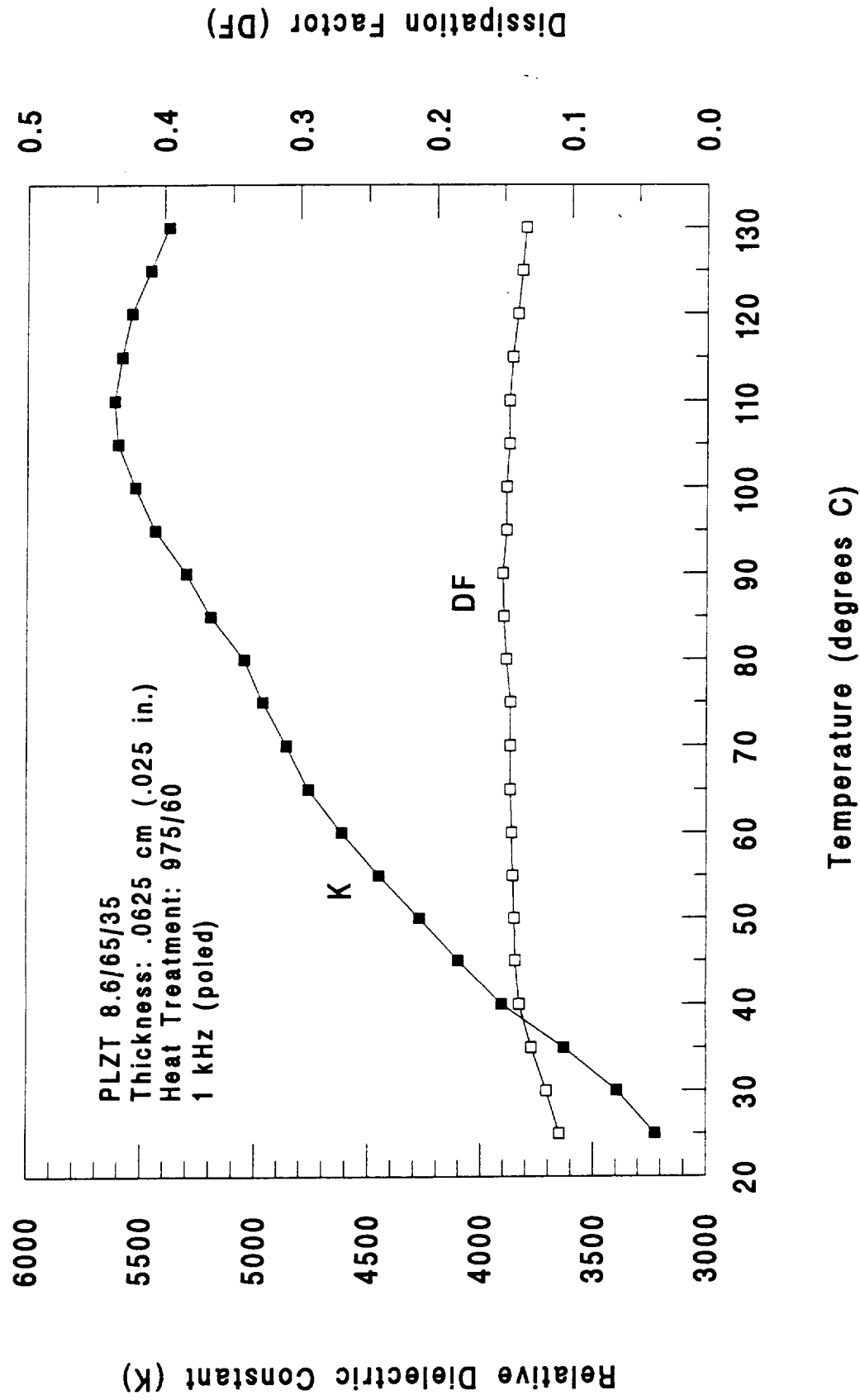


Figure 5. Effect of Temperature on the Dielectric Properties of PLZT 8.6/65/35 Rainbow Wafer



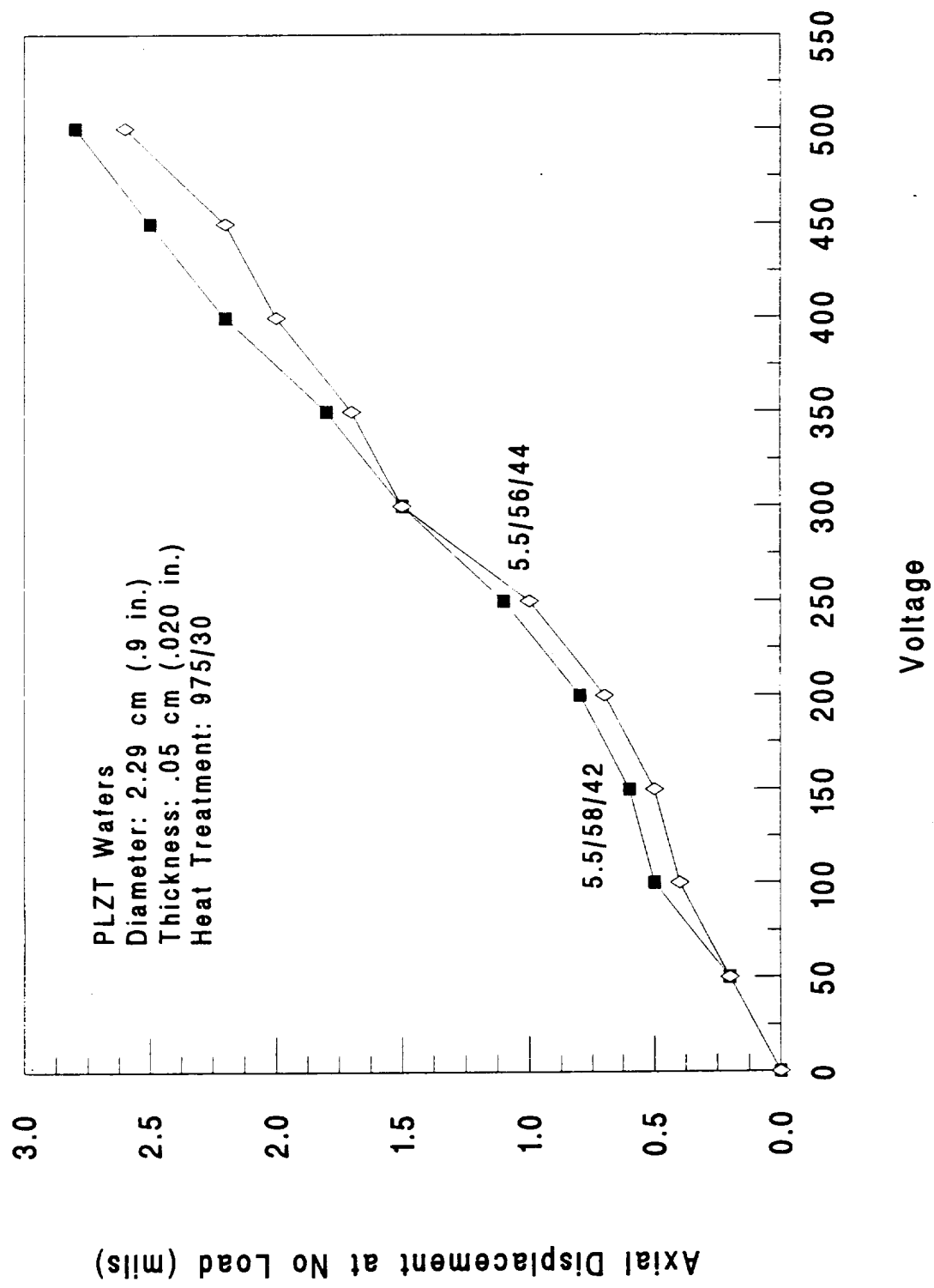


Figure 6. Voltage Dependent Axial Displacement Characteristics of PLZT 5.5/58/42 and 5.5/56/44 Rainbow Wafers

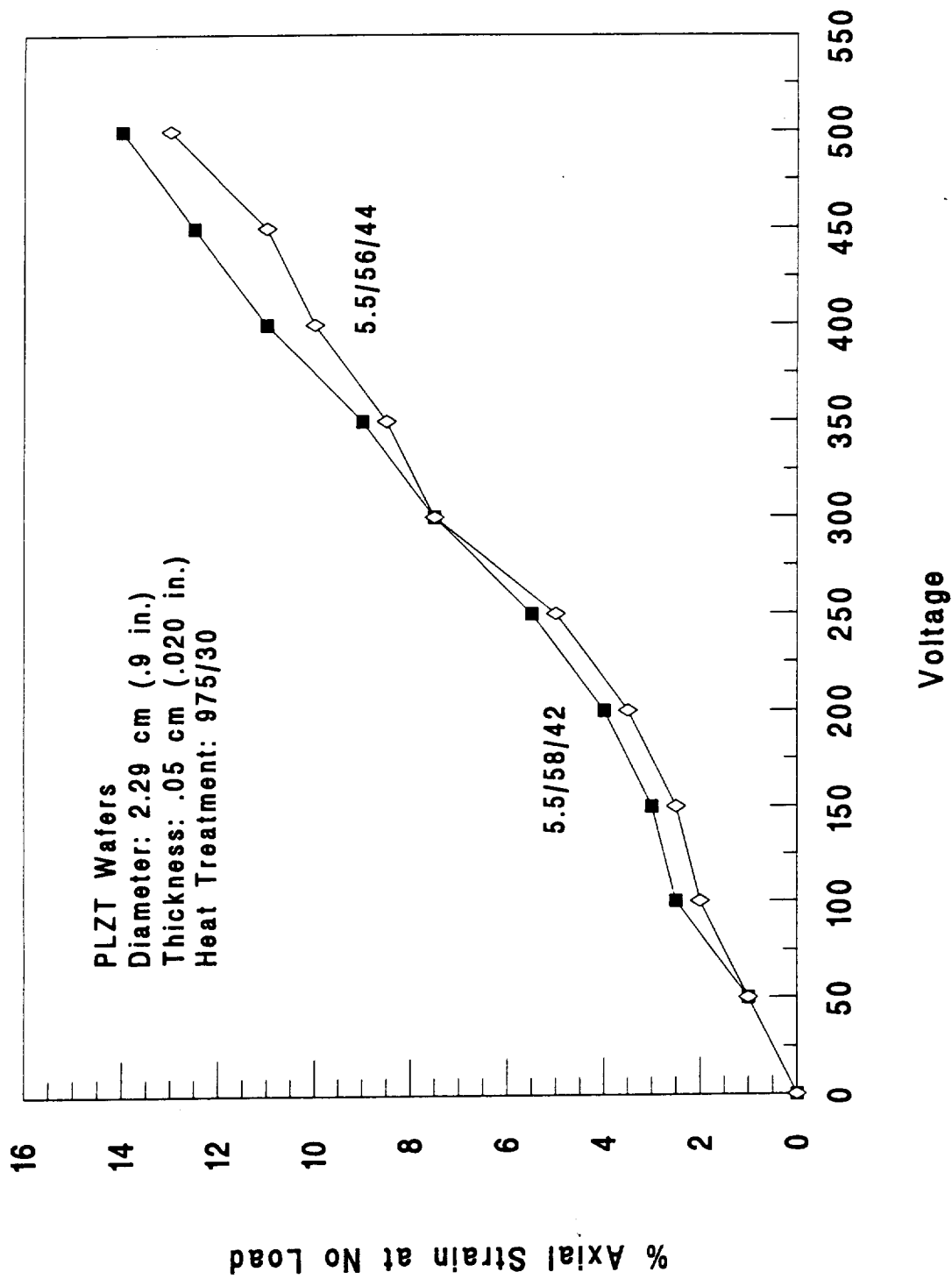


Figure 7. Voltage Dependent Axial Strain Characteristics of PLZT 5.5/58/42 and 5.5/56/44 Rainbow Wafers

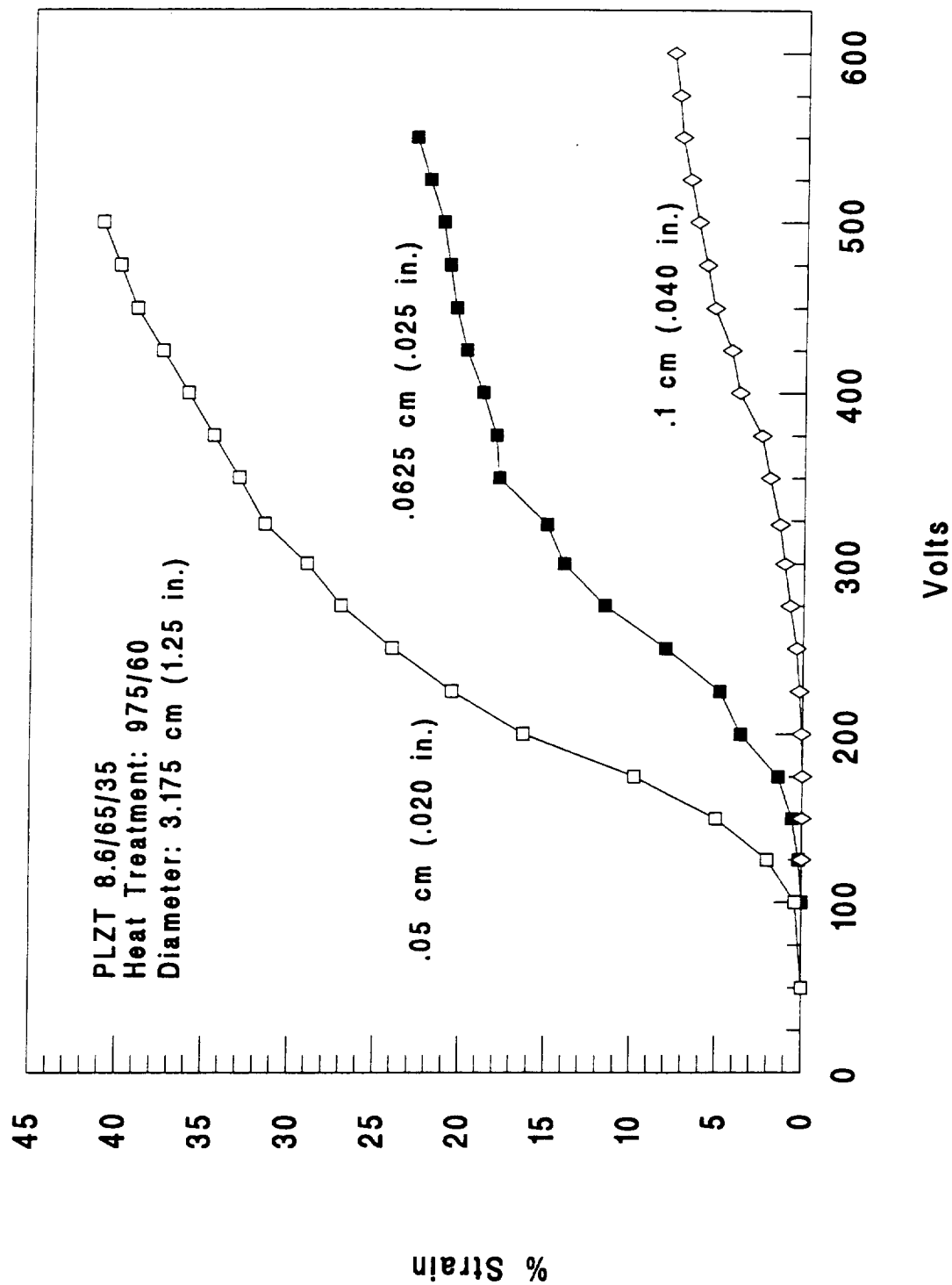


Figure 8. Voltage Dependent Strain Characteristics of PLZT 8.6/65/35 Rainbow Wafers

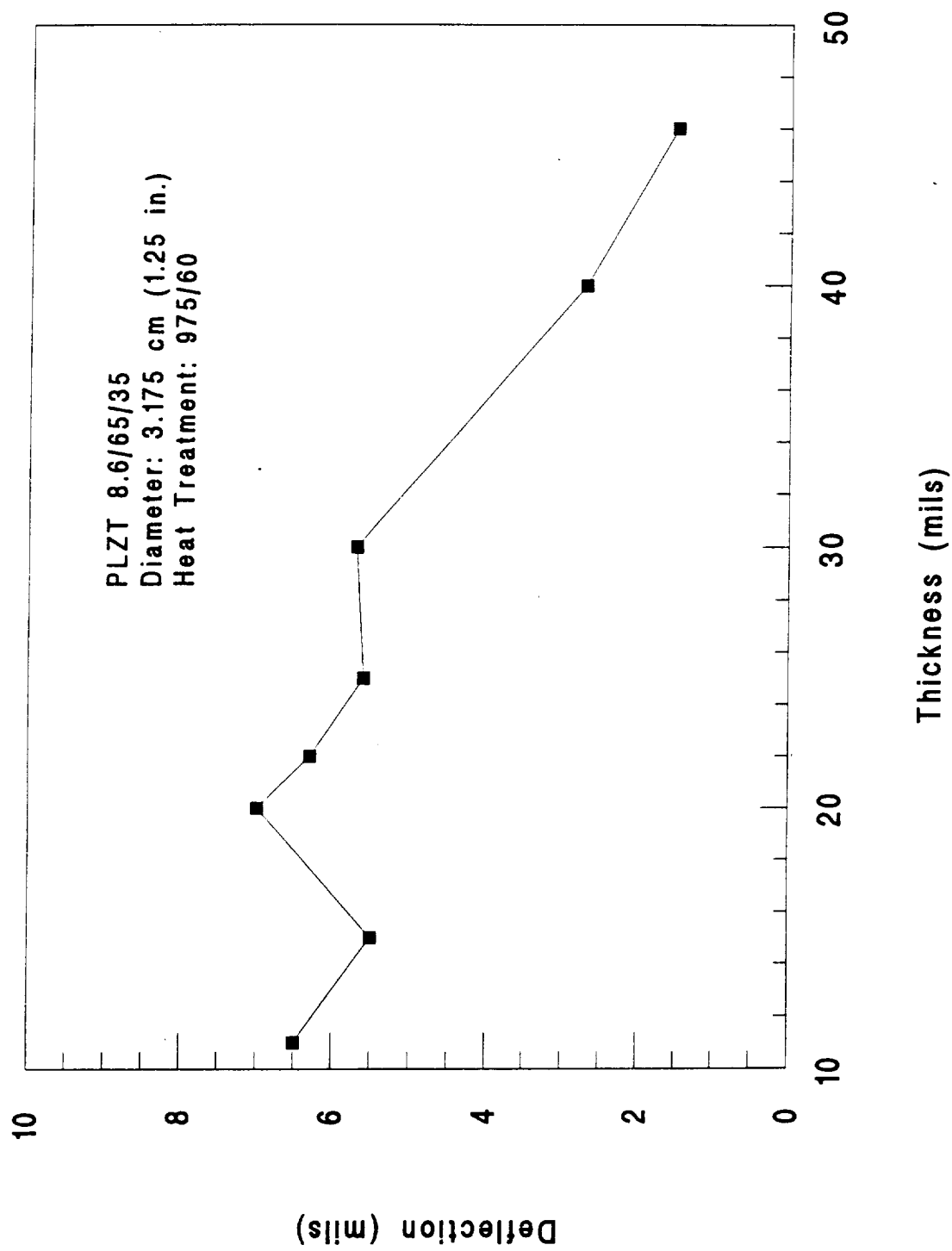


Figure 9. Effect of Thickness on Total Deflection of PLZT 8.6/65/35 Rainbow Wafer

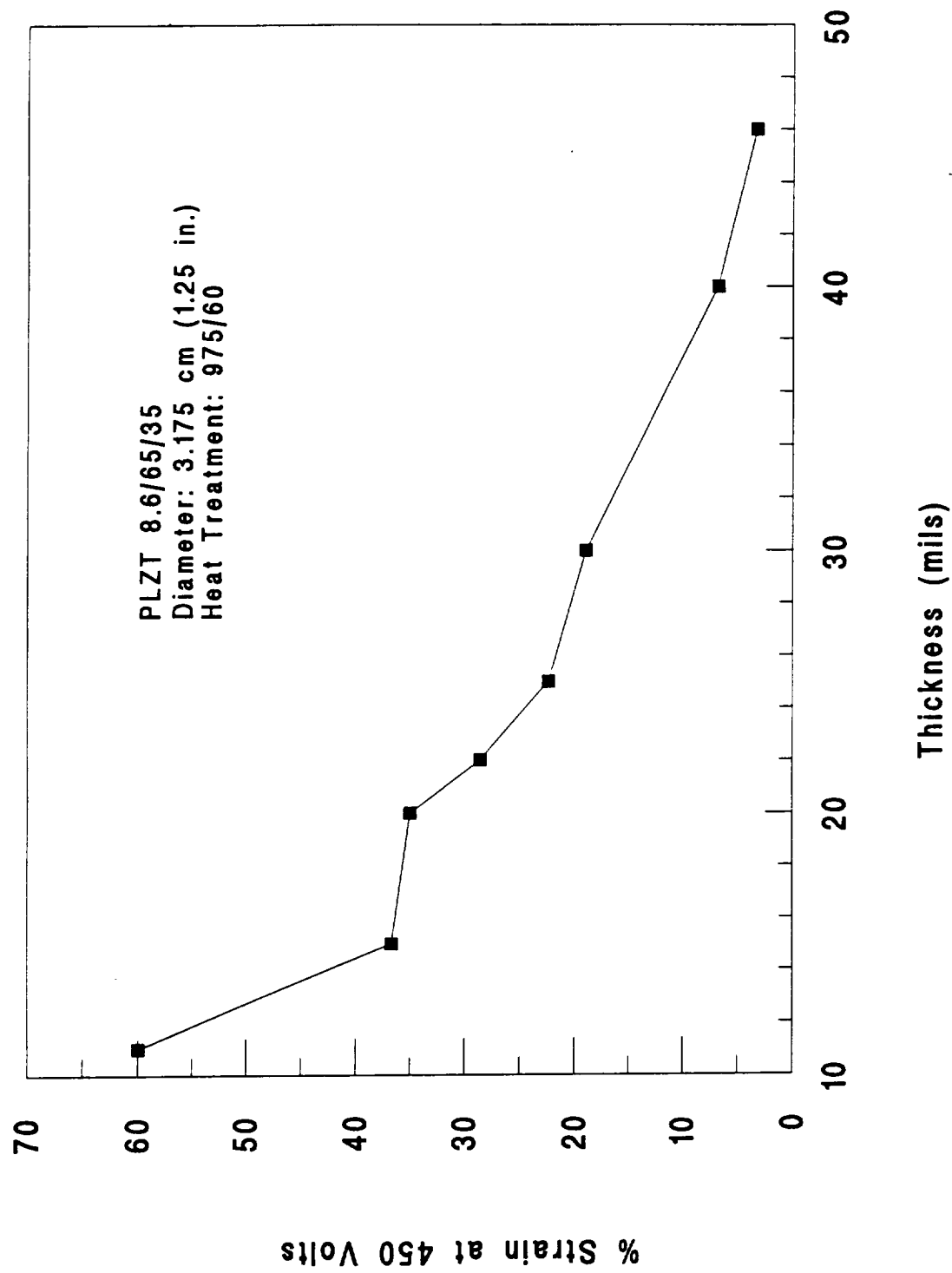


Figure 10. Effect of Thickness on Strain Characteristics of PLZT 8.6/65/35 Rainbow Wafers

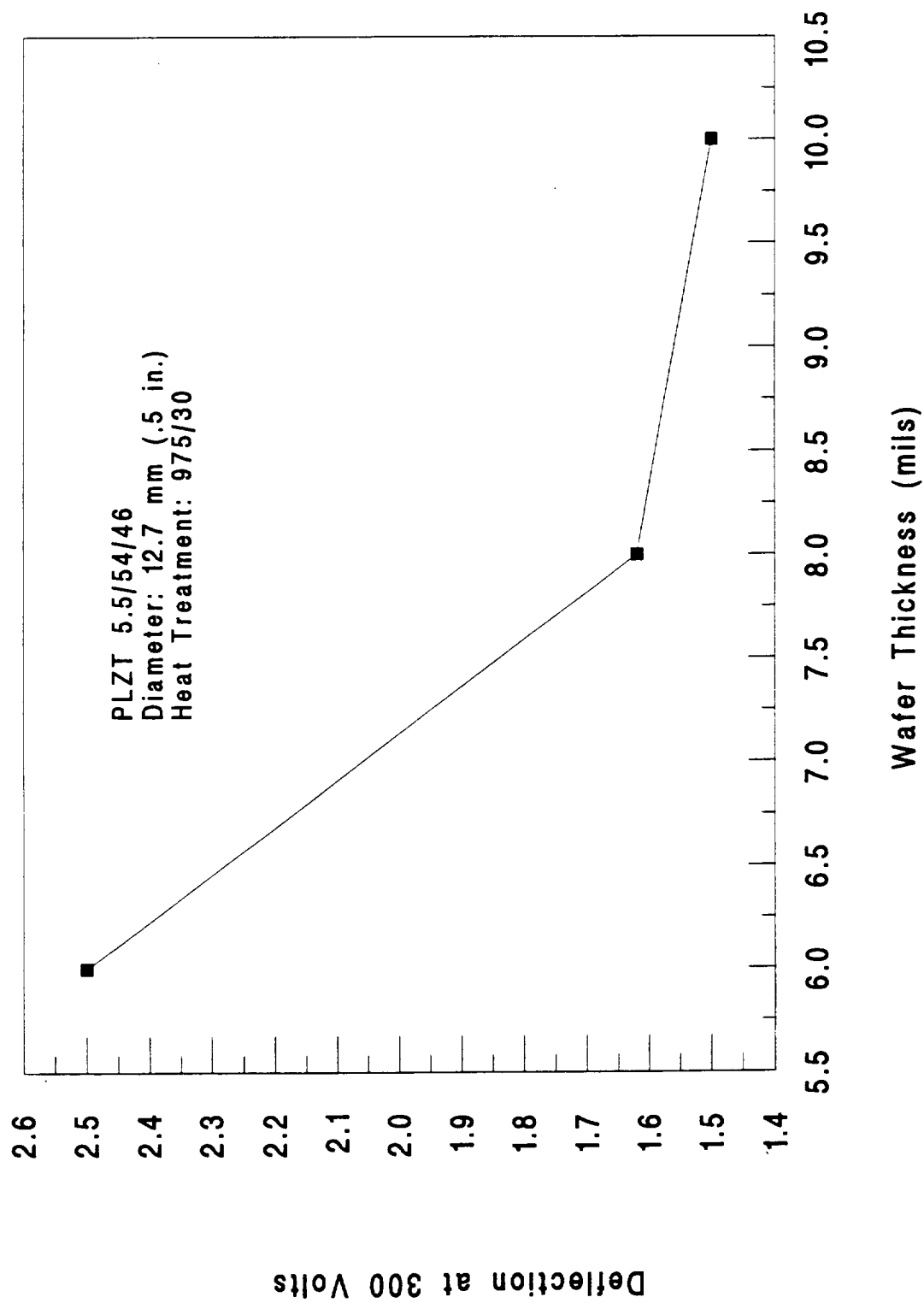


Figure 11. Deflection of PLZT Rainbow Wafers as a Function of Wafer Thickness

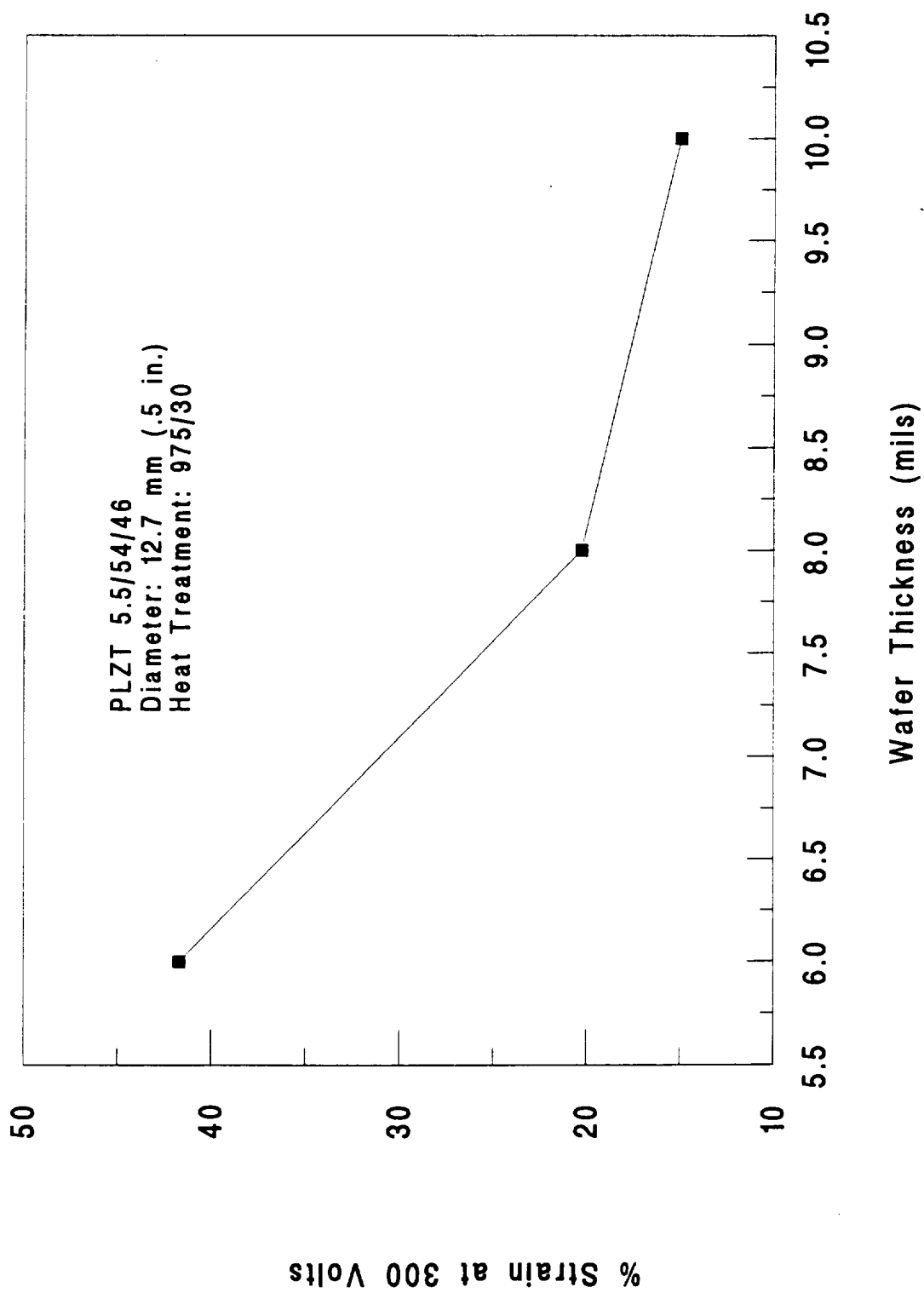


Figure 12. Strain Characteristics of PLZT Rainbow Wafers as a Function of Thickness

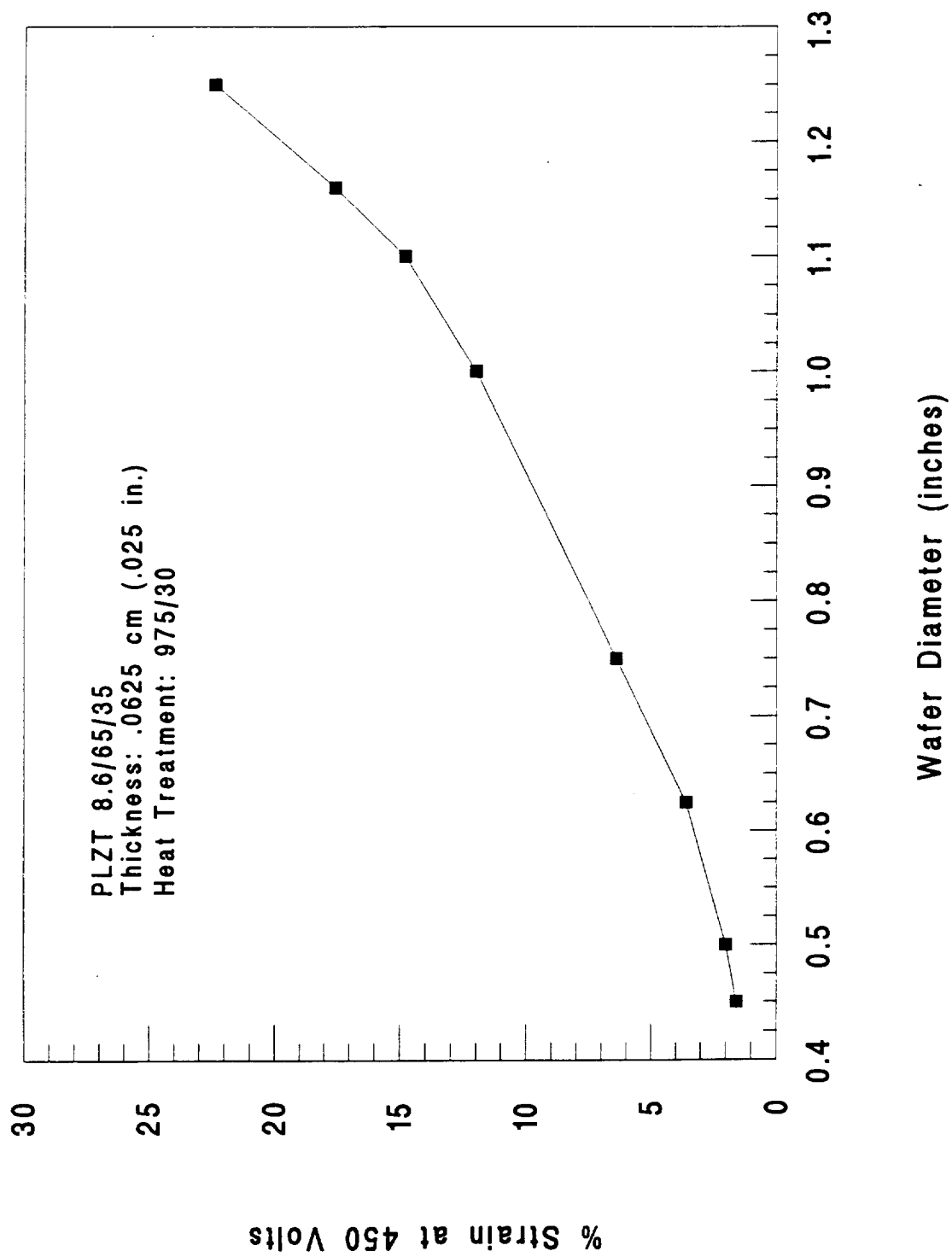


Figure 13. Strain Characteristics of PLZT Rainbow Wafers as a Function of Wafer Diameter



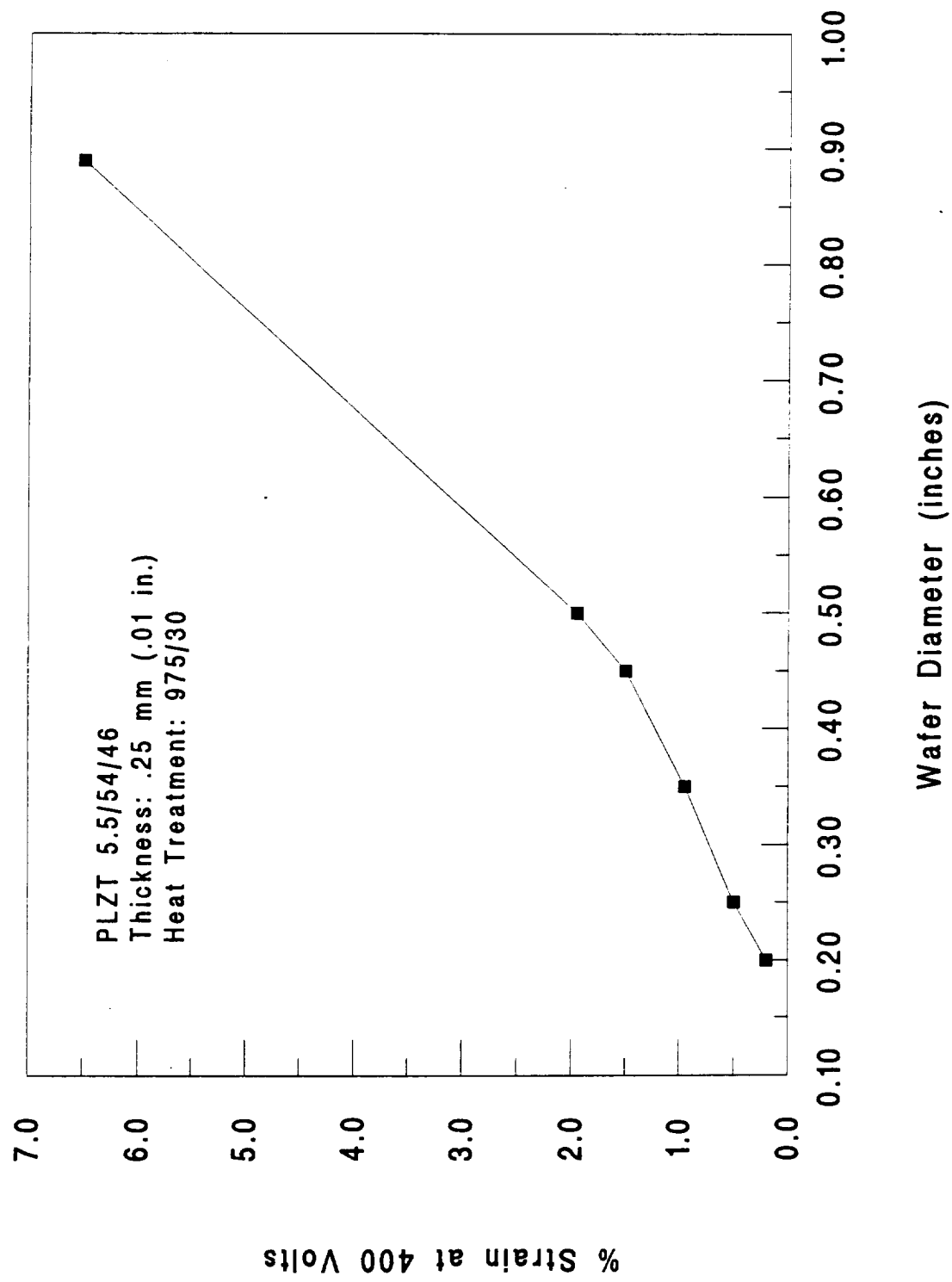


Figure 14. Strain Characteristics of PLZT Rainbow Wafers as a Function of Diameter

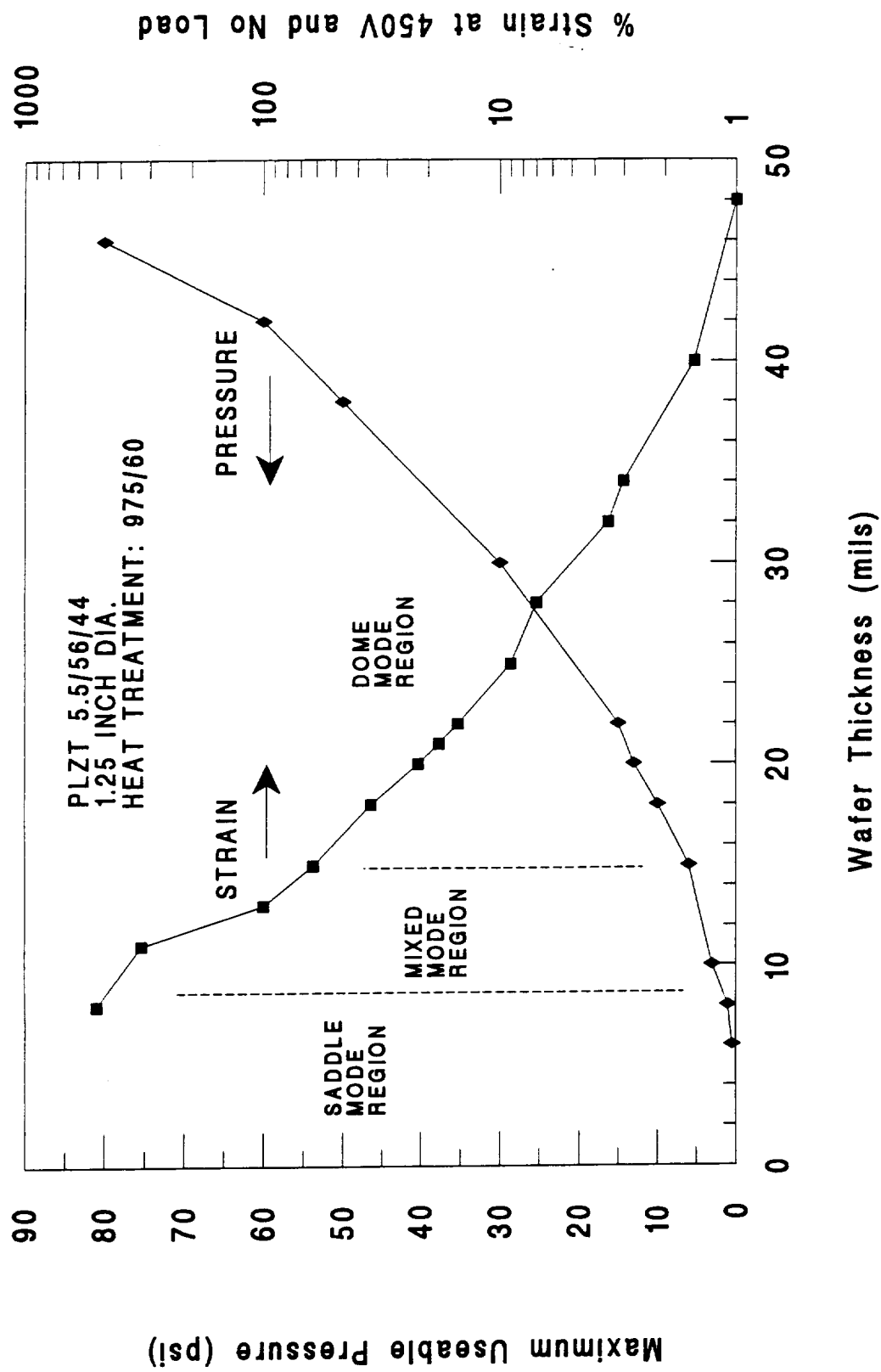


Figure 15. Pressure and Strain Characteristics of PLZT Rainbow Wafers

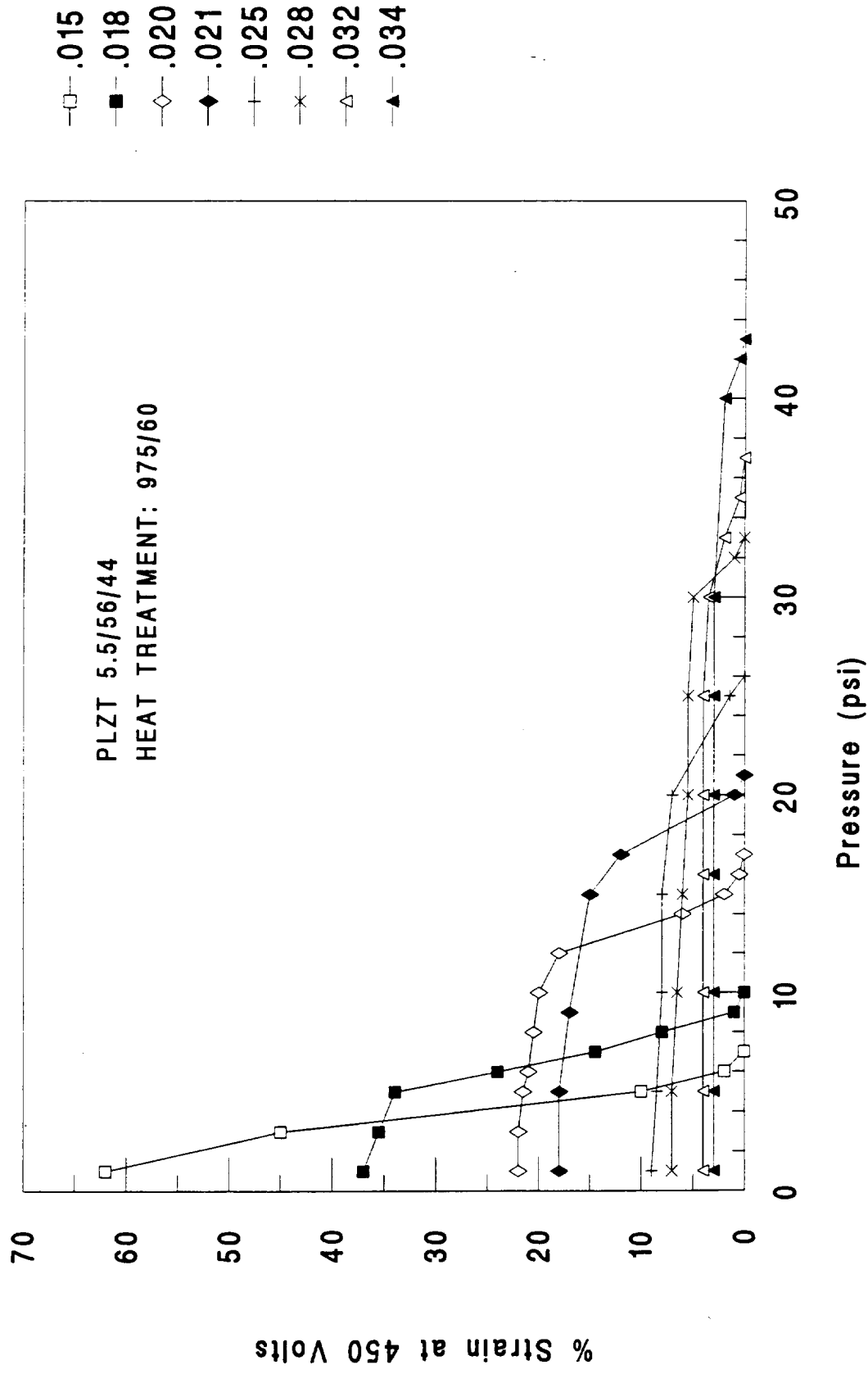


Figure 16. Effect of Pressure on Strain in PLZT Wafers of Varying Thickness

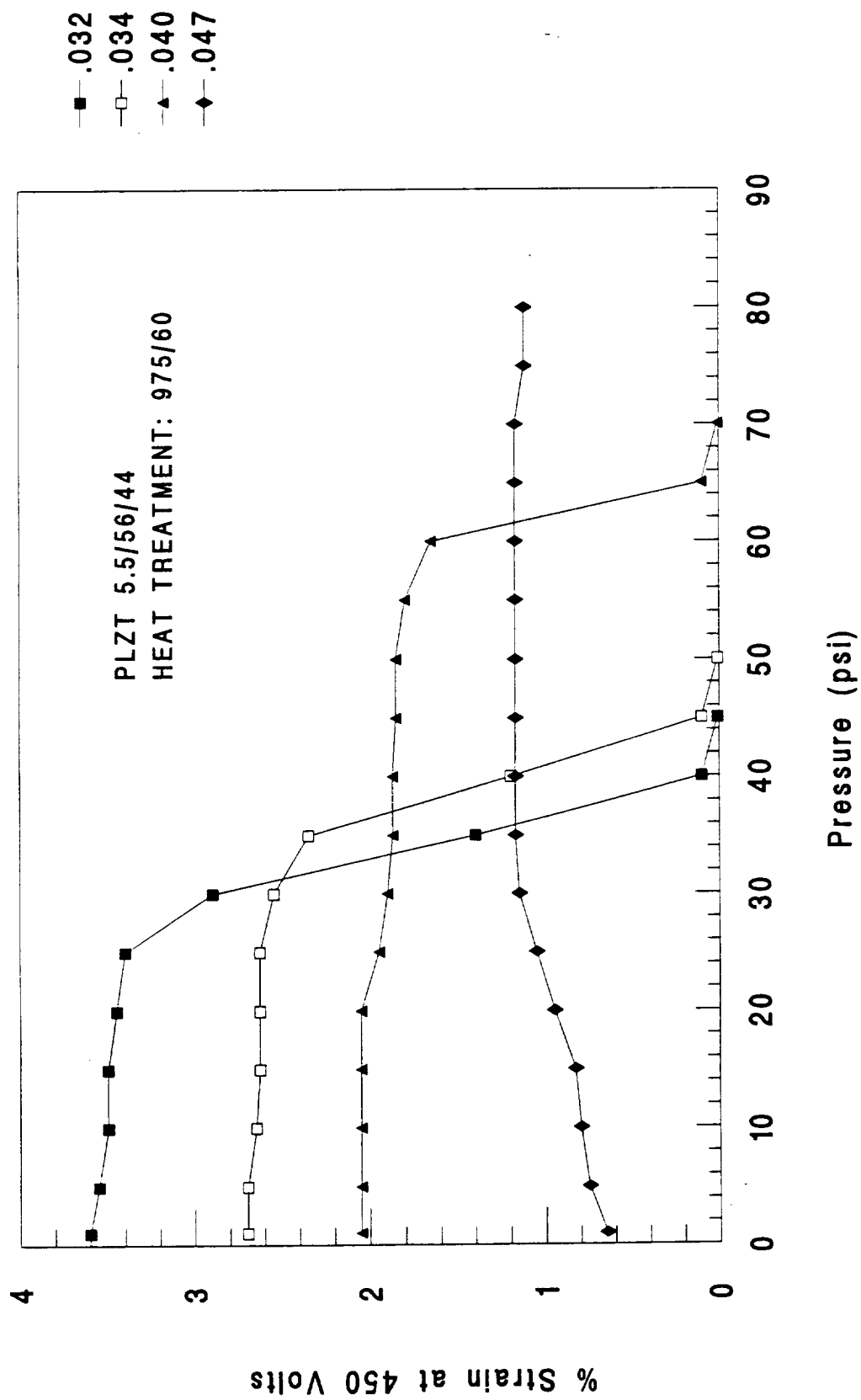


Figure 17. Effect of Pressure on Strain in PLZT Wafers of Varying Thickness

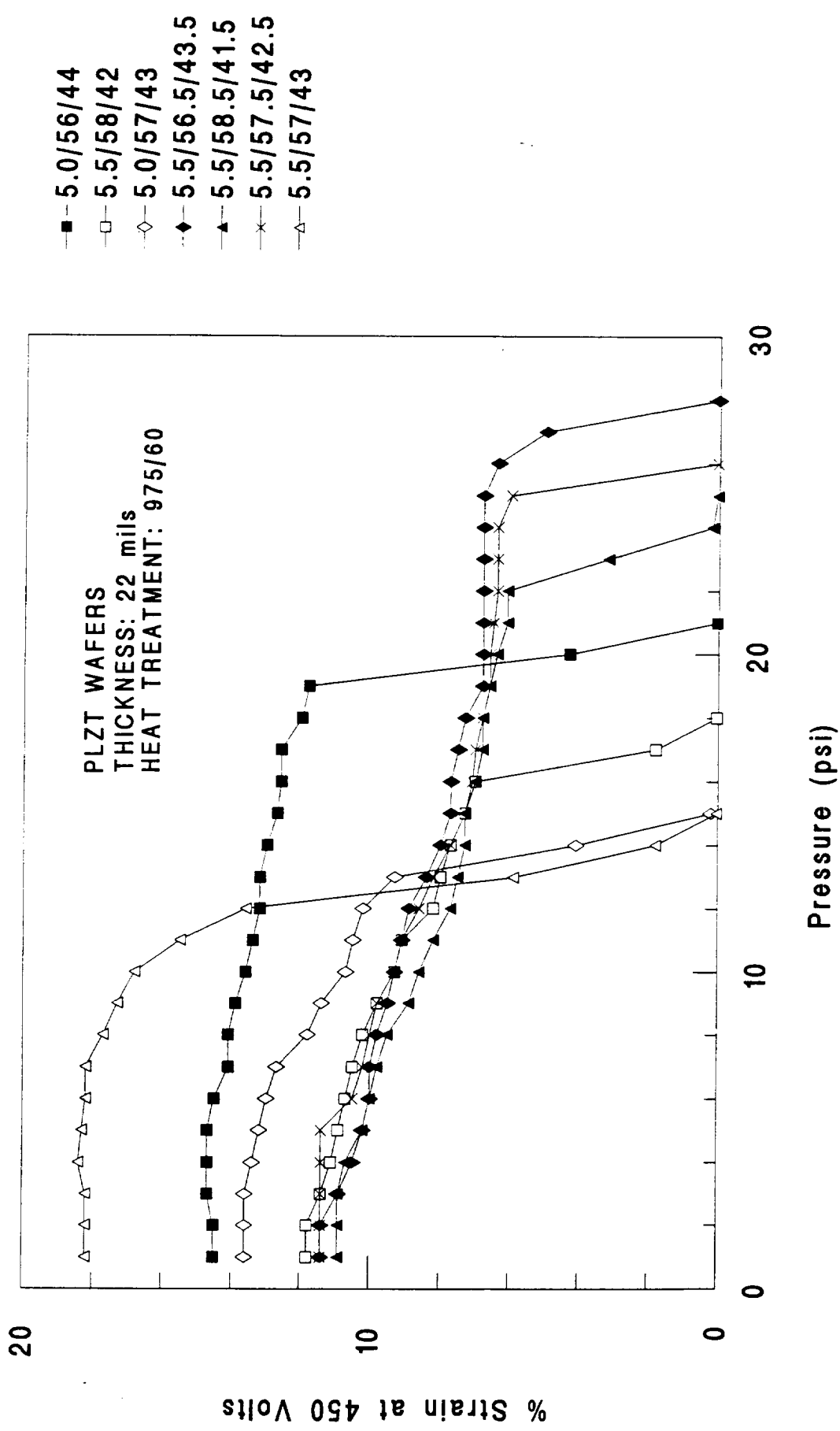


Figure 18. Effect of Pressure on Strain in the PLZT Rainbow Wafers

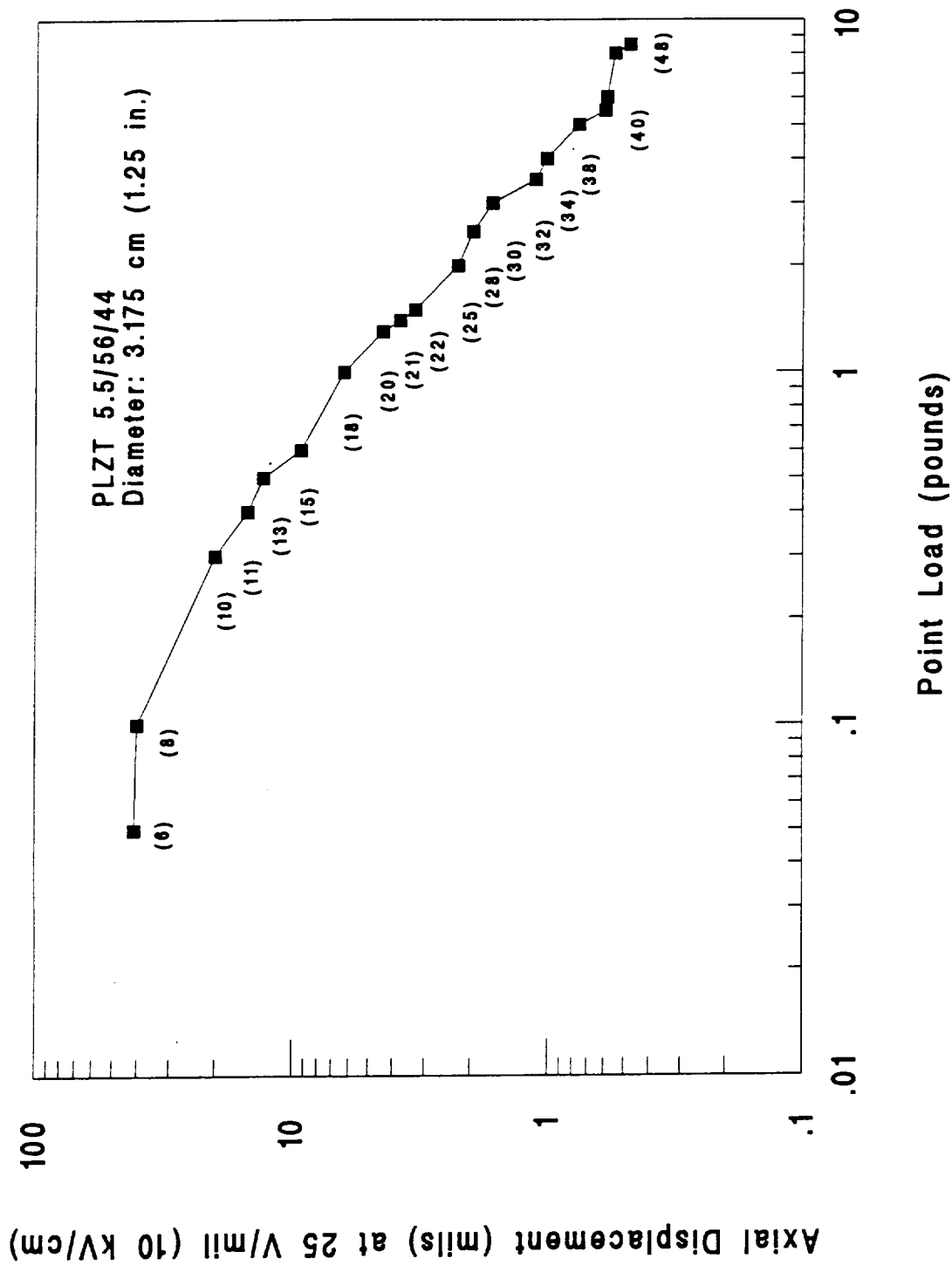


Figure 19. The Trade-Off of Displacement vs. Load for PLZT Rainbow Wafers of Varying Thicknesses (in parentheses)

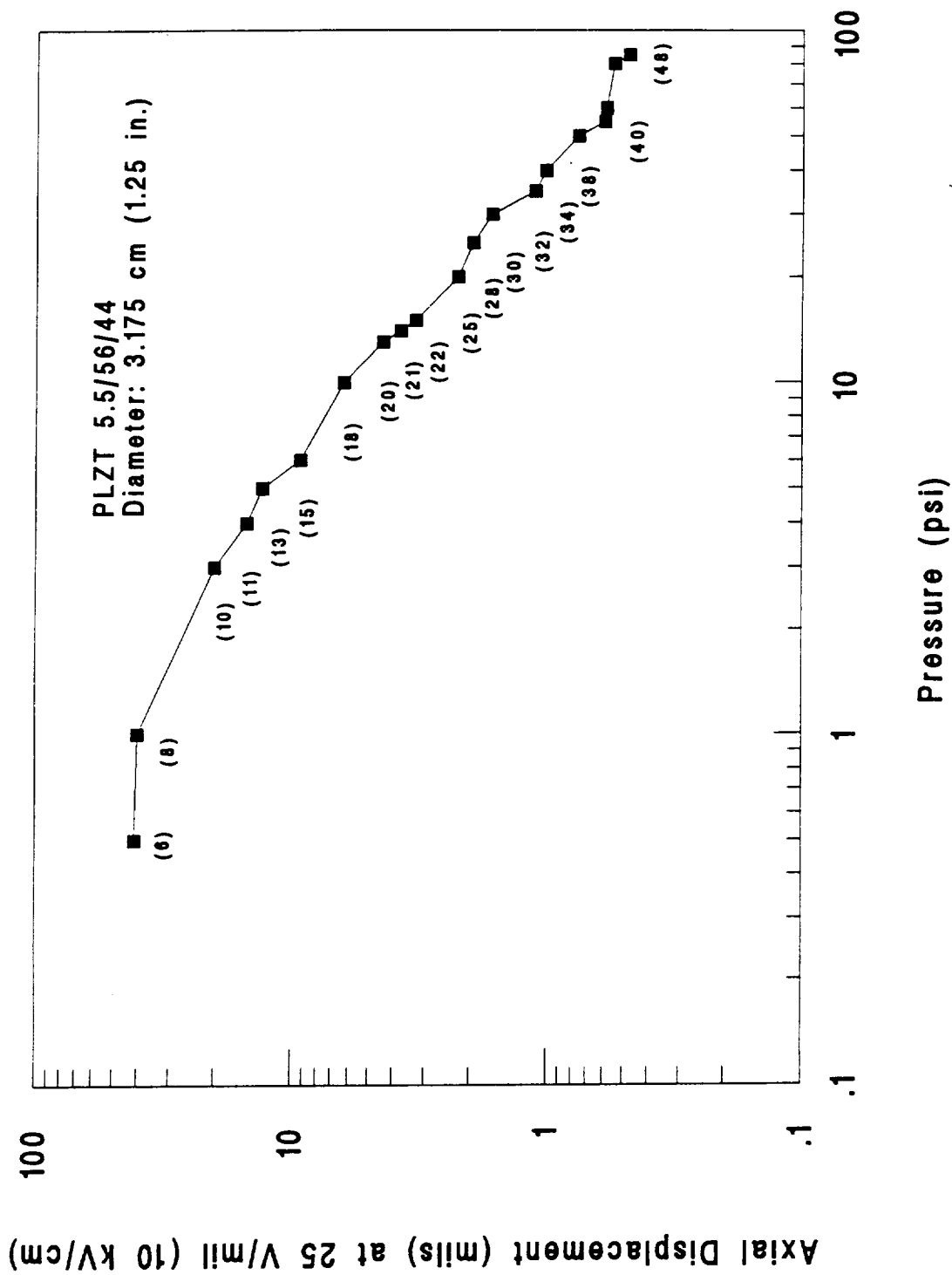


Figure 20. The Trade-Off of Displacement vs. Pressure for PLZT Rainbow Wafers of Varying Thicknesses (in parentheses)

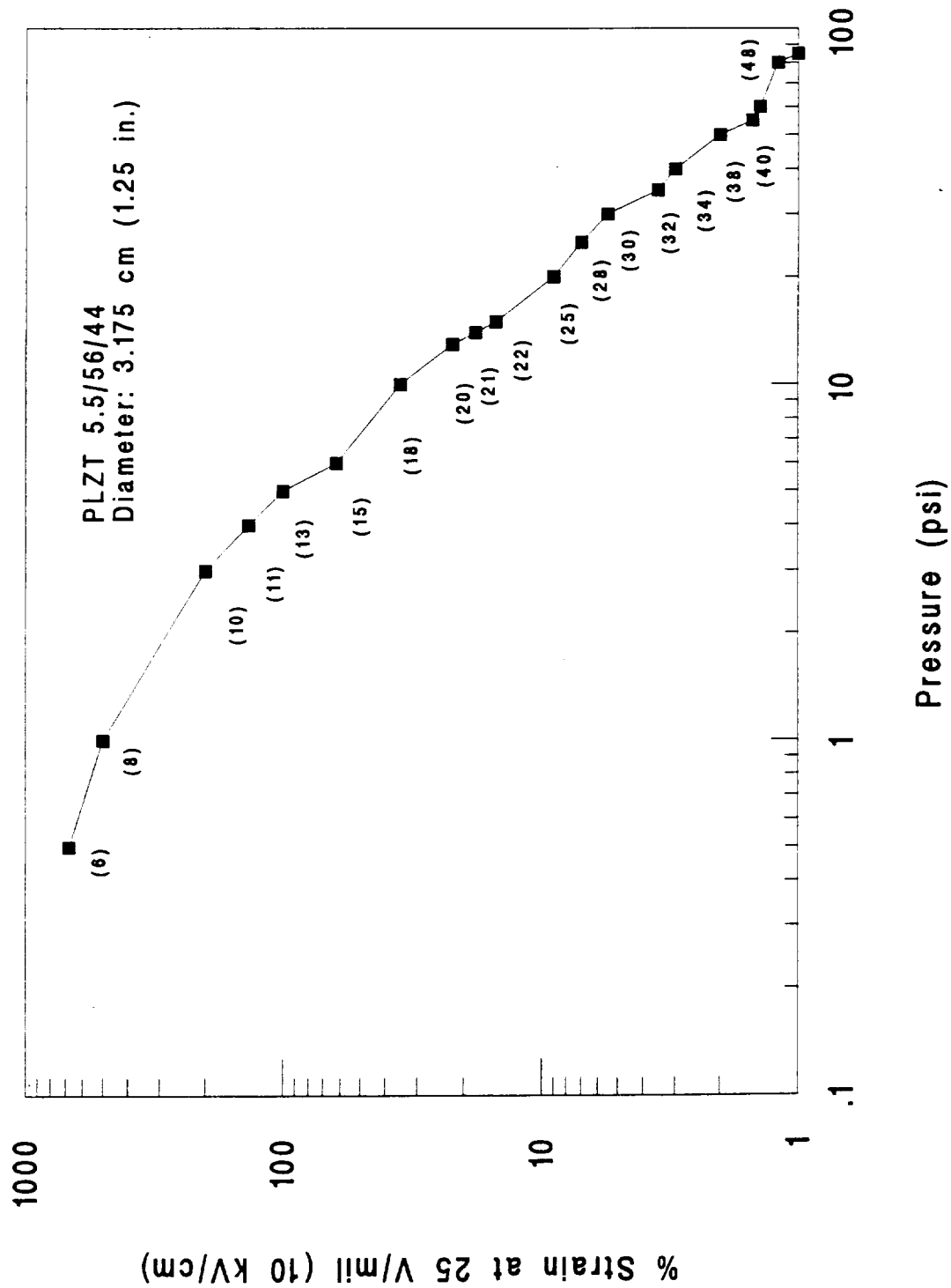


Figure 21. The Trade-Off of Strain vs. Pressure for PLZT Rainbow Wafers of Varying Thicknesses (in parentheses)



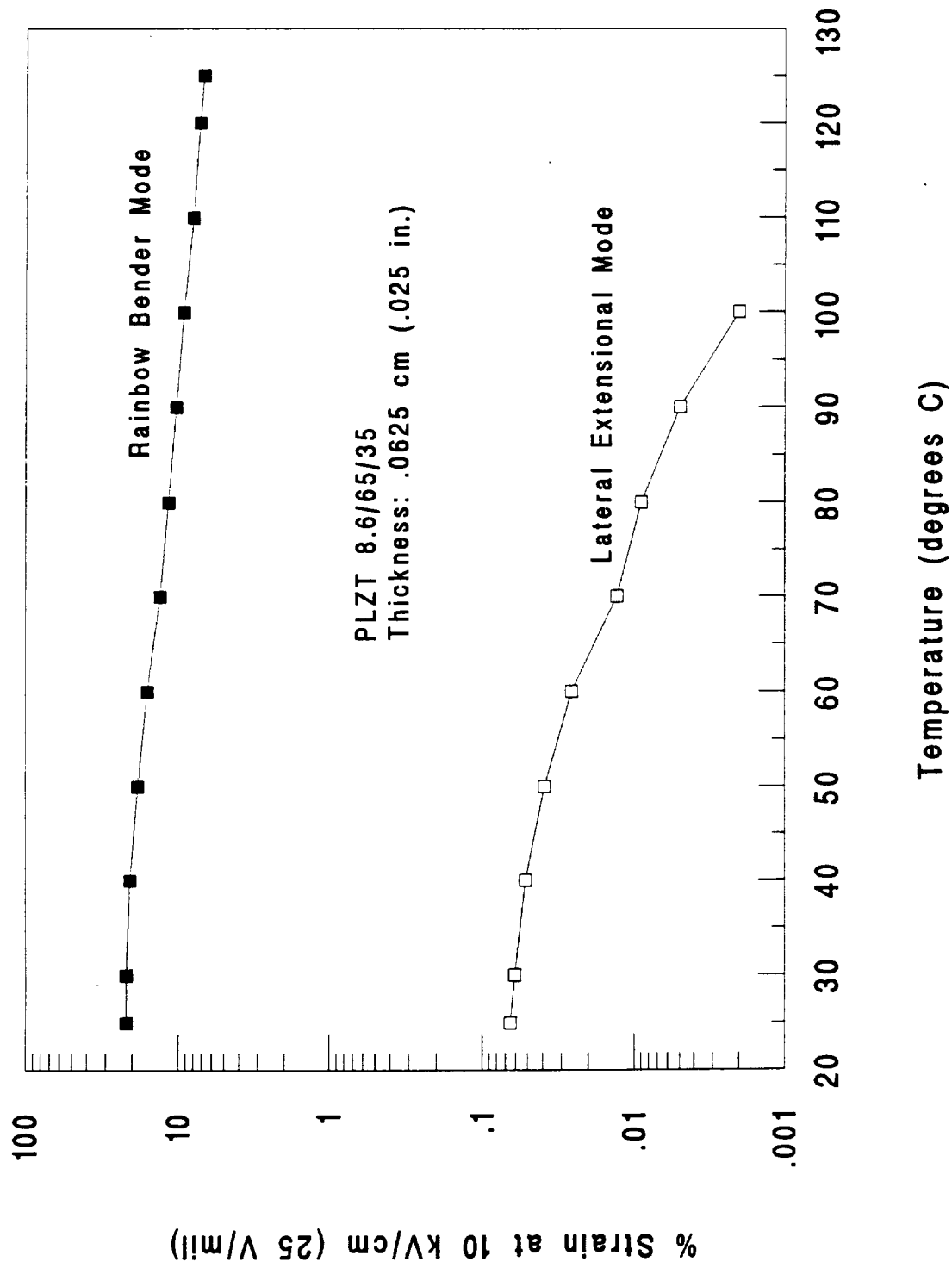


Figure 22. Temperature Dependence of Electrostrictive Lateral and Rainbow Strains in PLZT 8.6/65/35 Ceramics

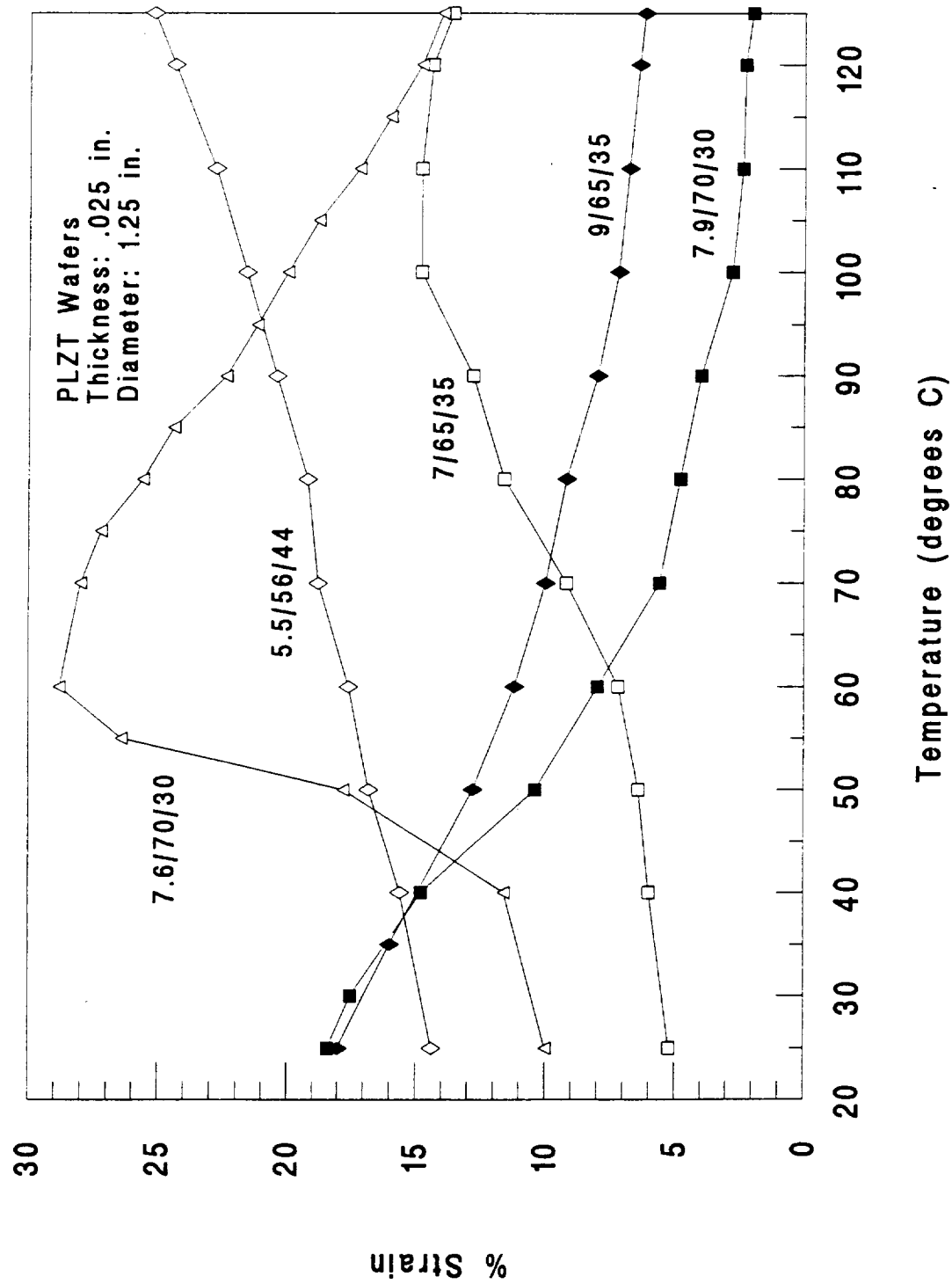


Figure 23. Temperature Dependent Strain Characteristics of PLZT Rainbow Wafers

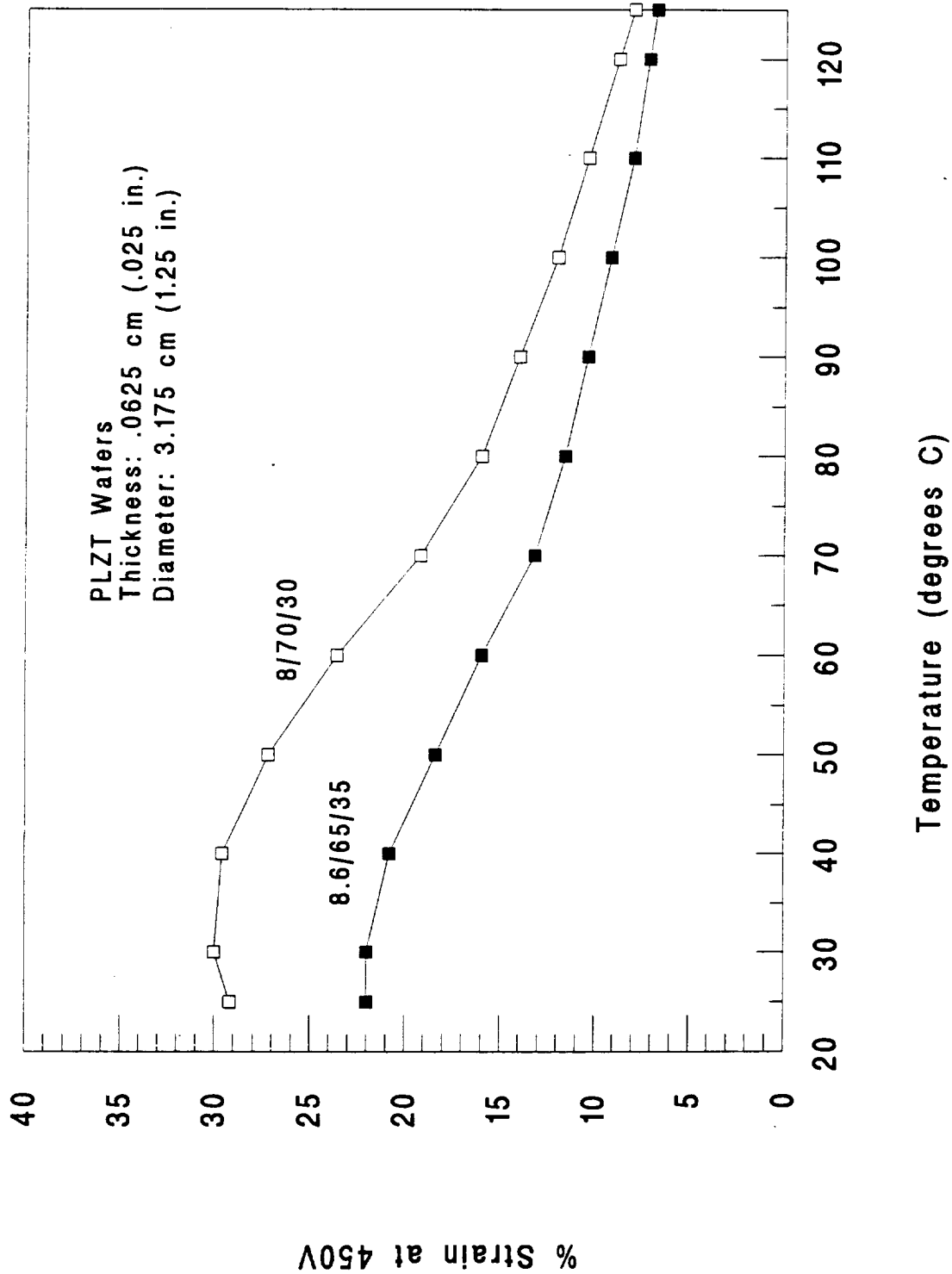


Figure 24. Strain Characteristics of Temperature Compensated PLZT Rainbow Wafers

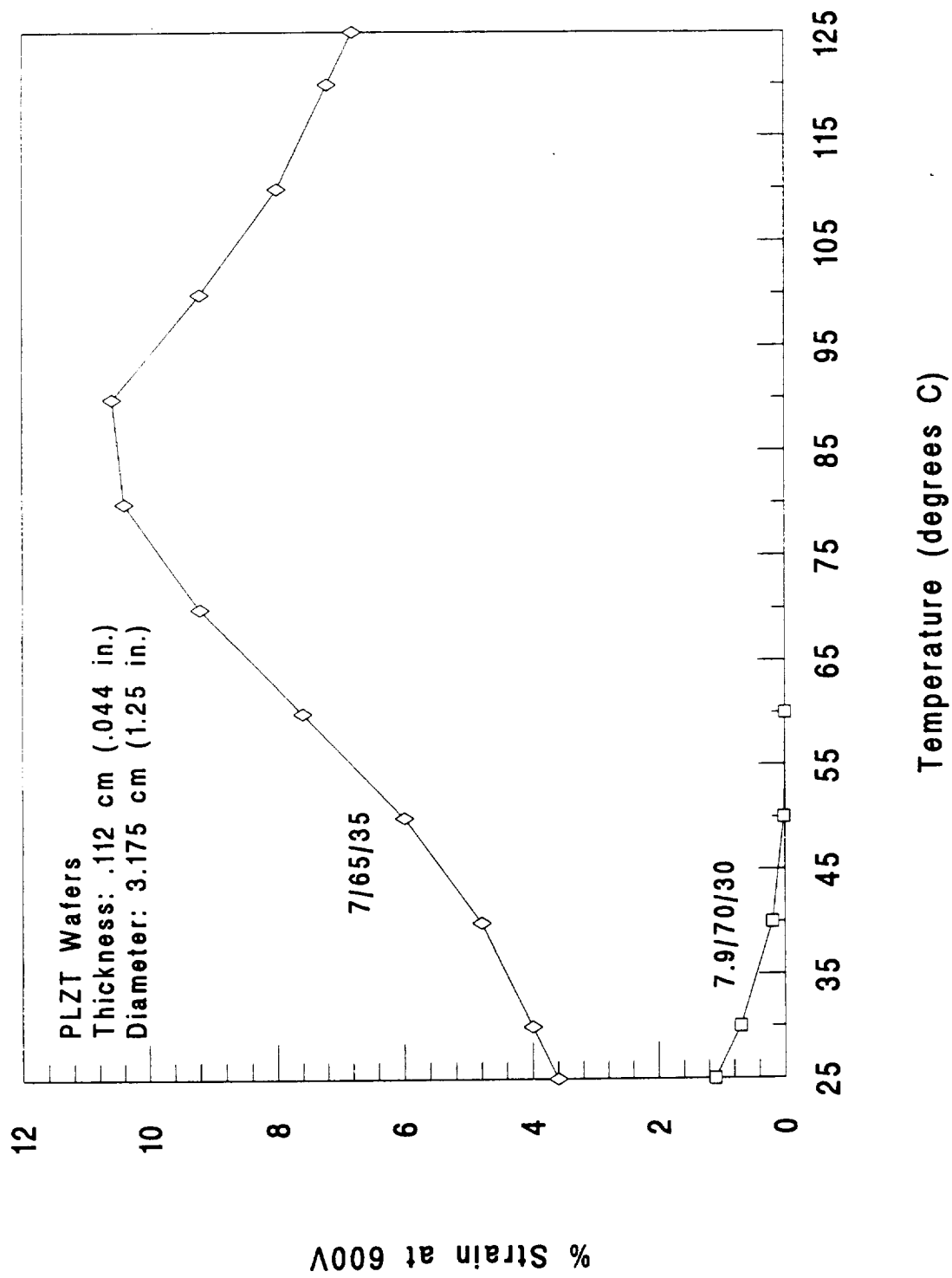


Figure 25. Strain Characteristics of Temperature Compensated PLZt Rainbow Wafers

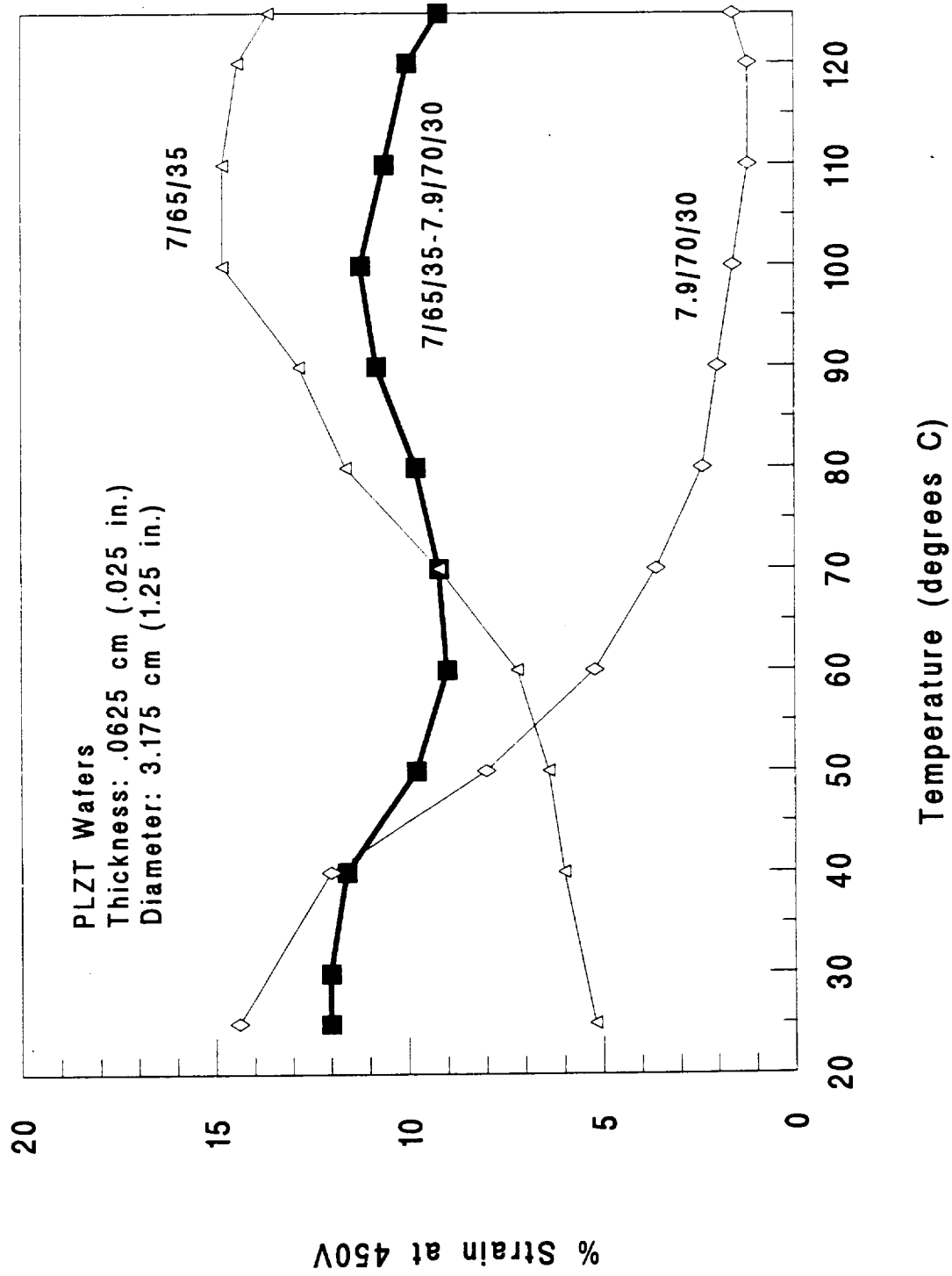


Figure 26. Strain Characteristics of Temperature Compensated PLZT Rainbow Wafers

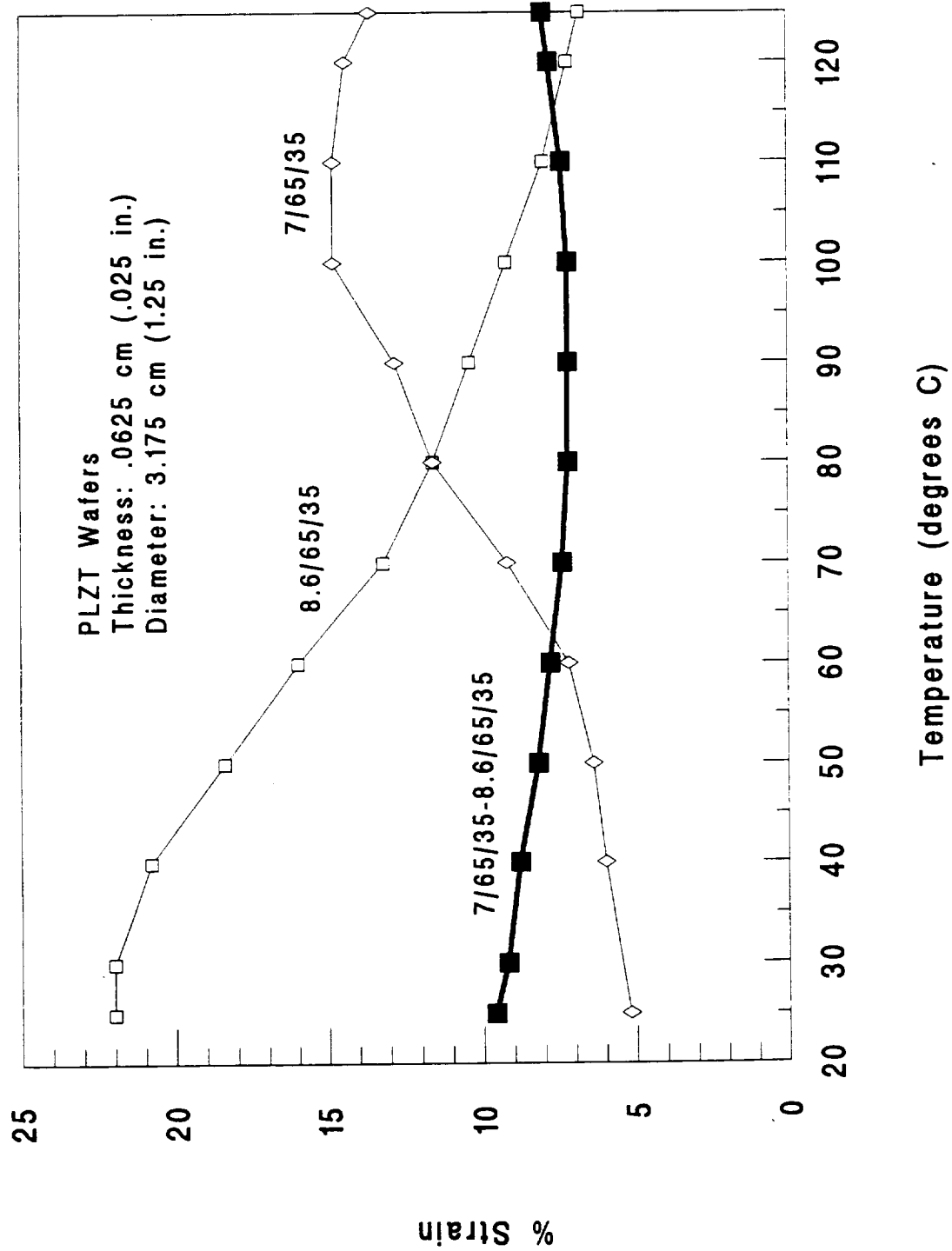


Figure 27. Strain Characteristics of Temperature Compensated PLZT Rainbow Wafers

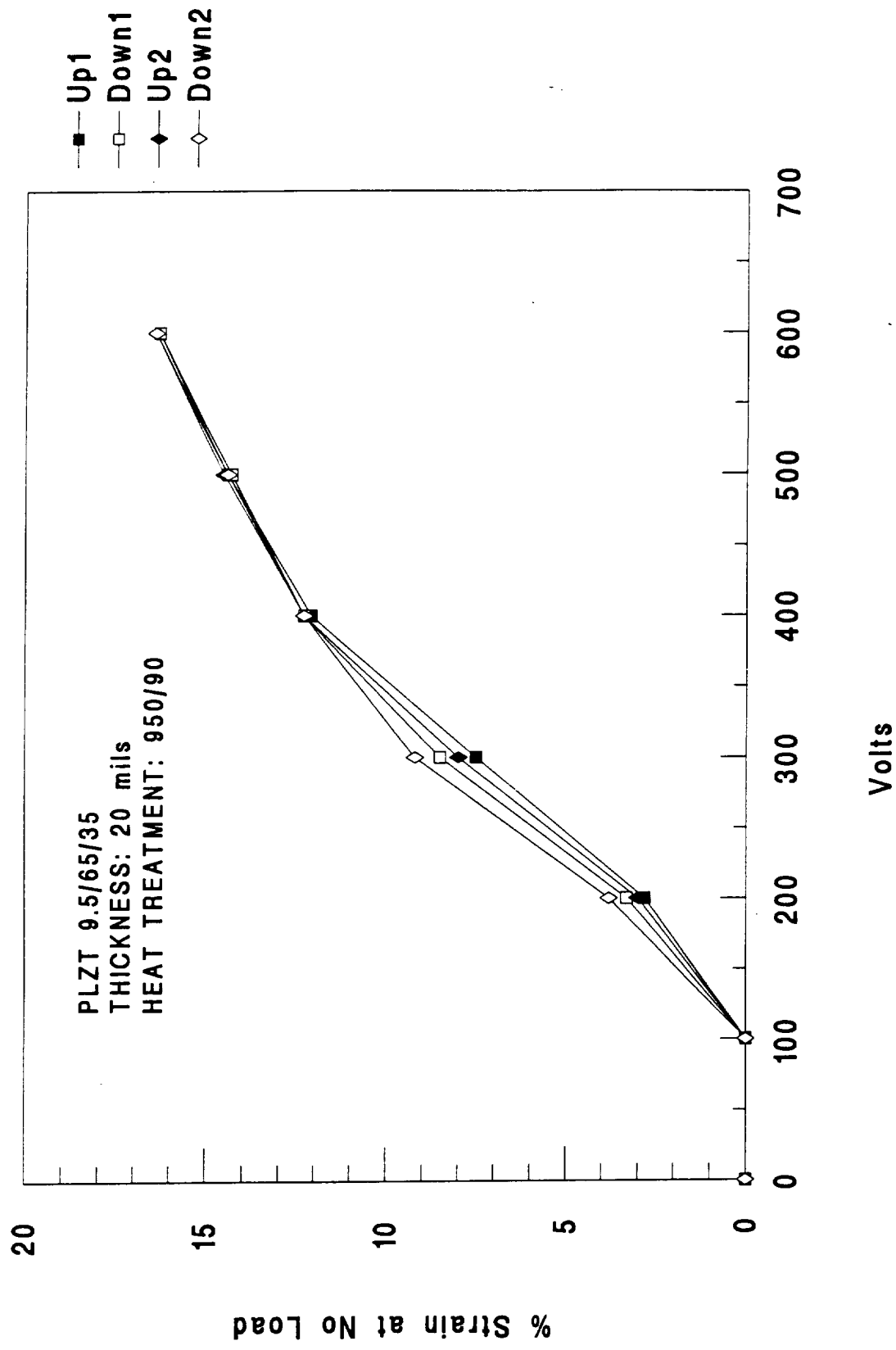


Figure 28. Voltage Dependent Strain and Hysteresis Characteristics of PLZT Rainbow Wafers

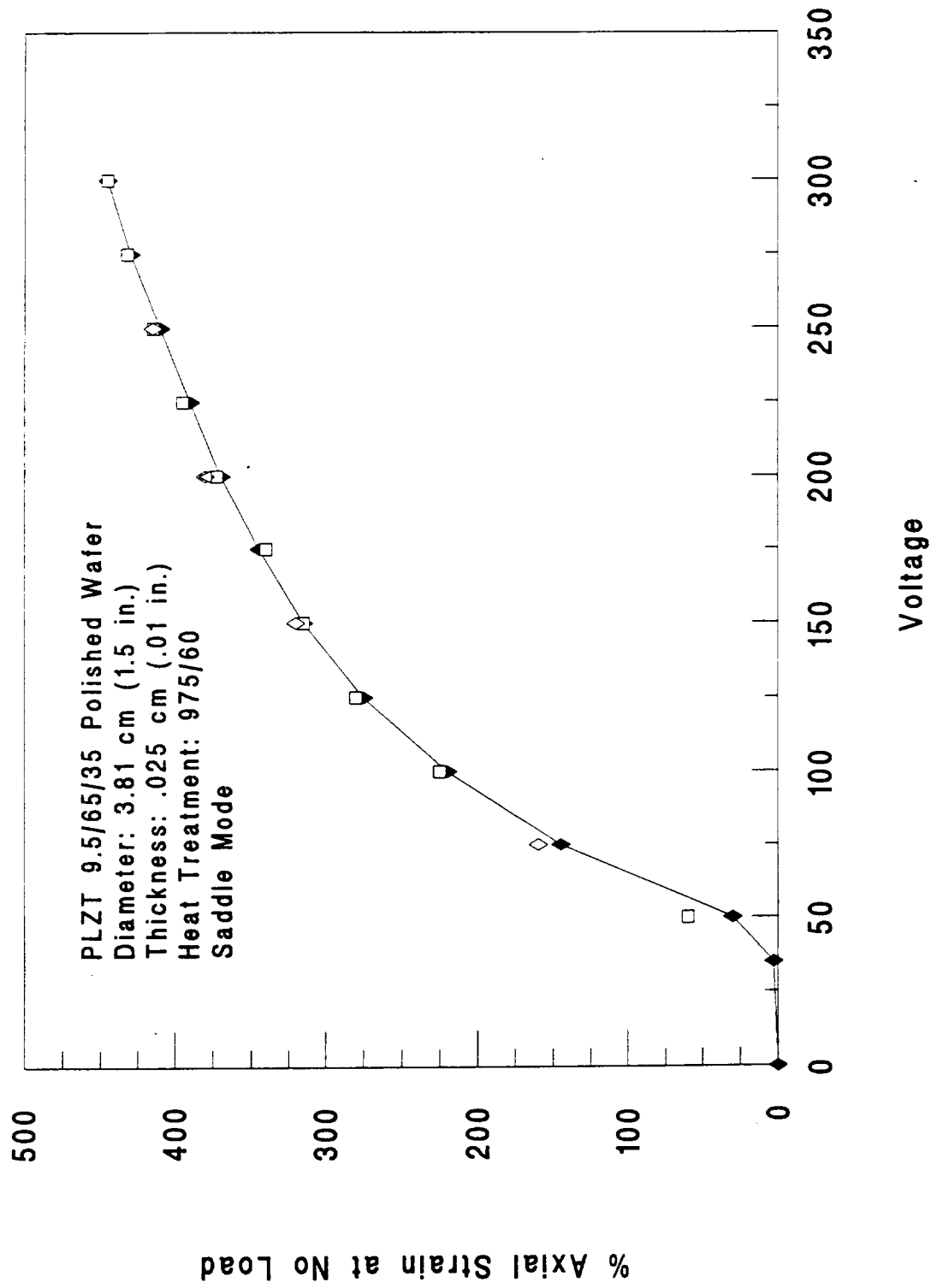


Figure 29. Voltage Dependent % Axial Strain Hysteresis Characteristics of PLZT 9.5/65/35 Polished Rainbow Wafers (open symbols are randomly selected voltages)



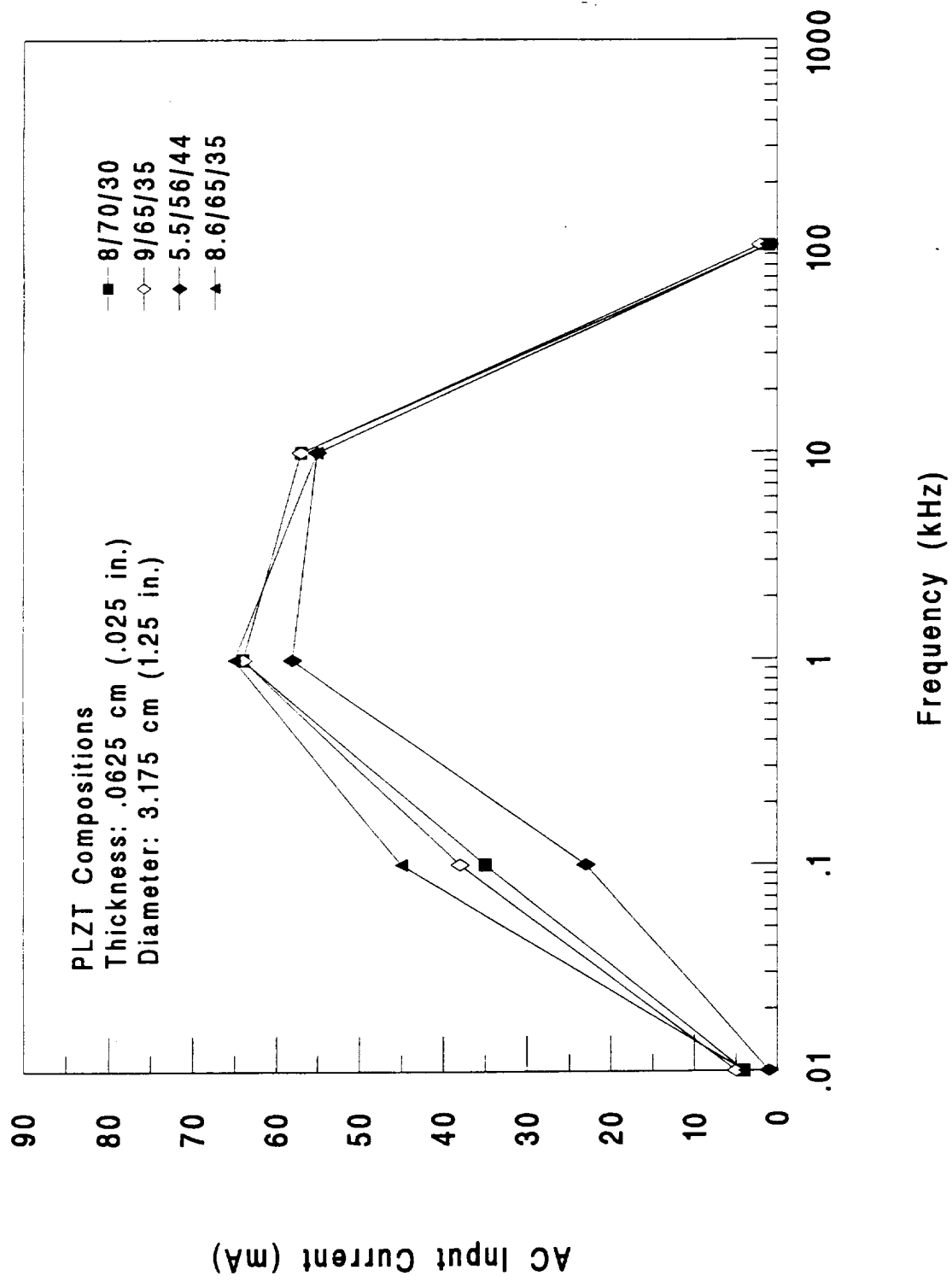


Figure 30. Effect of Operating Frequency on AC Input Current

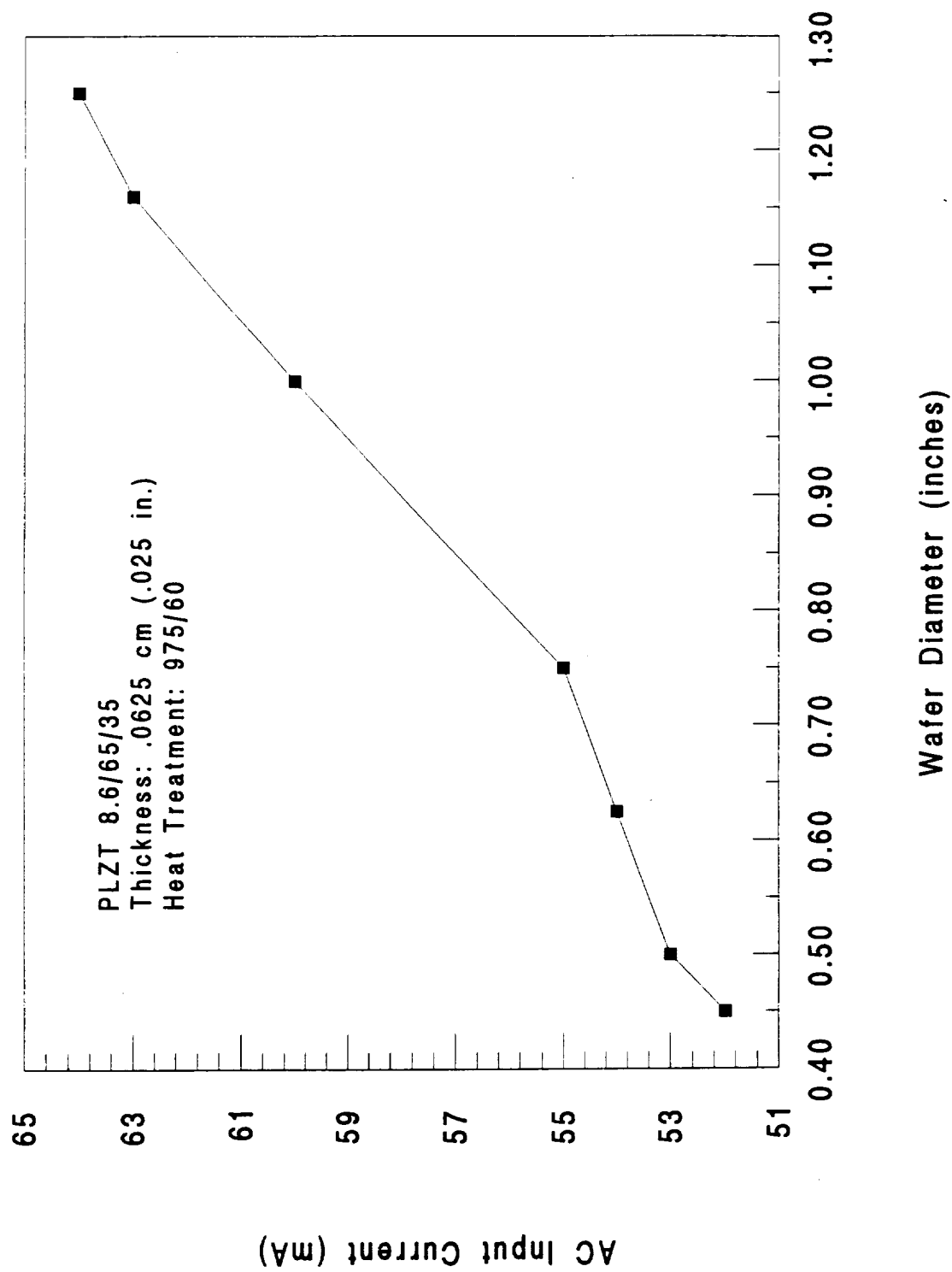


Figure 31. Effect of Wafer Diameter on AC Input Current

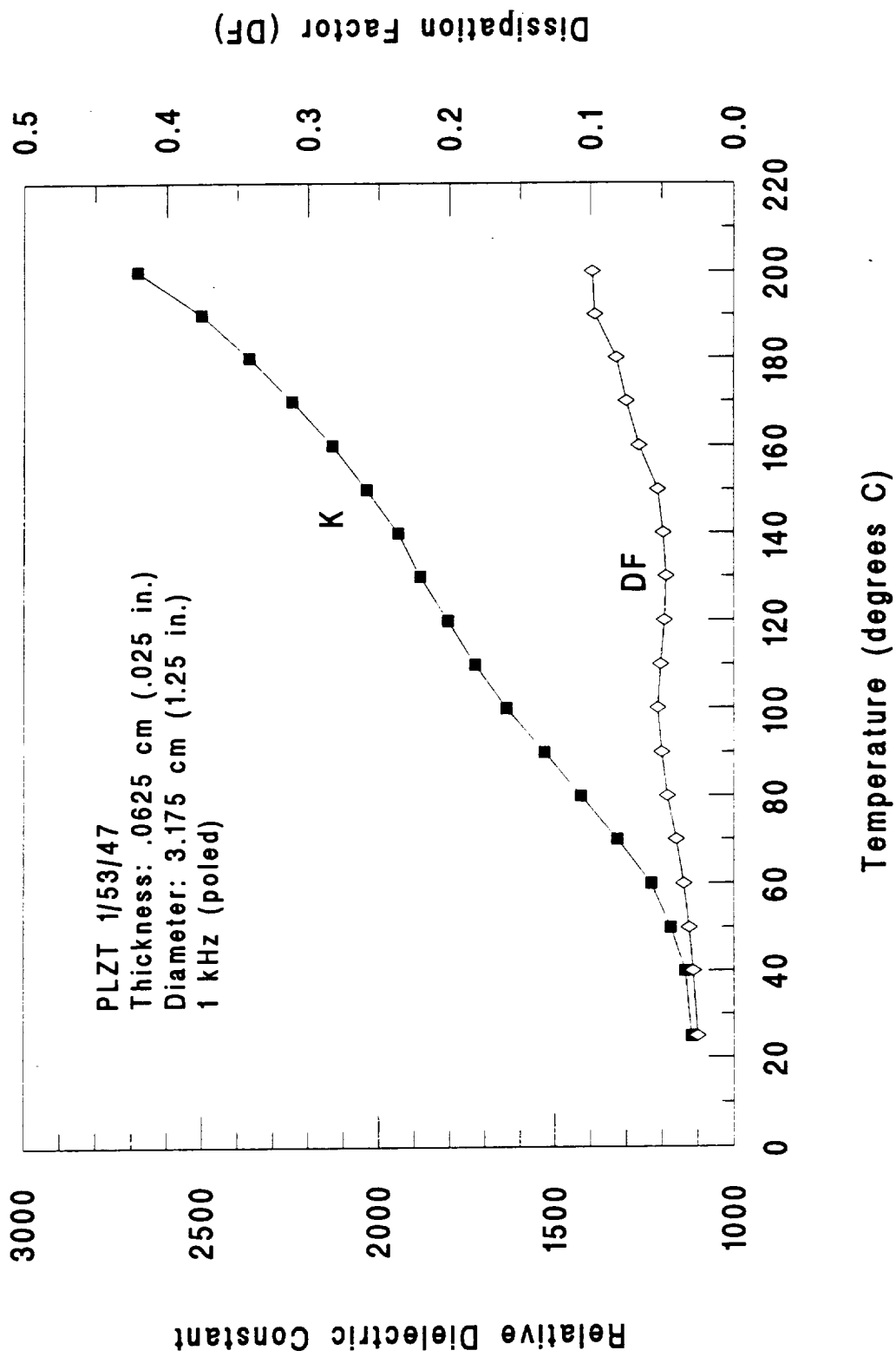
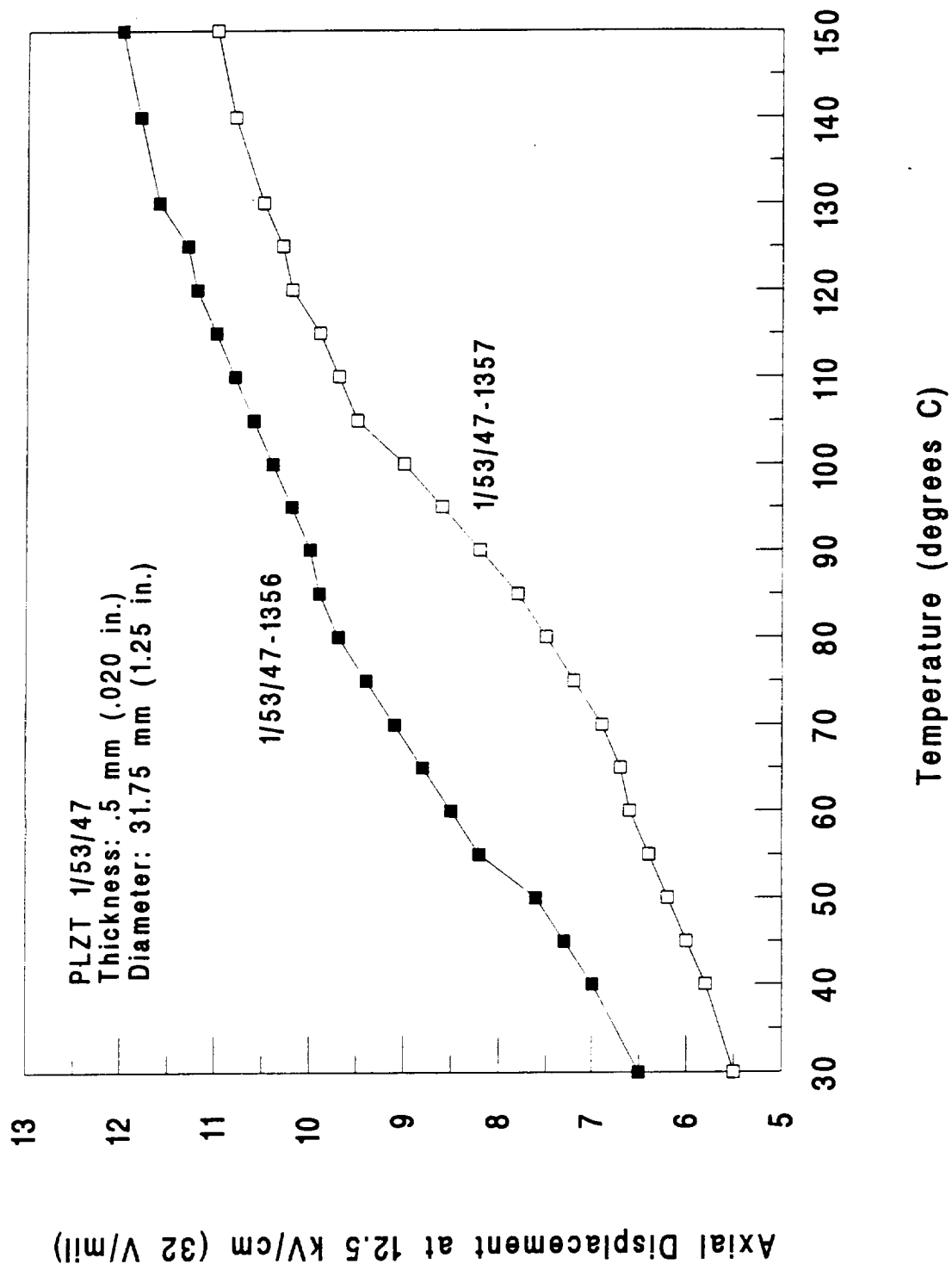


Figure 53. Temperature Dependent Dielectric Properties of PLZT Rainbow Wafers



Temperature Dependence of Axial Displacement for two batches of PLZT  
1/53/47 Rainbow Wafers

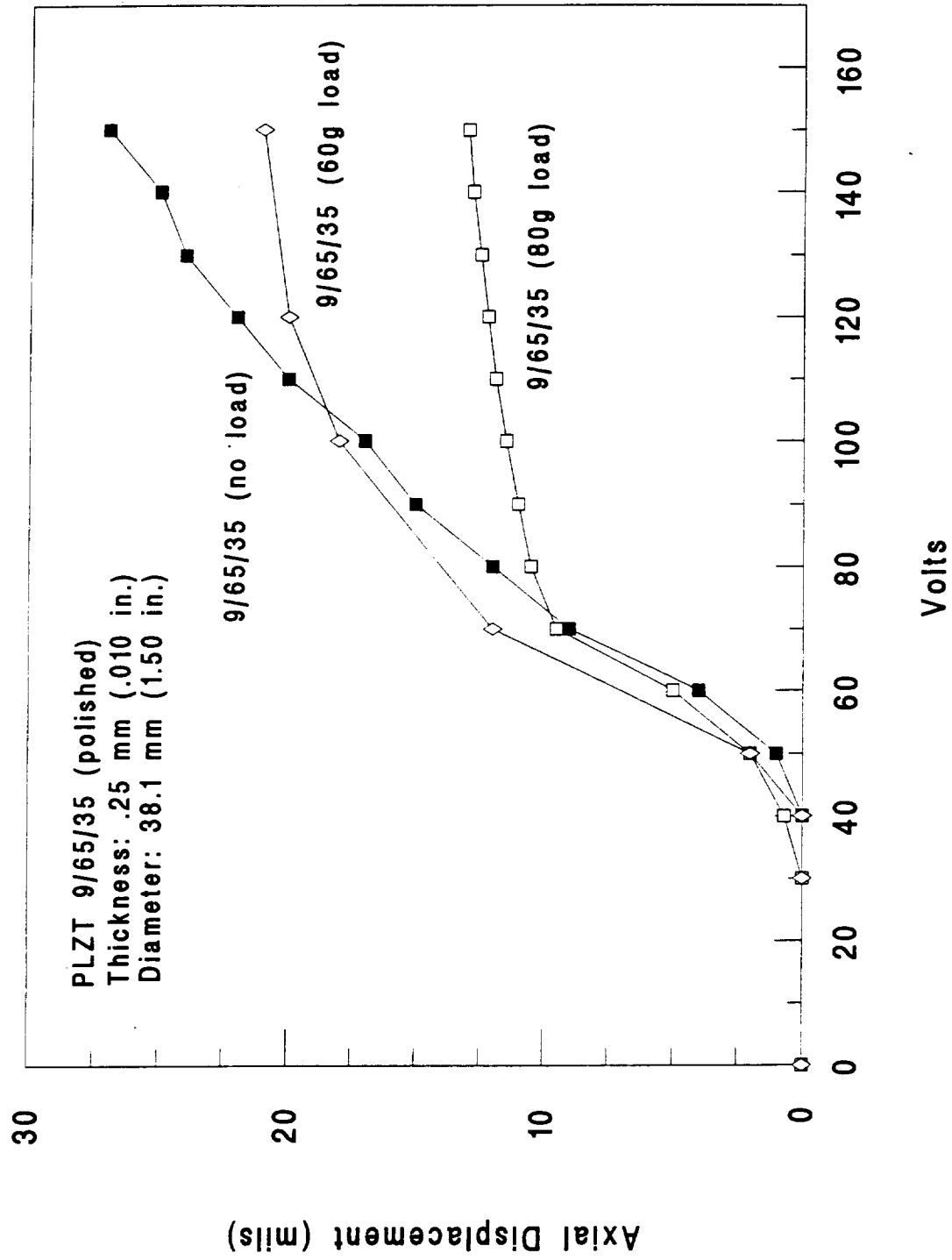


Figure 62. Voltage Dependent Axial Displacement for PLZT 9/65/35 under No Load and Loaded Conditions (Saddle-Mode Operation)

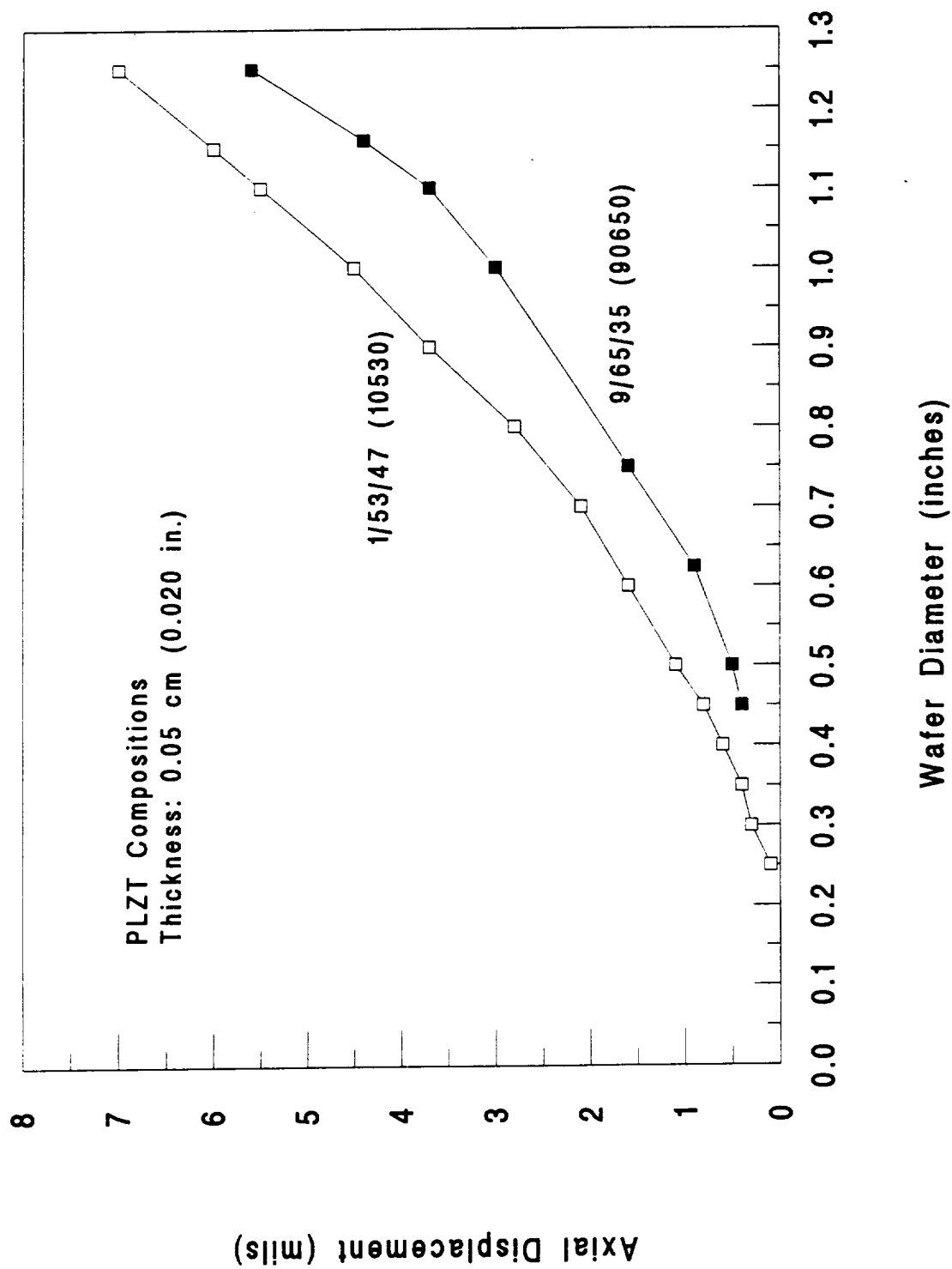


Figure 51. Variation of Axial Displacement as a Function of PLZT Rainbow Wafer Diameter

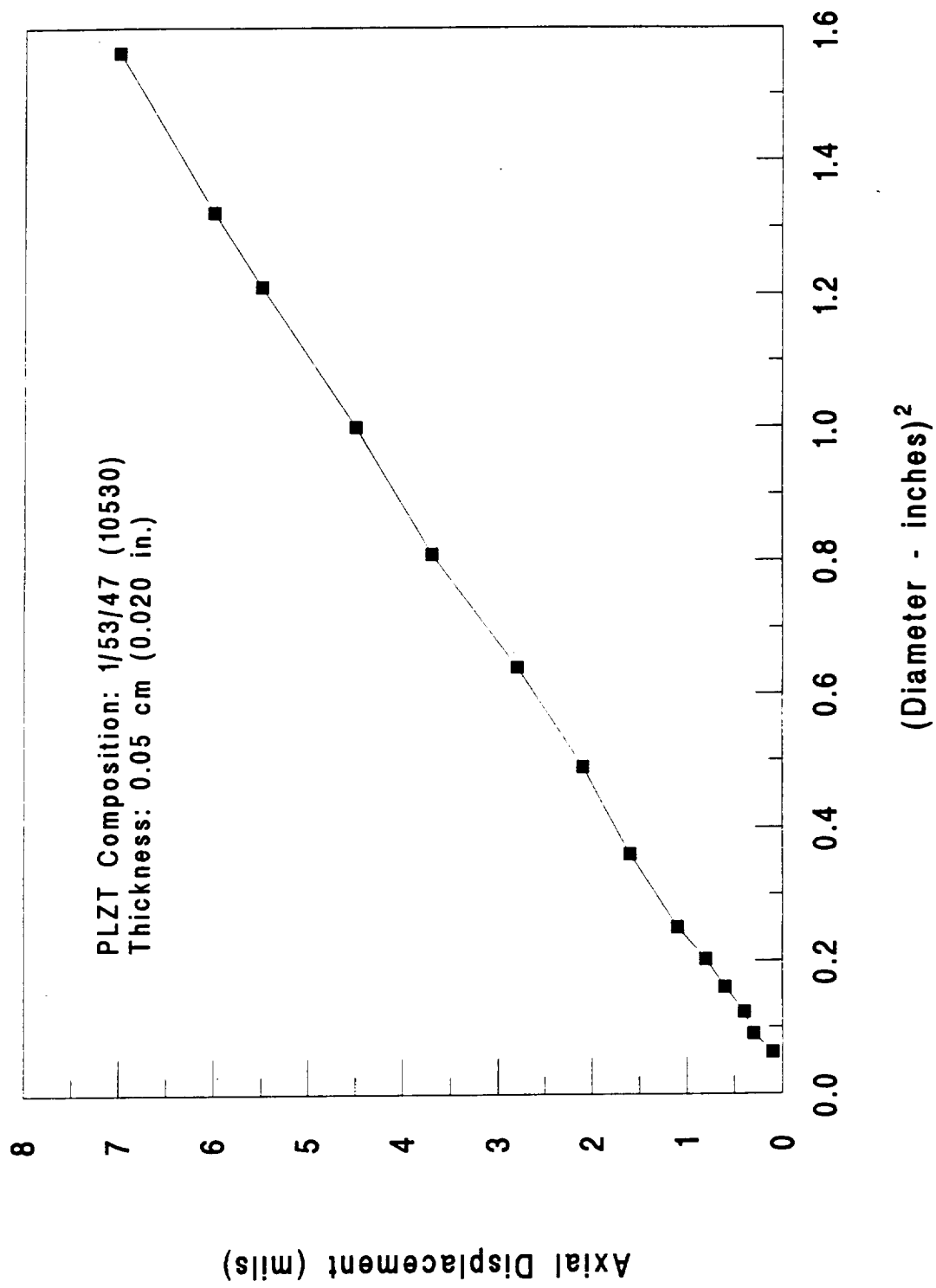


Figure 52. Axial Displacement as a Function of the Wafer Diameter Squared

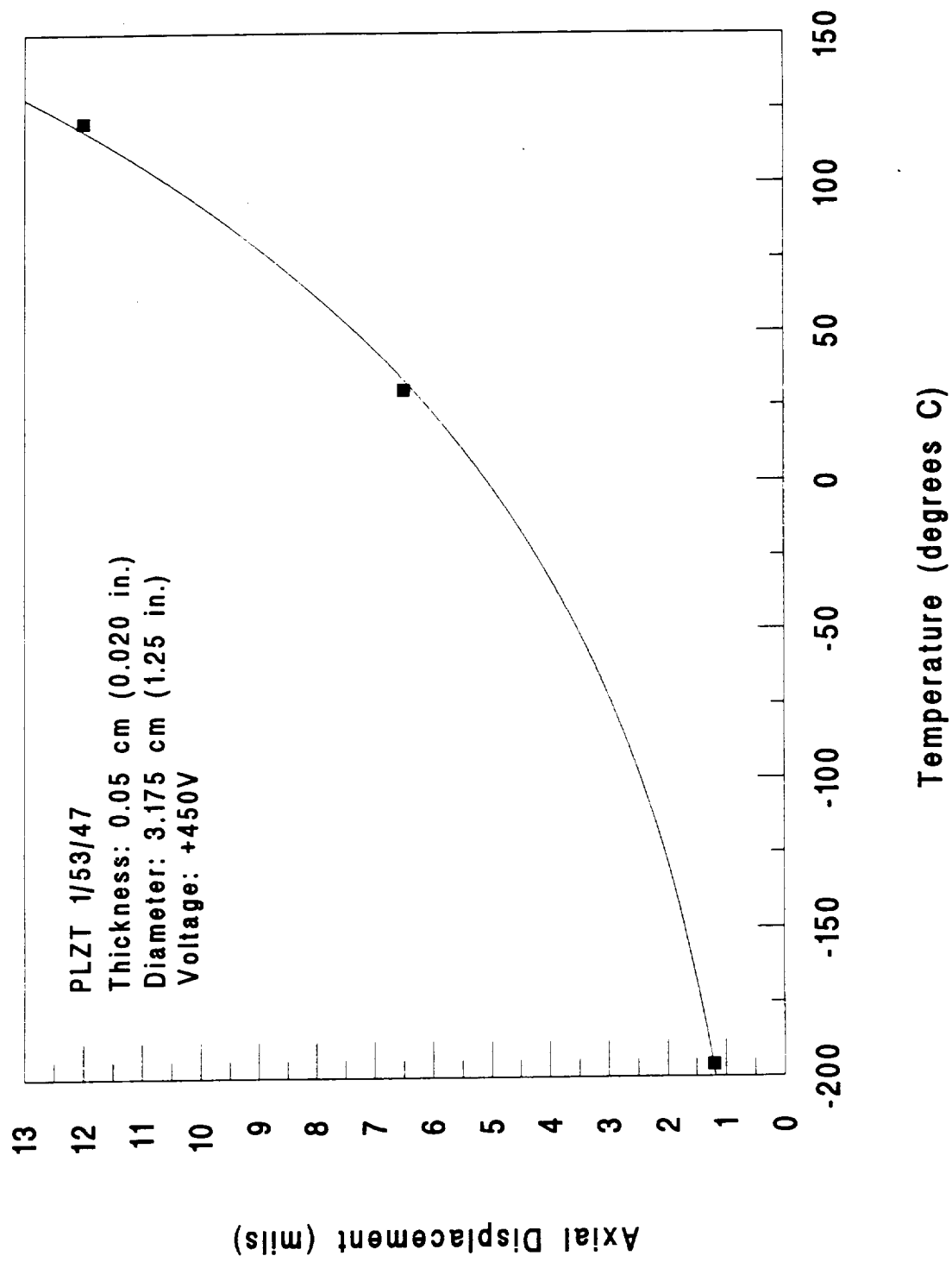


Figure 54. Variation of Axial Displacement as a Function of Temperature for PLZT 1/53/47 Rainbow Wafer



Table 1. Performance Specifications for Rainbow Wafers

d (wafer diameter)																					
t mil	0.5			0.75			1			1.25			1.5			1.75			2		
	y mil	L lb.	S %	y mil	L lb.	S %	y mil	L lb.	S %	y mil	L lb.	S %	y mil	L lb.	S %	y mil	L lb.	S %	y mil	L lb.	S %
6	14	0.7	233	21	0.5	350	28	0.4	467	35	0.3	583	42	0.3	49	0.2	817	56	0.2	933	
8	8	1.3	100	12	0.9	150	18	0.6	200	20	0.5	250	23	0.4	27	0.4	338	31	0.3	388	
10	5	2	50	8	1.3	80	10	1	100	13	0.8	130	15	0.7	18	0.6	180	20	0.5	200	
15	2	4.5	13.3	3	3	20	4	2.3	26.7	6	1.8	40	7	1.5	8	1.3	53.3	9	1.1	60	
20	1.3	8	6.5	1.9	5.3	9.5	2.5	4	12.5	3	3.2	15	3.8	2.7	4.5	4.5	2.3	22.5	5	2	25
25	0.8	12.5	3.2	1.2	8.3	4.8	1.6	6.3	6.4	2	5	8	2.4	4.2	2.8	2.8	3.8	11.3	3.2	3.1	12.8
30	0.6	18	2	0.8	12	2.7	1.1	9	3.7	1.4	7.2	4.7	1.7	6	1.9	1.9	5.1	6.3	2.2	4.5	7.3
35	0.4	24.5	1.1	0.6	16.3	1.7	0.8	12.3	2.3	1	9.8	2.9	1.2	8.2	1.4	1.4	7	4	1.6	6.1	4.6
40	0.3	32	0.8	0.5	21.3	1.3	0.6	16	1.5	0.8	12.8	2	0.9	10.7	1.1	1.1	9.1	2.8	1.3	8	3.3
45	0.3	40.5	0.7	0.4	27	0.9	0.5	20.3	1.1	0.6	16.2	1.3	0.7	13.5	0.9	0.9	11.8	2	1	10.1	2.2
50	0.2	50	0.4	0.3	33.3	0.6	0.4	25	0.8	0.5	20	1	0.6	16.7	0.7	0.7	14.3	1.4	0.8	12.5	2
55	0.2	60.5	0.3	0.3	40.3	0.5	0.3	30.3	0.6	0.4	24.2	0.7	0.5	20.2	0.6	0.6	17.3	1.1	0.7	15.1	1.3
60	0.1	72.1	0.2	0.2	48	0.3	0.3	36	0.5	0.4	26.8	0.7	0.4	24	0.5	0.5	20.6	0.8	0.6	18	1

Notes:

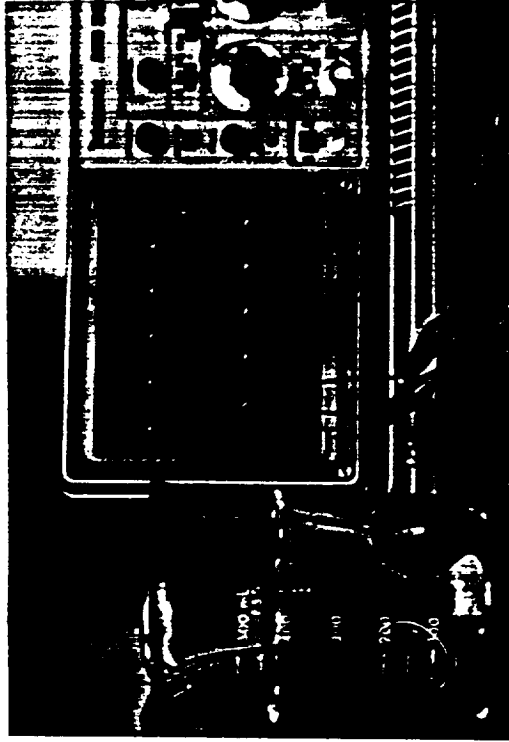
L = Load in pounds

S = Strain in percent (based on wafer thickness)

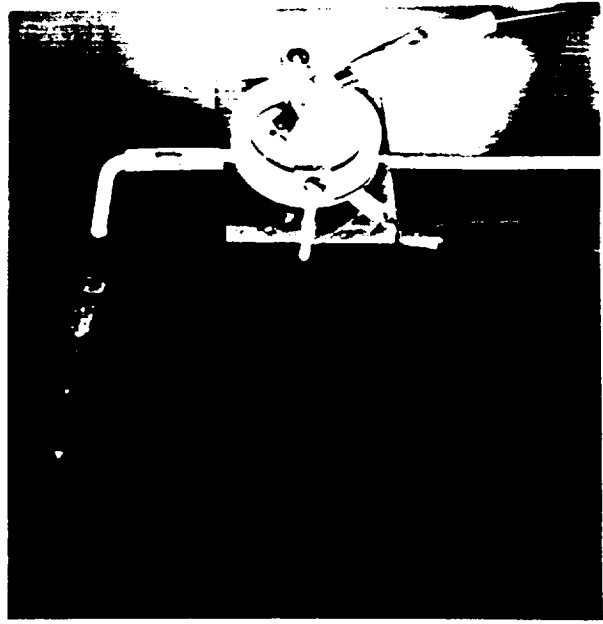
t = Wafer thickness in mils

d = Wafer diameter in inches

y = Wafer axial displacement in mils

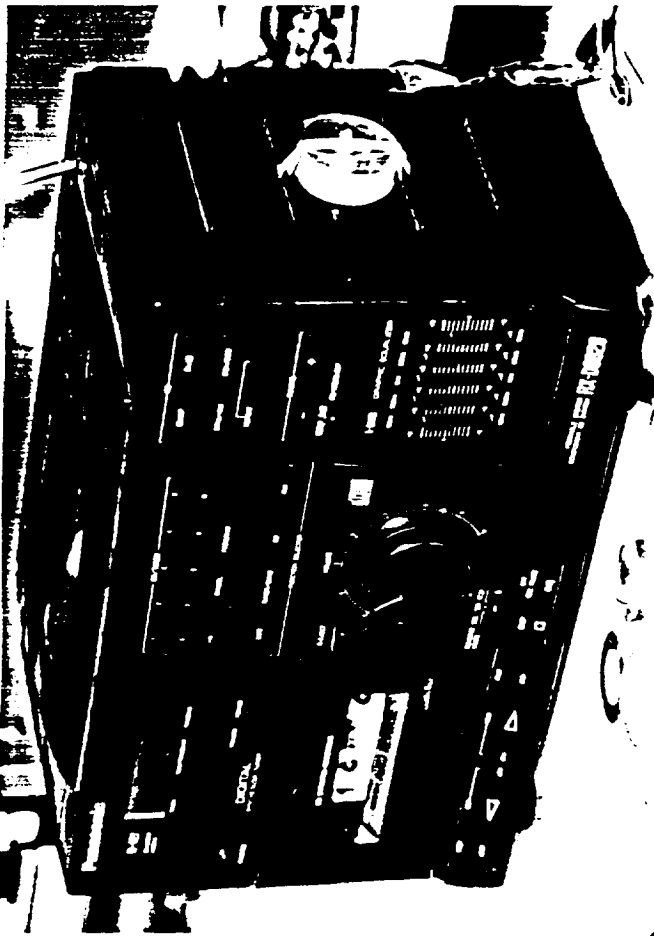


Hydrophones

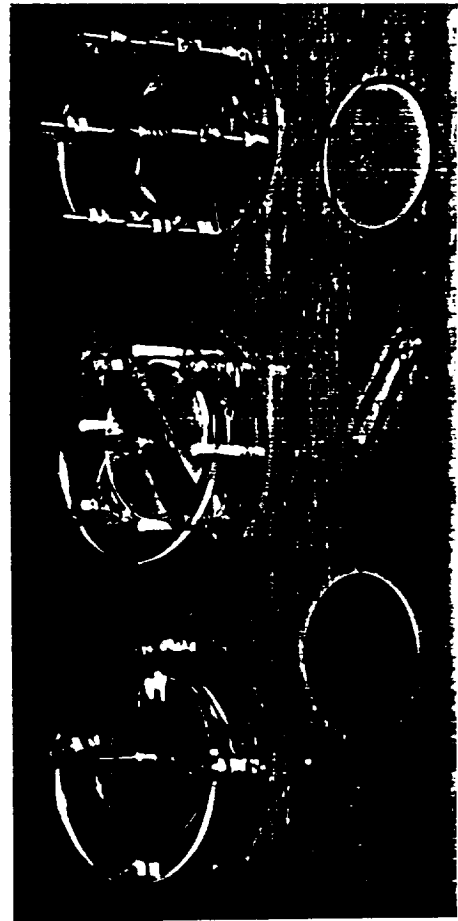


Pumps

## DEVICES



Speakers



Motors

**Part V.**

**Presentations and Publications**

### **Presentations**

1. C.S. Hsi, G.H. Haertling and J.D. Buckley, "Electrical Properties of Y- and Bi-Based Superconducting Thick Films Printed on  $\text{ZrO}_2$  Substrates," ACS 95th Annual Meeting, Cincinnati, OH, April, 1993
2. C.S. Hsi, G.H. Haertling and E.C. Skaar, "Computer Modeling of the Voltage Distribution in the Electrodes on a Superconductor," ACS 95th Annual Meeting, Cincinnati, OH, April, 1993
3. G. Li and G. Haertling, "Dielectric and Electrostrictive Properties of  $(\text{Pb}_{1-x}\text{Ba}_x)(\text{Zr}_{1-y}\text{Ti}_y)\text{O}_3$  Ceramics," ACS 95th Annual Meeting, Cincinnati, OH, April, 1993
4. E. Furman, G. Li and G.H. Haertling, "Modeling of Rainbow Devices," SE Section Meeting of the ACS, Charlotte, NC, July, 1993
5. J.P. Guha, G. Li and G.H. Haertling, "Dielectric and Piezoelectric Properties of Doped Lead Magnesium Niobate-Based Relaxors," SE Section Meeting of the ACS, Charlotte, NC, July, 1993
6. G.H. Haertling, "Monolithic, Multifunction, Ultra-High Displacement Actuators - A New Technology," ACS 95th Annual Meeting, Cincinnati, OH, April, 1993

### **Publications**

1. G. Li and G. Haertling, "The Electrostrictive and Related Properties of  $(\text{Pb}_{1-x}\text{Ba}_x)\text{Bi}_2(\text{Zr}_{1-y}\text{Ti}_y)\text{O}_3$  Ceramic System, Proceedings of 8th ISAF, pp. 569-572, Greenville, SC, September, 1992
2. C.S. Hsi, G.H. Haertling and E. Furman, "The Use of YBCO and BSCCO Electrodes to PLZT 9.5/65/35," Appl. Phys. Lett., (in press)

1. The first part of the document is a list of names and titles, including "The Hon. Mr. Justice" and "The Hon. Mr. Justice".

DEVICES: COMMERCIAL USE OF SPACE

Annual Report

to

Aeronautics and Space Administration  
Langley Research Center  
Hampton, VA 23665-5225

Period: July 3, 1992 - July 2, 1993

by  
e Haertling

Gene Furman

Shiung Hsi  
ng Li

September 6, 1993

---

The Gilbert C. Robinson  
Department of Ceramic Engineering  
College of Engineering